8-2018

Analysis of Metallic Shielding for Reduction of RF Induced Heating of Electrode During MRI for Active Implants

Krishna M. Singhal

ANALYSIS OF METALLIC SHIELDING FOR REDUCTION OF RF INDUCED HEATING OF ELECTRODE DURING MRI FOR ACTIVE IMPLANTS

by

Krishna Mukesh Singhal

A Dissertation

Submitted to the Faculty of Purdue University

In Partial Fulfillment of the Requirements for the degree of

Doctor of Philosophy

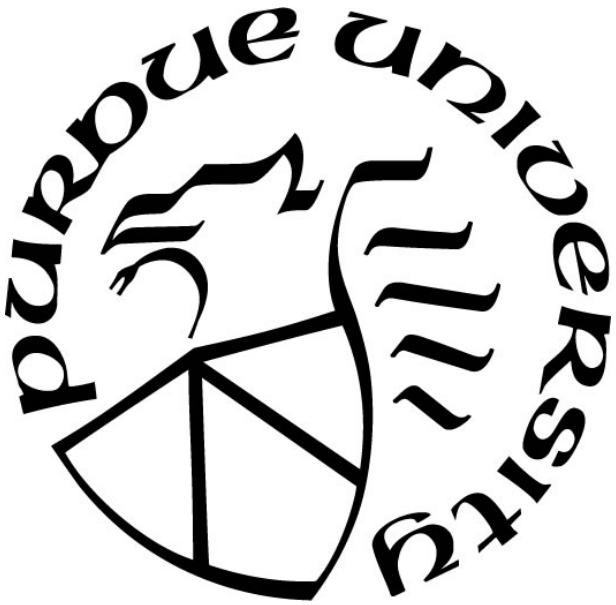

School of Electrical & Computer Engineering

West Lafayette, Indiana

August 2018

THE PURDUE UNIVERSITY GRADUATE SCHOOL
STATEMENT OF COMMITTEE APPROVAL

Dr. John A. Nyenhuis
School of Electrical & Computer Engineering
Dr. Thomas M. Talavage
School of Electrical & Computer Engineering
Dr. Mark R. Bell
School of Electrical & Computer Engineering
Dr. Joseph Rispoli
Weldon School of Biomedical Engineering

Approved by:

Dr. Venkataramanan (Raghu) Balakrishnan
Head of the Graduate Program

To my Family

श्रीमती विर्मा देवी*, Shri Mukesh Singhal, Smt Kumkum Singhal, Dr. Ashita Singhal*

ACKNOWLEDGMENTS

I would like to acknowledge the financial support of Purdue University over the course of this Ph.D. I am forever indebted to my research advisor, Prof. John A. Nyenhuis for supporting and mentoring me through this incredible journey. On all the projects, he has provided me with opportunities to develop both technical and personal skills and has been a role model for me in both these aspects.

I would also like to thank my committee members Prof Thomas Talavage, Prof Mark Bell and Prof Joseph Rispoli for their guidance, expert knowledge and taking time out to have essential discussions during my Ph.D. I am thankful to Prof Matthew Ohland, with whom I was a teaching assistant. Special thanks go to the excellent first year engineering operations teams – Jim, Jill, Dianne, Anne, Janet, and Rick. Thanks go to Prof Dhaval Pujara. I would have never considered further studies if it was not for the encouragement and guidance of Prof Dhaval Pujara during my undergraduate years at Nirma University.

For making Electrical Engineering building such a pleasant and comfortable place to work in, I would like to thank Matt Golden, Lacy, Steve, Cathy, and Bob. I would also like to thank Dr. Jigar Rajpura and Dr. Himanshu Joshi for guiding and mentoring me in situations outside of my research work. My friends have supported me and celebrated with me through good times and bad, and made this a journey to remember. Thanks are due to Sibhendhu, Sudhanshu, Dr. Ashish Vora, Dr. Atish Parekh, Punyasloka, Shikhar, Kshitiz, Angad, Mayank, Dr. Piyush Dak, Dr Harshad Lalit, Dr. Dev Verma, Tushar, K.N.S Vikrant, Surya A., Dr. Tejasvi P., Saikiran A, Soubhagya, Adarsh, Jwalant and Jose Rivera.

Lastly, and most importantly, I would like to thank my grandmother Smt Virma Devi, my parents Shri Mukesh Singhal and Smt Kumkum Singhal for everything they have taught me. They have always been the most prominent role model in my life. Words cannot describe the sacrifices and commitment they have done for me. Thanks to my sister Dr. Ashita Singhal, for sharing in most, if not all, of my interests and adventures. Finally, thanks to my entire family for the selfless love they have given me all my life, which I can never repay.

TABLE OF CONTENTS

LIST OF TABLES

LIST OF FIGURES

ABSTRACT

Author: Singhal, Krishna, M. PhD
Institution: Purdue University
Degree Received: August 2018
Title: Analysis of Metallic Shielding for Reduction of RF-Induced Heating of Electrode during MRI for Active Implants
Major Professor: John A. Nyenhuis

The options available to patients with implantable devices are limited. It is because there are multiple interactions between the MRI environment and the implantable medical devices. The three main components of MRI systems- static magnet, RF coil, and a gradient coil- interact with the implantable medical devices. These interactions can cause force, torque, device vibrations and RF-induced heating. Among all these potential hazards is the heating caused by the RF electromagnetic field. The lead wires of the implants can act as antennas and pick up the electric field generated by the RF coil. This results in the induced current traveling along the length of the device that will dissipate as heat where it is coupled to tissue. The combination of critically sensitive tissues and high heat makes this interaction the most significant risk for patient safety. Hence, there arises a need to design effective techniques that can minimize RF heating induced during an MRI. The technique of shielding has been proven to reduce RF-induced heating.

The focus of current research is to provide analysis of shielding technique for reduction of RF-induced heating of electrodes during MRI. Shielded leads have been developed as a method to reduce RF-heating responsible for temperature rise at the electrodes. The purpose of this work is to provide a quantitative understanding of how a conducting metallic shield over a lead will reduce RF heating at the electrode during MRI scans. A physical model and equations for reduction of RF heating by a shielded lead are presented. Temperature rises are calculated for different lengths of shielded and unshielded leads. Confirming measurements are made for a quarter-wavelength coaxial cable model of the lead. Measured temperature rise and transfer function depended on terminations

conditions, with the shorted lead exhibiting the temperature rise sixteen times less than an open-ended lead.

The information provided by this work is expected to facilitate the development of lead wires with reduced RF-induced heating. The availability of lead wires with reduced heating will allow expanded access to MRI by patients with implantable devices.

1. INTRODUCTION

1.1 Motivation

Magnetic Resonance Imaging (MRI) has become an essential imaging modality over the past three decades. The global demand for MRI imaging has more than doubled from 18 million scans in 2001 to 40 million scans in 2018 [1]. It is expected that the global MRI market which is valued at $27.4 billion in 2017, will reach $51.3 billion by the end of 2025, growing at a compound annual growth rate of 8.2% during 2018-2025 [2].

A recent study conducted on patients with spinal cord stimulation (SCS) implants estimated that about 84% of SCS-implanted patients will need an MRI scan within five years of receiving their SCS implant [3]. The number of joint reconstructions and spinal cord implant surgeries performed in UK, Germany, France, Spain, and Italy combined is expected to rise from 2.8 million in 2018 to more than 3.5 million in 2023. It is estimated that 19% of the population of these countries who are over the age of 65 years having orthopedic implants will rise to 30.5 % in 2020 [4].

Table 1.1 Prediction of the rise in surgical procedures and % of the population with implants [4]

	USA		European Countries	
Year	**2015**	**2020**	**2015**	**2020**
Procedures	**>2.6 M**	**>3.1 M**	**>3 M**	**>3.4 M**
Total Population	**322 M**	**345 M**	**321 M**	**326 M**
% with Implant	**3.1%**	**5.6%**	**3.9%**	**7.2 %**
Total 65+	**48 M**	**56 M**	**63 M**	**68 M**
%65+ with implant	**21.6%**	**31.3%**	**13.3%**	**28%**

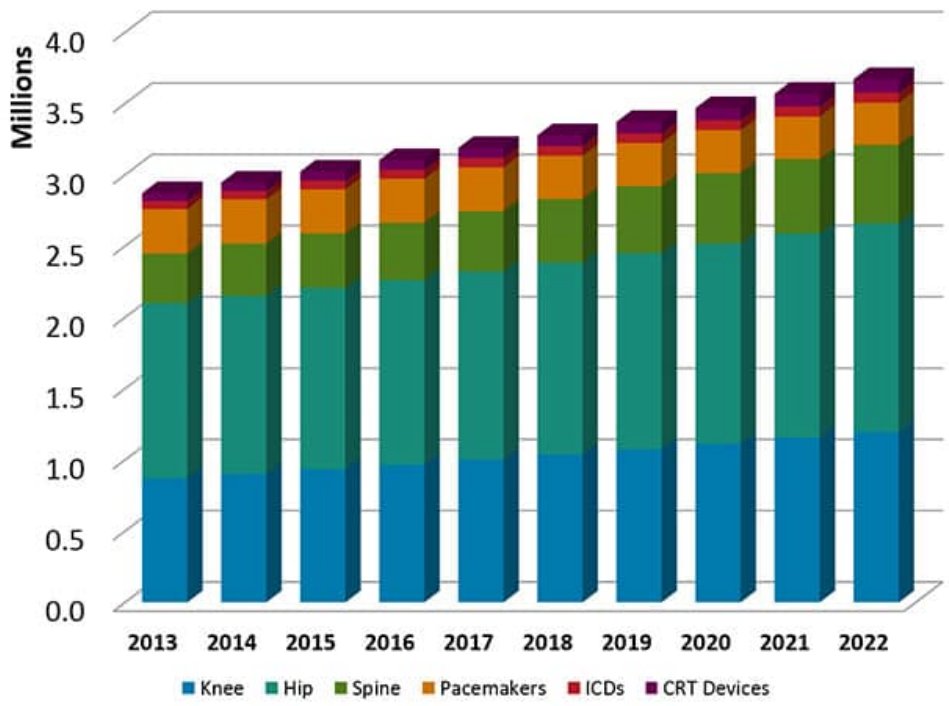

Figure 1.1 Forecast of the number of surgical procedures per year in Europe [4]

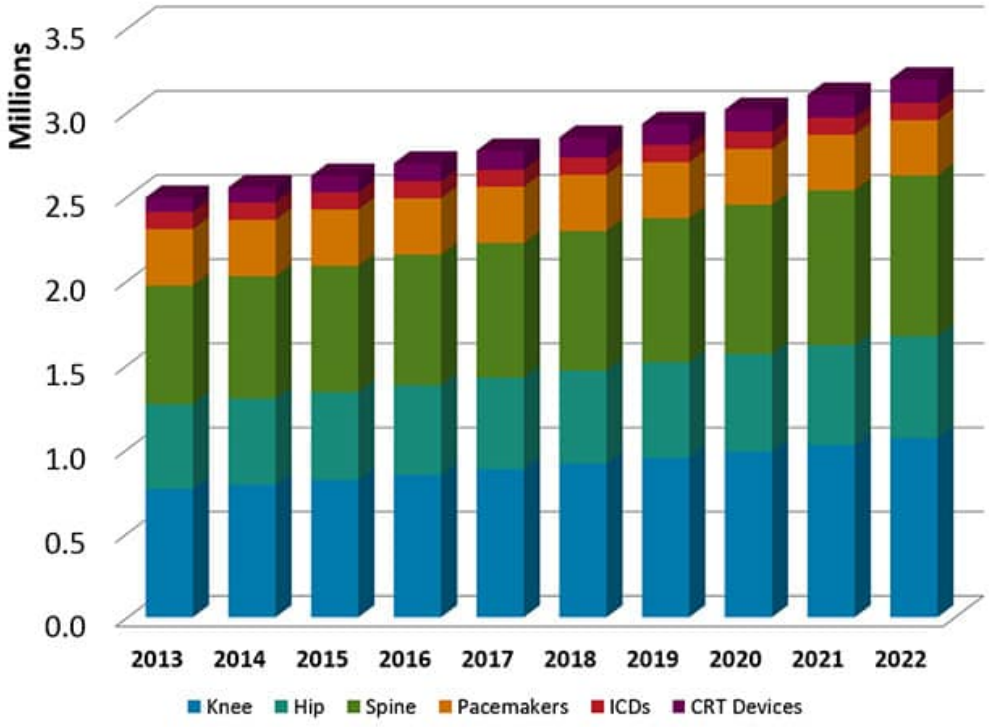

Figure 1.2 Forecast of the number of surgical procedures per year in the USA [4]

Hip and knee arthroplasty is projected to increase by 175% and 673%, respectively, from 2005 to 2030. It is also estimated that revision surgeries of total knee and total hip replacements will grow exponentially until 2030. Furthermore, the cardiac implant that is present in 4% of the population over 65 years of age is expected to rise to 12% in 2025 [4]. Currently, in the USA, 17% of the population over 65 years have a joint or spinal implant, and 10.4% of the same population have a cardiac implant. It is expected that these figures will rise to 26% and 11.8% respectively.

The projections as described above require accurate and cost-effective imaging modalities to diagnose complications arising due to implants and for post surgeries observations. Besides with the increased presence of medical implants in older people, the likelihood that the average person will need an MRI scan during the next ten years increases with age from around 47% at the age of 30, to about 69% at the age of 70 [4, 5].

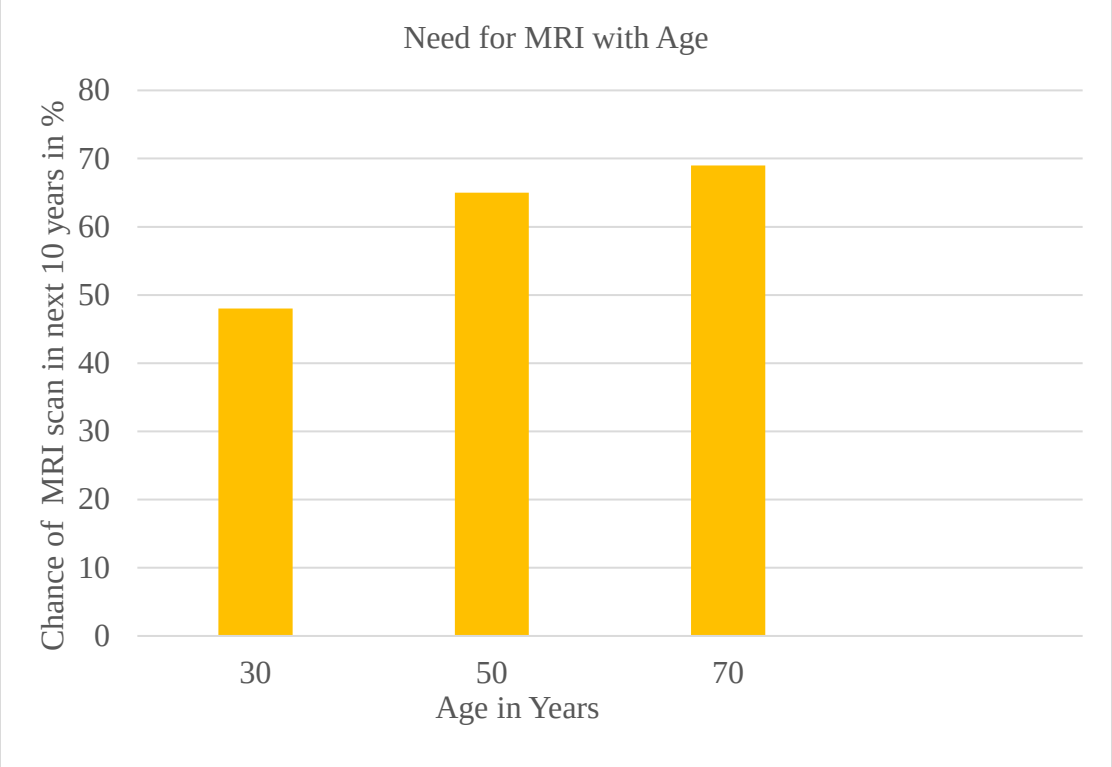

Figure 1.3 Estimation of the need for MRI with age in years [4]

For patients with implantable devices, there is a significant clinical need to undergo an MRI scan. However, due to safety concerns, patients carrying metallic medical implant or device may potentially be denied an MRI scan [6]. For some patients that require multiple MRI scans, let us say a cancer patient, for example, no therapy is possible for this patient, if a patient has multiple implantable devices; due to MRI safety concerns.

The other option available to patients with implantable devices is computed tomography (CT) scans or X-rays, i.e., instead of an MRI, these patients can undergo a CT scan. However, this is not an ideal option, as it possesses ionizing radiation. The third option would be the removal of the implantable device, receiving an MRI and then re-implantation of the device. This option results in exposing patients to multiple surgeries, which is not practical.

While X-ray is a first-look low-cost imaging modality, it should be noted that medical professional prefers MRI scan over other imaging modalities as it provides higher contrast and excellent resolution of images of various soft tissues. MRI is an excellent imaging modality for imaging organs, soft tissue with internal structures. MRI scans use non-ionizing radiation. When used instead of computed tomography (CT), MRI mitigates the significant health risks of ionizing radiation present in CT scans [7, 8]. On the other hand, CT scan is suitable for imaging bone, soft tissue, and blood vessels at the same time or imaging tissues with bony structures, evaluating lung/chest tissues, etc.

However, there are other hazards associated with MRI. The magnetic fields in the MR environments can present serious hazards to patients with implantable metallic devices. The three main components of MRI systems are a static magnet, an RF coil, and a gradient coil. Each of these can interact with an implantable metallic device [9]. These components generate a strong static magnetic field, an RF electromagnetic field, and a gradient field respectively, to form images of the body's tissues. The static magnet is a strong magnet and can cause force, torque, and vibration. RF electromagnetic fields can induce currents on the surface which results in heating [10]. Gradient fields cause unintended stimulation and device vibration. Among all these potential hazards is the heating caused by the RF electromagnetic field. The oscillating magnetic field of the RF coils generates an electrical

field within the human body. If an implantable device has metallic leads or wires, they can act as antennas and pick up the electrical field generated by the RF coils. The result is an electrical current traveling along the length of the device that will dissipate as heat where it is coupled to the tissue. The combination of tissues and heat makes this interaction the most significant risk for patient safety [11-14]. Hence, there arises a need to develop effective techniques that can minimize RF-induced heating to design implants that are MR safe for patients and do not possess any safety concern to patients during an MRI scan.

1.2 Components of MRI System

The first clinical MRI images were obtained in 1977. MRI uses a magnetic field and radio frequency rather than ionizing radiation used in X-ray and CT. The magnetic field strength of the MRI machine is measured in Tesla. Most MRI systems in clinical practice are 1.5 T or 3 T. These produce an extremely strong magnetic field up to 50000 times that of earth's magnetic field.

The body is made up of 70% water, which is composed of hydrogen and oxygen atoms. MRI relies on the magnetic properties of hydrogen atoms to produce images. The hydrogen nucleus is comprised of a single proton with no neutrons. As a spinning charged particle, this generates a magnetic field called magnetic moment. Usually, the protons are orientated randomly.

The components of the MRI system include primary magnets, gradient magnets, radio frequency coils and computer system. The primary magnetic field refers to the strength of the static permanent field. Hydrogen atoms align parallel or antiparallel to the primary magnetic field B_0. This is called longitudinal magnetization in the long axis of the magnetic field. A higher proportion of the hydrogen protons align in the direction parallel to the primary magnetic field (low energy state) than align anti-parallel to the primary magnetic field (high-energy state). The net result, called the net magnetic vector is therefore in the direction of the primary magnetic field. This is the patient's long axis. The protons spin around the long axis of the primary magnetic field. This is called precession. The precession rate is termed the Larmor frequency.

The gradient coils generate a secondary magnetic field over the primary field. They are located within the bore of the primary magnet. They are arranged in opposition to each other to produce a positive and negative pulse. The arrangement of these gradient coils gives MRI the capacity to image directionally along x,y, and z-axis. There are three gradient coils, which are named as per the axis along which they act. Gradient magnets alter the strength of the primary magnetic field, thereby changing the precession frequency between slices. This can then be used for slice selection or localization called spatial encoding of MR images. The z gradient runs along the longitudinal axis to produces axial images. The y gradient runs along the vertical axis to produce coronal images, and the x gradient runs along the horizontal axis to produce sagittal images.

The radiofrequency coils are used for transmitting RF pulse and receiving signals in MRI. They come in various design. The RF coil is used to transmit a second magnetic field or RF pulse, which results in the disturbance of the proton alignment, some low energy parallel protons flip to a high-energy state decreasing longitudinal magnetization. Secondly, protons become synchronized and precess in phase. As a result, the net magnetization vector turns towards the transverse plane, i.e., right angles to the primary magnetic field. This is known as transverse magnetization. The RF coil is used to receive the signal to create images as protons resume their normal state in the primary magnetic field before transmission of the RF pulse. This is called relaxation. The time constants of the relaxation in the longitudinal axis (parallel to B0) is T1 and in the transverse axis (perpendicular to B0) is T2. After the RF pulse, several protons flip back to their low energy state parallel to magnetic field z-axis giving energy to the surrounding. This results in changes to the T1 relaxation. After the RF pulse, protons that were in phase begin to diphase out of the Larmor frequency in the transverse axis. This results in changes to T2 relaxation.

The net magnetic vector is the sum of longitudinal and transverse magnetization. The net magnetic vector spirals around z-axis with net precession. The changing magnetic moment of the net magnetic vector results in free induction decay. This induces an electrical signal. The computer system receives the RF signal and performs an A/D conversion. The digital signal representing the image body part is stored in the temporary

image space called k-space vector. Fourier transform is applied to the digital signal and image of MRI scan is displayed on the monitor.

1.3 Review of techniques of RF-induced heating

Evaluation of RF-induced heating and RF characterization for implants is the focus of research nowadays. There is not much significant progress to study methods to reduce RF-induced heating for implants since last 15 years. In this chapter some of the design strategies that are in place to reduce RF heating.

Liu *et al.* [15-18] investigated the effects of an insulating layer material to reduce RF-induced heating for an external fixation system in 1.5 T MRI systems. For external fixation devices, he studied the impact of clamp spacing, insertion depth and material properties of a bar on RF-induced heating. It was concluded that shorter insertion depth, longer clamp spacing, and metallic connection bar contribute to higher temperature rise at the tip of the pin of these devices. During an MRI, currents are induced on metallic surfaces of the device. These induced currents travel towards the pin of the device, resulting in RF heating at the tip region. Isolating the pin from the metallic surface of the device can reduce the energy propagation onto the pin from other metallic components. Therefore, an insulating layer was kept between the pin and the clamp. Electrical properties of the insulating layer were varied to reduce RF heating. This study shows that a low permittivity material would reduce the RF heating. However, a higher permittivity material can increase the RF induced heating as it increases capacitive coupling of RF fields between pins and clamps. It was observed that using this method with appropriate electrical properties of the insulating material there is a 46 % reduction in the induced current and 67% reduction in RF-induced heating at the tip of the pin region.

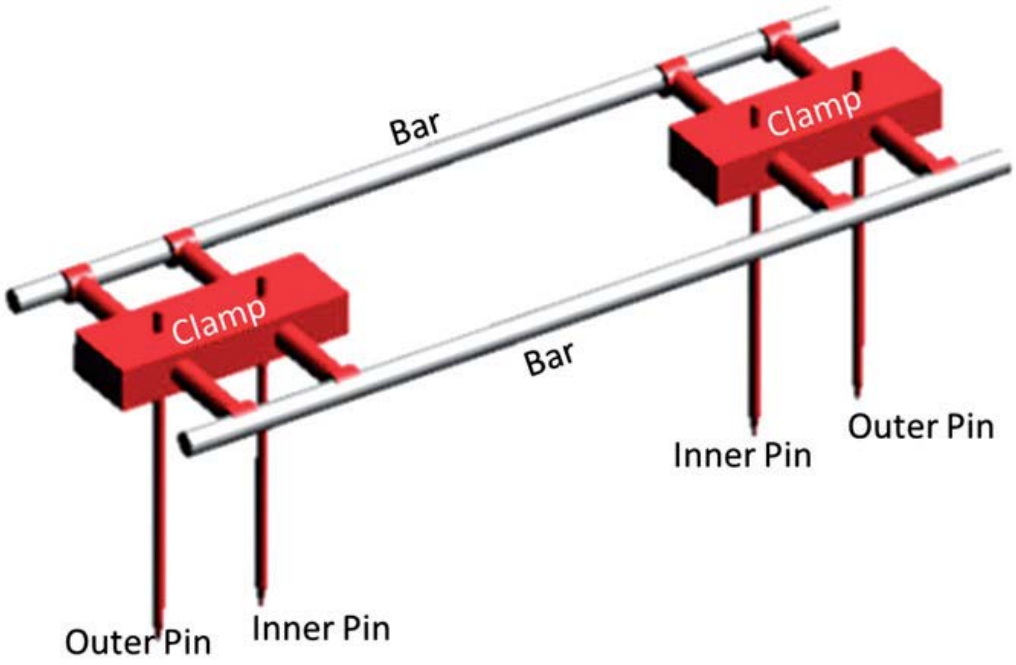

Figure 1.4 External fixation model structure [16]

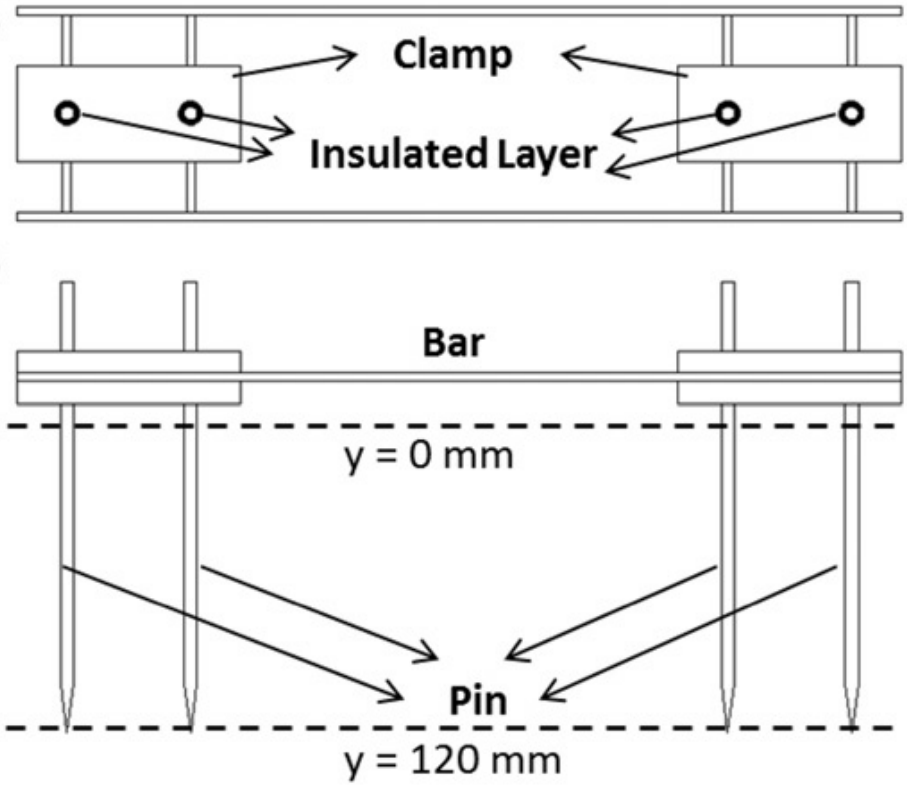

Figure 1.5 Position of the insulating layer to isolate pin from the metallic surface [16]

Huang *et al*. [19-21] proposed the use of an absorptive material instead of insulating material to reduce the RF-induced heating of external fixators. Huang's method used specific materials optimized for external fixator. Response Surface Methodology was used to search optimal parameters (permittivity, permeability, and conductivity) for the absorption material.

For the device with no absorptive material, the temperature rise was measured to be about 4.2^{o}C. However, temperature rise for the same device having absorptive material at two locations, one between clamps and pins and other between clamps and bars, was found to be 1.7^{o}C. It was concluded that the material could absorb part of RF induced energy between the bar, and the clamp of the medical device. Secondly, proper placement of the absorptive material can also alter the induced current and localized heating around the medical device. The drawback of this technique is the material used to reduce RF-induced heating is non-biocompatible. It is challenging when applied to implants.

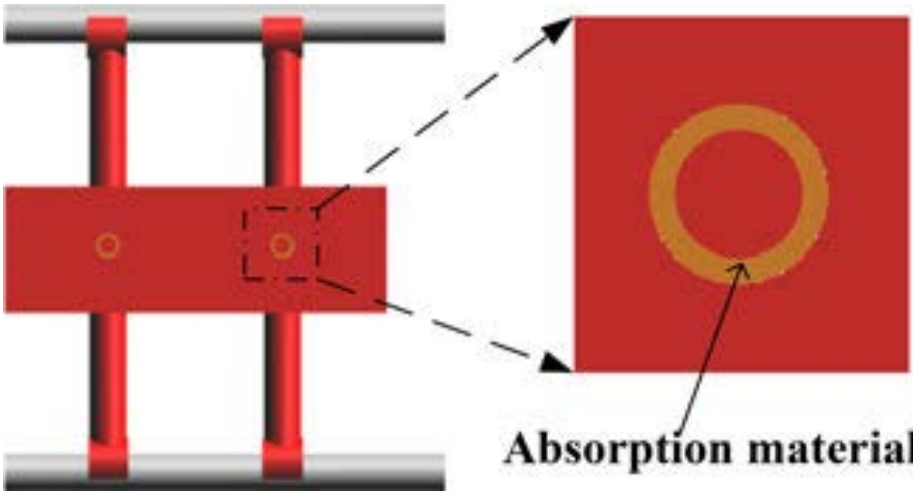

Figure 1.6 Geometry of absorption material on the external fixation device [19]. The material could absorb part of RF induced energy between the bar, and the clamp of the medical device. Secondly, proper placement of the absorptive material can also alter the induced current and localized heating around the medical device. Response Surface Methodology was used to search optimal parameters (permittivity, permeability, and conductivity) for the absorption material.

McCabe *et al*. [22-29] proposed a technique of decoy wire to minimize RF-induced heating. McCabe's method attached an additional bare conductor called a decoy to the exterior of the lead. The coupling between the decoy and the lead minimizes H-field around the conductor. This result in a reduction of RF induced current along the surface of the device during MRI. As a result, RF-induced heating is significantly reduced.

Simulations were performed to validate the concept of decoy in our FDTD solver for 3T/128MHz. The geometry of the decoy is shown in Figure 1.7. Rod radius is 0.4 mm, and insulation thickness is 0.35 mm. 6 mm insulation is stripped at one of the ends. The relative permittivity of insulation is 2.54. The maximum temperature rise of 2.248ºC was obtained for a 25 cm electrode with two decoys. The diameter of the decoy is 0.4 mm. The length of the decoy is 70% of electrode length. The maximum temperature rise of 8.854 ºC was obtained for an electrode with no decoy. McCabe reported temperature rise of 2.4 ºC for a 25 cm electrode with 70% decoy length. This is in good agreement with our simulations results with FDTD solver. This validates our simulation setup.

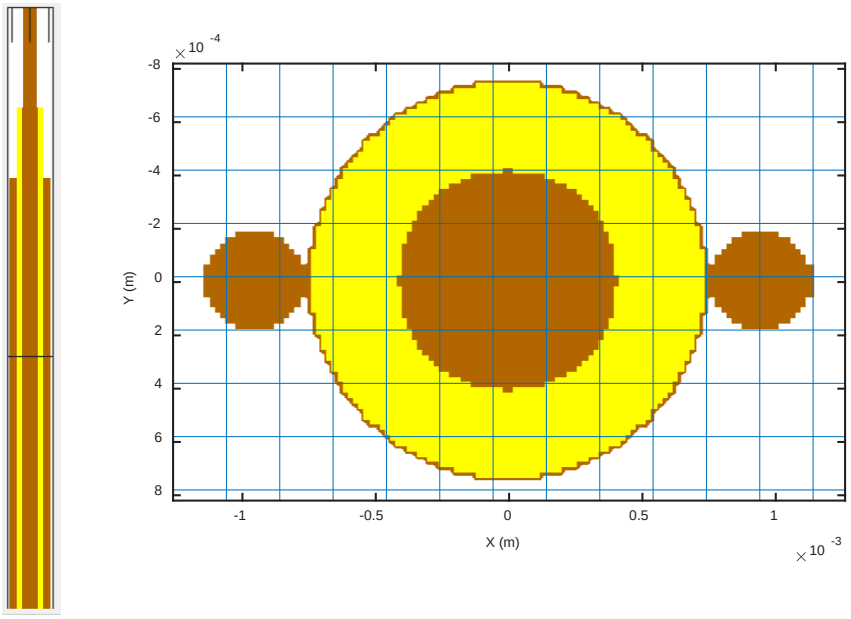

Figure 1.7 Geometry of electrode with two decoys [25] Left is the view in the x-z plane. Right is the cross-sectional view. The outer brown rods are the decoys. The yellow color is the insulation, and the inner brown section is the central conductor. The coupling between the decoy and the lead minimizes H-field around the conductor. This result in a reduction of RF induced current along the surface of the device during MRI. As a result, RF-induced heating is significantly reduced.

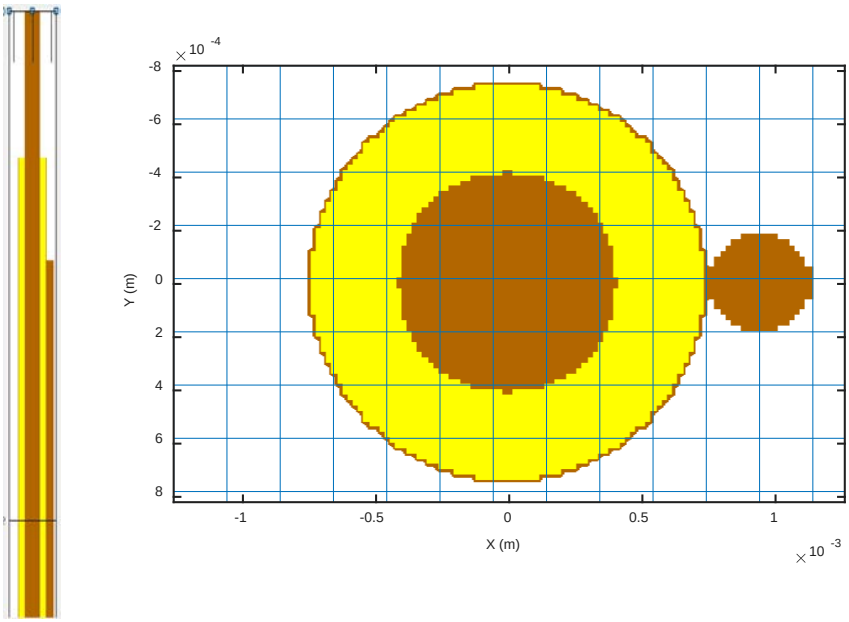

Figure 1.8 Geometry of electrode with one decoy. Left is the view in the x-z plane. Right is the cross-sectional view. The outer brown rod is the decoy. The yellow color is the insulation, and the inner brown section is the central conductor. The coupling between the decoy and the lead minimizes H-field around the conductor. This result in a reduction of RF induced current along the surface of the device during MRI. As a result, RF-induced heating is significantly reduced.

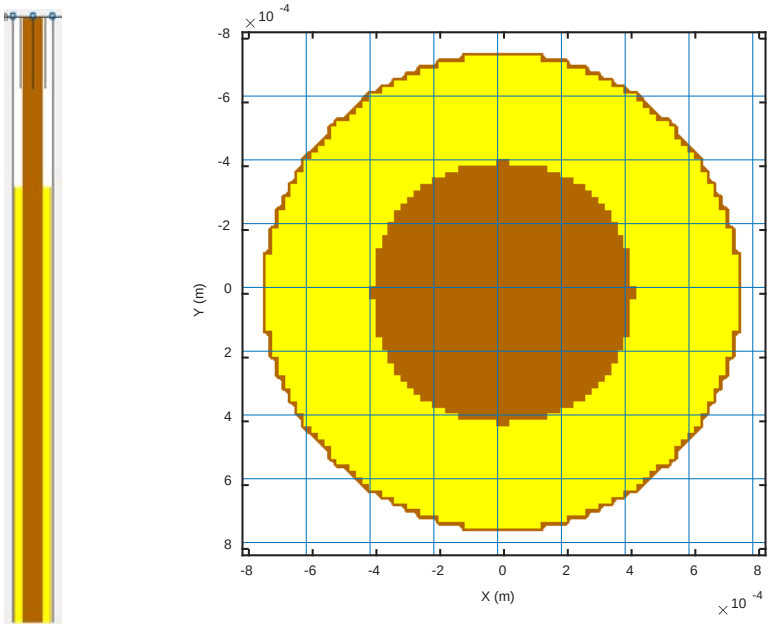

Figure 1.9 Geometry of electrode with no decoys. Left is the view in the x-z plane. Right is the cross-sectional view. The yellow color is the insulation, and the inner brown section is the central conductor.

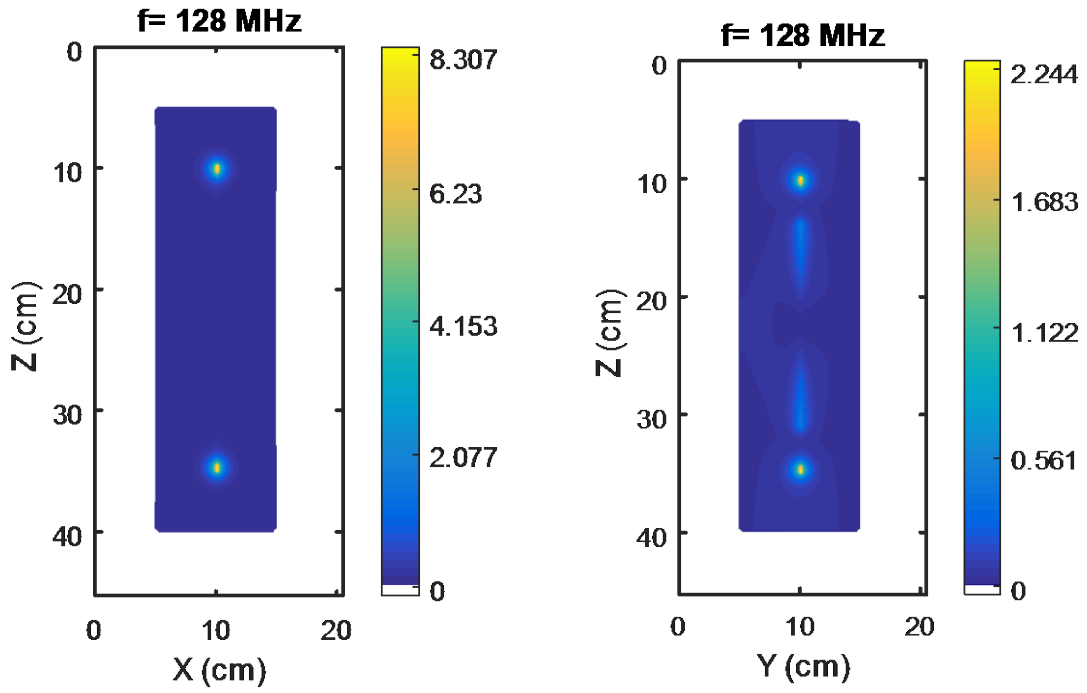

Figure 1.10 Calculated temperature rise for an electrode with the decoy. Length of the electrode is 25 cm. Electrode with no decoy (left) and with two decoys (right). Decoy length is 70% of rod length. All calculations are at 128 MHz and normalized at SAR 1 W/kg.

X. Wang and Helfer *et al*. introduced the concept of magnetic coating [30-38]. They proposed a conductor assembly that contained a flexible conductor and a layer of nanomagnetic material coated on the surface of the conductor. The coating of nanoparticles consists of a mixture of aluminum oxide and iron. Size of these nanoparticles was 10 nm. Particle density was low to minimize electrical conductivity. These particles deflect electromagnetic fields while remaining electrically non-conductive.

They hypothesize that when an electromagnetic field is incident on this coating, it gets partially or totally absorbed and/or reflected and/or transmitted with phase change. The phase of this new wave is now changed. The currents induced have a different phase and is canceled. This prevents the formation of RF-induced currents in metallic objects. Reduction of currents leads to the elimination of RF-induced heating during MRI as the SAR deposited is reduced significantly. The nanomagnetic material comprises of iron, cobalt, and nickel, gadolinium and samarium atoms. To quantify the effectiveness of shielding, a heat-shielding factor is defined. It is the ratio of change in temperature of the

nanomagnetic coated shielded assembly when tested in accordance with ASTM 2182-11a to the change in temperature of the unshielded conductor using precisely the same test conditions but omitting the shield. Typical values range from 0.2-0.5 [31, 35].

Reduction of RF heating in intravascular catheters using coaxial chokes was investigated by Ladd *et al*. [39]. In this work, two chokes with the length of quarter wavelength were added to coaxial cables to reduce the RF induced current on the cable shield. Chokes were prepared by soldering a short between the primary and secondary shields of the coaxial cable at one end and removing the secondary shield at the other end. The space between the primary and secondary shields acts as a waveguide, which translates the short into a high impedance at the open end of the choke. Maximum temperature rise measured at the RF coil of a 0.7 mm Diameter cable was 55^{o}C. However, with a choke maximum temperature rise was measured to be 3.4^{o}C. All measurements were performed at 64 MHz MRI system. However, this method was ineffective when used in combination of a lead implant (where lead acts a dipole antenna during MRI interventions).

Bottomley *et al.* applied the concept of RF chokes to lead heating [40-47]. He investigated RF heating for various passive lead designs. The goal of his work was to compare the performance and develop implantable lead designs and strategies that could eliminate the hazards of heating during MRI. His hypothesis was to minimize the passage of RF currents induced in the lead during MRI. He investigated five different implant designs having bare electrodes both experimentally and theoretically, at 64 MHz EM simulations were performed using Method of Moments program. These different designs Figure 1.11 include (i) leads with chokes (ii) leads including RF traps (iii) ‘billabong’ leads with reversed sections (iv)coiled ‘billabong’ leads. The presence of chokes, traps and coiled segments increases the impedance of the lead.

Heating performance as a function of design parameters was compared to that of straight wire in various configurations at a local background SAR of 4W/kg and RF frequency of 64 MHz It was observed that the maximum temperature rise for all proposed design was less than 2^{o}C. For coiled leads, pitch and diameter played an important role in RF heating, with the temperature rise inversely proportional to both.

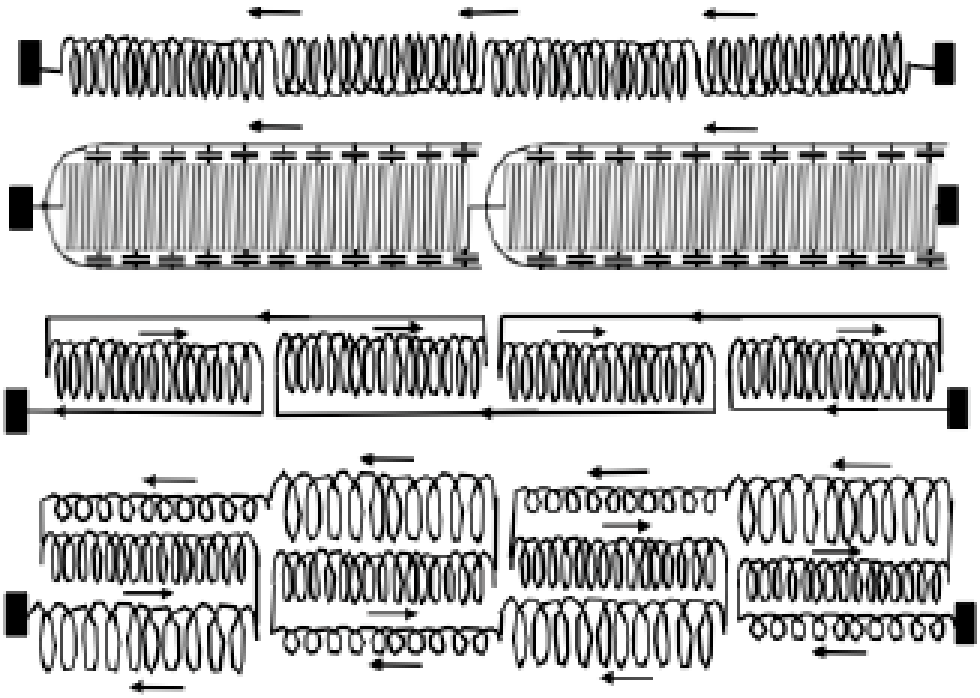

Figure 1.11 Implant designs as proposed by Bottomley *et al*. [46]. (i) leads with chokes (ii) leads with RF traps (iii) 'billabong' leads with reversed sections (iv) coiled 'billabong' leads

For leads with RF traps, an impedance of more than 0.8 kohm limited the temperature rise to less than 2^{o}C. However, minimum temperatures rise was exhibited for billabong leads with a triple coil layer billabong lead outperforming other designs and having a temperature rise of less than 1^{o}C. It was concluded that for simple, passive conductive leads connected to bare electrodes, insulation thickness, sample size, lead length and lead configuration could be optimized to reduce RF induced current during MRI scan. Thin insulation, high RF impedance, and short modular leads offer the best hope for the safety of leads connected to the bare electrode during MRI. It should be noted that the lead designs as proposed, were limited by the fabrication capabilities for practical implementation. Also, a lead with an RF trap does not consider variations in the implant environment and will not perform as expected during the entire life cycle of the implant.

Wahlstrand *et al*. [48-52] proposed the use of a jacket for housing conductive filar and providing a current path distributed along some portion of the length of the lead. He analyzed variations with a conductive jacket, dielectric jacket, porous jacket, multiple

jackets, etc. Serano *et al*. [53] proposed a novel resistive tapered stripline lead design that blocks RF fields induced by the MRI system to reduce temperature rise during lead heating. Readers are encourage referred to [54-62] for various other design aspects for lead heating.

1.4 Thesis Outline

Chapter 2: **BACKGROUND ON RF INDUCED HEATING OF ACTIVE IMPLANTS DURING MRI** provides background on the physics of RF-induced heating of active implants during MRI. RF heating mechanism is reviewed. Interaction of electric and magnetic fields with passive implants is discussed along with factors affecting RF heating. This chapter concludes with a brief description of computational methods to evaluate RF heating

Chapter 3: **CALCULATIONS AND MEASUREMENTS OF RF INDUCED HEATING FOR SHIELDED AND UNSHIELDED STRUCTURES WITHOUT METALLIC SHORT AT THE END** provides calculated and measured temperature rise values for shielded and unshielded model implants leads. Current calculations and parametric variations of the shield is discussed in this chapter.

Chapter 4: **CALCULATIONS AND MEASUREMENTS OF MRI INDUCED HEATING FOR SHIELDED AND UNSHIELDED STRUCTURES WITH METALLIC SHORT AT THE END** provides calculated and measured temperature rise values for shielded and unshielded model implants leads with a metallic short at the end.

Chapter 5: **MEASUREMENT OF ELECTRIC FIELD TRANSFER FUNCTION AND TEMPERATURE RISES FOR PROPOSED MODEL OF ELECTRODE** provides an introduction to transfer function concepts and materials and methods for experimental measurement of electric field transfer function. It presents results for measured and calculated temperature rise values for 80cm and 45cm model leads. Temperature rise values in this chapter are calculated using the measured transfer function.

Chapter 6: **TRANSMISSION LINE MODEL FOR THE SHIELDED LEAD WITH GENERATOR** is the main chapter of this dissertation, which provides a physical model of the shielded lead to understand the mechanism of RF heating for shielded and unshielded

model implants. Chapter 6 provides equations and mathematical understanding to use a shield at locations on the model implant to reduce RF heating. This chapter also validates the physical model by comparing the calculated transfer function from the model to the measured transfer function of 80 cm, and 45 cm model implant leads for different configurations.

Chapter 7: **EXPERIMENTAL VALIDATION AND CASE STUDY FOR A LEAD USED WITH A NEUROSTIMULATION SYSTEM** provides measurements of the transfer function and temperature rise values for Model 303 Cyberonics lead in different configurations. It also provides a comparison of measured values of temperature rise for different terminations and configurations to calculated values. Temperature rise is computed using the measured transfer function that is described in this chapter.

Chapter 8: **SUMMARY OF KEY ACCOMPLISHMENTS AND RECOMMENDATIONS FOR FUTURE WORK**. This chapter concludes the dissertation with the key accomplishments from this effort and directions for future work.

2. BACKGROUND ON RF INDUCED HEATING OF ACTIVE IMPLANTS DURING MRI

Implanted medical devices are categorized as passive and active implants. Passive devices generally do not use electrical power for their operation. Examples of passive devices include vascular stents, orthopedic implants such as replacement knees and hips and heart valves. Active implants use electrical power for their operation. Cardiac pacemakers and defibrillators, deep brain stimulators, spinal cord stimulators and cochlear implants are some of the examples of active devices.

Implanted devices are generally partly or entirely metallic. A distinguishing feature of a metal is that it has an electrical conductivity (~ 10^7 S/m) many orders of magnitude greater than that of tissue (~1 S/m). Thus, a metallic device in a tissue medium with a background electric field will scatter that background electric field in its vicinity. The background electric field in a tissue medium can also be due to external sources such as radio waves, security devices, occupational exposures and MRI scanning. The scattering of the background electric field present in the tissue medium will result in the localized heating near the implant. In the case of strong background electric field, such as those present during MRI exposure, the temperature rise may occur due to electromagnetic scattering. RF induced heating in the tissue medium due to this temperature rise tends to be greatest at the ends of the electrodes on the lead wire of an active implantable device.

Direct heating of the metal of an implant by the RF field is minimal compared to tissue heating. This is because the scattered electric field is concentrated at the implant ends. However, the metal of the implant may experience a temperature rise due to thermal transport from the surrounding warm tissues. At audio frequencies, direct heating of the metal due to induced eddy currents may be greater than that of heating of the tissue.

2.1 Review of RF heating Mechanism

The electric field in the patient is induced by the RF magnetic field referred to as the B_1 field. The RF magnetic field is applied in a direction perpendicular to the static magnetic field to induce precession in the nuclei of interest. It has a circular polarization with a cylindrical bore. The RF magnetic field has a frequency of 42.56 MHz multiplied by the static field strength in Tesla. Thus, for a field strength of 1.5T resulting RF frequency is 63.9 MHz and for 3T it is 127.7 MHz

A whole-body MRI System consists of a Human body and an appropriate coil. The RF field is applied with this coil, which typically is called Birdcage coil. It gets its name from the shape of the conductors. A representative coil has 16 arms along the length and two end-rings. Capacitors are placed on the arms and at the end rings so that the coil is at resonance at MR frequency. The current distribution in the birdcage coil is such that the overall polarization of the RF field is circular in nature. In circular polarization, rotation of RF field is synchronous with the precessing nuclear magnetization. This results in less power deposition in the patient [63]

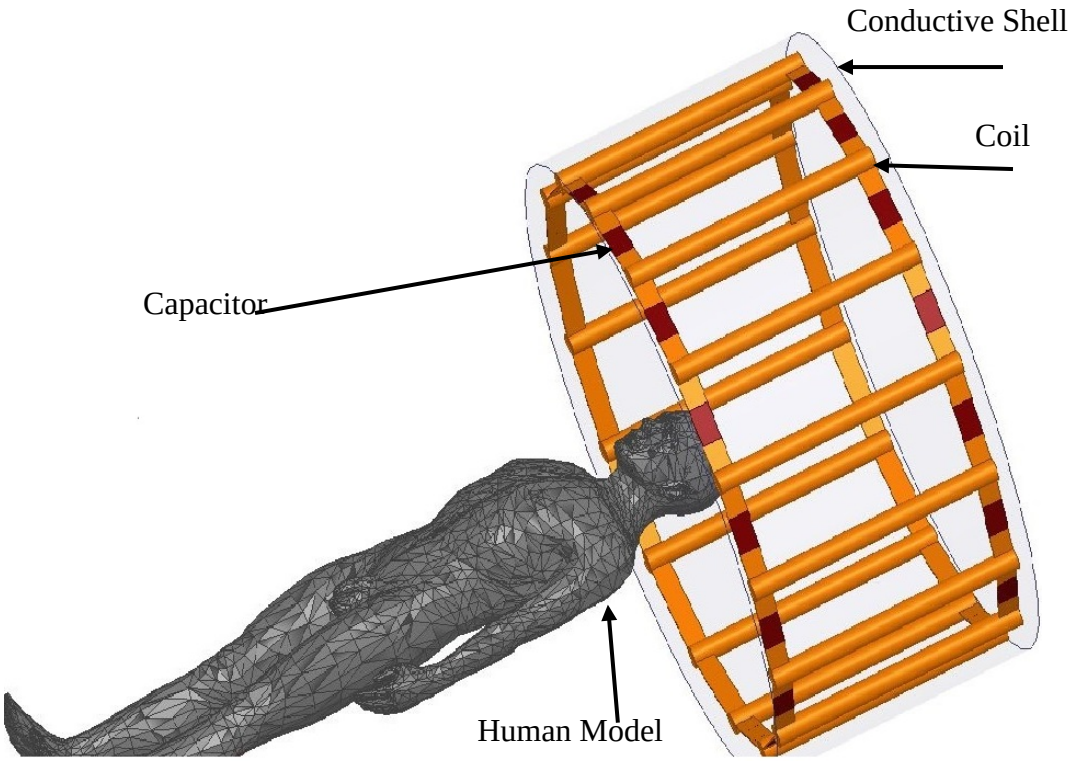

Figure 2.1 Whole Body MRI System. Hugo model in Birdcage Coil

A typical RF waveform pulse can be Gaussian, sinc, truncated sinc, etc. A time dependence modulation shape of RF waveform for a sinc pulse is given by

$$B_1(t) = B_{10} sinc\left[\frac{\pi}{\tau} t\right] \tag{2.1}$$

where B_{10} is the maximum amplitude of the pulse. The root mean square value of $B_1(t)$ is given by

$$B_{1rms} = \sqrt{\left[\frac{1}{T}\int_0^T B_1^2(t)\, dt\right]} \tag{2.2}$$

where T is the average time. The maximum value of B_{1rms} is 3.5μT at 64 MHz.

B_{10} is adjusted to achieve the desired flip angle of the nuclear magnetization. Flip angle is the amount of rotation the net magnetization experiences during application of RF waveform pulse and is affected by the shape of the RF waveform pulse as well as the slice-selection gradients, off-resonance excitations, and B_{10} field inhomogeneities. For a lossless condition, flip angle θ is proportional to the product of bandwidth Δf of the pulse and magnitude B_{10} and is given as

$$B_{10} = \frac{\Delta f}{\gamma}\theta \tag{2.3}$$

where γ is a constant of proportionality and bandwidth is Δf is given by

$$\Delta f = \frac{1}{\tau} \tag{2.4}$$

Equation 2.3 is valid only for relatively angles smaller than 30 degrees and for spin close to the central resonance frequency of RF pulse. The equation falls apart for angles greater than 90 degrees due to nonlinear behavior of Bloch equations [64]

Mechanism of RF-induced heating during MRI is a two-step process. It can be treated as a complete electromagnetic-thermal problem. The solution of the electromagnetic part is modeled by Maxwell's equations, and the solution of the thermal part can be modeled by the heat transfer equation. Power deposition in the tissues is quantified by specific absorption rate (SAR) given by

$$SAR(r) = \frac{\sigma |E^t(r)|^2}{\rho} \tag{2.5}$$

where σ denotes the electrical conductivity in S/m, E_t is the total electric field and ρ is the mass density. Temperature increase with respect to time in response to local SAR is given by

$$\frac{dT}{dt} = \frac{SAR}{C} \tag{2.6}$$

where C is the specific heat capacity (J/(kg·°C)). The bioheat equation is used to calculate the heating of tissue due to SAR and can be written as

$$\rho C_p = K\nabla^2 T + \rho SAR - b(T - T_b) \tag{2.7}$$

where T = T(r,z,t) is the temperature (°C) at time t, C_p is the specific heat (J/(kg·°C)), K is the thermal conductivity (W/m·°C), b is a constant related to blood flow, and T_b is the blood temperature [10]. Ignoring blood perfusion rate and metabolic heat, equation 2.7 is simplified as

$$\rho C_p = K\nabla^2 T + \rho SAR \tag{2.8}$$

As mentioned before, tissue-heating effects may be magnified locally near the ends of implanted medical devices due to device interactions with the tangential component of the incident electric field along the length of the device. It is critical to measure and simulate the temperature rise of tissue medium surrounding an electrode before an active or passive implanted medical device can be labeled MR Safe or MR Conditional [9, 10].

2.2 Interactions of Electric Fields with Passive implants and heating during MRI

The interaction between the RF field and the implant is treated as an electromagnetic scattering problem. During this interaction, a surface current is induced on the implant surface, and it generates a scatter electric field. The total field contributing to the SAR is the summation of the incident field and scatter field given by

$$E^t = E^i + E^s \tag{2.9}$$

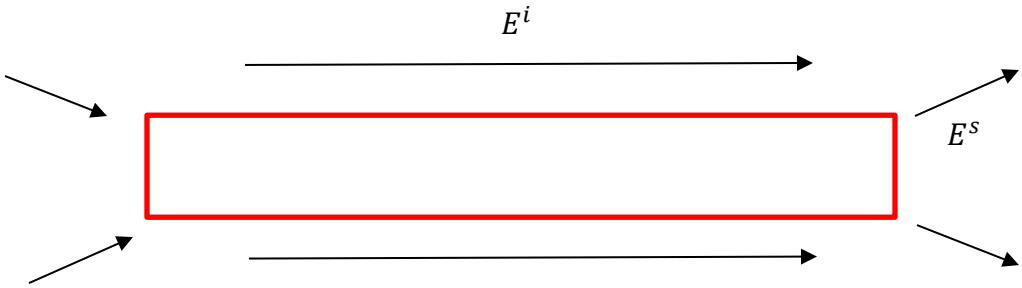

Figure 2.2 Mechanism of scattering of Electric Field

The regions where electric field intensity is high will have a large scattered electric field. In these regions, there will be increased power deposition, which is quantified as SAR. The induced current excited on the surface of the implant contributes to this scattered field. If we can control the phase of induced current by certain design techniques, such that destructive interference of phase occurs, then we may have a small scatter field. However, if we can reduce the magnitude of this induced current, SAR will also decrease and so will the effect of RF heating.

The amount of heating for a passive implant during MRI will depend on the dimensions of the implant. The heating tends to be greatest for thin, long implants, such as a stent or an orthopedic rod. As an approximate guideline, the greatest temperature rise will occur at device lengths with the length approximately equal to the half the wavelength in tissue. For phantom conductivity of 0.47 S/m, the value recommended in ASTM F2182-11a [65], and the relative electric constant of 78, the wavelength is calculated to be 43.6 cm at 64 MHz and 24.7 cm at 128 MHz.

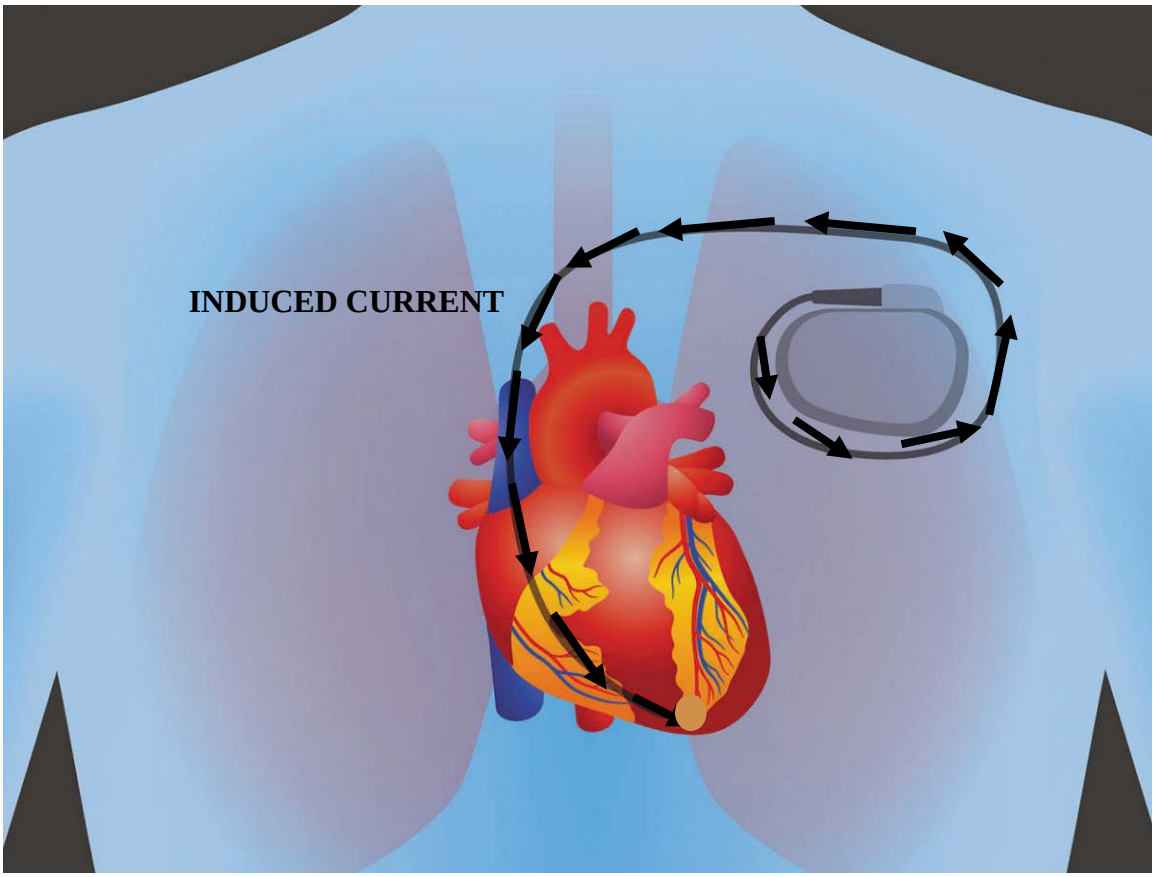

Figure 2.3 EM fields tangential to the lead couples with the implanted system. Because of this coupling, there will be some induce current in the lead body, and this is the induced current which is responsible for lead heating, which is occurring at the tip to tip interface of the heart, which is as shown that green dot here. This is the lead heating that can cause some thermogenic damage to heart tissue. Photo taken from [66]

2.3 Regulatory Landscape

Given the potential for electromagnetic scattering to produce SAR in surrounding tissues, the US Food and Drug Administration (FDA) and other regulatory agencies generally require an assessment of RF heating when an application is made for approval of a medical device [67, 68]. Implantable devices fall under one of the following three categories [69]

- MR Safe: The medical devices that fall under this category are non-conductive and non-magnetic. It is expected that there is no interaction between the medical device and the MR environment.

- MR Conditional: The medical devices that fall under this category safely undergo an MRI scan in predefined conditions. It is expected that these devices may or may not be electrically conductive; however, they are safe to use in certain conditions or within certain parameters.
- MR Unsafe: The medical devices that fall under this category are unsafe for MRI environment and have not been proven MR Safe.

ISO/IEC 10974 [70] technical specification describes requirements for establishing safety and compatibility of implants during MRI. The technical specification presents an approach with four tiers for assessment of RF heating of active implants. Tier 1 has the simplest test and computation requirements. Tier 2 and Tier 3 analysis progressively requires more measurements and simulations but can use successively less overestimation of test field magnitudes. In Tier 3 analysis, the temperature rise at an electrode is determined from the transfer function and tangential electric field E_{tan} along the lead. The more precise Tier 4 analysis calculates the temperature rise based on a full-wave model of the implant. It requires the most stringent computational analysis and utilizes the least overestimation of test field magnitudes. For the small dimensions of the filars of an active implant, the Tier 4 analysis is computationally intensive to the extent that the time required for the calculation is impractical. Sample calculations for a model implant based on Tier 3 and Tier 4 analysis methods presented in ISO/IEC 10974 [70] were performed by Cabot *et al.* [71, 72].

IEC 60601-2-33 [73] is a standard for MRI equipment that includes limits for maximum SAR that may be induced in the patient by the RF field. For occupational exposure during MRI, maximum whole-body SAR is 0.4 W/kg, and the maximum localized exposure SAR value is 20 W/kg. For a volume transmit coil, patients may be exposed to average whole-body SAR of 4 W/kg and average exposed body SAR of 10 W/kg. For a local transmit coil, SAR values can be as high as 40 W/kg. IEEE C95.1 [74] is a safety standard that describes the electromagnetic exposure to SAR levels for various frequencies from 3 KHz to 300 GHz.

ASTM F2182-11a [65] is a standard for testing passive medical implants for RF heating. Temperature probes are placed on the implant, and the implant is placed in the phantom. The phantom material has a conductivity of 0.47 S/m and volume of 27 liters. The conductivity of the phantom material is approximate to the electrical conductivity of soft tissues in the body. It is saline and gelled to prevent convection. This setup provides a reasonable estimate of worst-case conditions in the body near an implanted device during an MRI scan. It does not consider the effects of blood perfusion. For a case of stents, the in-vivo temperature rise will be reduced by the flow of blood inside the stent and blood perfusion in the tissues outside the stent [75].

Temperature probes are used to measure the value of temperature rise over the duration of a scan sequence (6 minutes or 15 minutes) in the phantom. The active areas of the probes are placed in direct contact with electrodes. For passive devices, they are placed near the device ends. A reference probe is placed on the side of the phantom opposite to the location of the device being tested. The purpose of the reference probe is to verify that the background conditions in the phantom remain the same from one heating test to the next in a given testing protocol.

The phantom is placed in the coil such that the center of the torso is aligned with the center of the RF coil in the MRI scanner or test system used for the heating tests. This location has been shown to provide the worst-case heating conditions in MRI heating tests and is referred to as the landmark.

2.4 Gradient heating of implants with a time-varying Magnetic fields

The scattering of the electric field as shown in Figure 2.2 will cause minimal heating of metal. The tissue will have an electrical conductivity much lower than that of the metal. The source impedance posed by the tissue and the reactive impedance of the implant will limit the amount of current passing through the metal. Also, the power deposition in the metal is minimal.

At audio frequency, gradient heating of a metal object in a body can occur due to coupling with the time-varying magnetic field produced by an external source such as an

MRI gradient coil [76]. The gradient heating is due to the same mechanism that is used for the induction heating of metals. The time-varying gradient has a frequency of the order of kHz and may expose implant to a time-varying magnetic field dB/dt as high as 100 T/s.

ISO/IEC 10974 [70] provides an equation for the power deposition in a conducting disk in the presence of a time-varying magnetic field.

$$P = \frac{\sigma h \pi R^4}{8}\left(\frac{dB}{dt} cos\beta\right)^2 \tag{2.10}$$

where σ the conductivity, h and R is being the height and radius and β is the angle of incidence. The height of the disk is assumed small compared to the skin depth ∂.

Exposure limits for dB/dt for occupational exposure is less than compared to those for MRI exposure. However, the minimal heating of passive implants by gradient intensity present in an MRI system is likely due to the following factor:

1. Implants tend to be made from metals with relatively low conductivity.
2. The small size of many implants will limit eddy current heating. The power deposited (equation 2.10) goes as the 4^{th} power of the radius
3. The elongated geometry of larger implants will restrict induced eddy currents.

2.5 Factors affecting RF heating

Lead heating is a very complex function of many variables [77-84]. As seen in the chart below there are at least six different parameters which will affect lead heating. To briefly explain, we have lead related parameters like the lead size, lead length and the lead path. The lead length and lead design define the antenna characteristics, as to how they pick up energy from MRI and how they heat up. Lead path determines the electromagnetic field that will couple to the implantable device. Secondly, we have patient-related parameters like the patient position, patient anatomy, avg SAR values- all these parameters determine directly RF electromagnetic field induced in the human body as well as its intensity [85-87]

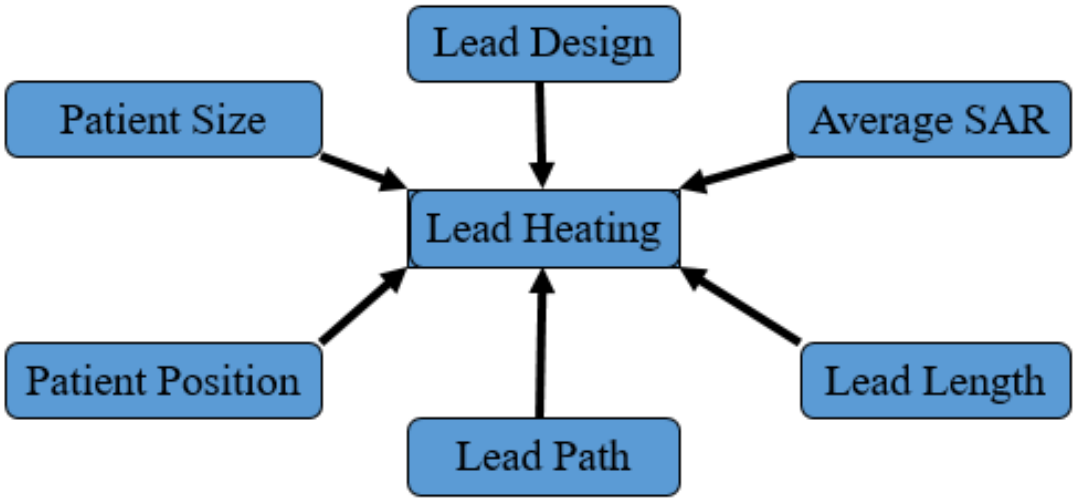

Figure 2.4 Factors affecting lead heating

All factors being same, the heating of tissues surrounding an implant will be proportional to the background SAR and proportional to the square of the background electric field. Whether or not the temperature rise measured in a phantom will pose a hazard to the patient will depend on the following factors:

1. Location of the implant in the body, as local SAR and electric field in the body, are non uniformly distributed throughout the body.
2. The degree of perfusion of tissues surrounding the implant
3. The intensity of background SAR induced by the MRI scanner.
4. Location of the patient relative to the coil of the MR system
5. Type of RF transmit coils used, such as head coil or body coil.

2.6 Numerical Methods and Calculations

Present day capabilities are such that the RF-induced temperature rise for most passive implants can be calculated with a technique such as the finite element method (FEM) or the finite difference time domain method (FDTD) [88-90].

To model the electromagnetic part of the RF-induced heating mechanism, Maxwell equations need to be solved. Larmor frequency for 3T is 128 MHz, and the corresponding

wavelength is 24.7 cm in human tissues. This is comparable to the size of the studied object, and this means full-wave simulations need to be performed. Approximations on Maxwell's equations cannot be made.

For a human phantom, running a full wave simulation leads to a large number of discretized cells leading to high memory requirements and high simulation time. The most favorable method for this type of problem is then FDTD. Compared to frequency domain solvers (FEM, MOM), FDTD solvers require less memory and less simulation time. Moreover, these algorithms can be implemented on GPUs. This allows tremendous acceleration of simulations with a hardware cost way below the cost of using clusters of CPUs. The only drawback of FDTD solvers is the mesh generated by them is less flexible as compared to tetrahedral mesh generated by FEM solvers.

To understand the physics of RF-induced heating mechanism, it is important to determine in vivo temperature rise of given device accurately. RF-induced heating of the implants can be attributed to charge accumulation at the device ends that results in a large electric field concentration. To calculate the tissue heating resulting from an implanted device, it is necessary to first calculate the surface current on the device. For a straight lead, this is accomplished by applying the Reaction Integral Equation (RIE) with the Lorentz reciprocity theorem [91].

The surface current values may be obtained by using a Method of Moments (MoM) solver. Again, the reader is referred to [91] for a detailed discussion. Once the unknown surface current values are obtained, it is necessary to calculate the scattered electric field induced from the surface currents. Once this scattered electric field distribution is determined, the SAR distribution near the device tip may be calculated. The SAR distribution may then be used to calculate the temperature rise of surrounding tissue by numerical calculation of the bioheat equation 2.7. FDTD solver is used to perform all these calculations [91].

The following steps outline the process for determining the temperature rises for an implanted device [92]:

1. Determine necessary input parameters such as incident E-field, device material properties, device orientation in phantom, etc.
2. Calculate induced surface current distribution along the device.
3. Calculating Total E-field around the structure using FDTD.
4. Calculate temperature rises from scattered E-field distribution using bioheat equation 2.7

Measurements of in-vivo RF-induced heating during MRI is a costly and time-consuming process. It involves regulatory approvals [93]. For a given medical device, the in-vivo RF-induced heating will depend on factors as describes in section [80,87]. Currently, most of the computational approach for evaluation of RF-induced heating is based on FDTD or FEM software. However, for a small dimension of the implant, performing Tier 4 analysis using FEM or FDTD software is impractical. The computation costs significantly increase as the size of the implant decreases. This is because we will need more computation power to mesh small features of the implant. Brute force simulation modeling of all possibilities is also impossible. Hence, there is need to devise techniques and methods that will help in efficiently computing RF heating of the implantable device.

2.7 Summary and Conclusion

This chapter presented an overview of RF heating mechanism of implants during MRI exposure. RF-induce heating can be simply described as an antenna in the dissipative medium. Here the antenna is our implanted medical device such as a pacemaker, stent with the lead, etc. and the dissipative medium is our human body. The solution of the electromagnetic part is modeled by Maxwell's equations, and the solution of the thermal part is modeled by the heat transfer equation. A complete quantitative understanding of RF heating mechanism is presented in section 2.1

In section 2.2, we have discussed the interaction of the electric field with the implantable device. When a human body is placed under an MRI system for diagnosis, strong electromagnetic fields are induced in the human body. If this person who is undergoing MRI is implanted with a cardiac pacemaker system or any implanted system, some of the electromagnetic fields tangential to the lead surface of the implant coupled to

the implantable system. As a result of this coupling, there will be some induce current in the lead body. This induced current is responsible for the lead heating which will cause some thermal damage to heart tissue

In section 2.3, a brief overview of regulatory landscape is provided wherein we discuss ISO/IEC 10974 [70] technical specification for the active implant. Upper limits for the whole body and local SAR for various MRI exposure has been stated IEC 60601-2-33 [73]. IEEE C95.1 is a safety standard that describes the electromagnetic exposure to SAR levels for various frequencies from 3 KHz to 300 GHz. Heating tests in the rectangular phantom is described in ASTM 2182-11a [65].

In section 2.4, a general discussion of implant heating with the magnetic field is provided. The scattering of the electric field will cause minimal heating of metal. Power deposited on the metal surface goes to the fourth power of the radius of the implant. Thus, for small radius, the size of the implant will limit the joule heating of the metal surface.

Next, we discuss the various factors affecting RF heating of implantable device in section 2.5. The RF heating is a very complex function of a large number of variables and is not dependent on a single factor. This is what makes it very complex. A general description of factors affecting RF heating is provided in this section. In section 2.6, we conclude with a brief overview of present-day capabilities for evaluating RF heating based on FDTD or FEM electromagnetic solvers.

3. CALCULATIONS AND MEASUREMENTS OF RF INDUCED HEATING FOR SHIELDED AND UNSHIELDED STRUCTURES WITHOUT METALLIC SHORT AT THE END

It is evident from the previous sections that RF-induced heating in an implant during MRI depends on its geometry, electrical properties of tissue and the electrical field near the implant. The main cause of RF-induced heating is due to the induced current on the implant. An implant whose length is in resonance with incident RF field maximizes RF induced current, thereby causing maximum temperature rise. If we can design our implants in such a way that induced current can be minimized, then RF heating can be reduced significantly.

The technique of shielding for implant design has been proven to reduce RF-induced temperature rise [30-35]. In this chapter, we provide physical models of shielded structures which can be used to reduce RF-induced heating. Numerical calculations were performed and SAR, temperature rises were calculated using FDTD program for our proposed physical models. Calculation of Current on Rod Surface and Shield Surface for the shielded and unshielded electrode is presented. To validate the simulations results obtained, corresponding measurements were performed. All measurements were done at 64 MHz. Finally, we conclude with the qualitative discussion of the induced tangential electric field on the electrode surface.

3.1 Physical description of the model lead with and without the metallic shield

The geometry of the proposed physical model for a generic implant is as shown in Figure 3.1. The top figure is the electrode without the metallic shield. The bottom one is the electrode with a metallic shield. The yellow color indicates a dielectric material of permittivity 2.1. Brown color indicates a metallic conductor.

We present a physical model of the electrode to evaluate temperature rises for a 20 cm length of the electrode with and without metallic shielding.

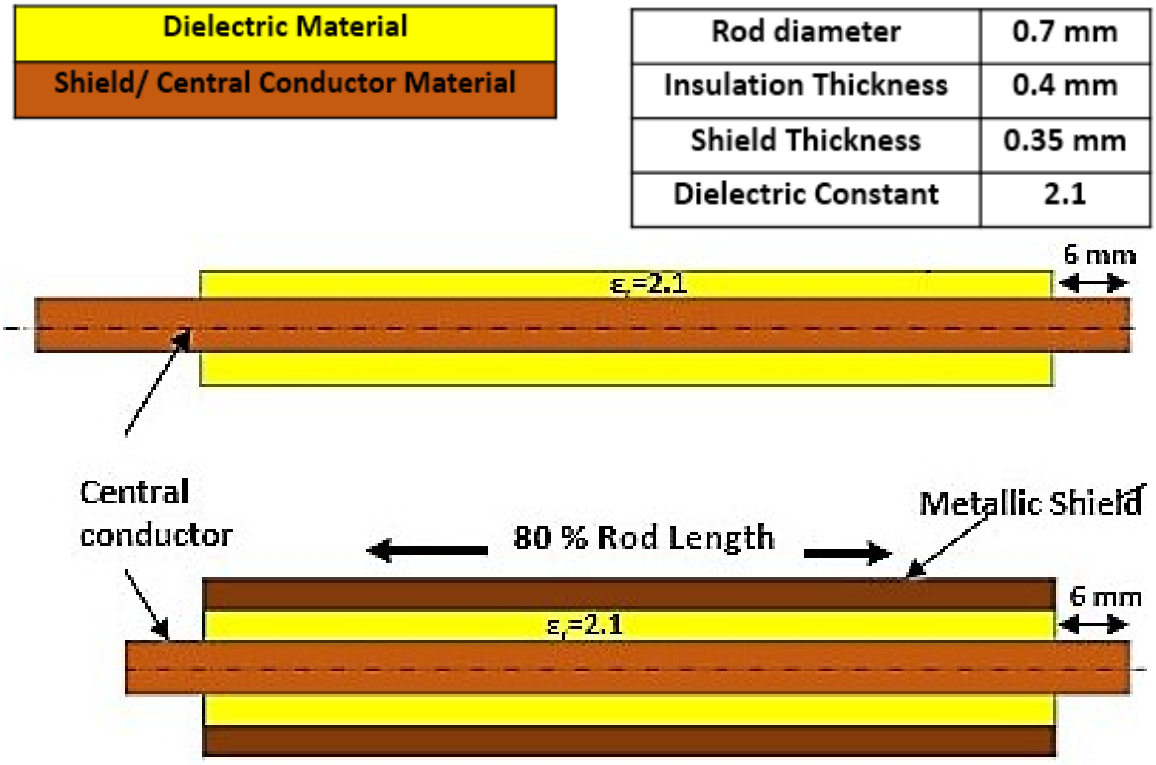

Figure 3.1 Geometry of model lead with and without the metallic shield. The yellow color indicates a dielectric material of permittivity 2.1. Brown color indicates a metallic conductor.

Figure 3.2 shows the FDTD model of our electrode with and without a conducting shield. In the bottom figure, a section of the electrode is covered with a conducting metallic shield of length 16 mm and thickness 0.35 mm. The top figure is electrode without the shield. The diameter of the metallic rod is 0.7 mm. It is covered with insulation of dielectric permittivity 2.1 and thickness 0.4 mm. 6 mm insulation is removed from both ends.

In both the models, the source impedance was modeled as a 20 cm long section of transmission line. The source impedance was set by adjusting the conductivity of the dielectric layer. Center to center spacing for both of these models was 0.05 mm. Simulations were performed with the per ASTM 2182-11a as described before.

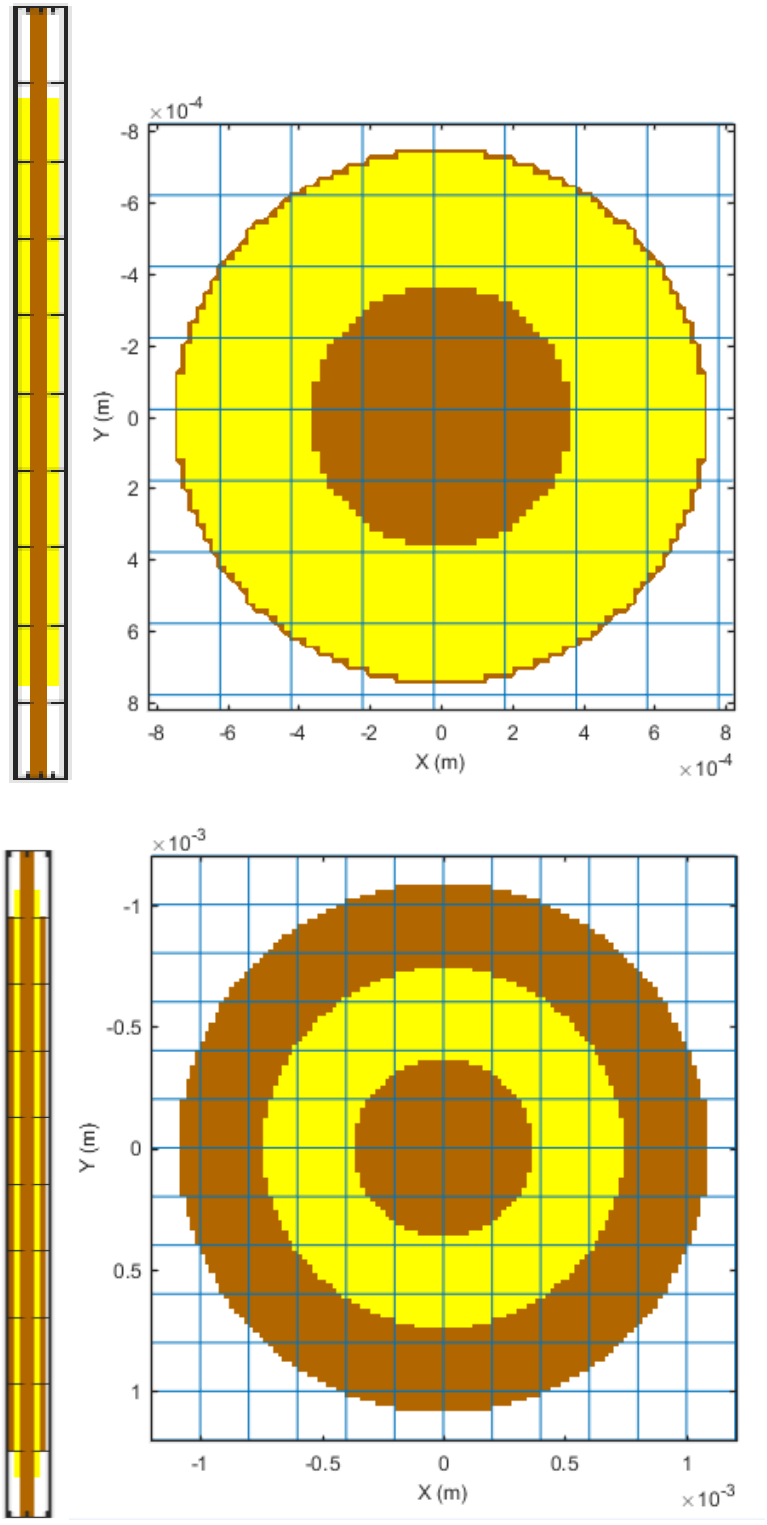

Figure 3.2 Geometry of model lead for simulation. The bottom figure is lead with a shield, and the top figure is without the shield. The thickness of the shield is 0.35 mm. The yellow color is insulation of thickness 0.40 mm. The inner brown section is the metallic rod of diameter 0.7 mm

Plane wave excitation was used for RF field. The direction of E-field is tangential to the electrode surface. To capture the fine features of the rod, the minimum resolution on the surface was 0.08 mm. Resolution increased along the rod length and was 0.02 mm at the mid-section (area of least interest). This leads to around 44 million finite difference time domain (FDTD) cells.

Electromagnetic simulations and corresponding thermal calculations were performed. These calculations were accelerated using NVIDIA Quadro 5200 GPU processor. Simulation time for EM solver was 9 hours. Thermal simulations were performed for 6 minutes of RF power. Simulation time for thermal solver was 5 hours.

3.2 Full wave calculations of unshielded electrode

Full wave calculations for electrode without a shield is shown in this section. Figure 3.3 shows the incident E field and incident H field plots. Figure 3.4 shows the calculated E field and H field distribution over the electrode surface. Figure 3.5 shows the SAR distribution plot along the surface of the implant and calculated distribution of temperature rise over the electrode. The temperature rises were calculated with the FDTD program. All calculations were performed at 64 MHz. The greatest rise occurs at the distal electrode. The temperature was localized near the electrodes. The local background SAR is 1 W/kg, and after 6 minutes of RF power, the maximum value of temperature rise anywhere near the electrodes is 8.99 ^{o}C. Noteworthy is that the temperature rise is concentrated near the ends of the electrodes.

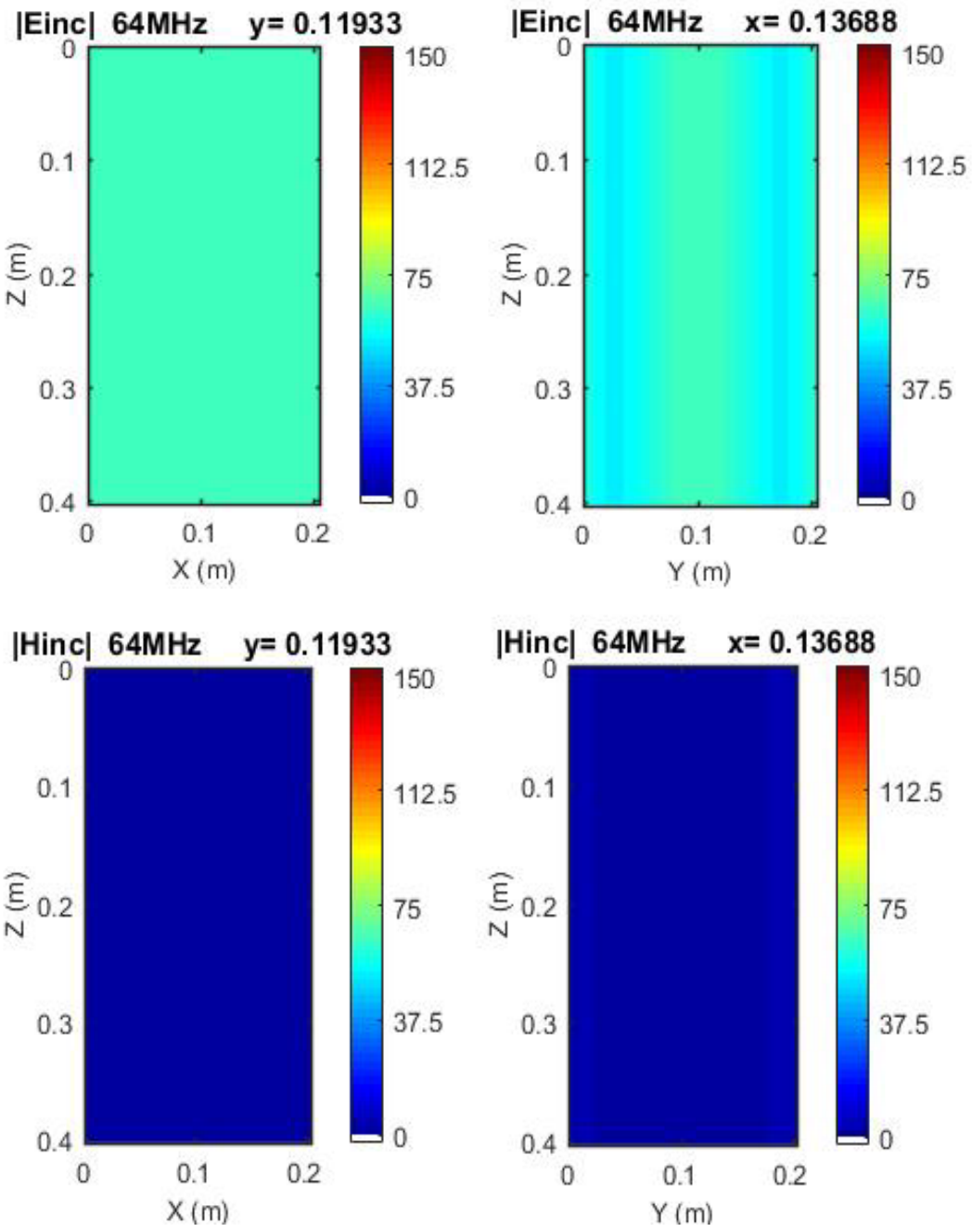

Figure 3.3 Incident E-field (top) and H field (bottom) in the plane of model lead for calculation at 64 MHz. Color base is rms in units of V/m. Local background SAR in the plane of the model lead is 1 W/kg.

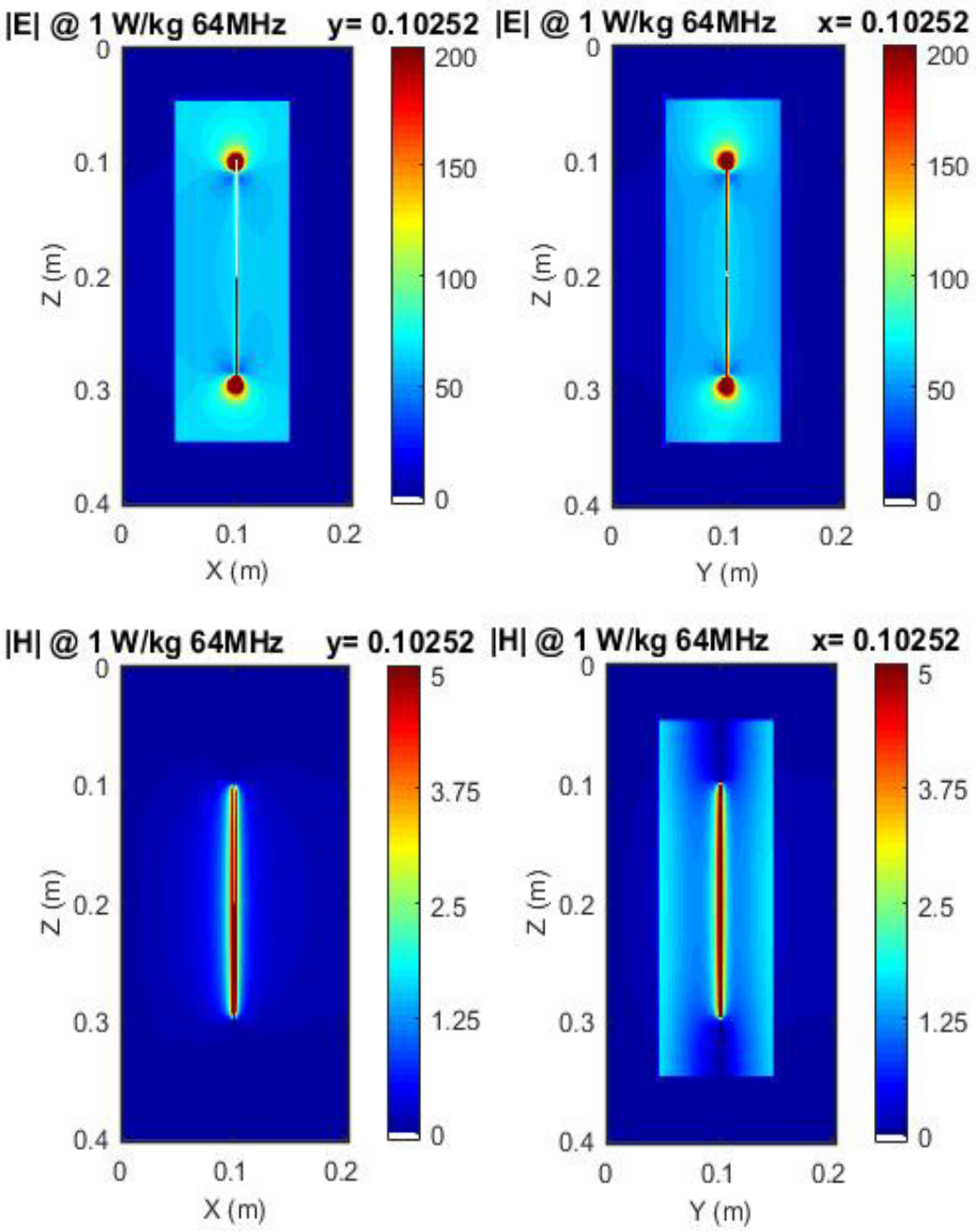

Figure 3.4 Calculated E-field and H-field distribution for electrode without the shield at 64 MHz

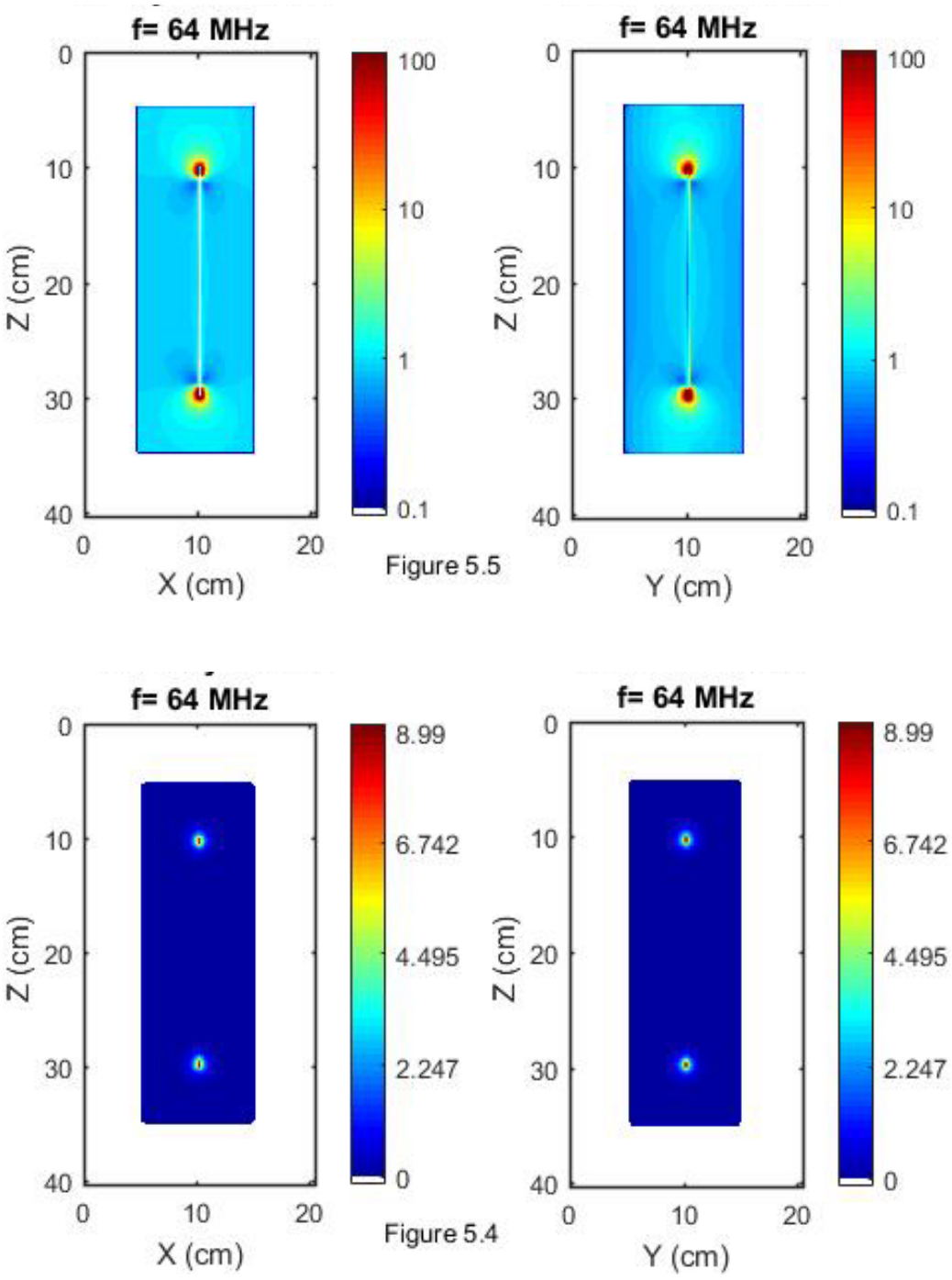

Figure 3.5 Calculated SAR (top) and Temperature rise distribution (bottom) for the unshielded model lead at 64 MHz normalized to local SAR of 1 W/kg

3.3 Full wave calculations of the shielded electrode

Full wave calculations for an electrode with the shield is shown in this section. Figure 3.6 shows the incident E field and incident H field plots. Figure 3.7 shows the

calculated E field and H field distribution over the electrode surface. All calculations are performed at 64 MHz Figure 3.8 shows the SAR distribution plot along the surface of the implant and the calculated distribution of temperature rise over the electrode. The greatest rise occurs at the distal electrode. The temperature is localized near the electrodes. The local background SAR is 1 W/kg, and after 6 minutes of RF power, the maximum value of temperature rise anywhere near the electrodes 4.55 ^{o}C. Noteworthy is that the temperature rise is distributed along the length of the electrode with maximum temperature rises at the distal end.

3.4 Measurement of Temperature Rise for shielded and unshielded electrodes

The 1.5 T/64 MHz heating tests on the model devices were performed in accordance with ASTM F2182-11a, using a GE Signa RF body coil. Equipment for the measurements is listed in Table 3.1.

The phantom was the rectangular ASTM phantom with inside dimensions of 42 cm wide x 65 cm long. The depth of the phantom material was 9 cm. The phantom material was prepared from distilled water with 10 g/l poly-acrylic acid (Sigma Aldrich) gelling agent and 1.32 g/l of NaCl. This phantom material has a conductivity of approximately 0.47 S/m at a temperature of 25 °C. Conductivity was confirmed with the Cole-Parmer meter. Temperature probes were Neoptix probes listed in Table 3.1.

The temperature probe signal conditioner was the Neoptix Reflex 4. The signal conditioner was calibrated by Neoptix, and the next calibration is due Jan. 17, 2019. RF power was applied continuous wave (CW) with a Warner radio amplifier. The forward power was set at either 25 W or 100 W; the 25 W power was used on model devices that yielded the greatest temperature rises.

A reference implant in the form of a 1/8” diameter x 10 cm long ASTM grade 5 titanium rod was placed on the patient side of the phantom. The sensing section of a Neoptix probe was placed at the end of the rod. The temperature rise of this rod was monitored to assess constancy of RF power application. This rod fulfills the requirement of the reference probe that is specified in ASTM F2182-11a.

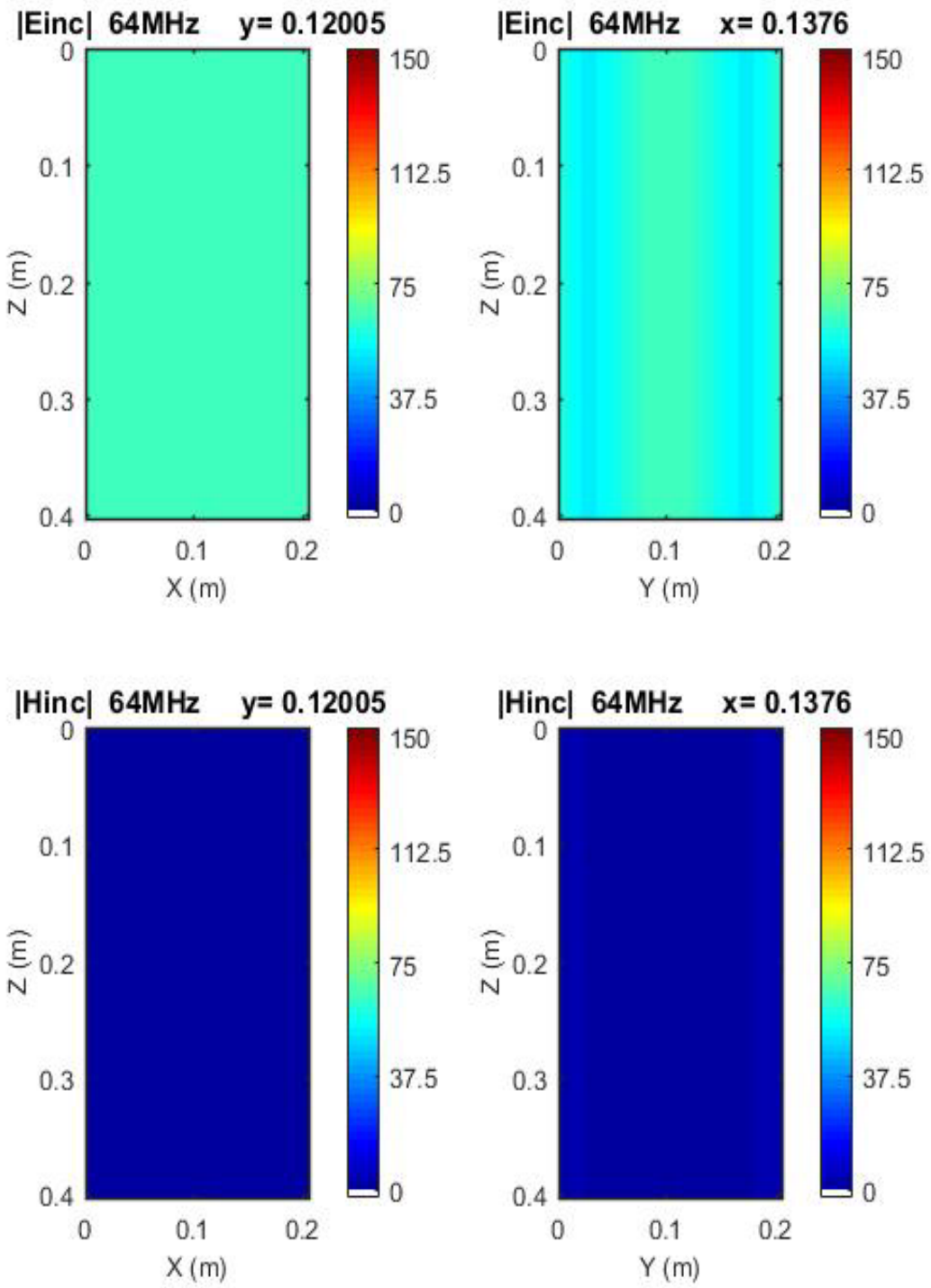

Figure 3.6 Incident E-field (top) and H field (bottom) in the plane of model lead for calculation at 64 MHz. Color base is rms in units of V/m. Local background SAR in the plane of the model lead is 1 W/kg.

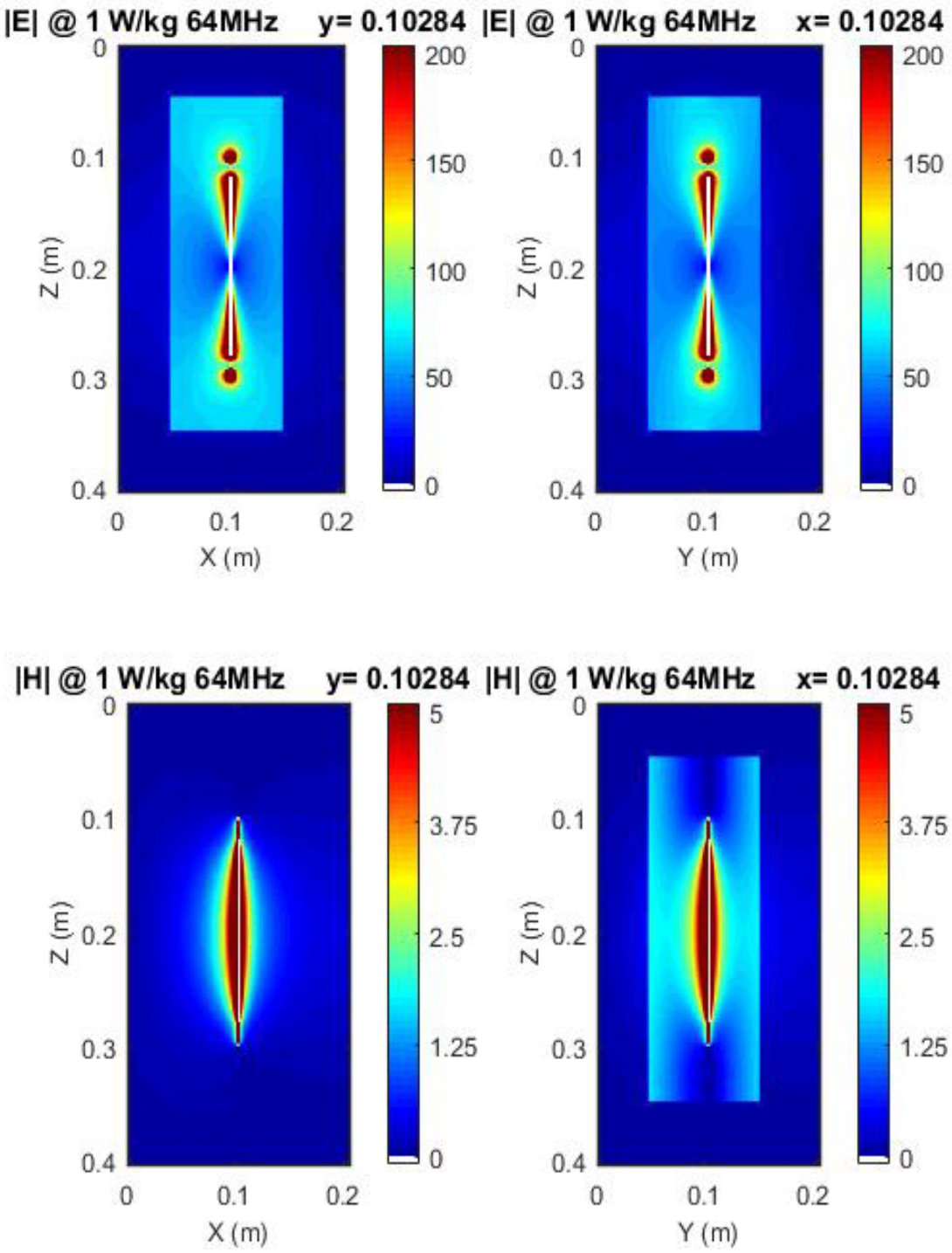

Figure 3.7 Calculated E-field and H-field distribution for an electrode with shield at 64 MHz

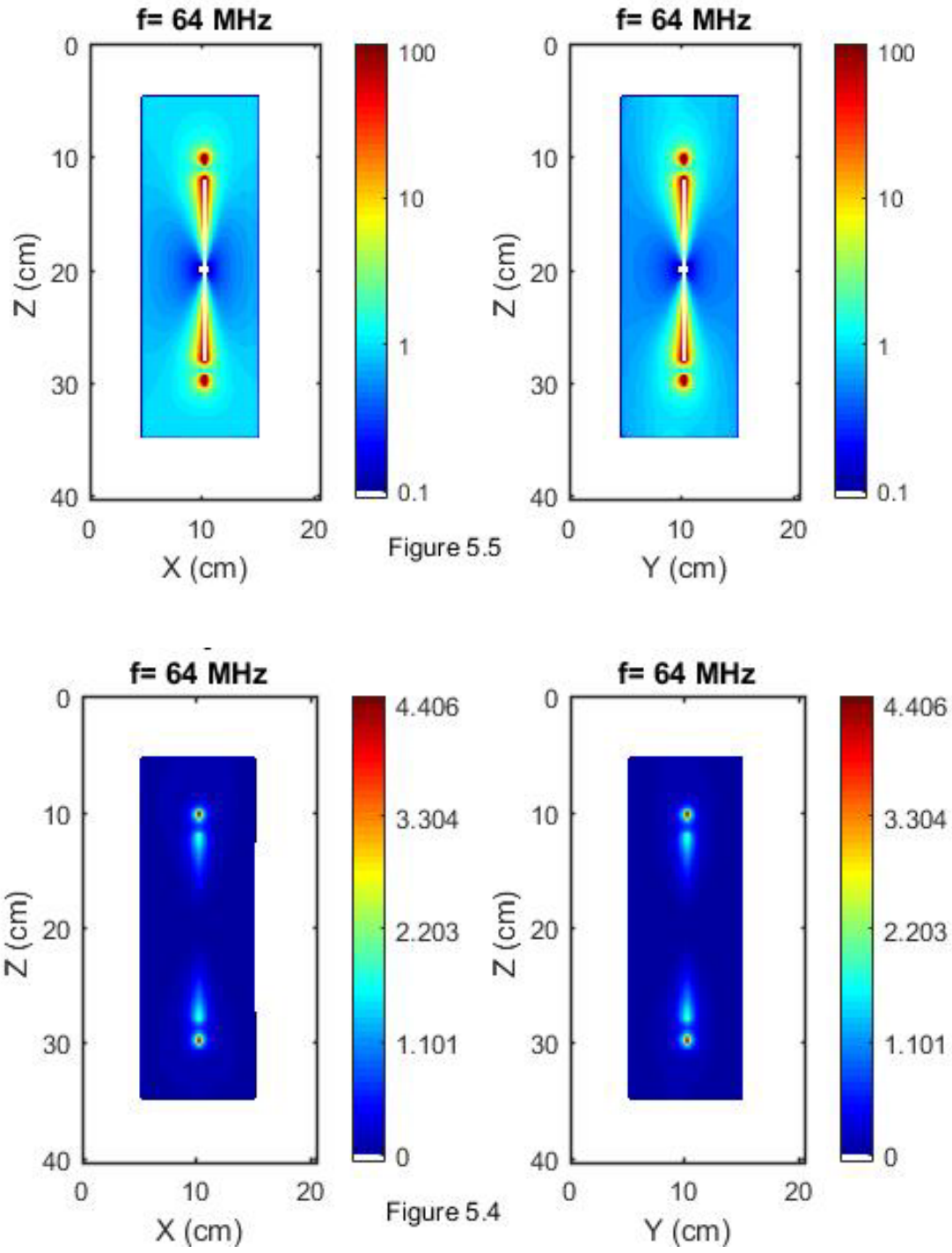

Figure 3.8 Calculated SAR (top) and Temperature rise distribution (bottom) for the shielded model lead at 64 MHz normalized to local SAR of 1 W/kg

Local background SAR at a section along the length of the leads was with the Ti rod method. The rod was placed along a 10-cm section of the model lead. This section was at the longitudinal center of the phantom, at the vertical center of the phantom, and at a distance of 4 cm from the wall. In the tests, the input RF polarization was vertical. This was achieved by applying the input RF power to one input of the quadrature coil. The electric field distribution in the phantom was calculated with Bemcalc FDTD. The accuracy of the calculated electric field was validated by Bemcalc.

Table 3.1 Equipment used for the heating tests at 64 MHz. The tests were performed in the Bemcalc Laboratory at 4842 State Road 157 South, Coal City, Indiana 47427.

Test	Equipment Description	Model	SN
Signal Generator for heating tests at 64 MHz	HP Network Analyzer	8711a	3325A-00860
Electrical Conductivity of phantom gel	Cole Parmer Conductivity Meter (cal. due Jan. 19, 2019.)	19601-03	101599724
RF coil for 64 MHz Heating tests	GE 1.5T Coil	306600G2	100948MR9
Power RF Amplifier for 64 MHz heating tests	Warner Radio RF Amplifier	AMP 600H	8800001304
Measurement of temperature rise	Neoptix Signal Conditioner (Cal. due Jan. 17, 2019.)	Reflex-4	RFX 356A
Temperature probe	Measurement of temperature rise	Neoptix	Varies

3.4.1 Determination of local background SAR

Figure 3.9 shows the Titanium rod that is described in ASTM F2182-11a for assessment of local background SAR. The rod was along a length of the model lead in the heating tests. Figure 3.10 plots temperature rises for the titanium SAR rod. Top and bottom plot is for amplifier reported output power of 100 W and middle is for amplifier reported output power of 25 W. Since the actual amplifier output power is only approximately proportional to the console reported power, the temperature rise at 25W is more than 25% of the temperature rise at 100% output power. Table 3.2 lists the temperature rises for the three runs with the Ti SAR rod. The right column lists the local background SAR along the line for the rod for nominal amplifier output power of 100 W and 25 W respectively.

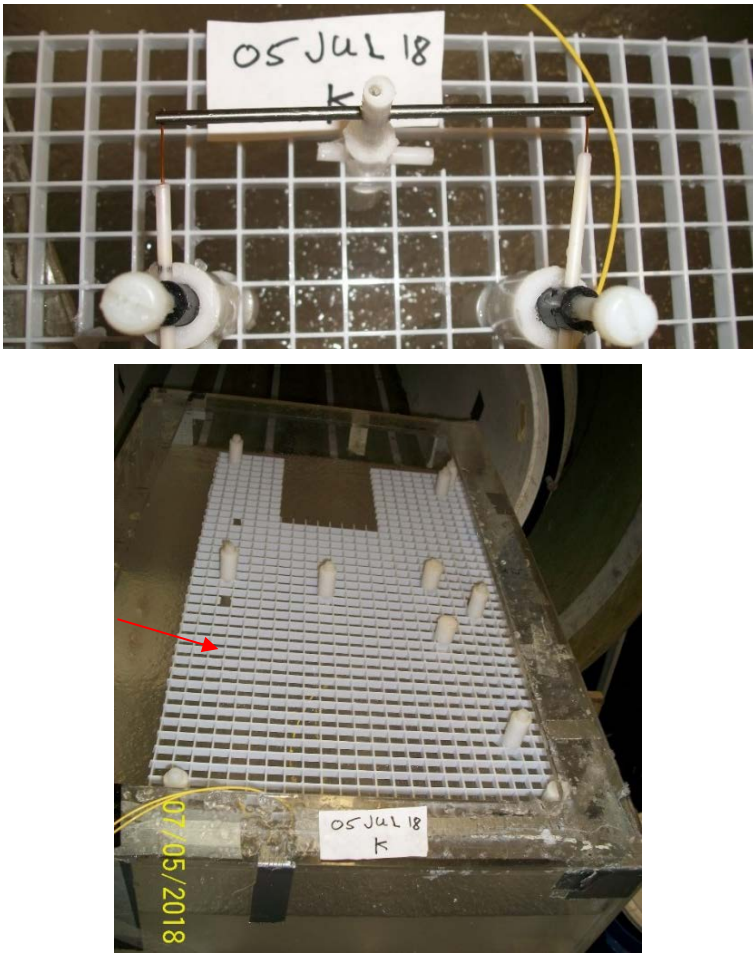

Figure 3.9 Temperature probe placement on Ti grade V rod for SAR calculations. Probes are at distal and proximal ends. Red area indicates the location of the rod in the phantom. The rod was along the length of the model lead in the heating tests.

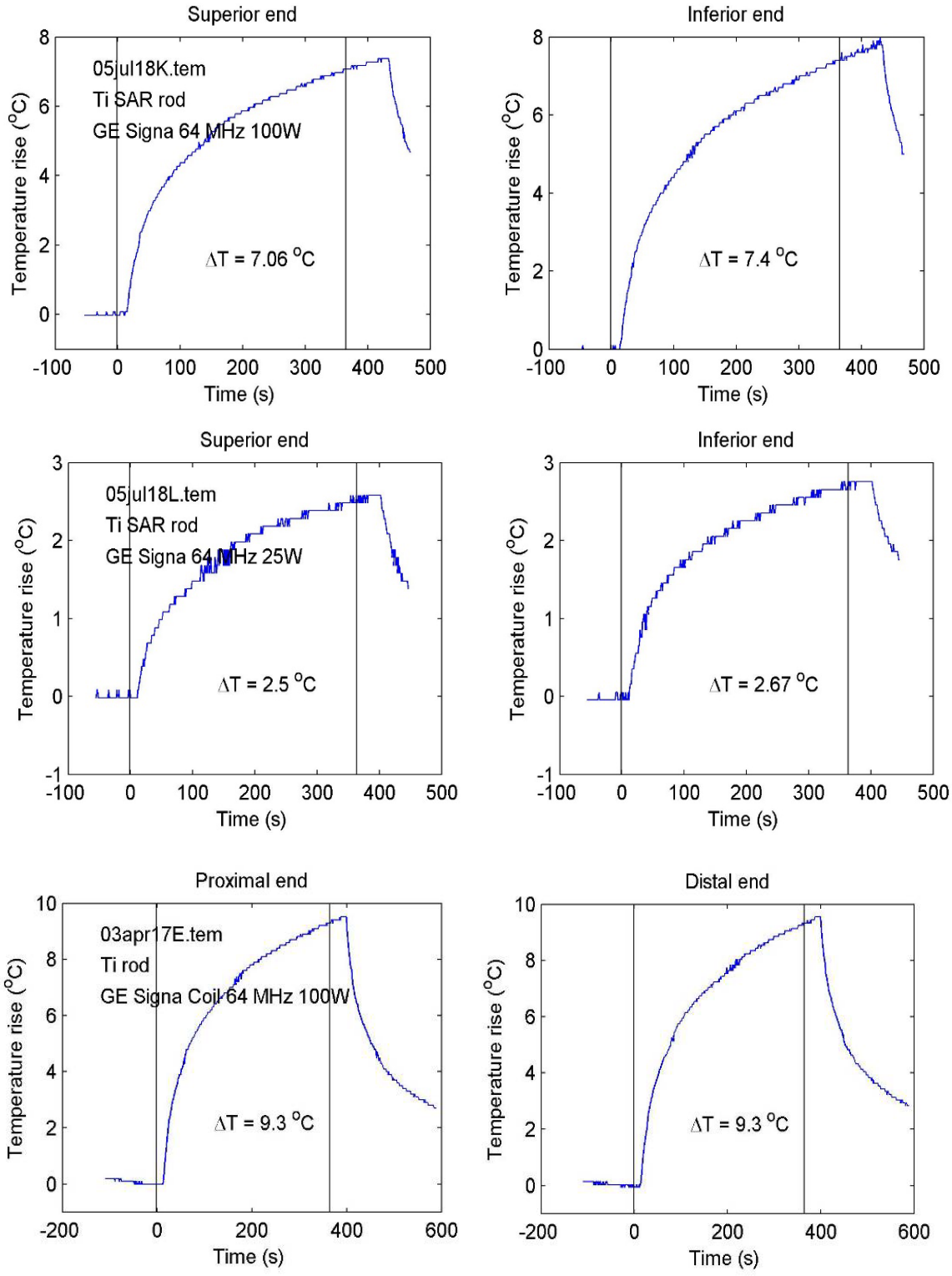

Figure 3.10. Temperature rises for the titanium SAR rod. Top and bottom plots are for amplifier reported output power of 100 W and middle is for amplifier reported output power of 25 W. (Test Run 05JUL18K and 05JUL18L and 03APR17E).

Table 3.2. Measured temperature rises for Titanium SAR rod for an input power of 100 W and 25 W

Test Run	Description	RF heat time (s)	ΔT Superior °C	ΔT Superior °C	ΔT_{avg} °C	Local background SAR (W/kg)
05jul18K.tem	Ti SAR rod - 100 W input	360	7.06	7.4	7.23	5.56
05jul18L.tem	Ti SAR rod - 25 W input	360	2.5	2.67	2.585	1.99
03apr17E.tem	Ti SAR rod - 100 W input	360	9.3	9.3	9.3	7.15

Temperature rises are for the two probes at the ends of the rod. According to ASTM F2182-11a, a local background SAR of 1 W/kg produces a temperature rise of 1.3 °C after 6 minutes.

For the nominal amplifier power of 100 W, average rise after 6 minutes is 7.23 °C. Local background SAR is then 7.23 °C/(1.30 °C/(W/kg)) = 5.56 W/kg.

For the nominal amplifier power of 25 W, average rise after 6 minutes is 2.585°C. Local background SAR is then 2.585°C/(1.30 °C/(W/kg)) = 1.99 W/kg.

For the nominal amplifier power of 100 W, average rise after 6 minutes is 9.3 °C. Local background SAR is then 9.33 °C/(1.30 °C/(W/kg)) = 7.15 W/kg.

The temperature rise curve for the shielded wire is shown in Figure 3.14 and Figure 3.15. The temperature curve remains stable at room temperature for initial 60s and starts to increase till 360s. After the RF power is turned OFF, it begins to decrease.

Figure 3.11 Temperature probe placement on Ti grade V rod for SAR calculations. Probes are at distal and proximal ends.

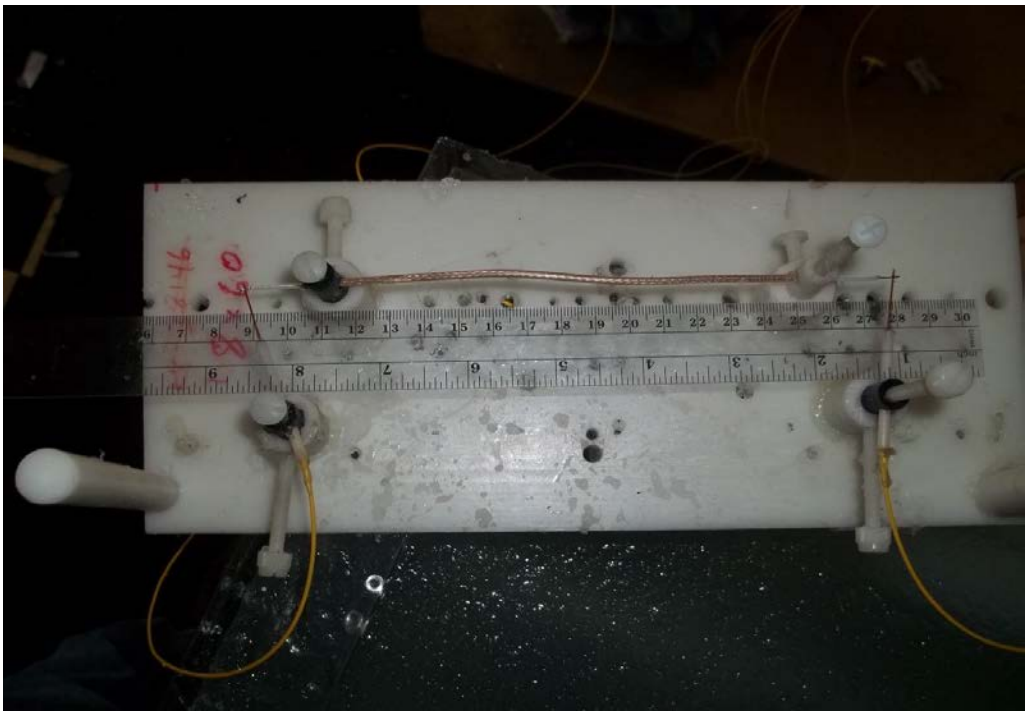

Figure 3.12 Temperature probe placement on 20 cm shielded model lead. Length of the shield is 16 cm. Probes are on the distal and proximal ends.

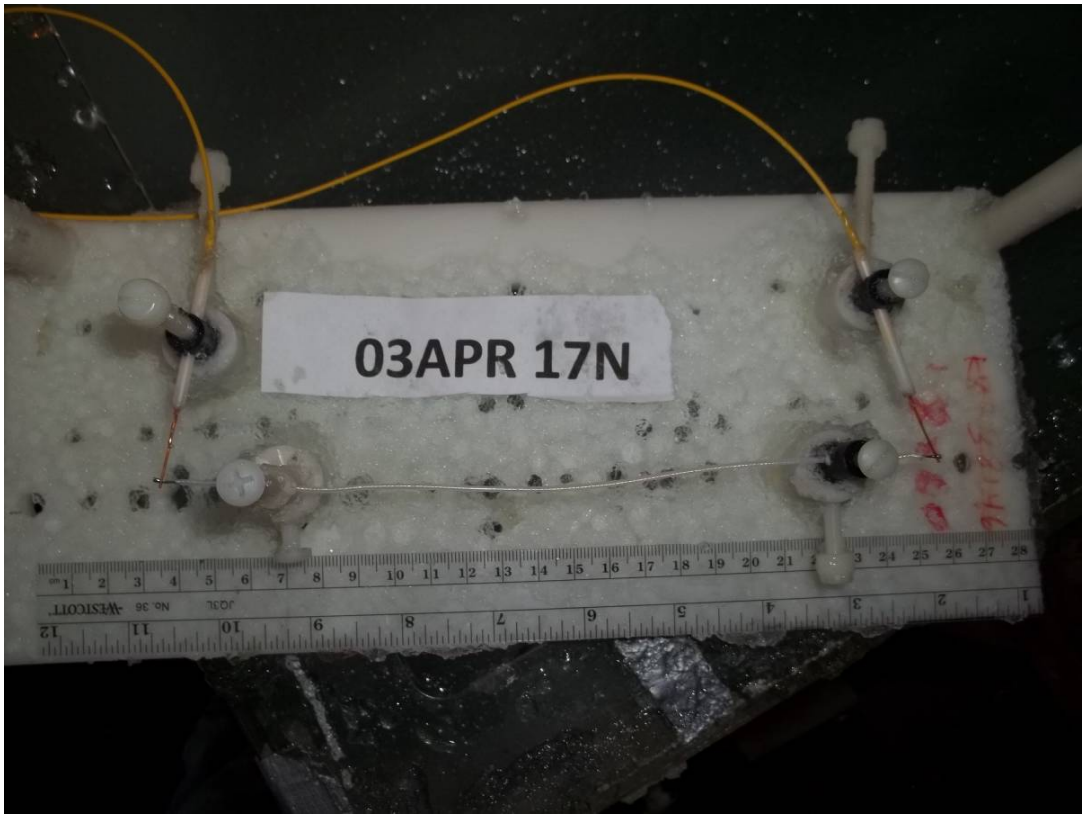

Figure 3.13 Temperature probe placement on 20 cm shielded model lead. Probes are on the distal and proximal ends

Average measured values of temperature rise are recorded as 40 ^{o}C and 50 ^{o}C for the proposed lead with shield and without a shield, respectively when local SAR is 7.15 W/kg. The greatest temperature rise occurs at the ends of the rod as expected. This gives a temperature rise of 5.5 ^{o}C/(W/kg) and 7 ^{o}C/(W/kg) for the proposed lead wire with and without a shield, respectively when local SAR is 1 W/kg. Compared to our simulated values of 4.45 ^{o}C and 8.99 ^{o}C for the proposed lead wire with and without shield respectively, this is within 20% of expected values.

Table 3.3 Comparison of Measured and Calculated Temperature rise values for 20 cm shielded and unshielded model lead

Parameter	**Value for shielded wire**	**Value for un-shielded wire**
Scaled measured ΔT	5.5 C/(W/kg)	7.3 C/(W/kg)
Scaled calculated ΔT	4.45 C/(W/kg)	8.99 C/(W/kg)

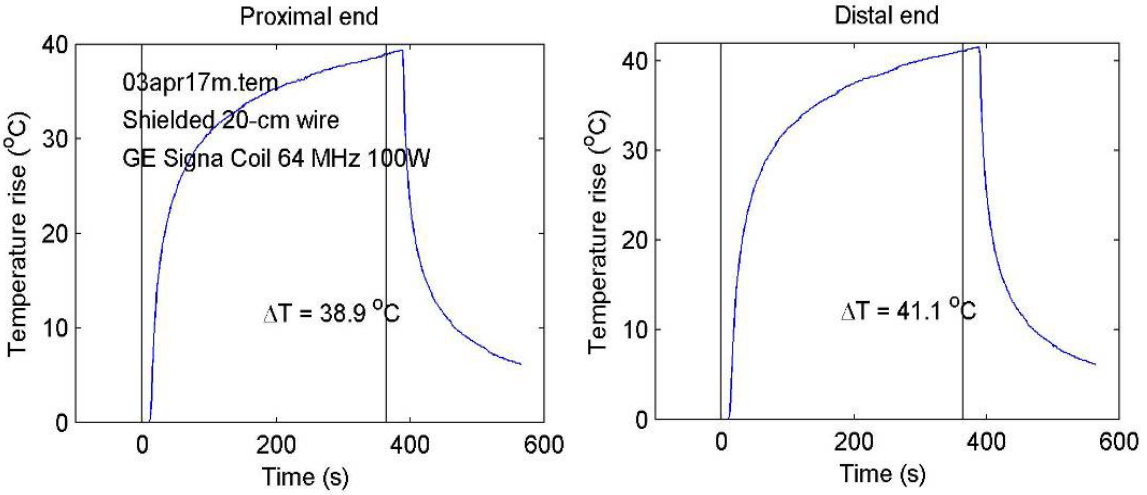

Figure 3.14 Temperature rises for the 20 cm shielded model lead at 64 MHz. The plot shows measured temperature rise vs. time for a 20 cm lead wire with a shield in an ASTM F2182-11a heating test with a local background SAR of 7.15 W/kg.

The in-vivo rise in the body will be less when compared to measured temperature rise in the ASTM phantom. This is because of the blood perfusion of the tissues present in the body. Also, convection in wet tissues and conduction due to blood vessels near the implant surface will reduce temperature rise [65]

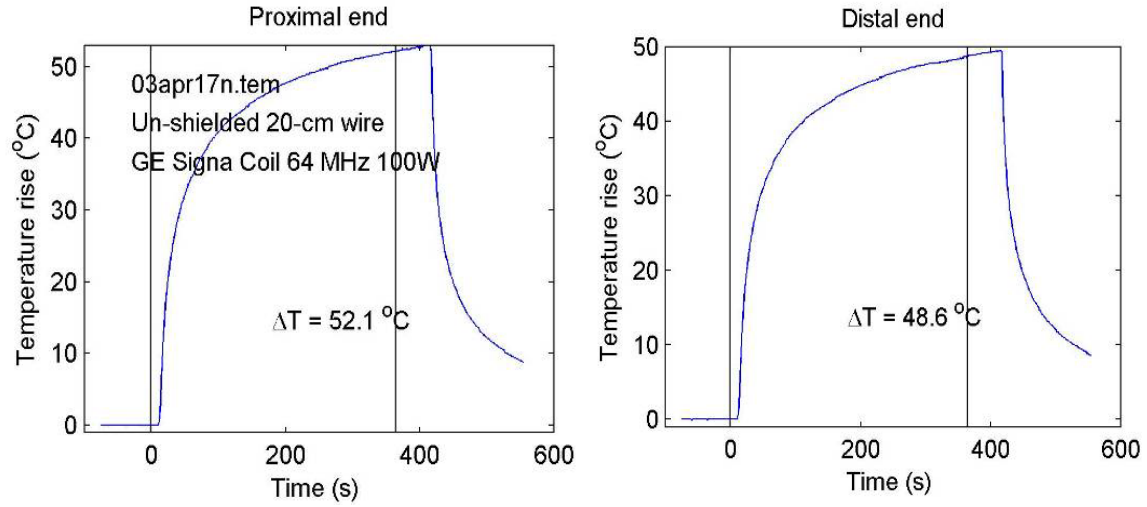

Figure 3.15 Temperature rises for the 20 cm unshielded model lead at 64 MHz. The plot shows measured temperature rise vs. time for a 20 cm lead wire with no shield in an ASTM F2182-11a heating test with a local background SAR of 7.15 W/kg.

3.5 Calculations of Current on Rod and Shield Surface of proposed electrodes

Figure 3.16 shows the calculated magnitude of induced current on the central rod surface of the unshielded structure of model lead for an incident electric field of 1 V/m at a frequency of 64 MHz. The current at the junction between the insulator and the start of the electrode is 0.84 mA/(V/m) and the current decreases linearly to the end of the electrode. This results in an approximately uniform electric field in the radial direction over the length of the electrode.

Figure 3.17 shows the calculated currents for the central rod and shield surface of the shielded model lead. The current at the electrode-insulator junction is 0.6 mA/(V/m), 30% less than the value for the unshielded structure. It should be noted that the induced current on the shield is greater than on the central rod.

Table 3.4 lists key values from the calculations and measurements. Measured and calculated temperature rises agree to within 15%, which is reasonable given the uncertainty in measurement and model conditions. The calculated temperature rise is proportional to the square of the current at the insulator-conductor junction.

Table 3.4 Comparison of calculated current on insulator-conductor junction for the shielded and unshielded wire.

Parameter	Value for shielded wire	Value for un-shielded wire
Scaled measured ΔT	5.5 C/(W/kg)	7.3 C/(W/kg)
Scaled calculated ΔT	4.45 C/(W/kg)	8.99 C/(W/kg)
Calculated current at insulator-conductor junction	0.6 mA/(V/m)	0.84 mA/(V/m)

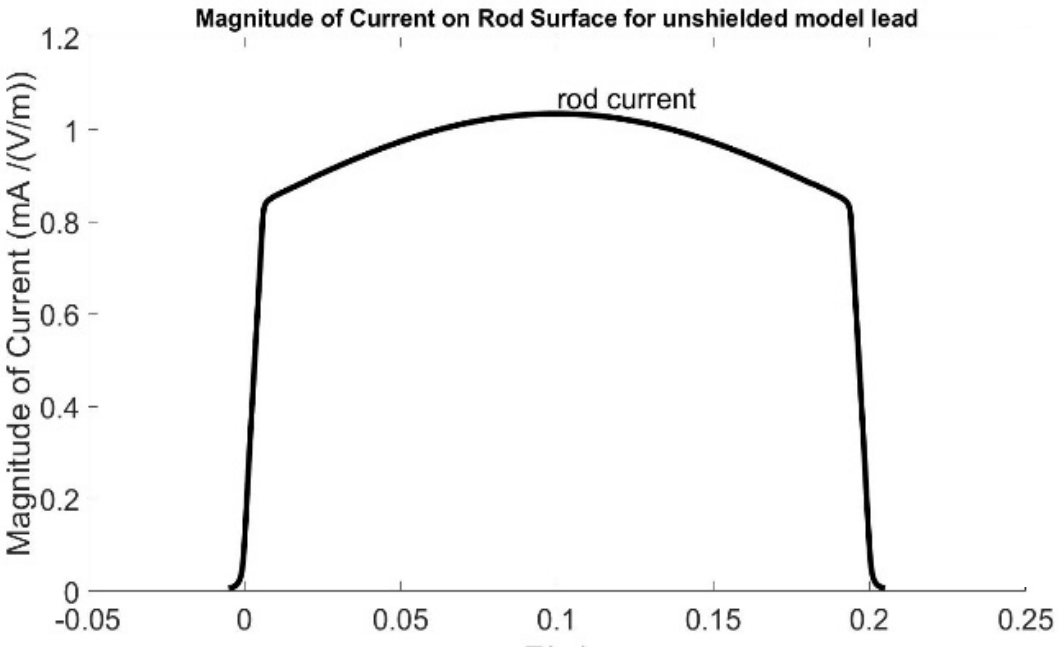

Figure 3.16 Magnitude of current induced on rod surface for unshielded model lead. Length of the lead is 20 cm from z=0 to z=0.2 m. Tip of the lead is at z=0

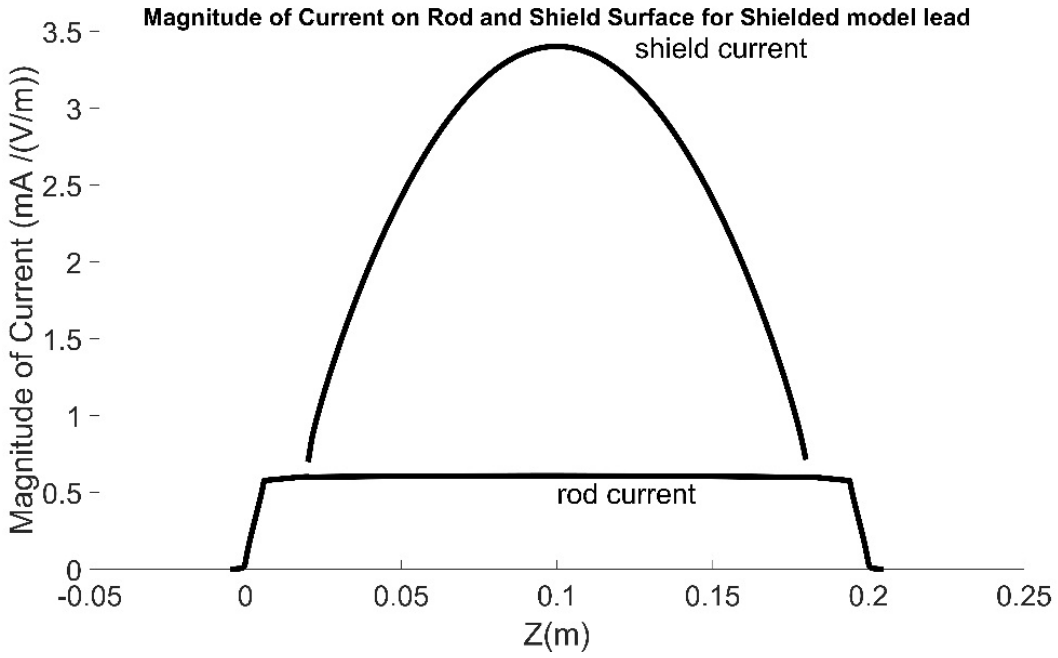

Figure 3.17 Magnitude of current on rod surface for the shielded model lead. Length of the lead is 20 cm. The shield is from z=0.02 m to z=0.18 m Tip of the lead is at z=0

3.6 Calculation of Temperature rise for an electrode with varying shield length

In this section, we provide simulated temperature rise heating predictions for varying shield length. We provide a parametric study to our physical model with a different length of the shield. It has been observed that the length of the shield around the electrode affects the RF heating during MRI.

Shield length is varied from 0.5L to 0.9L where L is the length of the electrode (25 cm, 12.5 cm). Insulation thickness is 0.35 mm, and its electrical permittivity is 2.1. The diameter of the metallic rod is 0.8 mm. 6 mm insulation is removed from both ends. The thickness of the shield is 0.25 mm, and shield length is varied from 50% to 95.2 % of rod length for L=25 cm and from 50% to 90% of rod length for L=12.5 cm. Figure 3.18 and Figure 3.19 shows the model used for parametric shield study of RF heating. Shield lengths are varied from 50% of electrode length Figure 3.18 to entire insulation length. RF power is applied for 5 minutes, and temperature rise values are calculated for a local background SAR of 1 W/kg.

Figure 3.18 Geometry of model with shield length 50% of electrode length. Physical dimensions of the model are as shown above. The yellow color indicates a dielectric material of permittivity 2.1. Brown color indicates a metallic conductor.

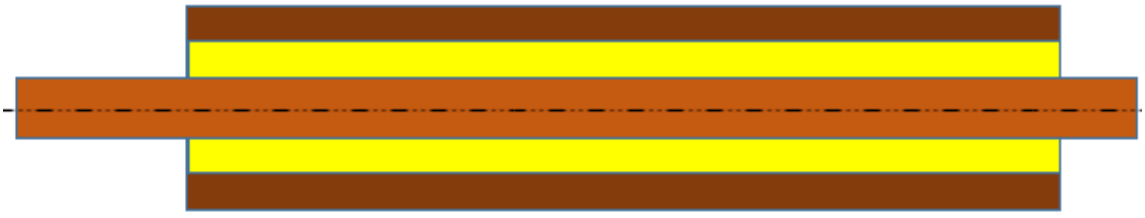

Figure 3.19 Geometry of model with complete shield length (i) 90% of electrode length for electrode length of 12.5 cm (ii) 95.2% of electrode length for electrode length of 25 cm.

Figure 3.20. Provides the variation of temperature rise values with respect to shield percentage for the case of 25 cm length of the electrode. Simulations are performed on this

electrode with and without the shield at 128 MHz. Temperature rise value is calculated with a local background SAR of 1 W/kg and after 5 minutes of RF power. A maximum temperature rise of 8.34 ^{o}C occurs in an electrode with no shield. However, when the same electrode is covered with 23.8 mm of metallic shield (95.2% electrode length) calculated temperature rise value is 0.65 ^{o}C again with local background SAR of 1 W/kg and 5 minutes of RF power. This is a reduction of 90% in temperature rise value for the same length of the electrode with no shield.

Figure 3.21. Provides the variation of Temperature rise values with respect to shield percentage for the case of 12.5 cm length of the electrode. Simulations are performed on this electrode with and without the shield at 128 MHz. Temperature rise value is calculated with a local background SAR of 1 W/kg and after 5 minutes of RF power. A maximum temperature rise of 5.16 ^{o}C occurs in an electrode with no shield. However, when the same electrode is covered with 11.3 mm of metallic shield (90% electrode length) calculated temperature rise value is 1.78 ^{o}C again with local background SAR of 1 W/kg and 5 minutes of RF power. This is a reduction of 70% in temperature rise value for the same length of the electrode with no shield.

3.7 Discussion and Conclusion

In terms of the physical model, the incident tangential electric field E_{tan} induces a current on the surface of the shield. The induced current produces a reaction tangential electric field. As a result, the tangential electric field on the central rod that is under the shield is effectively zero. However, the charge at the edge of the shield will produce a tangential electric field on the section of central rod surface that is adjacent to the shield. Because of this, the total tangential electric field on the center rod conductor is due to the summation of the incident tangential electric field and the tangential electric field from the shield surface.

$$E_{tan\_total} = E_{tan\_incident} + E_{tan\_shield} \tag{3.1}$$

In this example, the shield results in a reduction of induced current on the electrode, and hence a reduced temperature rise. By strategic placement of the shield, it should be possible to optimize the reduction of temperature rise at the electrode of an active implant.

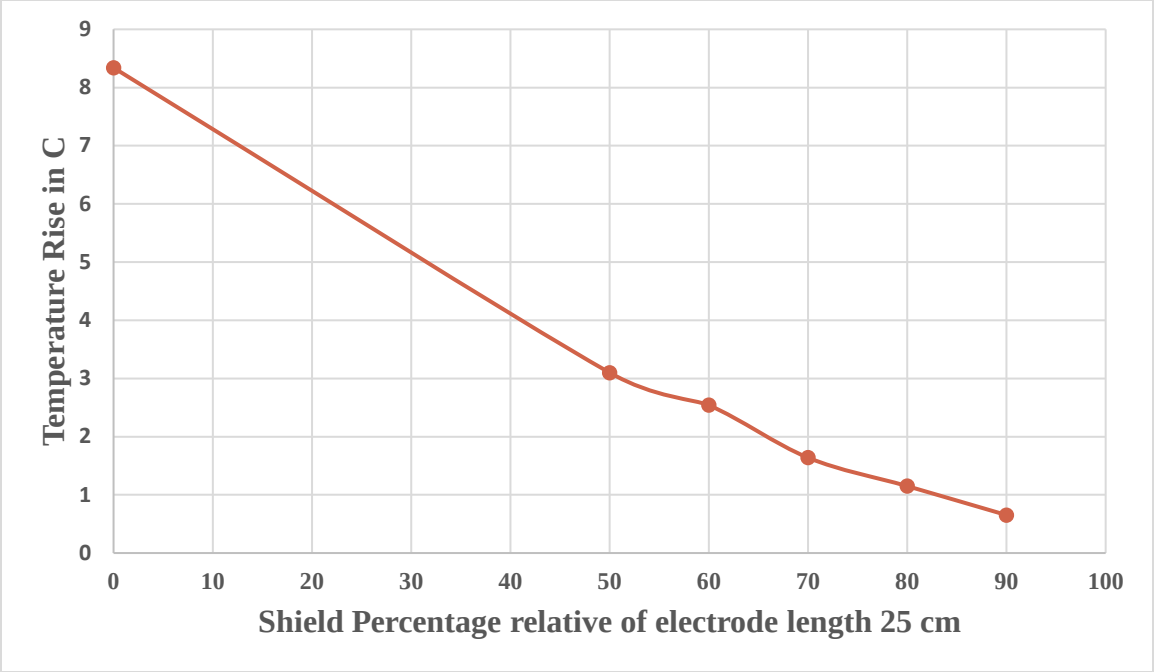

Figure 3.20 Temperature rise vs. Shield % for 25 cm length of model lead at 3T

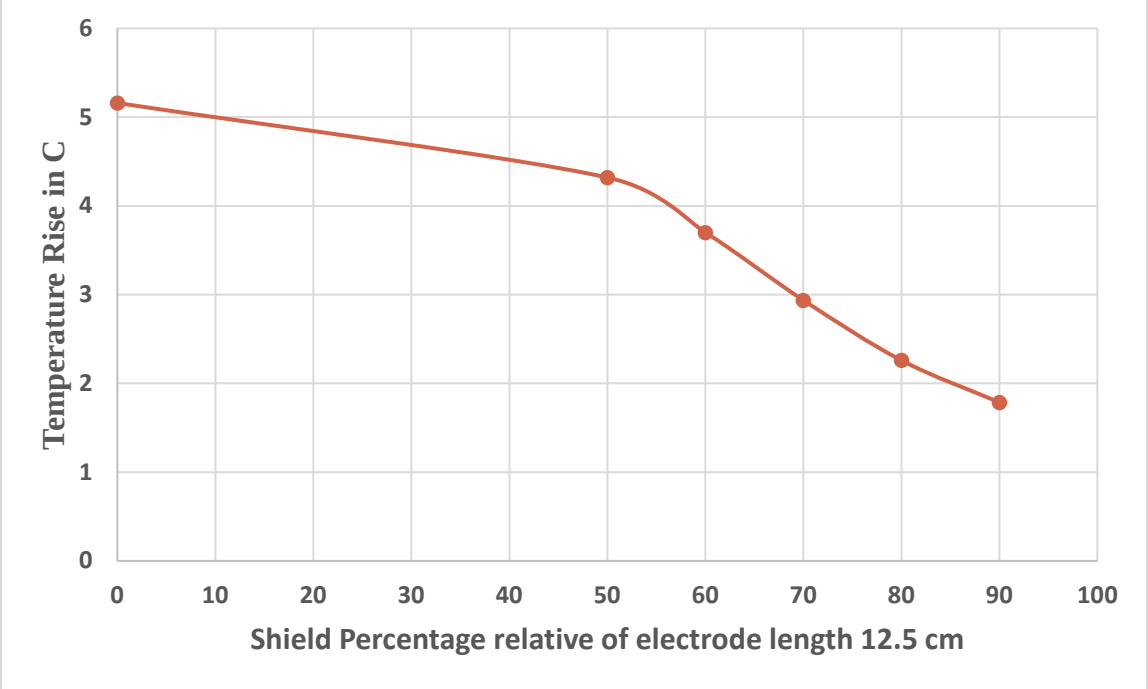

Figure 3.21 Temperature rise vs. Shield % for 12.5cm length of model lead at 3T

Measured Temperature rise of proposed model lead with and without shield

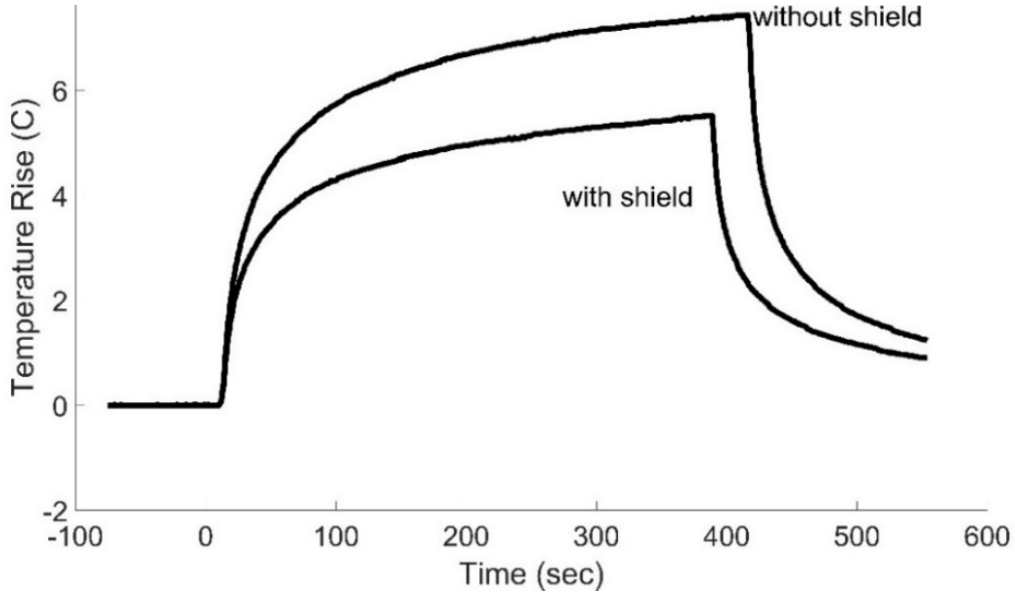

Figure 3.22 Measured Temperature rise of model lead with and without the shield.

A physical model of a lead wire with and without a metallic shield is proposed in section 3.1. Full wave calculations are performed on this wire to evaluate temperature rise and Induced Currents. Measured values of temperature rise are recorded as 5.5 ^{o}C and 7 ^{o}C for the proposed lead with and without shield respectively when local SAR is 1 W/kg Compared to our simulated values of 4.45 ^{o}C and 8.99 ^{o}C for the proposed lead wire with and without shield respectively, this is within 20% of expected values.

Calculated magnitude of the induced current is presented in section 3.5. The current at the electrode-insulator junction for the shielded structure is 30% less than the value for the unshielded structure. The calculated temperature rise is proportional to the square of the current at the insulator-conductor junction. Measured and calculated temperature rises agree to within 15%, which is reasonable given the uncertainty in measurement and model conditions. We provide a parametric study to our physical model with a different length of the shield and calculate the temperature rise for each case in section 3.6. It has been observed that the length of the shield around the electrode affects the RF heating during MRI. Increasing the shield decreases temperature rise. The technique of shielding for implant design has been proven to reduce RF-induced temperature rise.

4. CALCULATIONS AND MEASUREMENTS OF MRI INDUCED HEATING FOR SHIELDED AND UNSHIELDED STRUCTURES WITH METALLIC SHORT AT THE END

The main cause of RF-induced heating is due to the induced current on the implant surface. If the high-frequency impedance of the electrode is increased using certain design techniques then induced current can be minimized. As a result, RF heating for that particular implant can be reduced. In this chapter, we present one such technique to increase the electrical impedance of the electrode. In this design methodology, a metallic short is attached at the end of the electrode. The dimensions of the metallic short (called generator) are as shown in Figure 4.1. The electrode with a short at the end acts as a transmission line with infinite impedance. Increasing impedance decreases induced a current and thereby decreasing temperature rises. Corresponding simulations are presented to validate our model. Experimental measurements are performed to measure temperature rise.

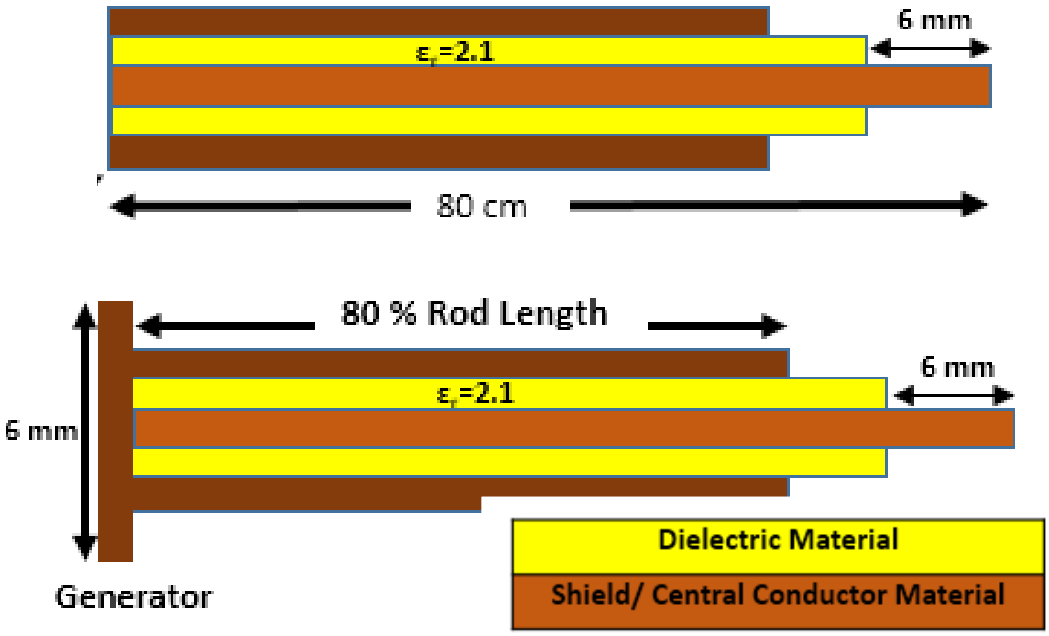

Figure 4.1 Geometry of physical model with and without shield and a short at the end. The yellow color indicates a dielectric material of permittivity 2.1. Inner brown section indicates a metallic conductor.

Table 4.1 Physical dimension of the proposed electrode

Rod diameter	0.7 mm	Generator length	1 mm
Insulation Thickness	0.4 mm	Generator radius	3 mm
Shield Thickness	0.35 mm	Rod Length	80 cm
Dielectric Constant	2.1	Shield Length	64 cm

4.1 Physical description of the model lead with and without metallic shield and a metallic short attached the end.

We present a physical model of electrode terminated at the end with a metallic generator to evaluate temperature rises for 45 cm electrode with and without metallic shielding.

Figure 4.2 shows the FDTD model of our proposed electrode terminated at the end with a metallic generator with and without the shield for calculation. The top figure is the model lead without a shield, and the bottom figure is model lead with a shield. The diameter of the metallic rod is 0.7 mm. It is covered with insulation of dielectric permittivity 2.1 and thickness 0.4 mm. 6 mm insulation is removed from one end. A metallic generator is attached to the other end. A metallic generator is a circular disk of thickness 1 mm. The diameter of the metallic generator is 6 mm. In both the models, the source impedance is modeled as 45 cm long section of transmission line. The source impedance is set by adjusting the conductivity of the dielectric layer. Center to center spacing is 0.05 mm for both the models.

Simulations are performed with the same ASTM standards as described before. Plane wave excitation is used for RF field. The direction of E-field is tangential to the electrode surface. To capture the fine features of the rod, the minimum resolution on the surface is 0.08 mm. Resolution increases along the rod length and is 0.02 mm at the mid-section (area of least interest). This leads to around 85 million finite difference time domain (FDTD) cells. Electromagnetic simulations and corresponding thermal simulation are performed. These simulations are accelerated using NVIDIA Quadro 5200 GPU processor.

Simulation time for EM solver is 12 hours. Thermal simulations are performed for 6 minutes of RF power. Simulation time for thermal solver is 6 hours.

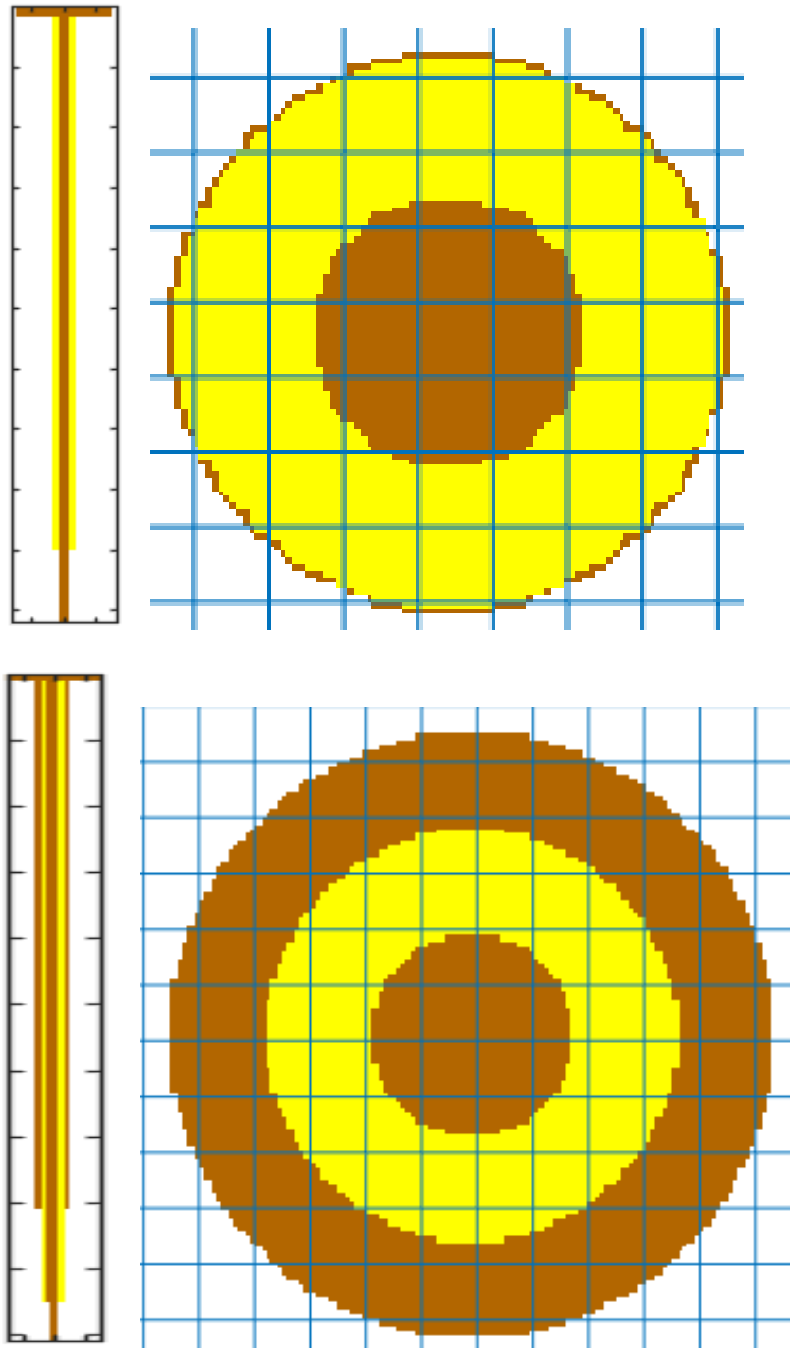

Figure 4.2 Geometry of physical model with a metallic short at the end for simulation without shield (top) and with a metallic shield(bottom). Shield thickness is 0.35 mm. The yellow color is insulation of thickness 0.40 mm. The inner brown section is the metallic rod of diameter 0.7 mm. Short is at the end of the rod

4.2 Full wave calculations of unshielded electrode with a metallic short at the end

Full wave calculations for electrode without shield and a metallic generator is presented in this section. Figure 4.3 shows the calculated incident E field and incident H field plots. Figure 4.4 shows the calculated distributed E fields and H fields plots over the electrode surface. Figure 4.5 shows the calculated distribution of temperature rise over the electrode with conducting shield and SAR distribution plot along the surface of the implant. All calculations are performed at 64 MHz. The greatest rise occurs at the proximal electrode. The temperature is localized near the electrode ends. The local background SAR is 1 W/kg, and after 6 minutes of RF power, the maximum value of temperature rise anywhere near the electrodes 30.308 ^{o}C. Noteworthy is that the temperature rise is localized at the distal end and proximal end of the electrode.

4.3 Full wave calculations of shielded electrode with a metallic short at the end.

Full wave calculations for an electrode with shield and a metallic short is shown. Figure 4.6 shows the calculated incident E field and incident H field plots. Figure 4.7 shows the calculated distributed E fields and H fields plots over the electrode surface. Figure 4.8 shows the calculated distribution of temperature rise over the electrode with conducting shield and a generator attached at the end and shows the SAR distribution plot along the surface of the implant. All calculations are performed at 64 MHz. The temperature rises were calculated with the FDTD program. The temperature rise is distributed along the length of the electrode due to thermal transport. There is some temperature rise at the generator end as it provides a path of least impedance to flow of induced current. The local background SAR is 1 W/kg, and after 6 minutes of RF power, the maximum value of temperature rise anywhere near the electrodes is 9.9 ^{o}C. Noteworthy is that the maximum temperature rise is concentrated near the ends of the electrodes.

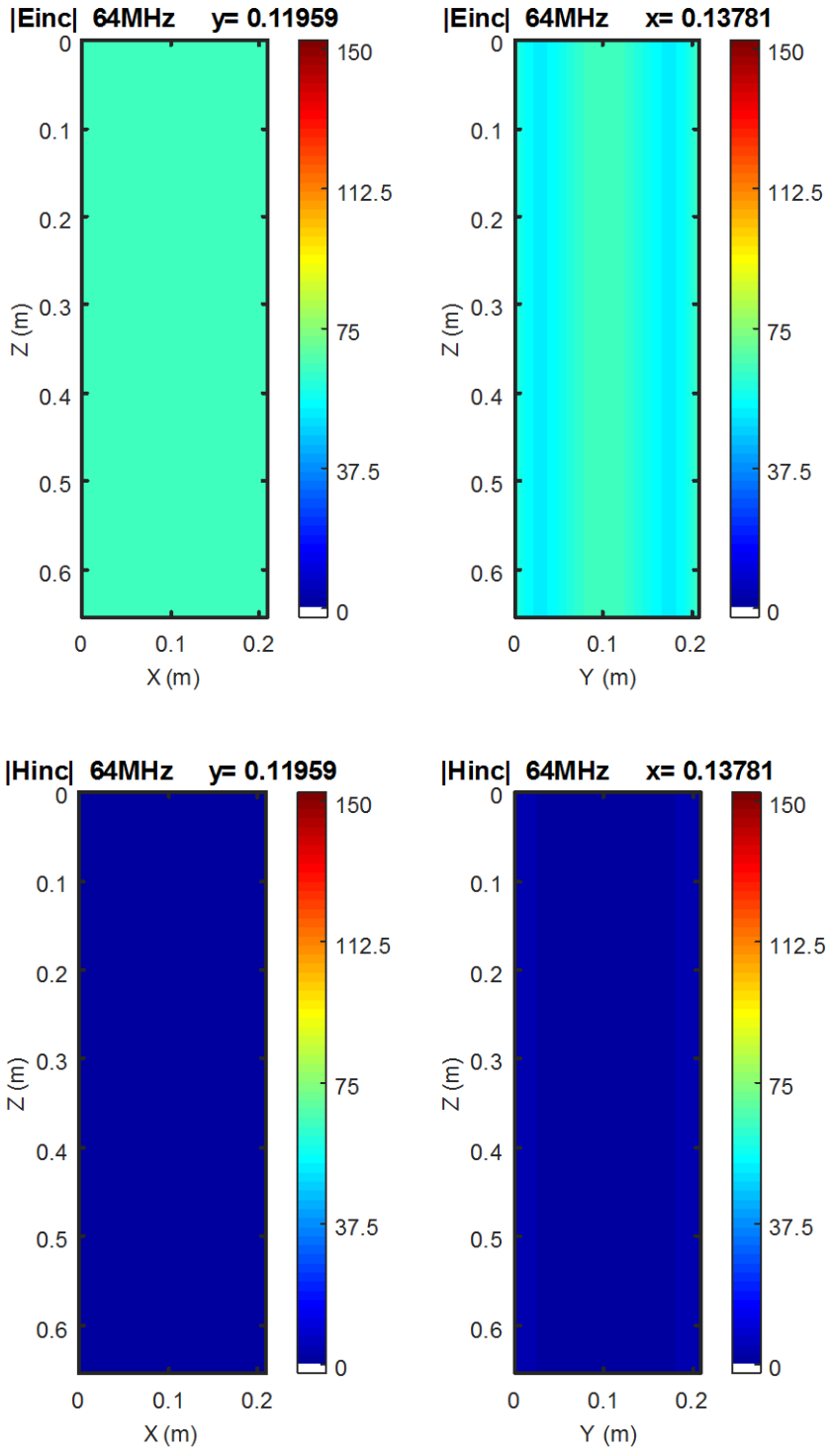

Figure 4.3 Incident E-field and H-field for heating calculation at 64 MHz. Color base is rms in units of V/m. Local background SAR in the plane of the unshielded model lead with a short is 1 W/kg.

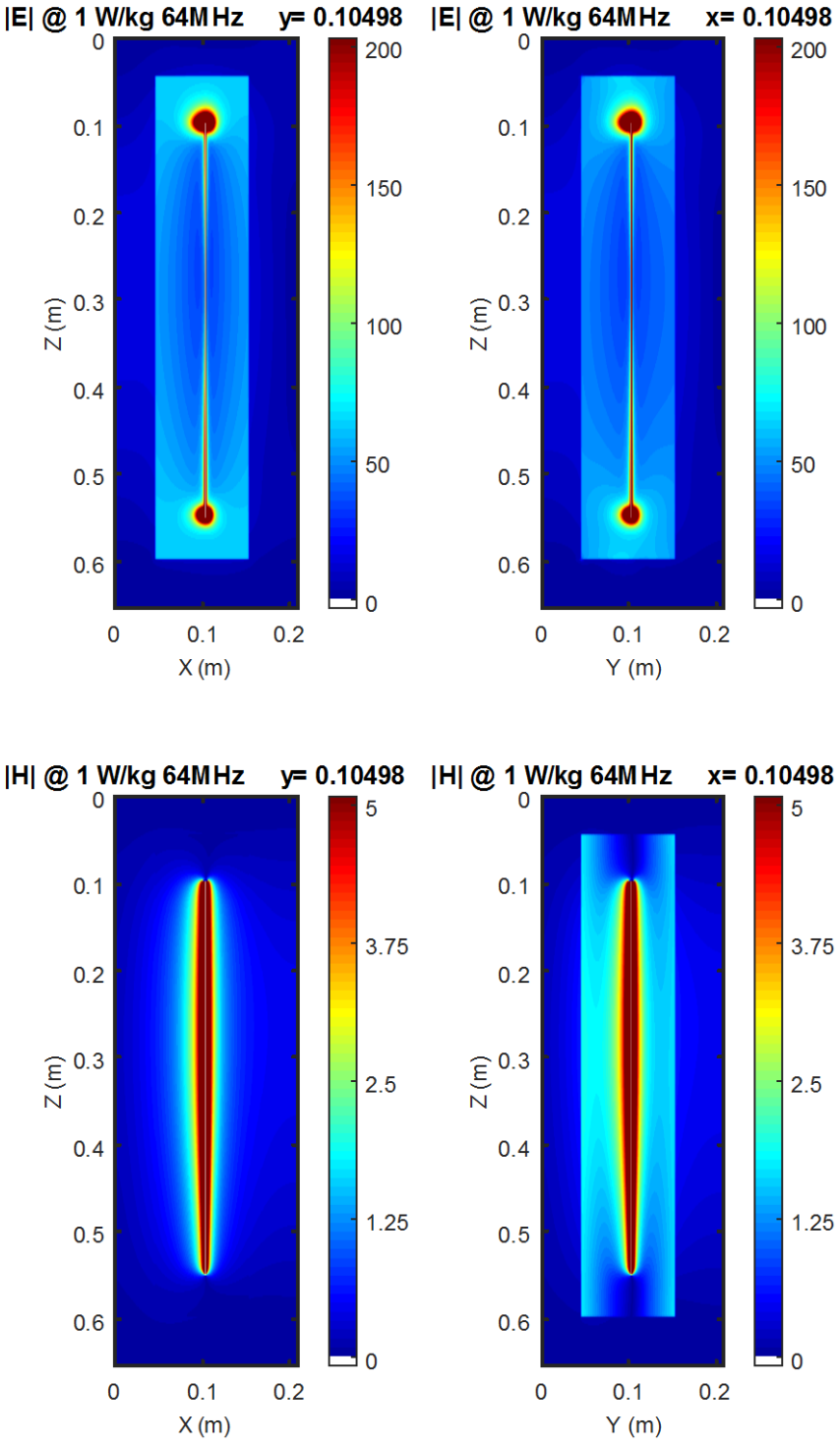

Figure 4.4 Calculated E-field and H-field distribution for electrode without the shield at 64 MHz

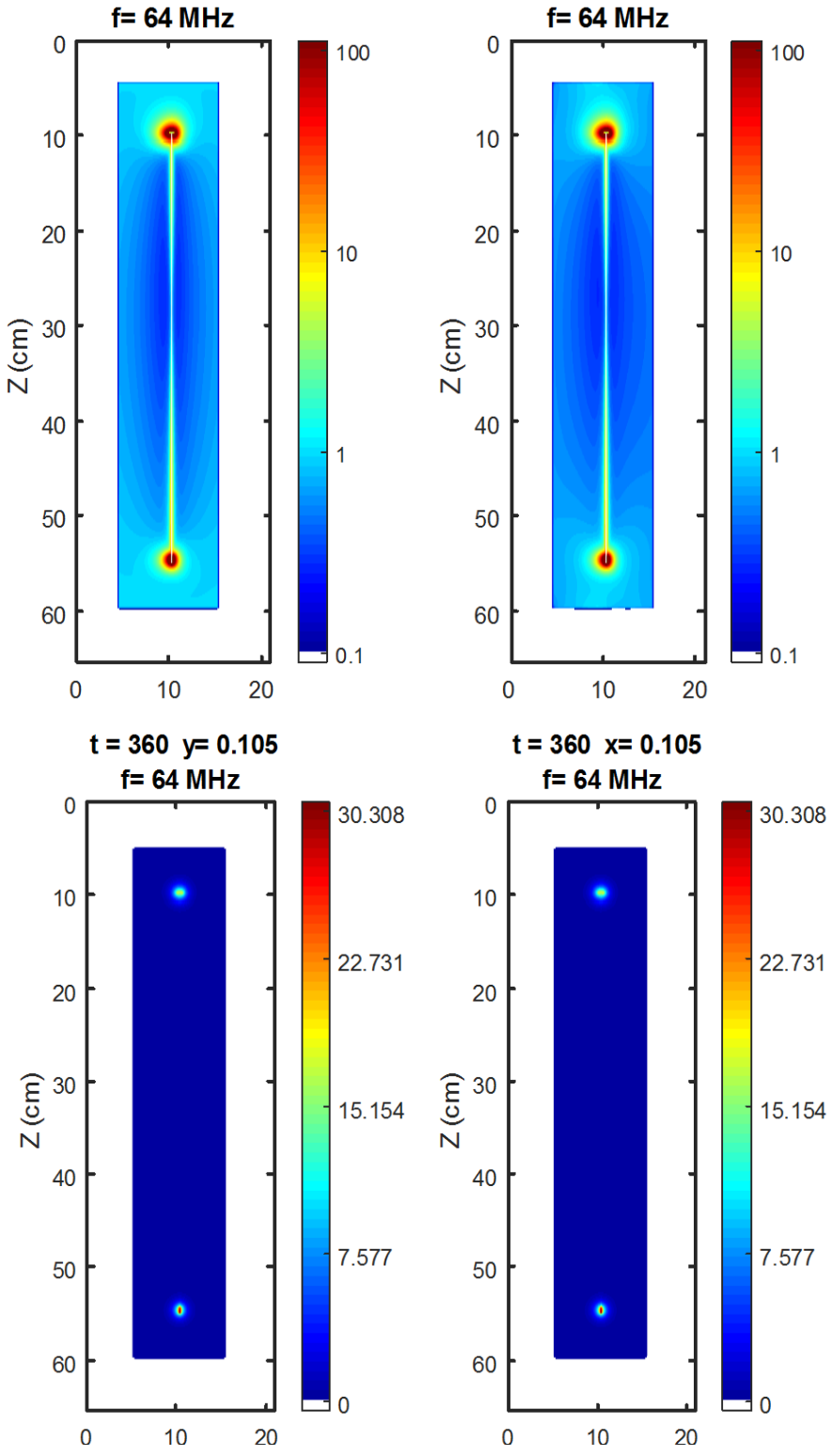

Figure 4.5 Calculated SAR (top) and Temperature rise distribution (bottom) for 45 cm unshielded model lead with a short at 64 MHz normalized to local SAR of 1 W/kg

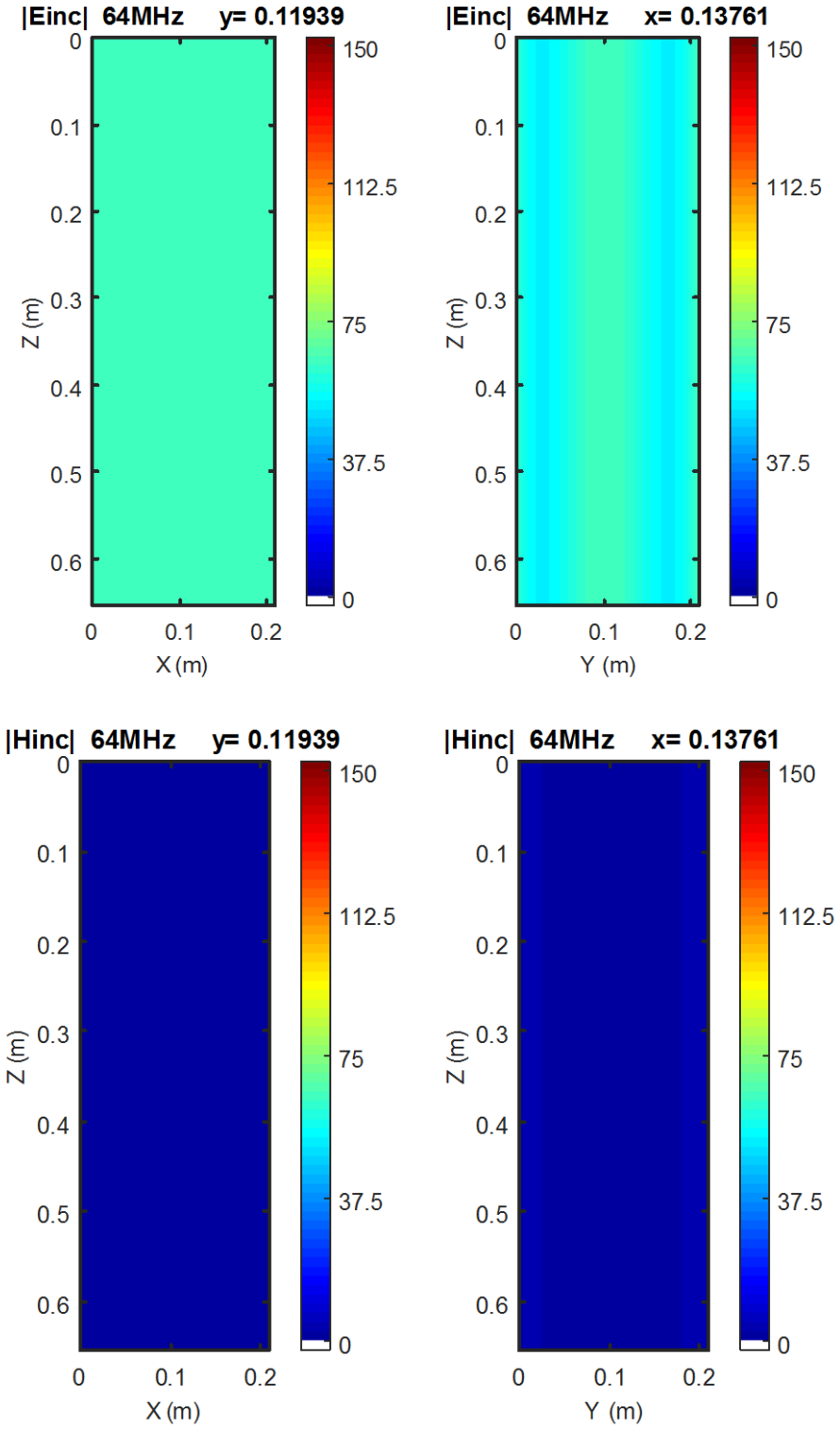

Figure 4.6 Incident E-field and H-field for heating calculation at 64 MHz. Color base is rms in units of V/m. Local background SAR in the plane of the shielded model lead with a short is 1 W/kg.

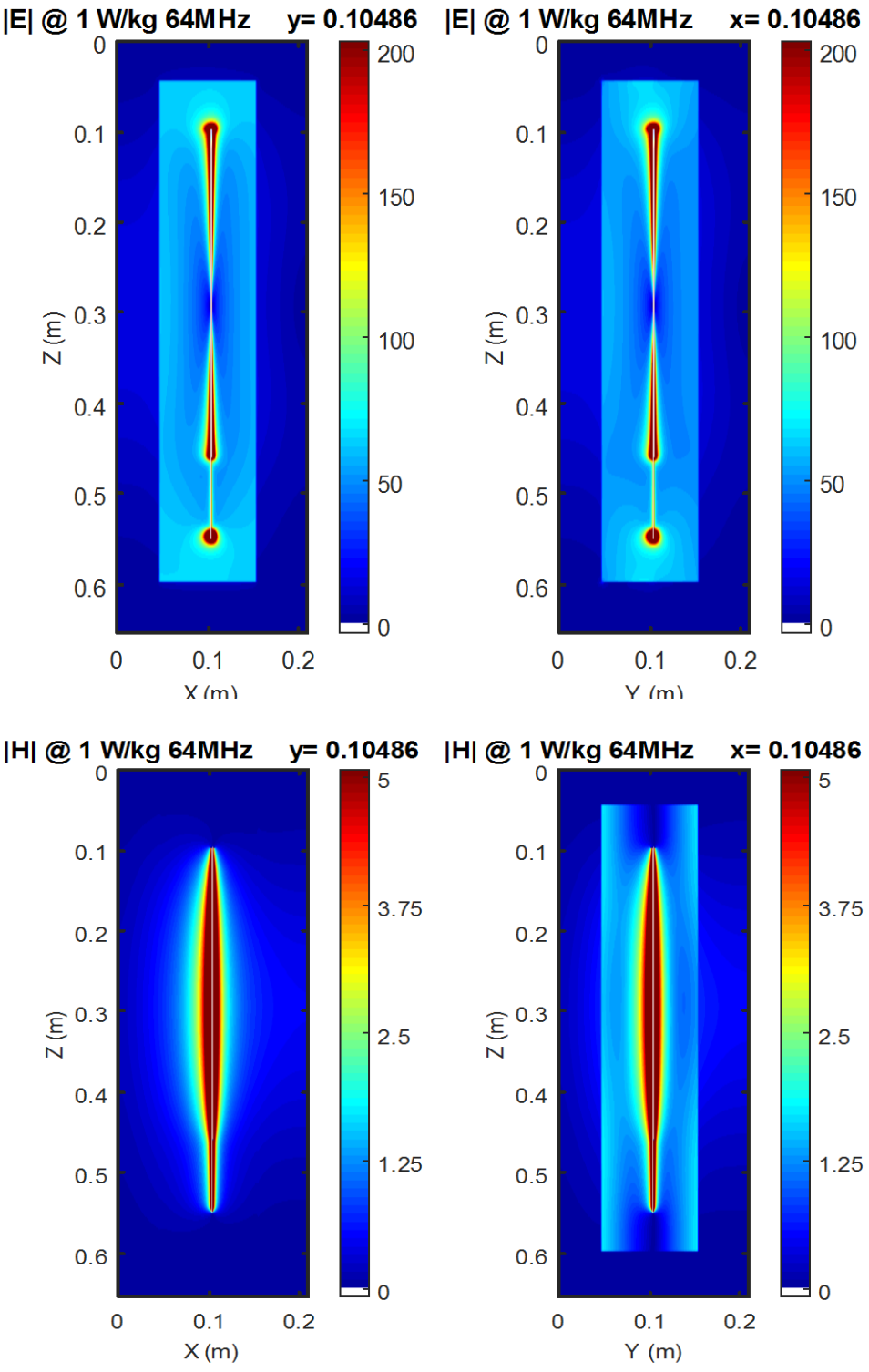

Figure 4.7 Calculated E-field and H-field distribution for an electrode with shield at 64 MHz

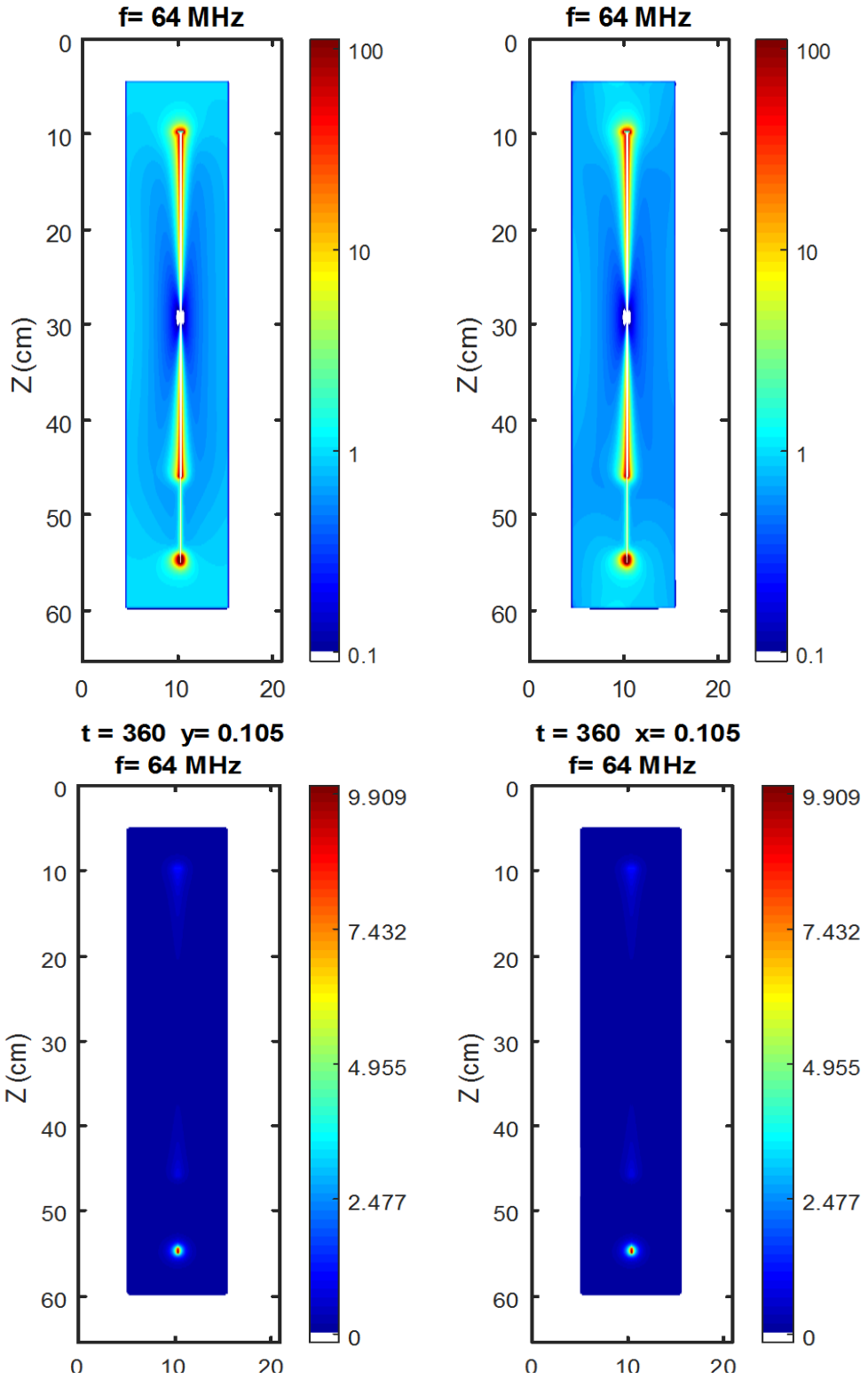

Figure 4.8 Calculated SAR (top) and Temperature rise distribution (bottom) for 45 cm shielded model lead with a short at 64 MHz normalized to local SAR of 1 W/kg

4.4 Measurement of Temperature rise for proposed electrodes.

To quantitatively test the model, temperature rise for shielded and unshielded model leads with a metallic short were simulated with the FDTD method, and measurements corresponding to the simulations are performed. For measurement purposes, the length of the model lead was 80 cm. RG 316 cable was used as a model implant as shown below Readers are referred to section 3.4 for a detailed explanation of methods and materials used for temperature rise purposes.

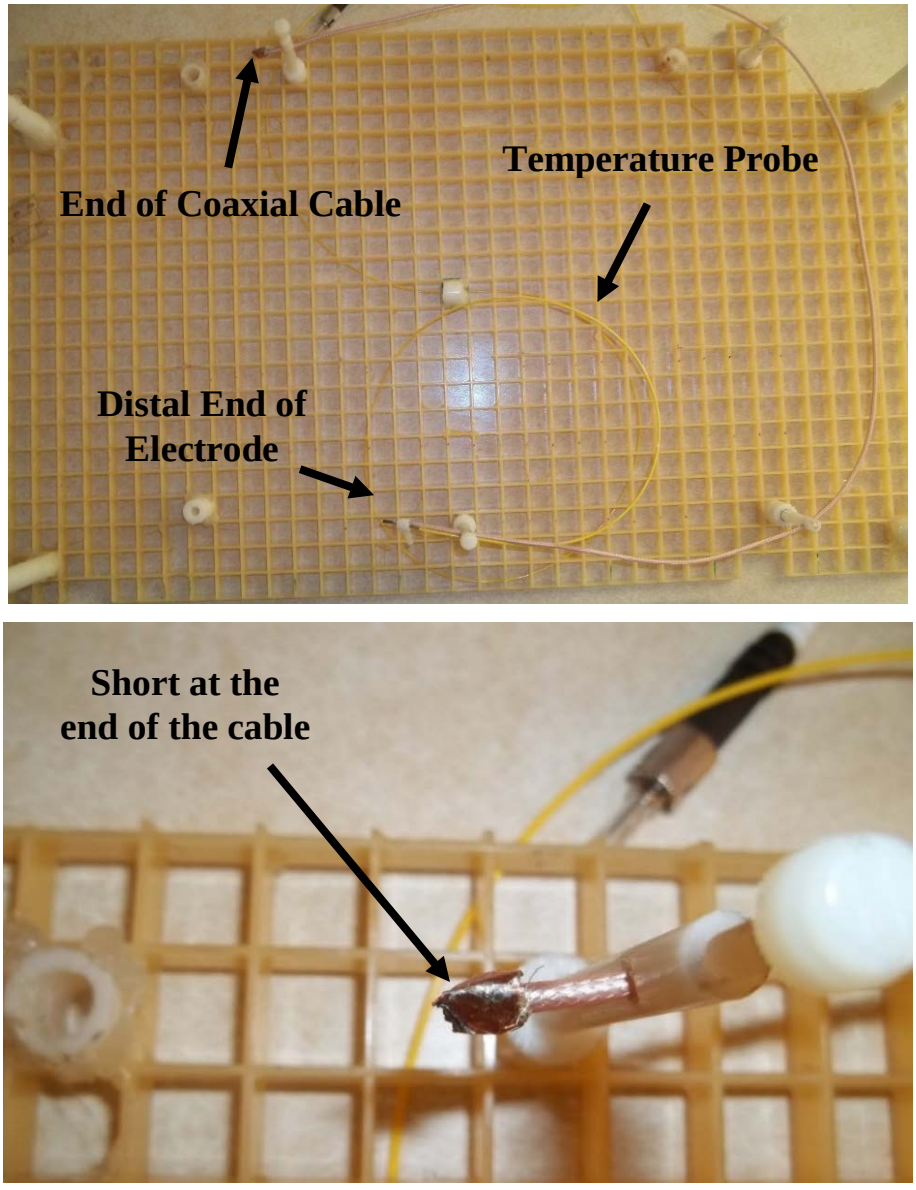

Figure 4.9 80-cm RG 316 coaxial cable that serves as a model implant. Copper cap at the proximal end of the 80 cm cable to achieve short configuration.

4.5 Results and Discussion

For the case of 80 cm shielded electrode, the shield is present from z=0.03 m to z=0.8 m. For the case of 45 cm shielded electrode, the shield is present from z=0.09 m to z=0.45 m. For the case of short at the end, physically a solder short is present to contact shield with the central metal rod. In the case of a generator attached at the end, a US 50 cent coin is attached to the end of the electrode. The generator is in direct contact with the central metal rod but not with a shield. For the case of a generator attached at the end, shield and central metal rod are not completely short on account for practical design purposes. There is a gap of ~5mm between shield and generator. The US half dollar coin model has a surface area like that of a small pacemaker.

Table 4.2 Comparison of scaled measured and simulated temperature rises for 45-cm model leads in different configurations at 64 MHz. Measurements are from the physical tests in the ASTM phantom based on average SAR along the length of the lead. The calculations are from FDTD. RF heat time is 360 seconds.

Structure	Test run	Scaled measured ΔT (°C/(W/kg))	Scaled calculated ΔT (°C/(W/kg))
Unshielded 45 cm open	05JUL18F	27.31	74.36
Unshielded 45 cm with model generator	05JUL18G	17.83	30.308
45 cm with 80% shield; open at the end	05JUL18H	7.94	7.13
45 cm with 80% shield; shorted at the end	05JUL18I	9.33	9.909

Table 4.2 shows a comparison of heating tests for measured and simulated temperature rise. There is a considerable difference in measured and calculated temperature rise for the unshielded model lead. This is because calculations performed in FDTD are assuming infinite plane. However, measurements are done in an ASTM phantom. The model lead is 4 cm from the wall. Therefore, temperature rise may reduce due to scattering from the walls. Secondly, the thermal conductivity of the copper central conductor used in calculations is more compared to the thermal conductivity of silver-coated copper central conductor of RG 316 model lead used in measurements. Thus, the temperature rise in calculations is more compared to measured values.

When a short is attached at the end of the cable, the input impedance of the cable is open circuited. As a result, the impedance is theoretically infinite. This causes minimal RF induced current on the electrode surface, resulting in minimal temperature rise. The Figure 4.10 shows measured scaled temperature rise vs. time for open and short conditions for 80 cm shielded lead electrode at 64MHz. Length of the shield is 77 cm. The maximum temperature rise for open, shielded lead is 16.35^{o}C and for short shielded lead is 1.01^{o}C.

Figure 4.11 shows calculated temperature rises vs. lead length at 128 MHz for different configurations of lead. Length of the shield is 80% of rod length. For a case of the electrode of length 40 cm (quarter wavelength at 128 MHz), the temperature rise is minimum in the presence of shield and generator (short) and is 0.2^{o}C. Local background SAR along the length of the lead is 1 W/kg. The maximum temperature rise for open, shielded lead is 6^{o}C and for short shielded lead is less than 4^{o}C. The significant temperature rises are due to the lead being quarter-wave in length. For the shorted able, the input impedance at the electrode end is essentially open-circuit, resulting in minimal temperature rise whereas the cable with open end has a short-circuit input resulting in large temperature rise.

Figure 4.12 shows calculated temperature rises vs. lead length at 64 MHz for different configurations of lead. Length of the shield is 80% of rod length. The temperature rise is minimum in the presence of shield for open configuration and is around 10^{o}C. Local

background SAR along the length of the lead is 1 W/kg. The maximum temperature rise for open unshielded lead is 74.36°C and for short unshielded lead is 30.308°C.

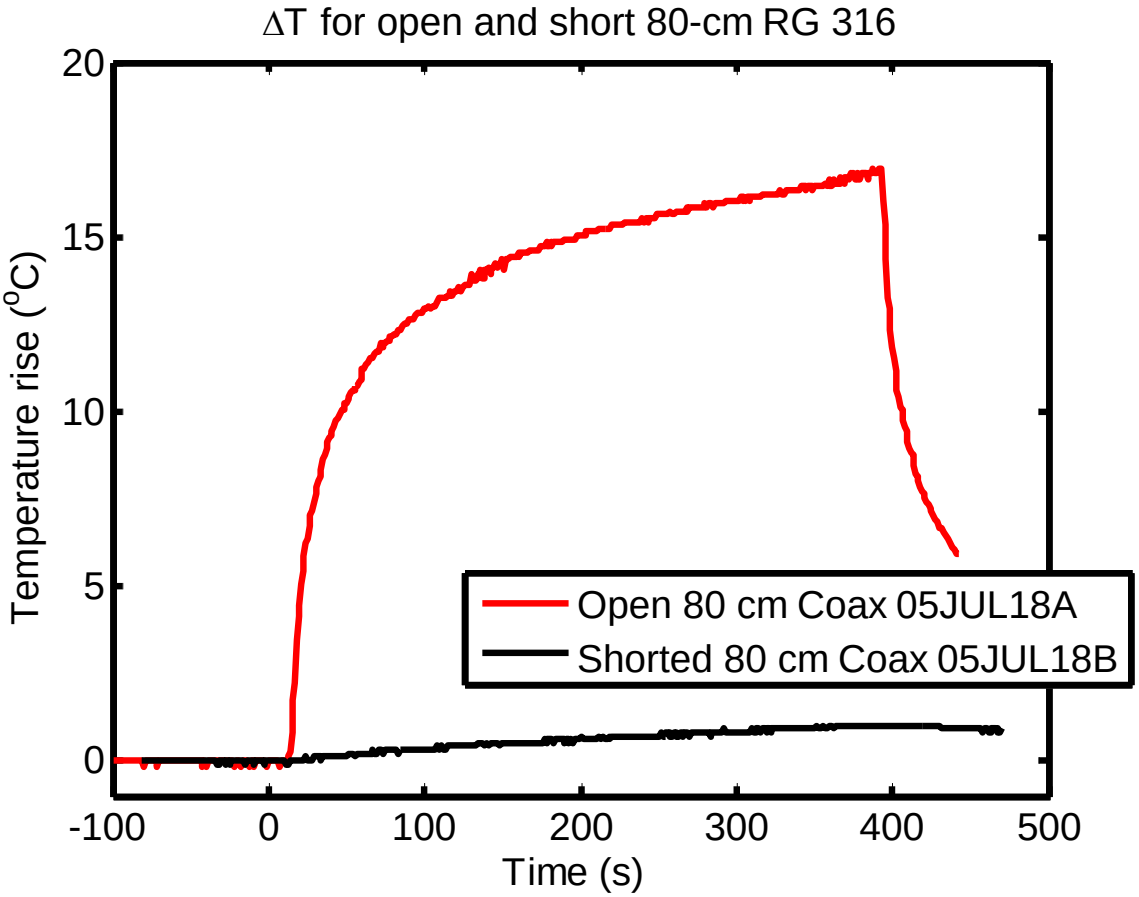

Figure 4.10 Comparison of measured temperature rise for 80 cm RG 316 model lead in open and short configurations. Length of the shield is 77 cm. The maximum temperature rise for open, shielded lead is 16.35°C and for short shielded lead is 1.01°C. The significant temperature rises are due to the lead being quarter-wave in length. For the shorted cable, the input impedance at the electrode end is essentially open-circuit, resulting in minimal temperature rise whereas the cable with open end has a short-circuit input resulting in large temperature rise.

The temperature rise is consistently less than 10 °C for open lead without the shield. For the case of electrode length 80 cm and 45 cm, experimental validation is performed at 64 MHz, to calculate temperature rise for all four configurations. Readers are referred to section 5.3.2. A comparison of scaled measured and calculated temperature rises for different 45-cm model leads at 64 MHz is presented in Table 4.2.

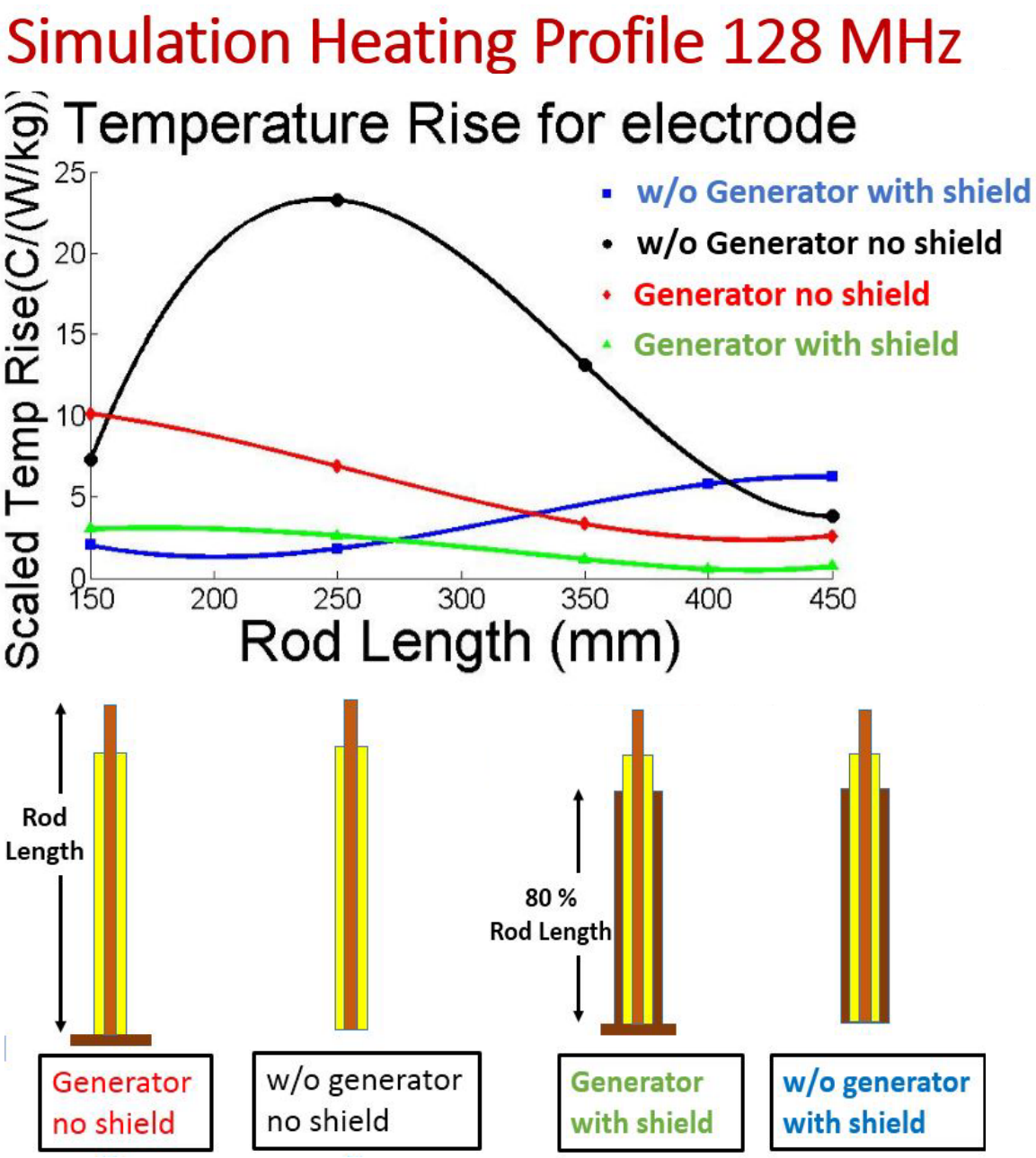

Figure 4.11 Simulation heating profile for all model implants at 128 MHz. Length of the shield is 80% of rod length. For a case of the electrode of length 40 cm (quarter wavelength at 128 MHz), the temperature rise is minimum in the presence of shield and generator (short) and is 0.2°C. Local background SAR along the length of the lead is 1 W/kg. Maximum temperature rises occur for unshielded model lead without a generator. The maximum temperature rise for open shielded lead is 6°C and for short shielded lead is less than 4°C. The significant temperature rises are due to the lead being quarter-wave in length. For the shorted able, the input impedance at the electrode end is essentially open-circuit, resulting in minimal temperature rise whereas the cable with open end has a short-circuit input resulting in large temperature rise. The temperature rise is consistently less than 4°C throughout the length.

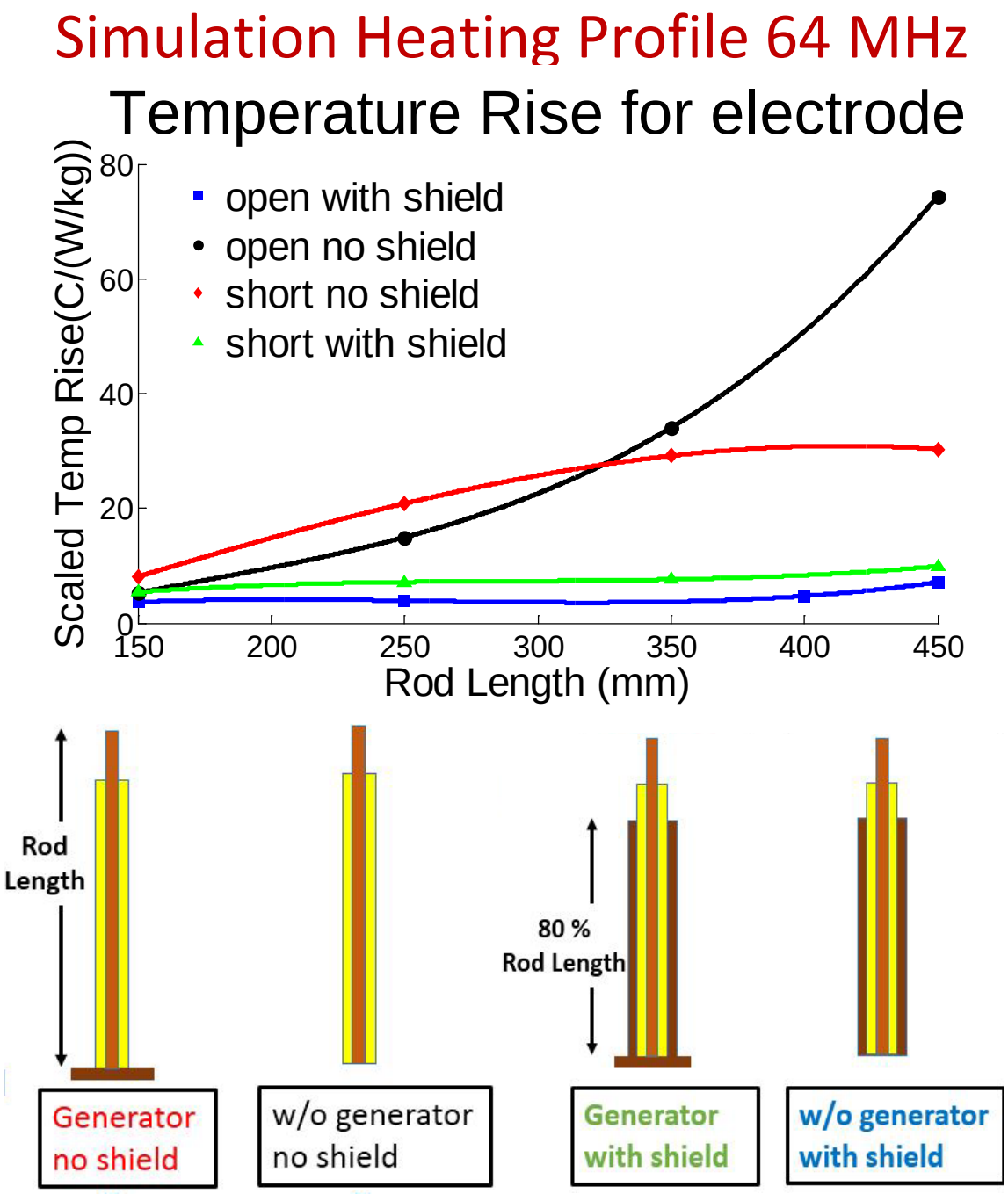

Figure 4.12 Simulation heating profile for all model implants at 64 MHz. Lowest rises occur for the shielded leads with a generator. Length of the shield is 80% of rod length. The temperature rise is minimum in the presence of shield for open configuration and is around 10°C. Local background SAR along the length of the lead is 1 W/kg. The maximum temperature rise for open unshielded lead is 65°C and for short unshielded lead is 35.8°C. The temperature rise is consistently less than 10 °C for open lead without the shield.

4.6 Summary and Conclusion

In this chapter, we introduced physical models of electrodes with short configuration. A short is achieved by placing a metallic generator at the distal end of the electrode. For measurement purposes, we attach a generator to the proximal end. There is a small gap of around ~3 mm between generator and shield. However, for all analysis purposes, attaching a generator can be treated as short. Numerical simulations are performed for 45 cm length of the electrode.

To validate proof of concept, experimental validations are performed for 80 cm and 45 cm length of the electrode. Temperature rise was calculated for different lengths of shielded and unshielded leads. Confirming measurements were made for a quarter-wavelength coaxial cable model of the lead. Measured temperature rise and transfer function depended on terminations conditions, with the open lead exhibiting a temperature rise sixteen times greater than the shorted lead.

A comprehensive analysis of simulation profile for different lengths of the electrode at all configurations is provided at 1.5 T and 3 T. At 128 MHz, the temperature rise is consistently less than 5 ^{o}C for an electrode with shield and short attached to the end. The minimum temperature occurs for the length of 45 cm at 128 MHz. At 64 MHz, the temperature rise is consistently less than 10 ^{o}C for an electrode with a shield and short attached to the end. The minimum temperature occurs for the case of the electrode without shield and short. Lengths more than 45 cm are not simulated due to computational limitations.

5. MEASUREMENT OF ELECTRIC FIELD TRANSFER FUNCTION AND TEMPERATURE RISES FOR PROPOSED MODEL OF ELECTRODE

Temperature rise due to RF-induced heating has received increasing importance from the MR safety community. To understand RF-induced heating, numerical simulations and measurements are conducted, with more emphasis on former. Park *et al*. [91] proposed a transfer function method to evaluate the worst case RF-induced heating. In this chapter, a brief introduction of transfer function concepts to evaluate RF-induced heating is discussed in following section 5.1. A general background review is also presented. Next, we describe the experimental setup used to evaluate transfer function in detail. We present measurement results of the transfer function and temperature rise for our proposed electrodes for all four structures. Finally, we conclude with a qualitative understanding of the relationship between transfer function and placement of shield on the electrode.

5.1 Introduction

The coupling between the electric field in the body to the lead is the main cause of RF heating at the electrode [94]. Current is induced on the lead surface due to the tangential electric field along the length of the lead. The induced current has characteristics of standing waves. It gets partially reflected and partially transmitted at the generator-electrode interface. Power deposited by the transmitted current in the tissue surrounding the electrode is given by SAR, which is ultimately responsible for the tip-to-tip heating of the electrode lead.

Current density J in the tissue due to electric field E is given as

$$J = \sigma E \tag{5.1}$$

where σ is the electrical conductivity of the tissue medium. Power deposited due to Electric field is quantified by SAR and is given by

$$SAR = \frac{\sigma E_{rms}^2}{\rho} \tag{5.2}$$

where ρ is the mass density, and E_{rms} is the rms value of electric field E given by [94]

$$E_{rms}(P) = K(P)\left|\int_0^L E_{tan}(\tau)S(\tau)\,d\tau\right| \tag{5.3}$$

Here, K is the constant that is a function of location near the electrode. S is the transfer function that physically represents the degree of coupling between the tangential electric field along the lead length. E_{tan} is the background tangential electric field along the lead length in the tissue medium (phantom) in the absence of actual lead. At a fixed position surrounding the electrode, the temperature rise is proportional to power deposited which is further proportional to the square of E_{rms}, and is given by

$$\Delta T = A\left|\int_0^L S_1(z)E_{tan}(z)dz\right|^2 \tag{5.4}$$

where A is a constant which is determined by a heating test [94], S_1 is the complex electric field sensitivity transfer function of the lead, E_{tan} is the complex background tangential component of the electric field and z is the distance along the lead. Length of the lead is Z =L, and Z=0 is on the electrode. Once we know background tangential electric field E_{tan} and constant A, temperature rise for any distribution of E_{tan} can then be calculated for known values of transfer function S.

The transfer function is calculated by measuring the surface currents along the device. This device is exposed to a uniform incident tangential electric field (E_{tan}) of 1 V/m which is then used to determine the scattered electric field E_1 induced by the device at a test point **P**. The radial component of the scattered electric field at **P** is calculated by applying a normalized E_{tan} of 1 V/m at location τ on the device over a width of Δτ. The incident electric field is set to 0 V/m over the remaining length of the device. The normalized transfer function may then be calculated as

$$S_1(\tau) = \frac{\Delta E_r(P)}{\Delta \tau} \frac{1}{E_{1r}(P)} \tag{5.5}$$

where E_{1r} is the radial component of E_1 at test point **P** resulting from the applied E_{tan} of 1 V/m over the device length and ΔE_r is the radial component of the scattered electric field at point **P** resulting from the applied E_{tan} of 1 V/m over the length $\Delta\tau$.

Feng *et al.* [93] used the reciprocity theorem in conjunction with Huygens principle and identified the transfer function as induced electric currents. A dipole is placed at the tip of a practical pacemaker leads, and the transfer function is tested. The transfer function is first obtained through simulations and measurements. The incident fields are then calculated using electromagnetic simulations. Finally, the induced electric fields are calculated by integrating the transfer function with the incident electric field along the surface of the wire. Based on this approach numerical simulations and experimental validation is performed on various sets of wires. The paper concludes that one can investigate the behavior of complex pacemaker leads using computational models and measurements, without performing a complete simulation involving complex lead, phantom, human model and RF coil.

Li *et al.* [95, 96] proposed an efficient approach to estimate RF-induced *in vivo* heating for small medical implants. The approach assumes that for implants less than a quarter wavelength in length, the incident field can be assumed a constant quantity. As a result, in equation 5.4, the incident electric field can be moved outside of integral. Instead of evaluating complex transfer function on the surface of the implant, the integral of the transfer function is sufficient to determine heating. This assumption is valid if the dimensions of the implant are small compared to the wavelength.

Another novel method to simulate transfer functions for implantable leads using a circuit simulator was introduced in [97]. The usage of a circuit simulator for transfer function extraction eliminates performing complex EM simulations that significantly reduce simulation time. Two-port measurements inside the saline with a ground plane are performed to create a lead transmission line model. Transfer function model is developed

by dividing the transmission line model into multiple sections and then evaluating S_{21} parameters for each section. Measurements and simulation at 64 MHz and 128 MHz were in good agreement.

5.2 Materials and Methods

Figure 5.1 shows the geometry for the assessment of the electric field transfer function. It consists of an electric field sensor, an exciting coil, and a vector network analyzer. A tangential electric field is applied over a short length of the lead with a transmitter in the form of a toroidal coil. The coil is translated along the lead to get the transfer function with respect to the position on the lead. The scattered electric field at the electrode is proportional to the voltage induced in an electric field sensor. A typical implementation for the transfer function measurement will be for V_1 to be the amplified output from port 1 of the vector network analyzer. The sensor voltage V_2 is applied to the port 2. The transfer function is proportional to the ratio of the voltage V_2 at the sensor to the input voltage V_1 applied to the coil. Also, the transfer function is proportional to the S_{21} that is measured by the vector network analyzer.

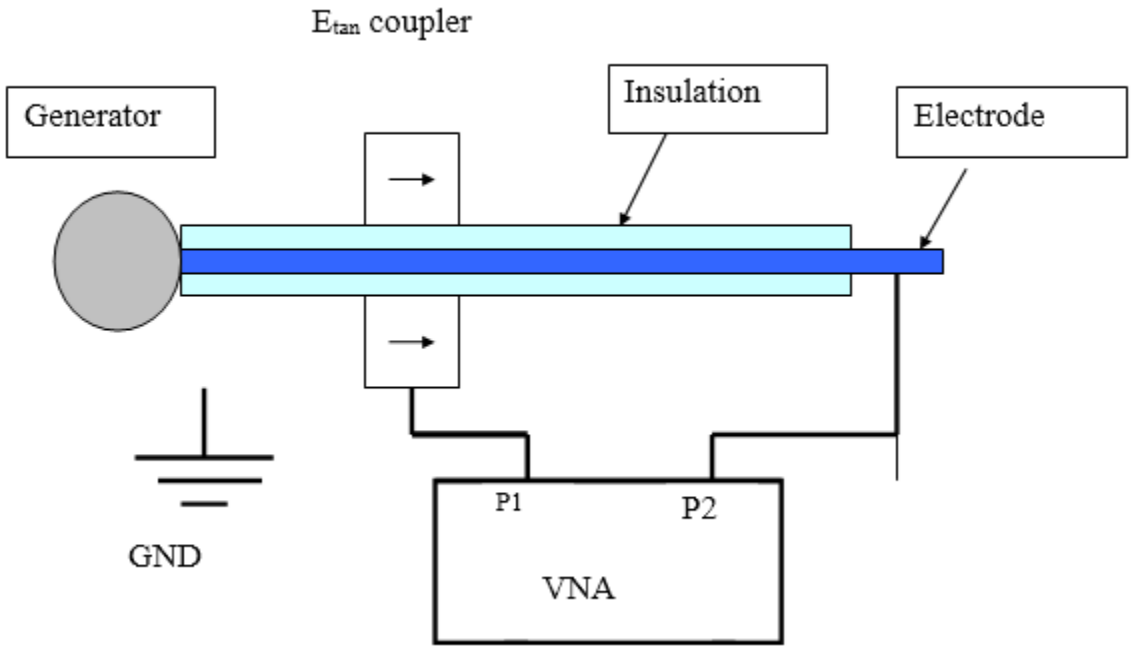

Figure 5.1 Geometrical representation of Transfer Function measurement

The transmitter probe is made up of RG 316 cable on which a metallic coil is wound on the small torus core. The number of turns of winding is 2. The reflection coefficient as measured from the torus to the cable is approximately 0.2. The torus core is ferromagnetic. The plane of the torus is orthogonal to the electrode under test. The electrode passes through the center of the torus. The coil is fixed to the torus with a strong glue. The coil is then translated manually along the length of the electrode under test to get the transfer function.

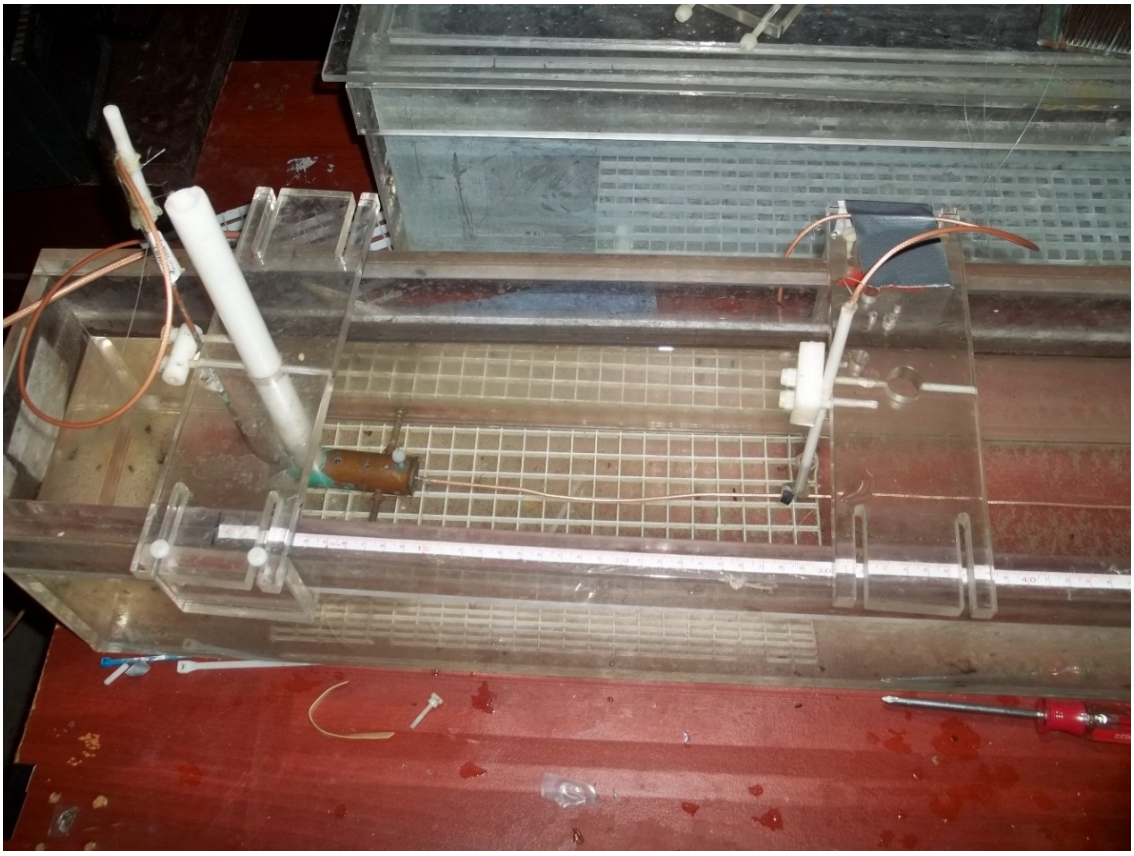

Figure 5.2 Setup for measurement of electric field transfer function. Receiving and transmitting probes are as shown. Probes are kept in a phantom of size 100 cm by 20 cm by 10 cm. The torus coil is manually translated by 1 cm along the length of the model implant surface to measure magnitude and phase of the transfer function. The transfer function is measured for each model implant length of 80 cm and 45 cm for all four different configurations of the model implant.

The scattered field at the end of the electrode is proportional to the voltage induced at the E field sensor. The sensor is called an E_{tan} coupler as shown in Figure 5.1. One end

of the coupler is connected to the VNA cable. The main function of the screw is to provide a coupling mechanism to the electrode lead.

To perform transfer function measurements, receiving probe and transmitting probes are kept in a phantom of size 100 cm by 20 cm by 10 cm. All the measurements are performed using a two-port HP 8712A RF network analyzer at 64 MHz and 128 MHz. Standard calibration techniques are used to calibrate VNA before measurements. The S_{21} parameter is measured at a different position along the length of the electrode. Magnitude and phase of the transfer function for all four physical model of the lead configurations is reported in subsequent sections in this chapter.

5.3 Results

5.3.1 Measurement of Electric Field Transfer Function for proposed electrodes

In this section measured magnitude and phase of the transfer function is presented for the proposed physical model of structures. In the plots, the magnitude of the transfer function is the S_{21} from the measurements. All transfer function measurements were performed at 64 MHz and 128 MHz. Length of the electrodes was 80 cm and 45 cm. For 80 cm shielded electrode, the length of the shield is 77 cm. For 45 cm shielded electrode, the length of the shield is 36 cm. Tip of the electrode is z=0. For the case of 80 cm shielded electrode, the shield is present from z=0.03 m to z=0.8 m. For the case of 45 cm shielded electrode, the shield is present from z=0.09 m to z=0.45 m. No shield is present for the unshielded electrode. For the case of short at the end, physically a solder short is present to contact shield with the central metal rod. In the case of a generator attached at the end, a US half dollar coin is attached to the end of the electrode. The generator is in direct contact with the central metal rod but not with a shield. For the case of a generator attached at the end, shield and central metal rod are not completely short on account for practical design purposes. There is a gap of ~5mm between shield and generator. The US half dollar coin model has a surface area like that of a small pacemaker. All other physical dimensions of the electrode are the same as described in Chapter 3 and Chapter 4.

5.3.1.1 Measurement of the electric field transfer function for 80 cm unshielded model lead with no generator (open at the end)

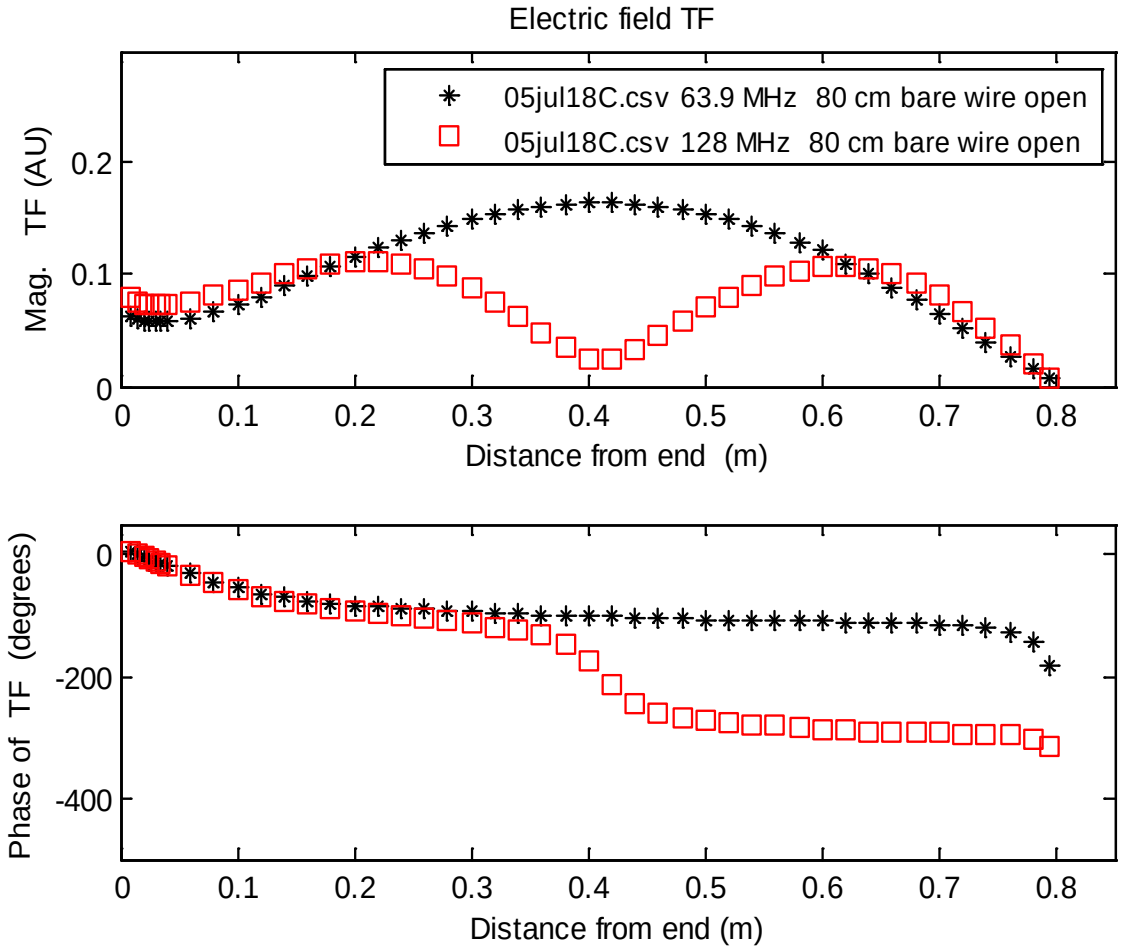

Figure 5.3 Measured transfer function plot for the open 80 cm RG316 unshielded lead Top plot is the magnitude, and the bottom plot is the phase of the transfer function. For open configuration, the magnitude of the reflection coefficient at the end of the lead is unity. That means the current and the voltage is out of phase. Since the lead is in open configuration, at half-wavelengths, the voltage is maximum which results in the minimum current at the proximal end. Hence, the current at the end of the lead is minimum. At quarter wavelengths, the voltage will be minimum, and the current will be maximum. Thus, for 128 MHz, for 80 cm model lead, the magnitude of the transfer function is maximum at quarter wavelengths, i.e., at z=60 cm and z=20 cm. The magnitude of the transfer function for 80 cm model lead at 128 MHz is minimum at half-wavelengths, i.e., at z=80 cm as shown. For 64 MHz, for 80 cm model lead the magnitude of the transfer function is maximum at quarter-wavelengths, i.e., at z=40 cm and minimum at half-wavelengths, i.e., at z=80 cm as shown above.

5.3.1.2 Measurement of the electric field transfer function for 80 cm shielded model lead with no generator (open at the end)

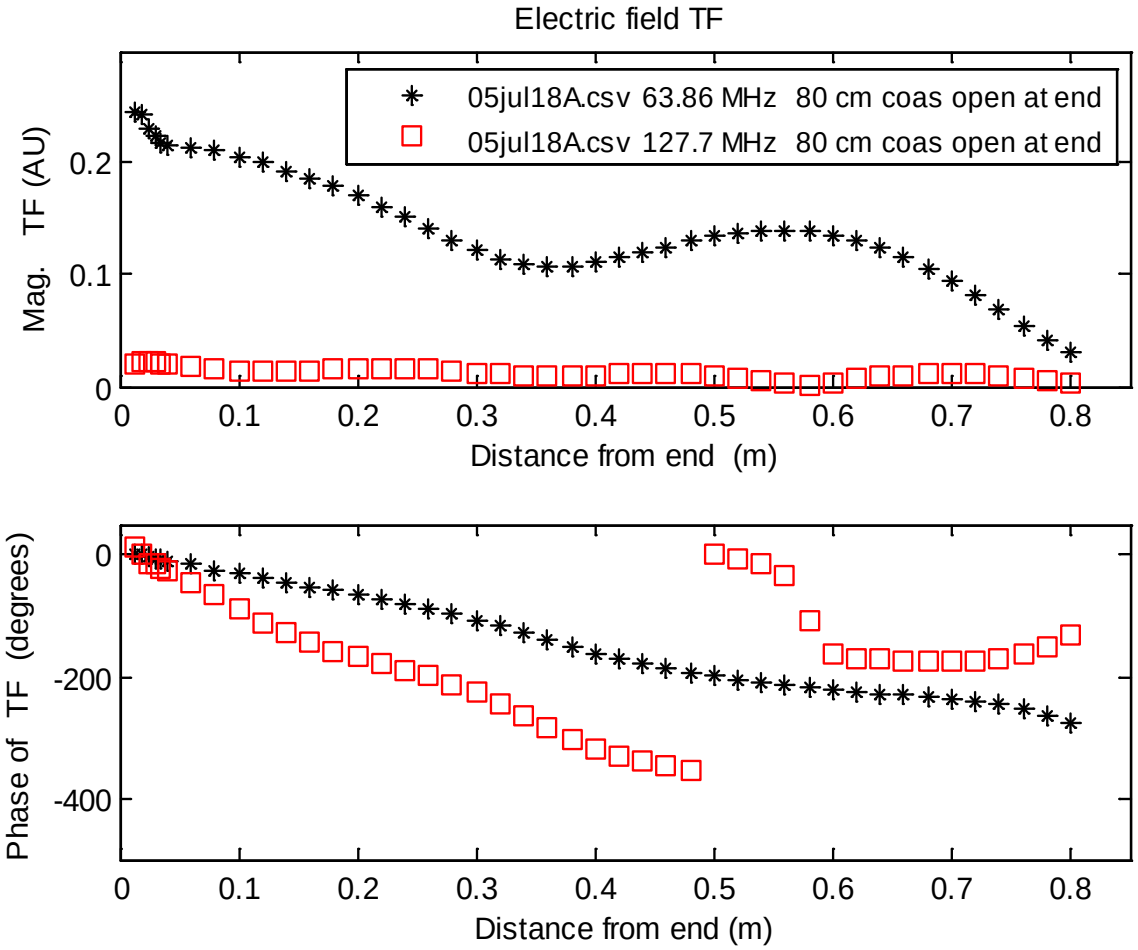

Figure 5.4 Measured transfer function for 80 cm RG 316 shielded wire open at the end. The top plot is the magnitude, and the bottom plot is the phase of the transfer function. The shield is present from z=3 cm to z=80 cm. The presence of shield decreases the magnitude of the transfer function when compared to unshielded 80 cm model lead in the open configuration. Impedance at the proximal end z=80 cm is infinite (open); hence current is zero at the end of the model lead. Therefore, the magnitude of the transfer function is zero at the proximal end.

5.3.1.3 Measurement of the electric field transfer function for 45 cm unshielded model lead with no generator (open at the end)

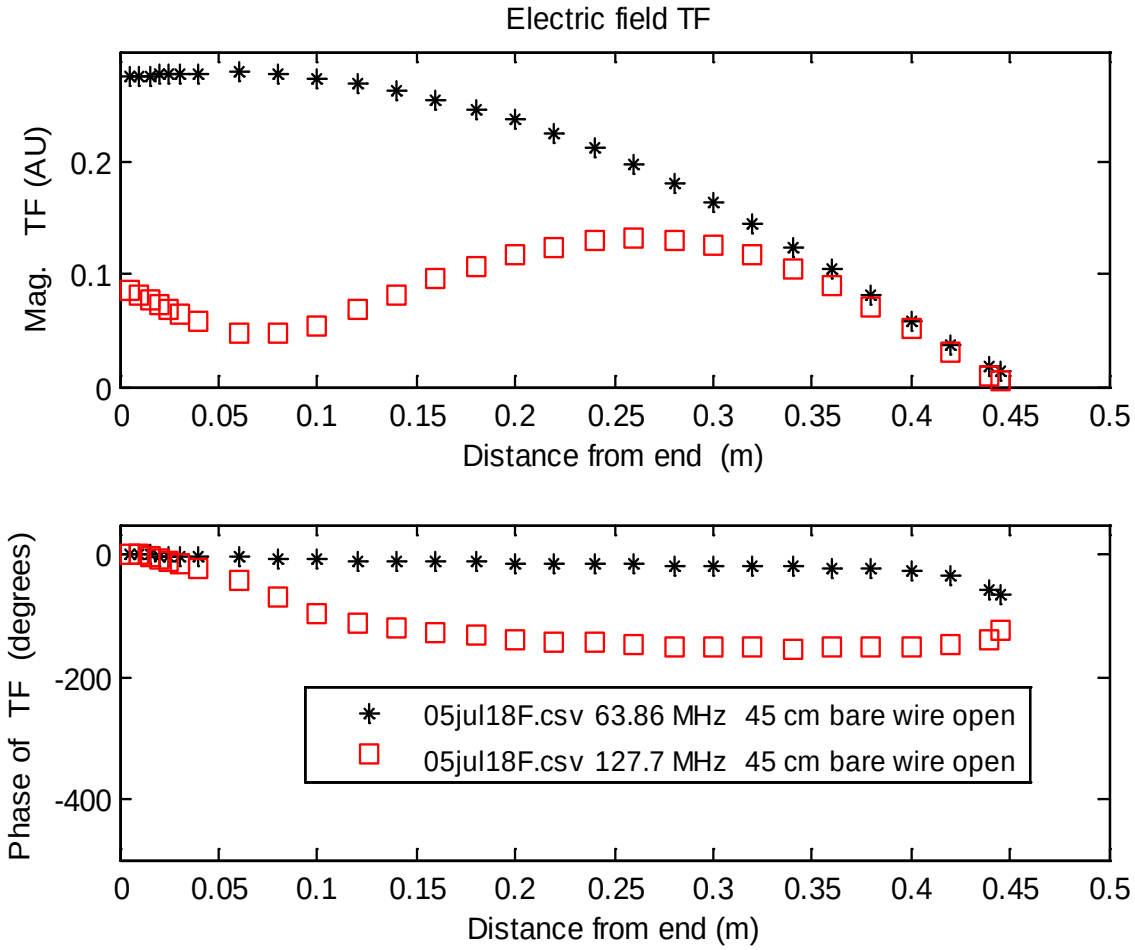

Figure 5.5 Measured transfer function plot for the open 45 cm RG316 unshielded lead The top plot is the magnitude, and the bottom plot is the phase of the transfer function. For open configuration, the magnitude of the reflection coefficient at the end of the lead is unity. That means the current and the voltage is out of phase. Since the lead is in the open configuration, at half-wavelengths, the voltage is maximum which results in the minimum current at the proximal end. Hence, the current at the end of the lead is minimum. At quarter wavelengths, the voltage will be minimum, and the current will be maximum. Thus, for 128 MHz, for 45 cm model lead, the magnitude of the transfer function is maximum at quarter wavelengths, i.e., at z=25 cm. The magnitude of the transfer function for 45 cm model lead at 128 MHz is minimum at half-wavelengths, i.e., at z=45 cm as shown. For 64 MHz, for 45 cm model lead the magnitude of the transfer function is maximum at quarter-wavelengths, i.e., at z=0 cm and minimum at half-wavelengths, i.e., at z=45 cm as shown above.

5.3.1.4 Measurement of the electric field transfer function for 45 cm shielded model lead with no generator (open at the end)

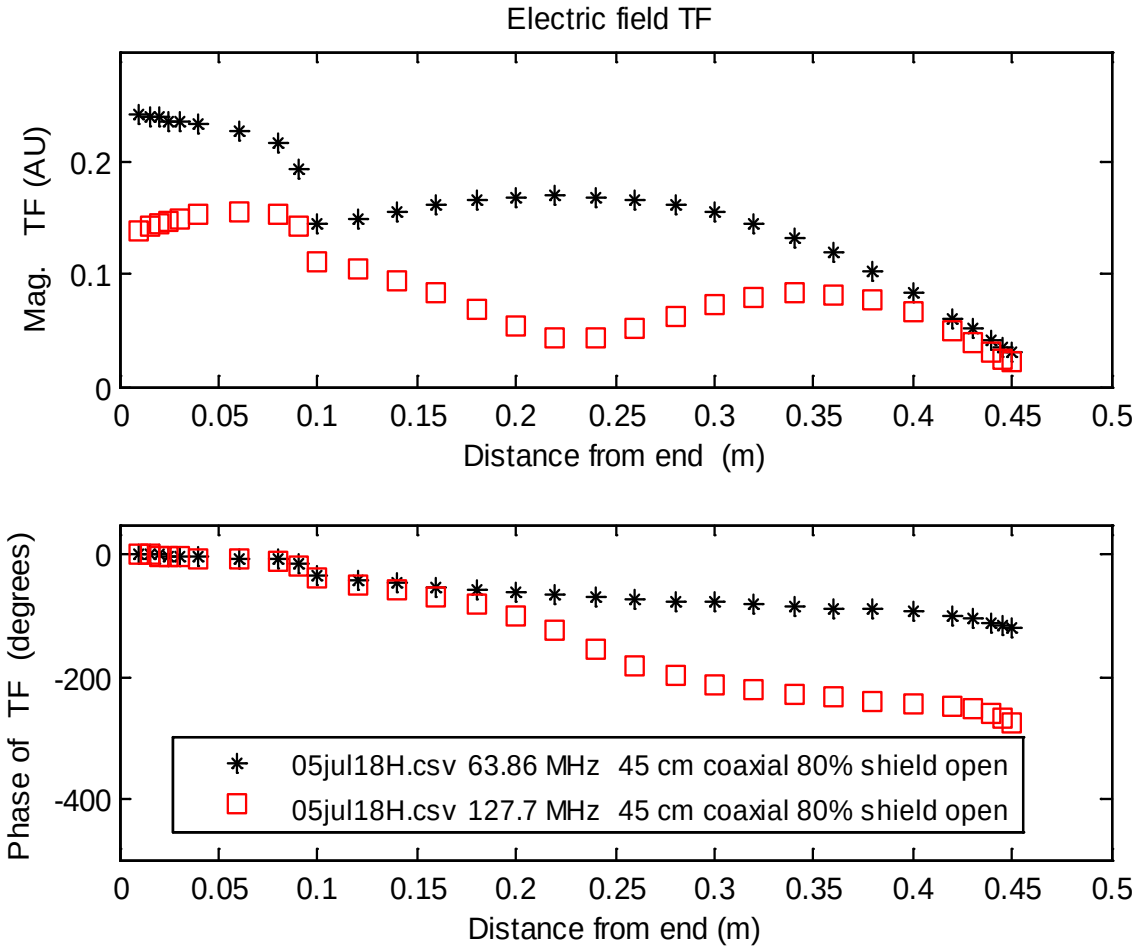

Figure 5.6 Measured transfer function for 45 cm RG 316 shielded wire open at the end. The top plot is the magnitude, and the bottom plot is the phase of the transfer function. The shield is present from z=9 cm to z=45 cm. The presence of shield decreases the magnitude of the transfer function when compared to unshielded 45 cm model lead in the open configuration. Impedance at the proximal end z=45 cm is infinite (open); hence current is zero at the end of the model lead. Therefore, the magnitude of the transfer function is zero at the proximal end.

5.3.1.5 Measurement of the electric field transfer function for 80 cm shielded model lead with a metallic short at the end

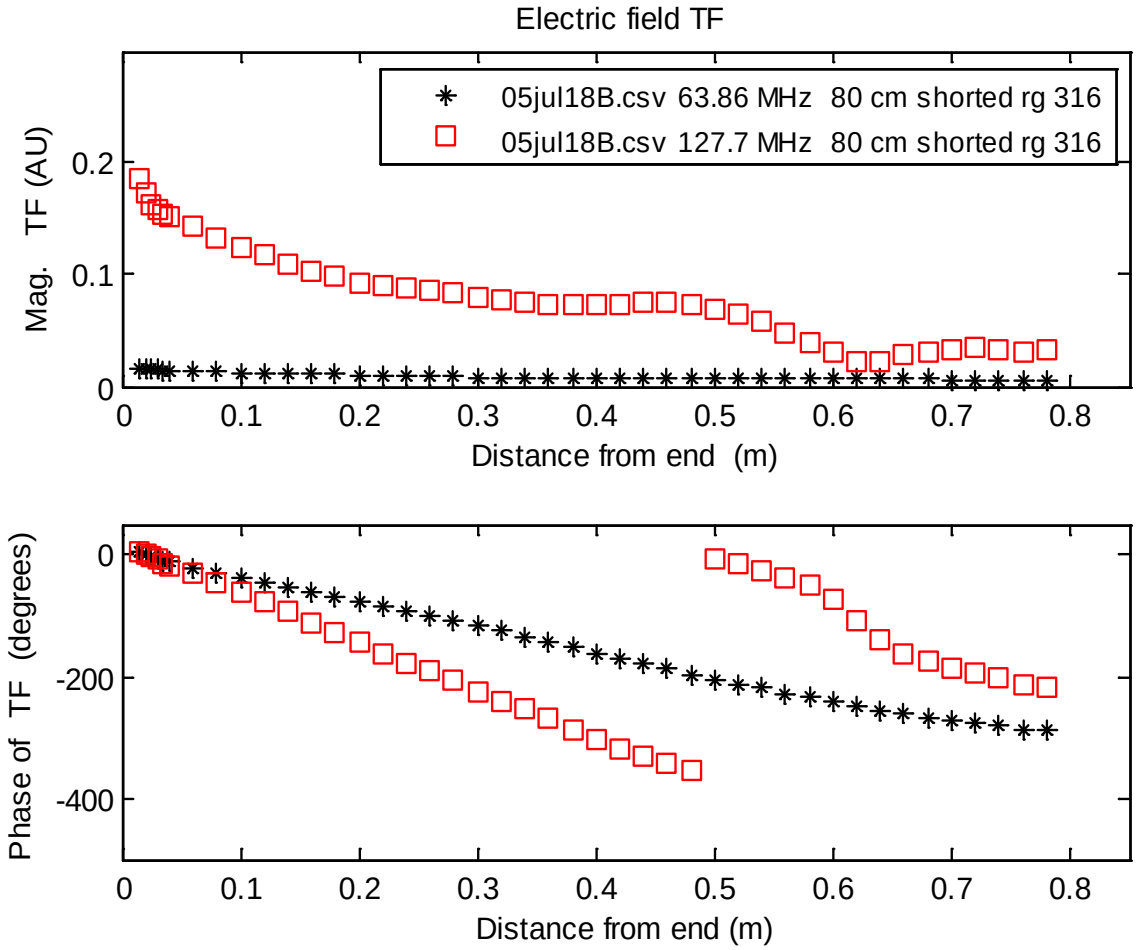

Figure 5.7 Measured transfer function for shorted 80 cm RG 316 shielded lead. The top plot is the magnitude, and the bottom plot is the phase of the transfer function. The shield is present from z=3 cm to z=80 cm. The presence of shield decreases the magnitude of the transfer function when compared to shielded model lead in the open configuration. At 64 MHz, for a quarter wavelength section of the transmission line (80 cm), the input impedance at distal end z=0 looking towards the proximal end of the model lead is infinite in short configuration. Hence, the current is minimum. As a result, the magnitude of the transfer function is minimum as shown above.

5.3.1.6 Measurement of the electric field transfer function for 45 cm shielded model lead with a metallic short at the end

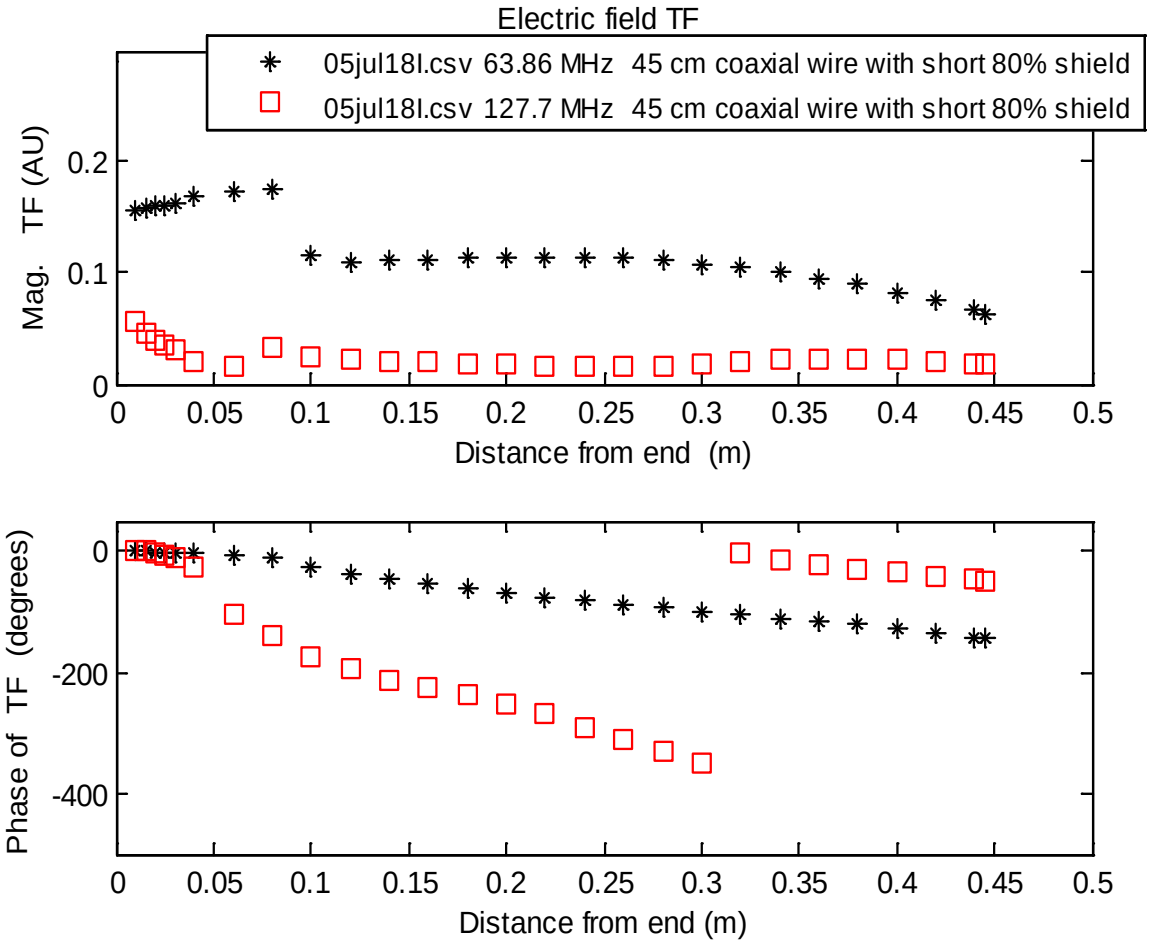

Figure 5.8 Measured transfer function for shorted 45 cm RG 316 shielded lead. The top plot is the magnitude, and the bottom plot is the phase of the transfer function. The shield is present from z=9 cm to z=45 cm. The presence of shield decreases the magnitude of the transfer function when compared to shielded model lead in the open configuration. At 128 MHz, for a quarter wavelength section of the transmission line (45 cm), the input impedance at distal end z=0 looking towards the proximal end of the model lead is infinite in short configuration. Hence, the current is minimum. As a result, the magnitude of the transfer function is minimum as shown above.

5.3.1.7 Measurement of the electric field transfer function for 80 cm unshielded model lead with the generator at the end.

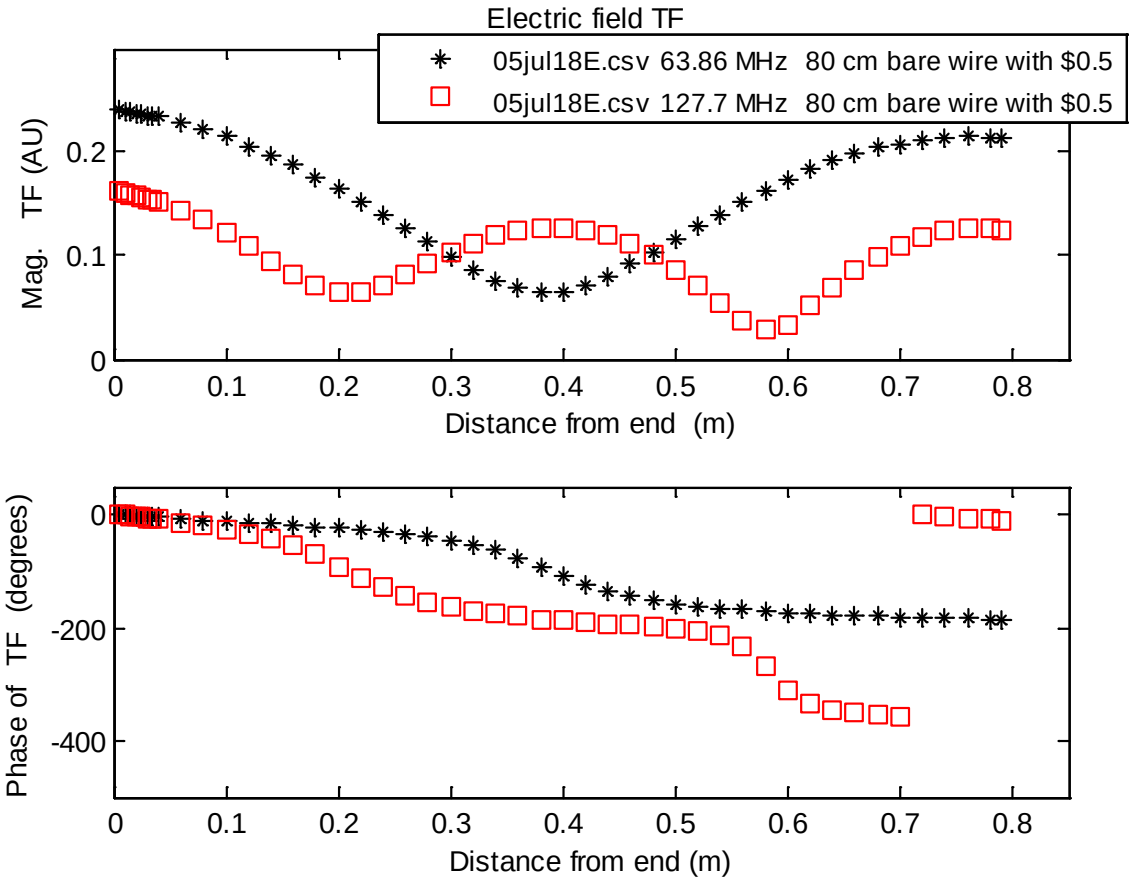

Figure 5.9 Measured transfer function for 80cm RG316 unshielded lead with generator The US $0.5 coin is attached at the end. The top plot is the magnitude, and the bottom plot is the phase of the transfer function. For short configuration, the magnitude of the reflection coefficient at the end of the lead is -1. Since the lead is in the short configuration, at half-wavelengths, the voltage is minimum which results in the maximum current at the proximal end. Hence, the current at the end of the lead is maximum. At quarter wavelengths, the voltage will be maximum, and the current will be minimum. Thus, for 128 MHz, for 80 cm model lead, the magnitude of the transfer function is minimum at quarter wavelengths, i.e., at z=60 cm and z=20 cm. The magnitude of the transfer function for 80 cm model lead at 128 MHz is maximum at half-wavelengths, i.e., at z=80 cm as shown. For 64 MHz, for 80 cm model lead the magnitude of the transfer function is minimum at quarter-wavelengths, i.e., at z=40 cm and maximum at half-wavelengths, i.e., at z=80 cm as shown above.

5.3.1.8 Measurement of the electric field transfer function for 80 cm shielded model lead with the generator at the end.

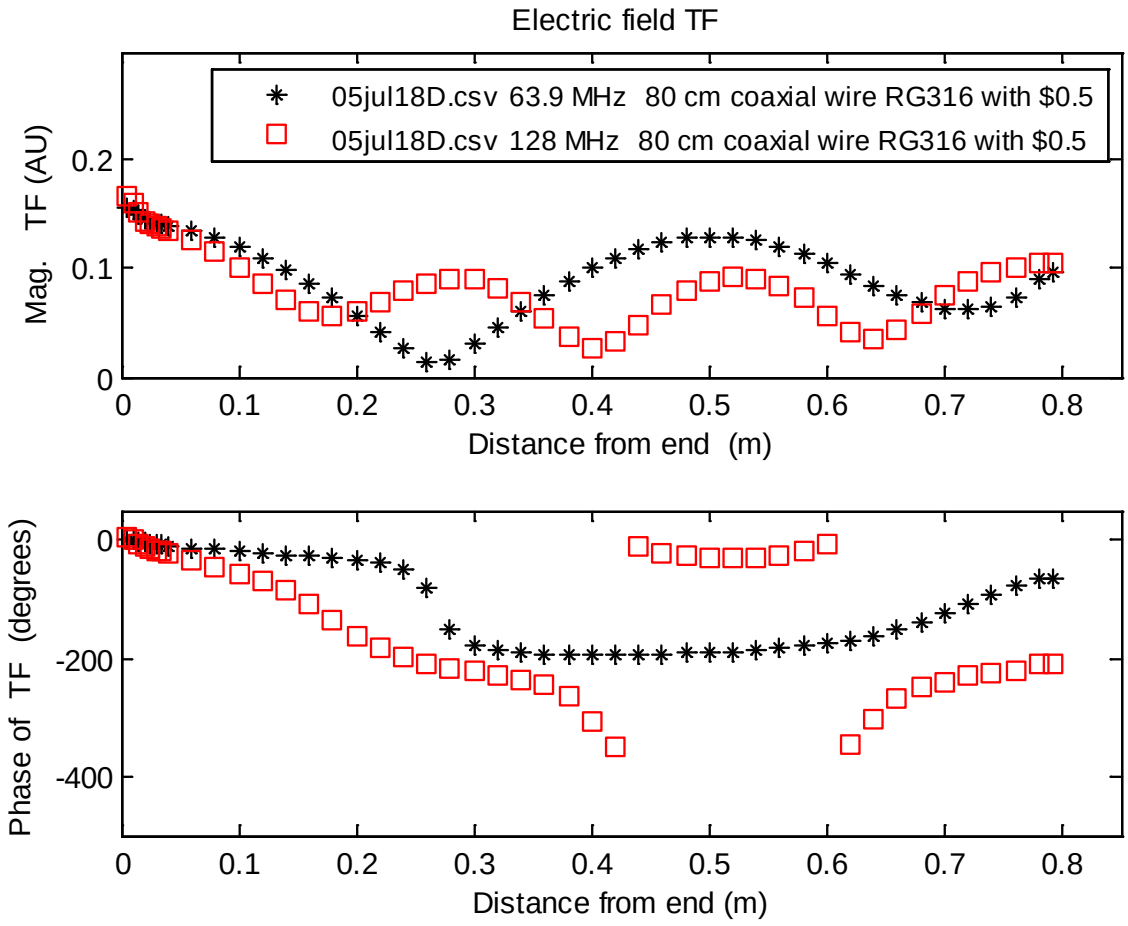

Figure 5.10 Measured transfer function for 80cm RG316 shielded lead with generator The US $0.5 coin is attached at the end. The top plot is the magnitude, and the bottom plot is the phase of the transfer function. The shield is present from z=3 cm to z=80 cm. The presence of shield decreases the magnitude of the transfer function when compared to unshielded 80 cm model lead in the short configuration. Impedance at the proximal end z=80 cm is zero (short); hence current is non-zero at the end of the model lead. Therefore, the magnitude of the transfer function is non-zero at the proximal end.

5.3.1.9 Measurement of the electric field transfer function for 45 cm unshielded model lead with the metallic generator at the end.

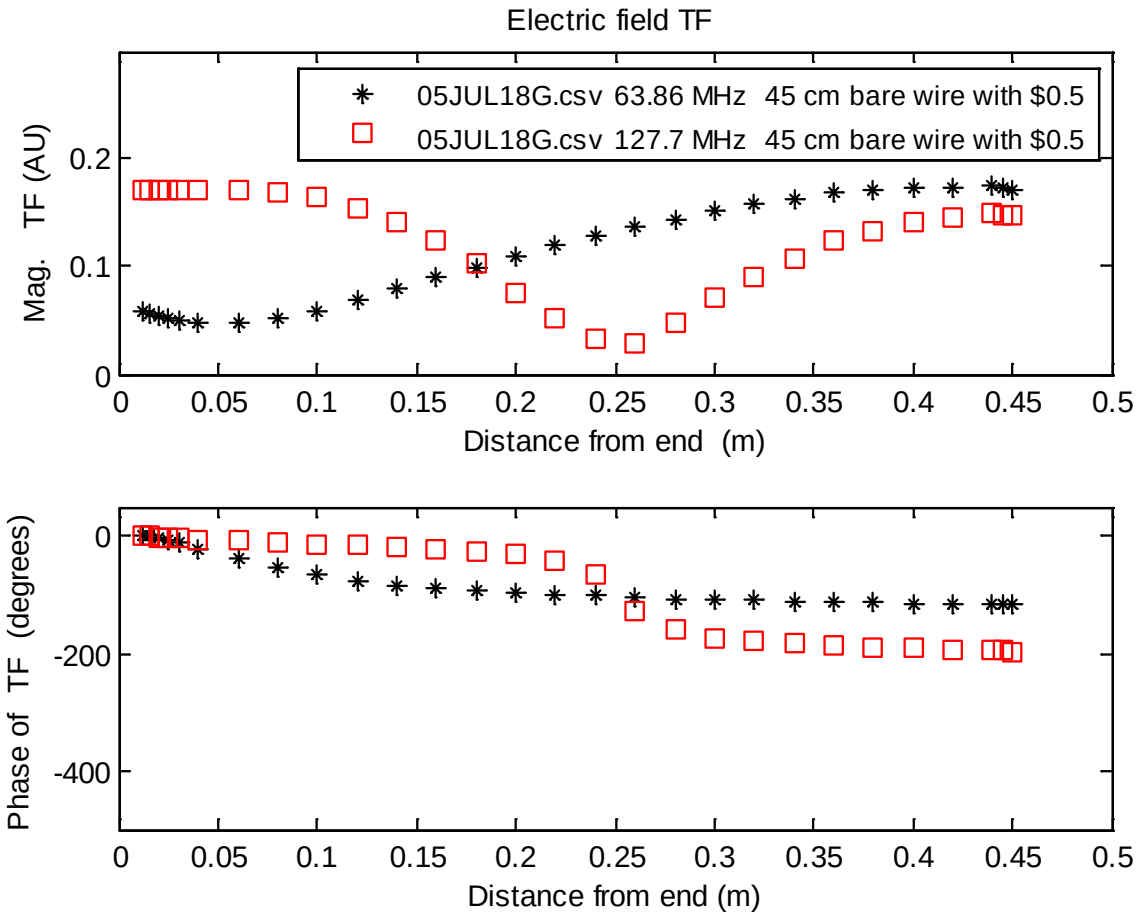

Figure 5.11 Measured transfer function for 80cm unshielded lead with generator The US $0.5 coin is attached at the end. The top plot is the magnitude, and the bottom plot is the phase of the transfer function. For short configuration, the magnitude of the reflection coefficient at the end of the lead is -1. Since the lead is in the short configuration, at half-wavelengths, the voltage is minimum which results in the maximum current at the proximal end. Hence, the current at the end of the lead is maximum. At quarter wavelengths, the voltage will be maximum, and the current will be minimum. Thus, for 128 MHz, for 45 cm model lead, the magnitude of the transfer function is minimum at quarter wavelengths, i.e., at z=25 cm. The magnitude of the transfer function for 45 cm model lead at 128 MHz is maximum at half-wavelengths, i.e., at z=45 cm as shown. For 64 MHz, for 45 cm model lead the magnitude of the transfer function is minimum at quarter-wavelengths, i.e., at z=0 cm and maximum at half-wavelengths, i.e., at z=45 cm as shown above.

.

5.3.1.10 Measurement of the electric field transfer function for 45 cm shielded model lead with the metallic generator at the end.

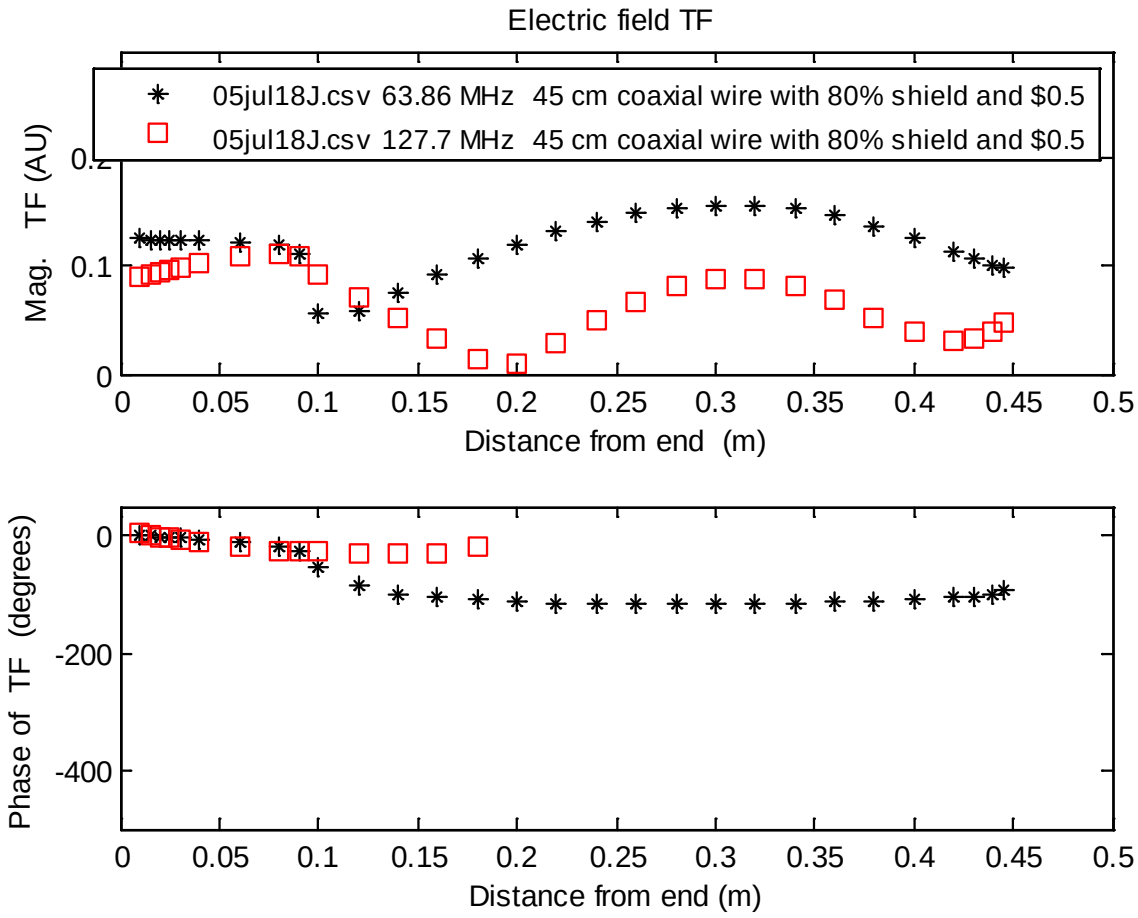

Figure 5.12 Measured transfer function for 45 cm RG316 shielded lead with generator The US $0.5 coin is attached at the end. The top plot is the magnitude, and the bottom plot is the phase of the transfer function. The shield is present from z=9 cm to z=45 cm. The presence of shield decreases the magnitude of the transfer function when compared to 45 cm unshielded model lead in the short configuration. Impedance at the proximal end z=45 cm is zero (short); hence current is non-zero at the end of the model lead. Therefore, the magnitude of the transfer function is non-zero at the proximal end.

5.3.2 Temperature Rise Measurement for proposed electrodes

In this section measured temperature rises is presented for the proposed physical model of structures. The reader is referred to section 3.4 for a detailed explanation of the temperature rise measurements. All measurements were performed at 64 MHz.

a) Implant lead on a plastic mat with US $0.5 coin

(b) Plastic mat kept in a phantom

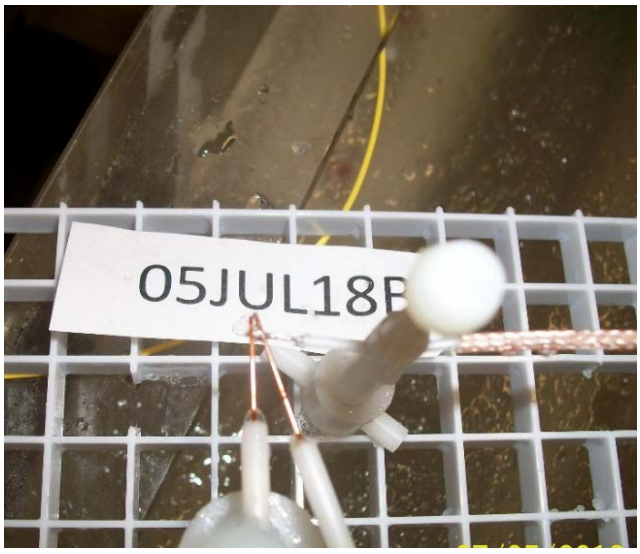

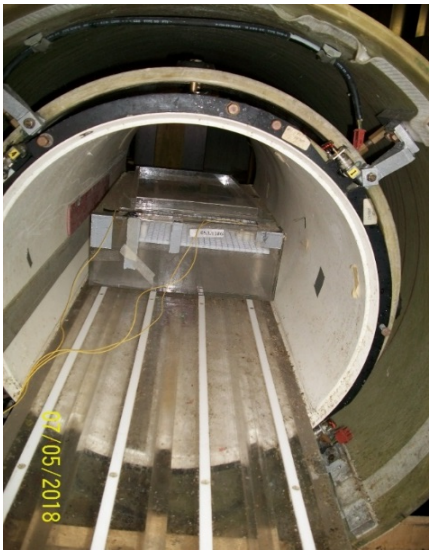

(c) Neoptix probe in contact with an electrode of the model implant (left) and phantom with the model implant kept in an MR coil (right)

Figure 5.13 Placement of model implant lead for temperature rise measurement

5.3.2.1 Measurement of Temperature rise for unshielded RG 316 model lead with no generator (open at the end)

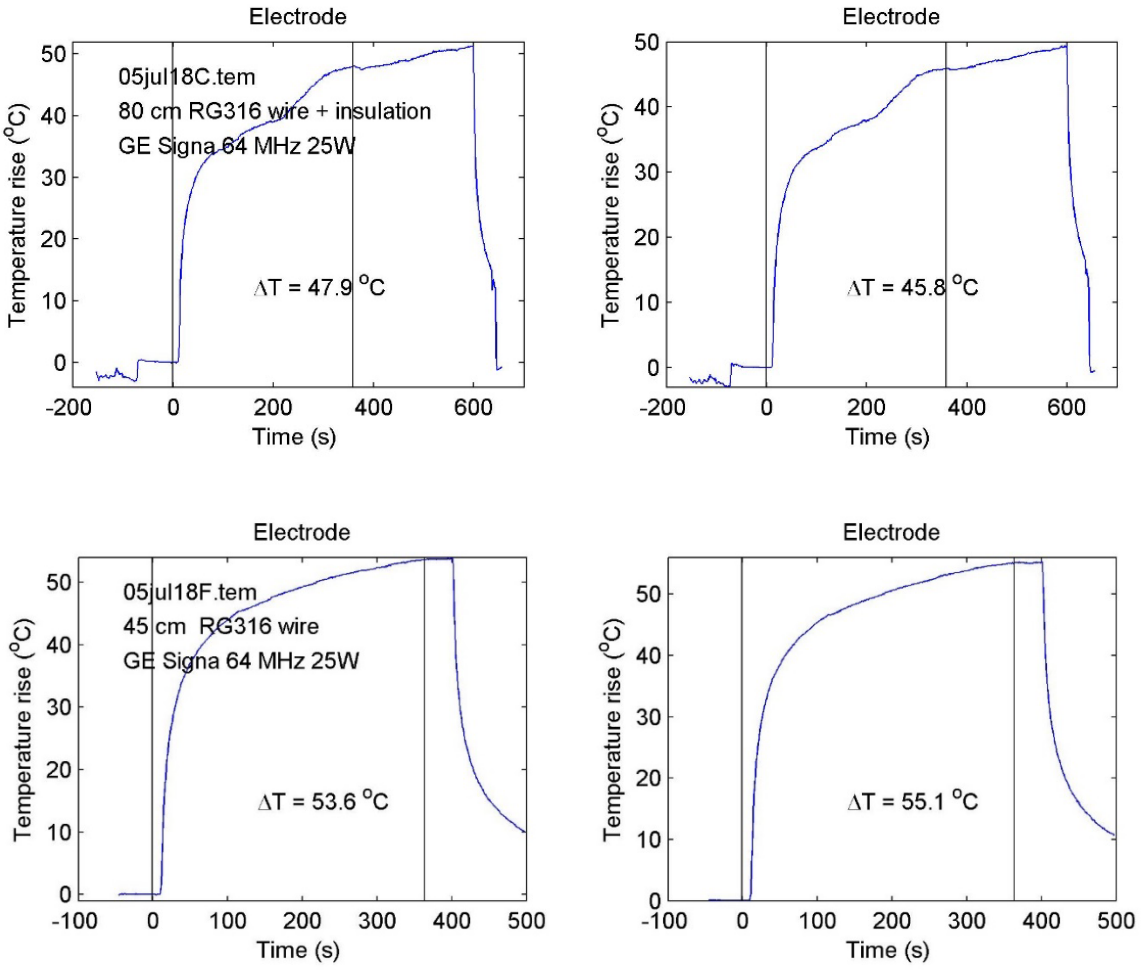

Figure 5.14 Measured Temperature rise for open unshielded RG 316 model lead at 64 MHz after 6 minutes of RF power of 25 W. The top plot is for lead length 80 cm and bottom for 45 cm. Two neoptix temperature probes are used for temperature rise measurement for redundancy. For 80 cm model implant, the average measured temperature rise at the tip of the lead is 46.85°C. For 45 cm model implant, the average measured temperature rise at the tip of the lead is 54.35°C. Local background SAR at 25 W of RF power is 1.99 W/kg.

5.3.2.2 Measurement of Temperature rise for shielded RG 316 model lead with no generator (open at the end)

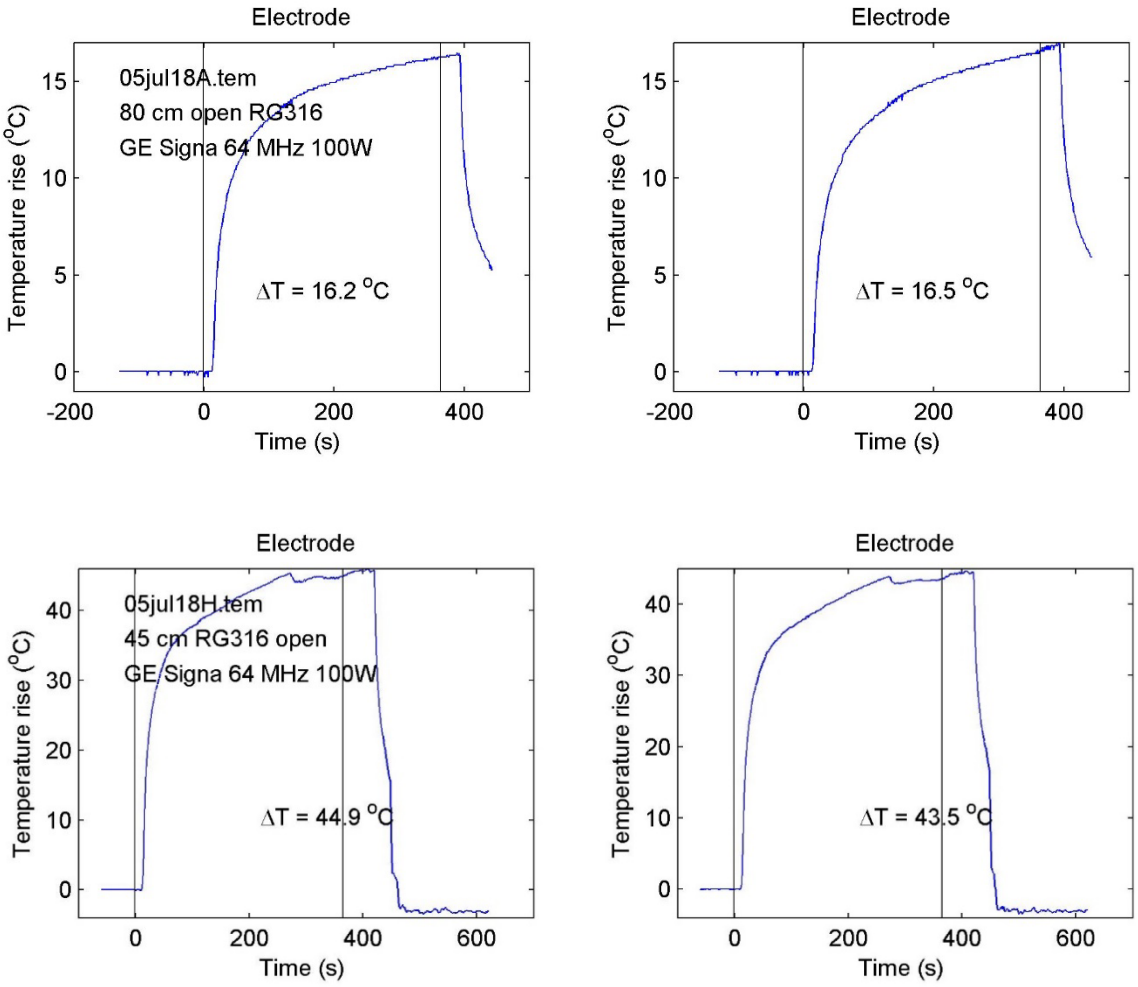

Figure 5.15 Measured Temperature rise for open shielded RG 316 model lead at 64 MHz after 6 minutes of RF power of 100 W. The top plot is for lead length 80 cm and bottom for 45 cm. Two neoptix temperature probes are used for temperature rise measurement for redundancy. For 80 cm model implant, the average measured temperature rise at the tip of the lead is 16.35ºC. For 45 cm model implant, the average measured temperature rise at the tip of the lead is 44.2ºC. Local background SAR at 100 W of RF power is 5.56 W/kg.

5.3.2.3 Measurement of Temperature rise for shielded RG 316 model lead with a metallic short at the end

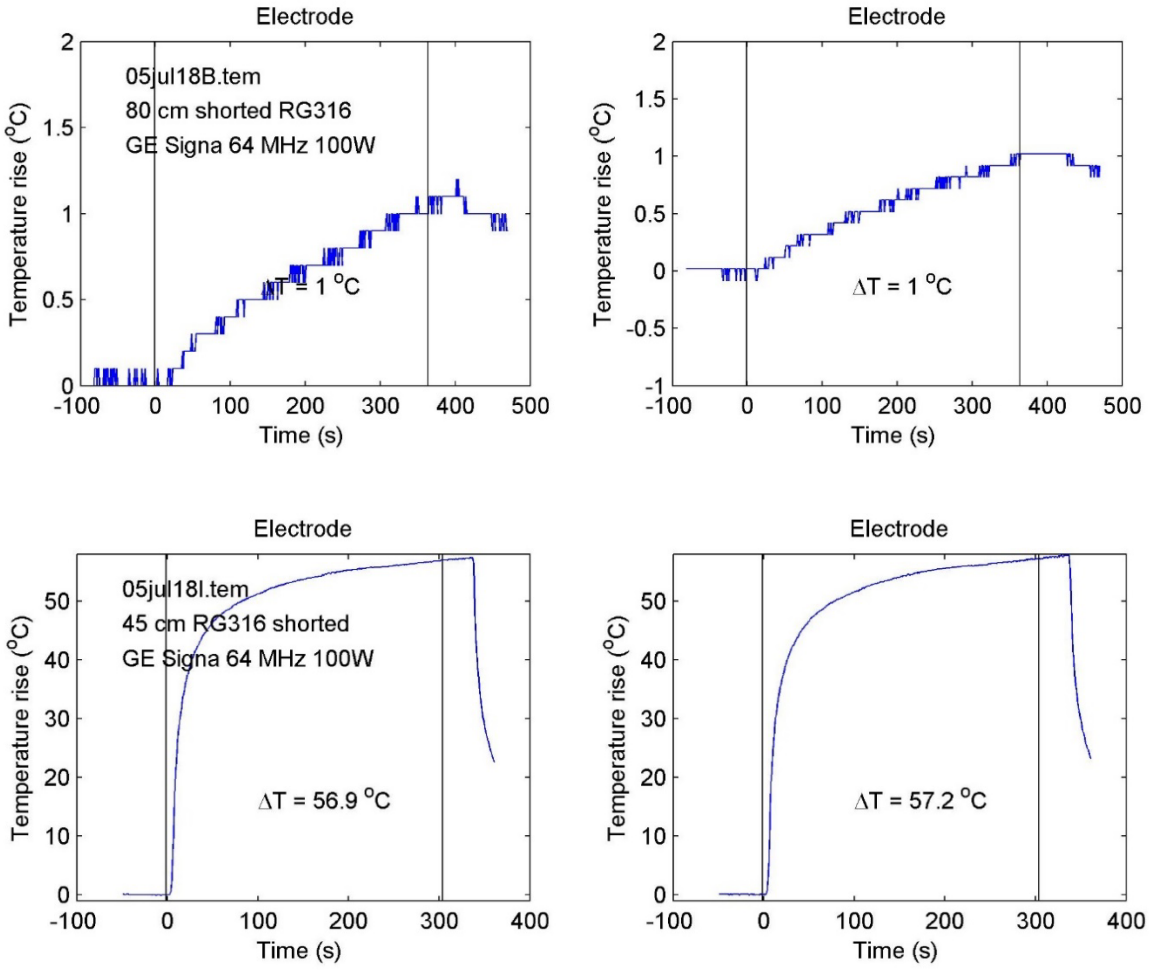

Figure 5.16 Measured Temperature rise for short shielded RG 316 model lead at 64 MHz after 6 minutes of RF power of 100 W. The top plot is for lead length 80 cm and bottom for 45 cm. Two neoptix temperature probes are used for temperature rise measurement for redundancy. For 80 cm model implant, the average measured temperature rise at the tip of the lead is 1°C. For 45 cm model implant, the average measured temperature rise at the tip of the lead is 57.05°C. Local background SAR at 100 W of RF power is 5.56 W/kg.

5.3.2.4 Measurement of Temperature rise for unshielded RG 316 model lead with the generator at the end

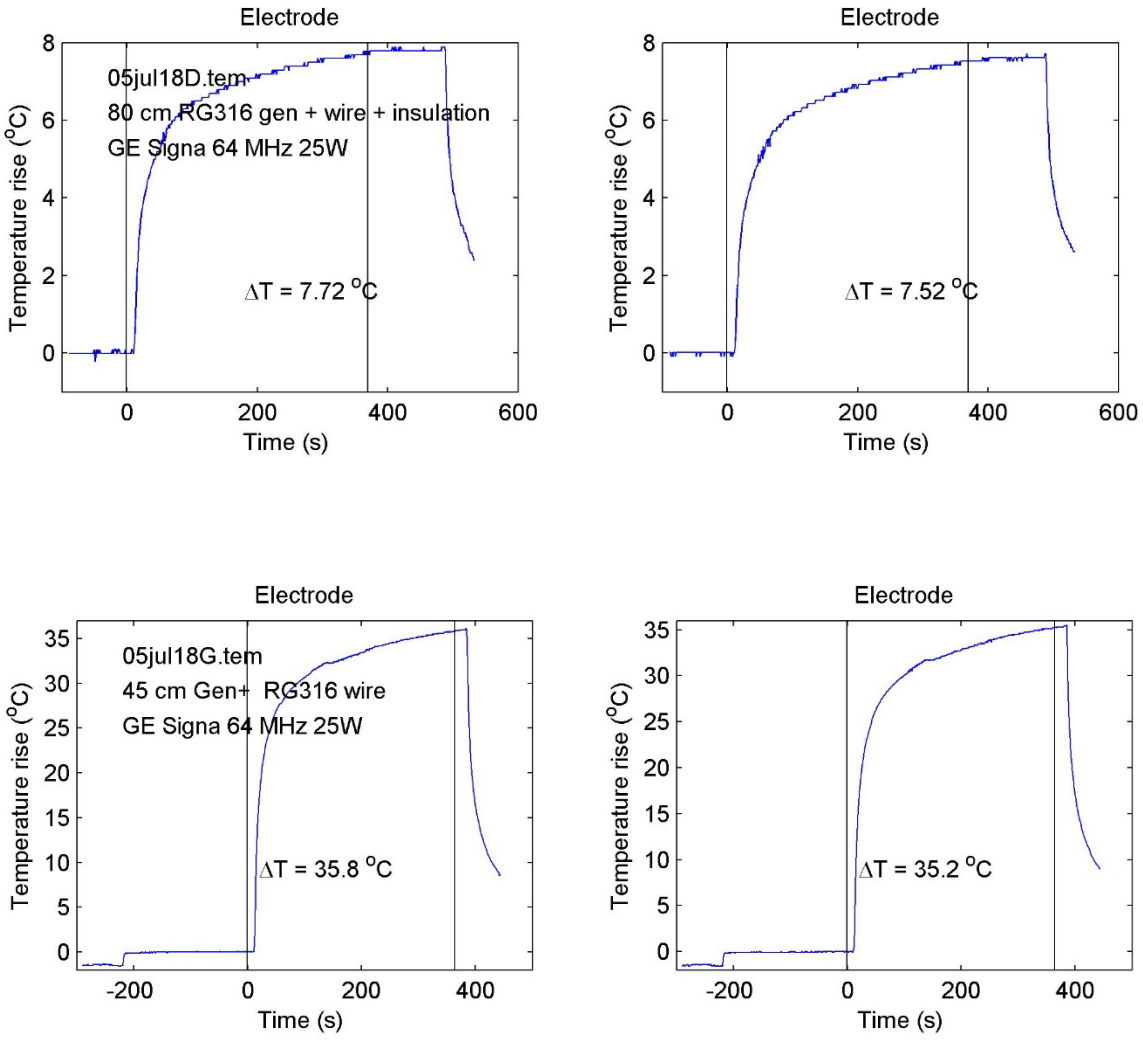

Figure 5.17 Measured Temperature rise for unshielded RG 316 model lead with the generator at 64 MHz after 6 minutes of RF power of 25 W. The US $0.5 coin acting as a generator is attached at the end. The top plot is for lead length 80 cm and bottom for 45 cm. Two neoptix temperature probes are used for temperature rise measurement for redundancy. For 80 cm model implant, the average measured temperature rise at the tip of the lead is 7.62°C. For 45 cm model implant, the average measured temperature rise at the tip of the lead is 35.5°C. Local background SAR at 25 W of RF power is 1.99 W/kg.

5.3.2.5 Measurement of Temperature rise for shielded RG 316 model lead with the generator at the end

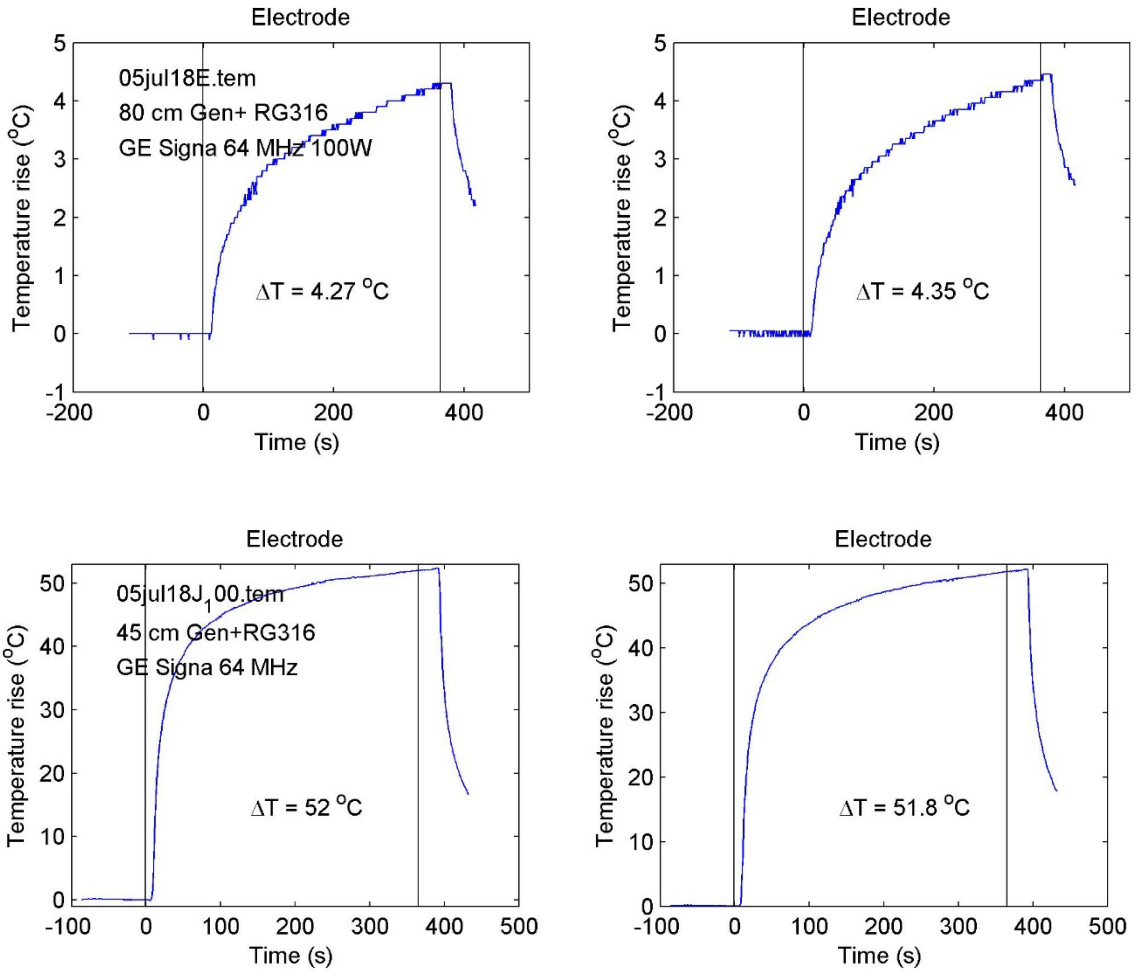

Figure 5.18 Measured Temperature rise for unshielded RG 316 model lead with the generator at 64 MHz after 6 minutes of RF power 100 W. The US $0.5 coin acting as a generator is attached at the end. The top plot is for lead length 80 cm and bottom for 45 cm. Two neoptix temperature probes are used for temperature rise measurement for redundancy. For 80 cm model implant, the average measured temperature rise at the tip of the lead is 4.31°C. For 45 cm model implant, the average measured temperature rise at the tip of the lead is 51.9°C. Local background SAR at 100 W of RF power is 5.56 W/kg.

5.4 Discussion

Figure 5.3 and Figure 5.5 shows the measured magnitude and phase of the transfer function for an unshielded electrode with no generator (open at the end) for 80 cm wire (Figure 5.3) and 45 cm wire (Figure 5.5) at 64 MHz and 128 MHz. Maximum heating occurs when electrode length is in resonance with the wavelength. At 64 MHz, maximum heating is expected for 80 cm wire. This is evident from the Figure 5.3, as transfer function magnitude is maximum. Similarly, at 128 MHz, maximum heating is expected for 45 cm, which is evident from Figure 5.5 where transfer function is maximum.

Figure 5.4 and Figure 5.6 shows the measured magnitude and phase of the transfer function for a shielded electrode with no generator at the end. Length of the electrode is 80 cm, and shield length is 77 cm (Figure 5.4). For Figure 5.6, the length of the electrode is 45 cm, and shield length is 36 cm. All measurements are at 64 MHz and 128 MHz. Tip of the electrode is at z=0. The shield is present at the same locations as described above. At 64 MHz, for both 45 cm shielded electrode and 80 cm shielded electrode, due to the presence of shield, the transfer function is considerably less in magnitude and phase when compared to Figure 5.3 and Figure 5.5. As a result, the temperature rise for this electrode is less when compared to an unshielded open electrode of the same length. At 128 MHz, the magnitude of the transfer function for 80 cm shielded electrode is close to zero when compared to Figure 5.3 of the same frequency. On the other hand, for 45 cm shielded electrode, the transfer function decreases at locations where the shield is present, i.e., from z=0.09 m to z=0.45 m.

Figure 5.9 - Figure 5.12 shows the measured magnitude and phase of the transfer function for unshielded and shielded electrode with a generator at the end for both lengths of the electrode at 64 MHz and 128 MHz. The generator was in the form of a US half dollar coin. This model has a surface area like that of a small pacemaker. Comparing it to Figure 5.3 - Figure 5.6 we observe that the magnitude of the transfer function is maximum at the proximal end; where the generator is located. This is because the generator provides a path of low impedance for the induced current to flow to the phantom medium. As a result, there is considerable heating at the generator end, resulting in a large magnitude of the transfer function.

Figure 5.7 and Figure 5.8, shows the measured magnitude and phase of the transfer function for a shielded electrode with a complete short at the end. Shield and central metal rod are completely connected through this short. Short is achieved by placing a solder ball at the end of the electrode. As expected, a short at the end of the electrode increases the impedance of the transmission line. As a result, induced current decreases. Thus for 80 cm unshielded electrode in open configuration, which achieves maximum transfer function at 64 MHz, Figure 5.7 shows that the transfer function is almost zero in this case. Similarly, for a 45 cm unshielded electrode with achieves maximum transfer function at 128 MHz, the transfer function is almost negligible. Section 5.3.2 shows measured temperature rise values for all configurations.

Table 5.1 shows measured temperature rise values scaled to unit SAR for all test runs that were performed. For the case of 80 cm electrode length at 64 MHz (where maximum heating is expected due to the length of electrode 80 cm in resonance with wavelength at 64 MHz), a minimum temperature rise occurs for a shielded electrode with a short at the end. This is evident as the transfer function for this electrode is almost negligible Figure 5.7. Maximum temperature rise occurs for bare wire with no shield and no generator. This is evident from the transfer function plot also Figure 5.3. As expected from transfer function measurements, temperature rise for the case of the shielded electrode with the generator is less when compared to the unshielded electrode with or without a generator.

As expected, temperature rises exhibited by 45 cm shielded electrode with short at the end is minimum compared to all other configurations for the same length. This is evident from measured transfer function values too. Readers are referred to Chapter 4 for discussion on temperature rise for 45 cm length of the electrode for different lead configurations.

Table 5.1 Measured Temperature Rise Values for proposed model implants lead at all configurations at 64 MHz. For 80 cm model lead, shield length is 77 cm and for 45 cm model lead shield length 36 cm. The generator is the US $0.5 coin at the end.

Test Run	Structure	Scaled measured ΔT (°C/(W/kg))
05jul18A.tem	80 cm coaxial RG316 open at the end	2.94
05jul18B.tem	80 cm coaxial RG316 short at the end	0.17
05jul18C.tem	80 cm unshielded RG316 open at end	23.54
05jul18D.tem	80 cm unshielded RG316 + generator	3.82
05jul18E.tem	80 cm coaxial RG316+ generator	0.77
05jul18F.tem	45 cm unshielded RG316 open at end	27.35
05jul18G.tem	45 cm unshielded RG316 + generator	17.83
05jul18H.tem	45 cm coaxial RG316 open at the end	7.94
05jul18I.tem	45 cm coaxial RG316 short at the end	10.26
05jul18J_100.tem	45 cm coaxial RG316+ generator	9.33

5.5 Comparison of measured temperature rise values for model leads

In this subsection, we compare measured temperature rise values of the model leads to temperature rises predicted by the electric field transfer function. Temperature rise values are calculated using the measured electric field transfer function that is presented in section 5.3.1.

5.5.1 Pathways for the model leads and background E_{tan} in the physical tests

To calculate the temperature rise from measured electric field transfer function, we need to measure background tangential electric field along the same pathway where the electrode was kept in the phantom. In the physical tests for the measurement of temperature rise, the same pathway in the phantom was used for all tests on the 80-cm long leads. Similarly, the same pathway in the phantom was used for all tests on the 45-cm long leads.

Figure 5.19 shows the 80 cm RG 316 coaxial cable on the test grid. The grid was flipped over, and the lead was that serves as a model lead. The same pathway was used for all of the tests on the 80-cm long structures.

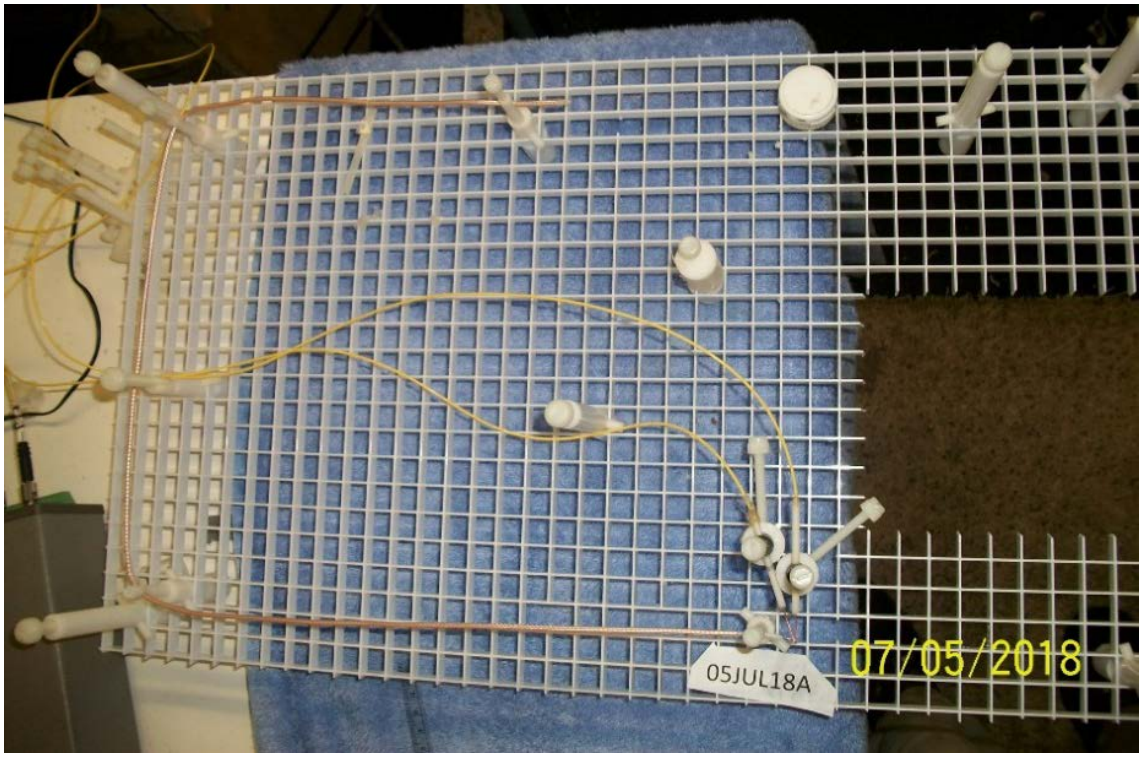

Figure 5.19 Pathway for 80 cm RG 316 coaxial cable that serves as a model lead. The same pathway was used for all of the tests on the 80-cm long structures

Figure 5.20 shows the pathway for the 80-cm lead superimposed on the calculated electric field distribution in the phantom. Also shown is the background tangential electric field along the pathway. The electric field is scaled for the input RF power of 100 W, which produces a local background SAR near the wall at the longitudinal center of the phantom at (x,y,z) = (0.165, 0, 0.325).

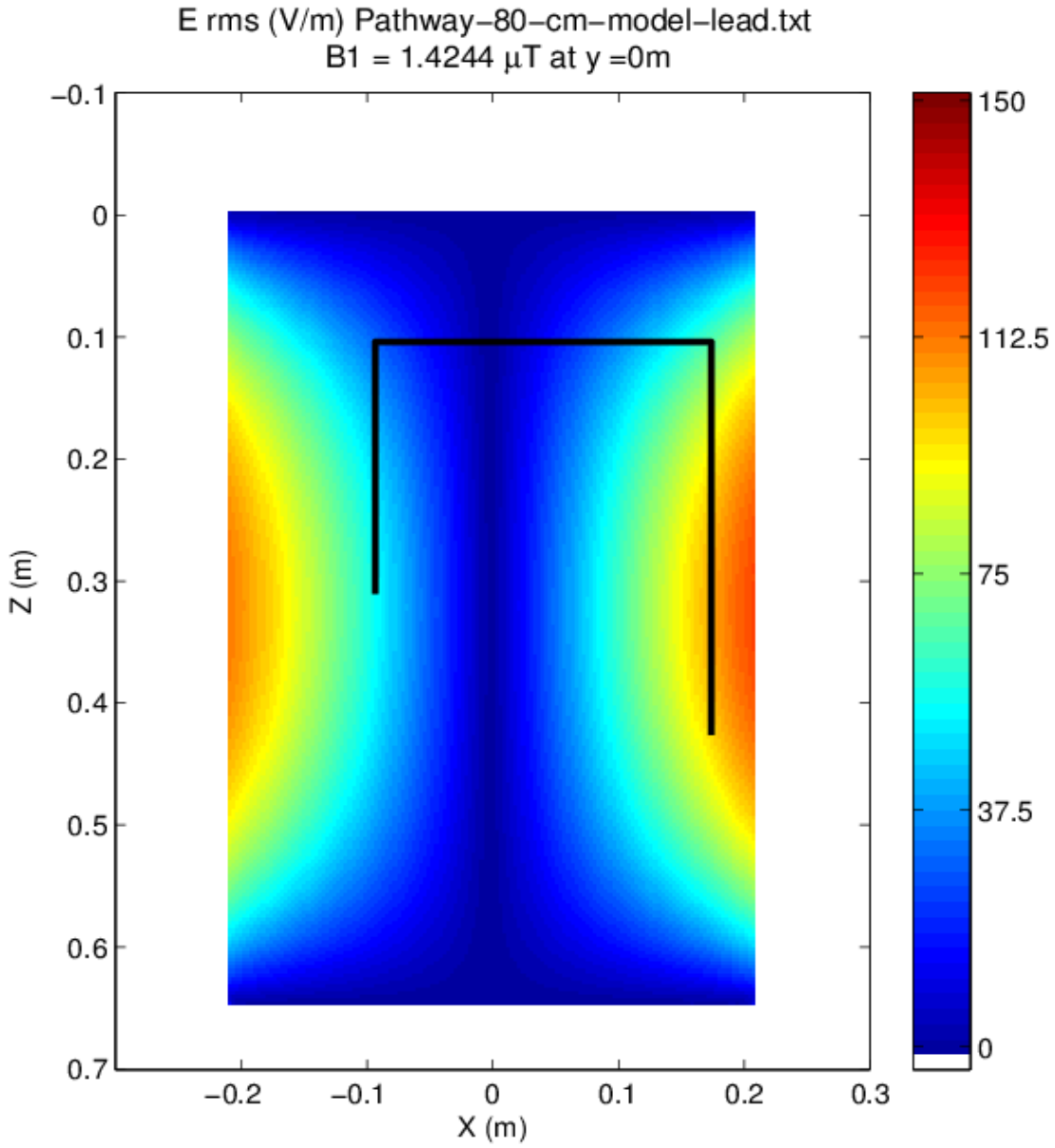

Figure 5.20 Path for the 80-cm model lead superimposed on the E_{rms} in the physical tests in the ASTM phantom. Also shown is the background tangential electric field along the pathway. The electric field is scaled for the input RF power of 100 W, which produces a local background SAR near the wall at the longitudinal center of the phantom at (x,y,z) = (0.165, 0, 0.325). The plot is the background tangential electric field in the ASTM phantom using the B_1 field from the RF coil. The magnitude of B_{1rms} is 1.4244 μT.

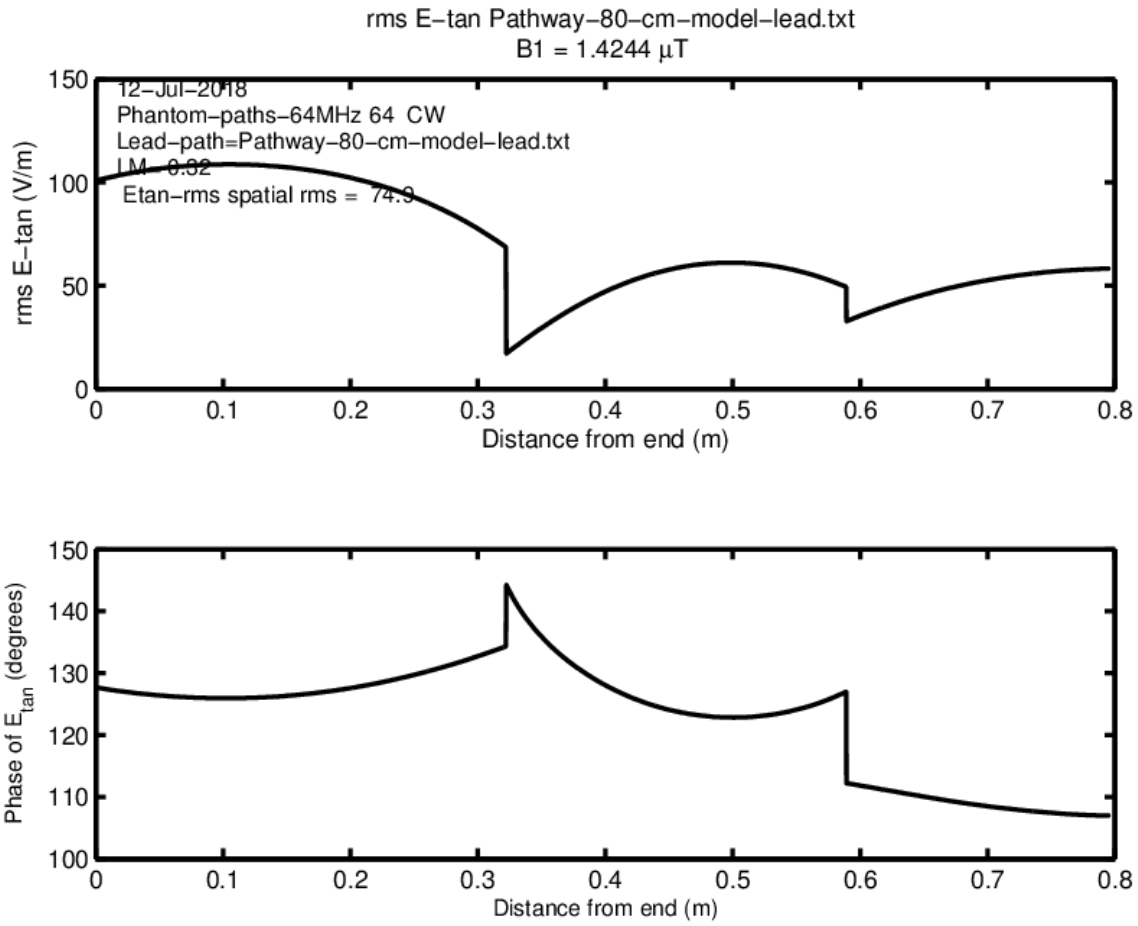

Figure 5.21 Magnitude and phase of trajectory for background tangential electric field E_{tan} over the length of the lead. The phase of background tangential electric field E_{tan} is approximately constant over the length of the lead. The plot is the background tangential electric field in the ASTM phantom using the B_1 field from the RF coil. The magnitude of B_{1rms} is 1.4244 μT.

Figure 5.22 shows the 45 cm RG 316 coaxial cable on the test grid. The grid was flipped over, and the lead was that serves as a model lead. The same pathway was used for all of the tests on the 45-cm long structures. Figure 5.24 shows the pathway for the 45-cm lead superimposed on the calculated electric field distribution in the phantom. Also shown is the background tangential electric field along the pathway. The electric field is scaled for the input RF power of 100 W, which produces a local background SAR near the wall at the longitudinal center of the phantom at (x,y,z) = (0.165, 0, 0.325).

Figure 5.22. Pathway for the 45-cm insulated inner conductor of RG 316. The same pathway was used for all of the tests on the 80-cm long structures.

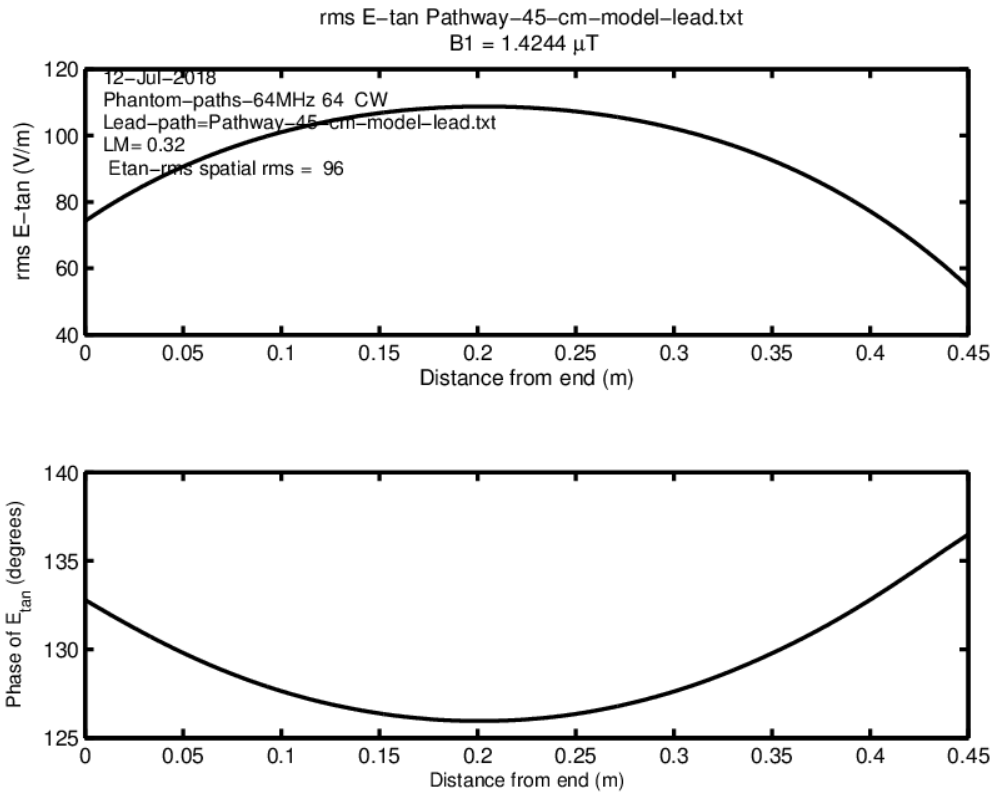

Figure 5.23 Magnitude and phase of trajectory for background tangential electric field E_{tan} over the length of the lead. The phase of background tangential electric field E_{tan} is approximately constant over the length of the lead. The plot is the background tangential electric field in the ASTM phantom using the B_1 field from the RF coil. The magnitude of B_{1rms} is 1.4244 µT.

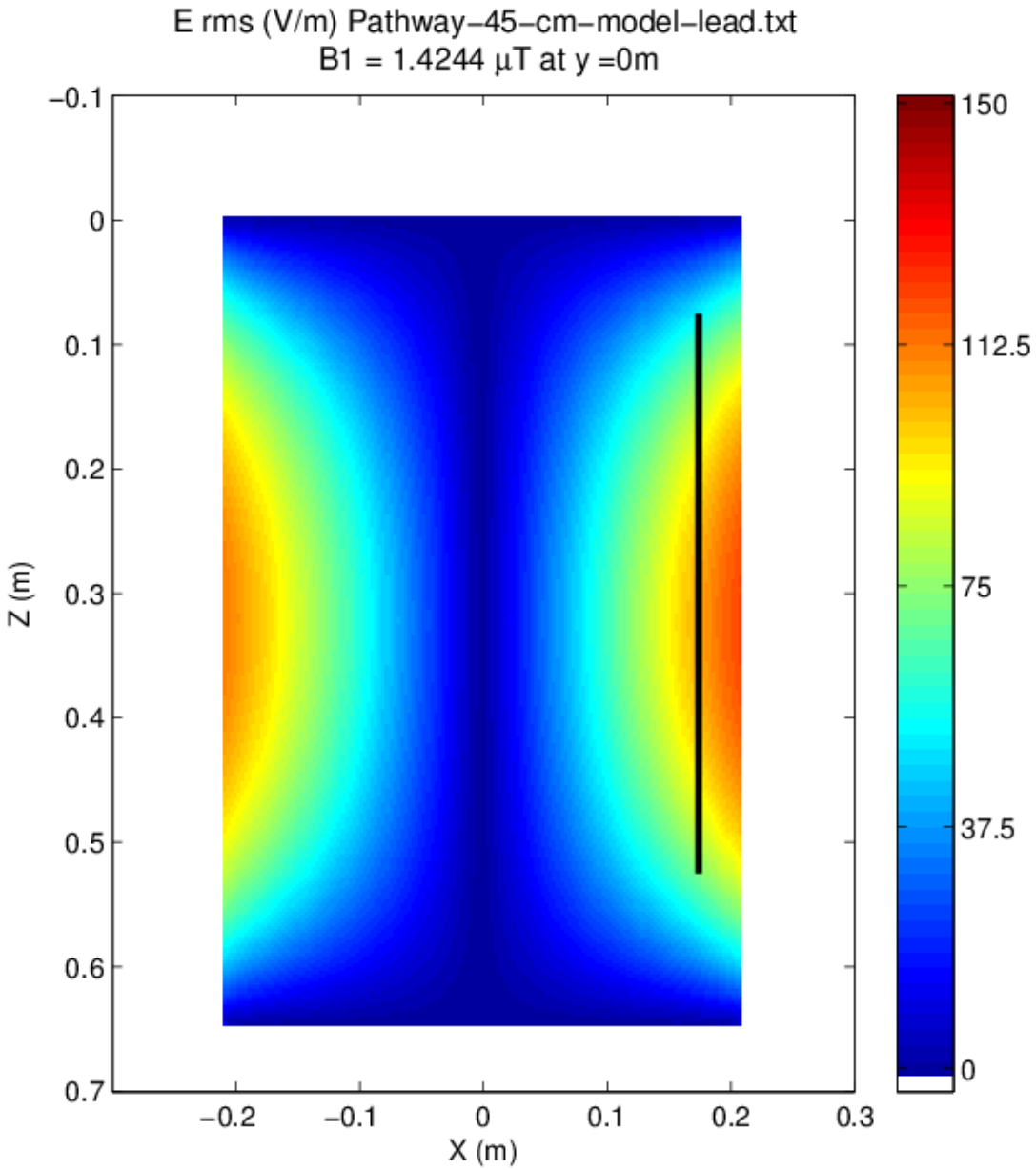

Figure 5.24 Path for the 45-cm model lead superimposed on the E_{rms} in the physical tests in the ASTM phantom Also shown is the background tangential electric field along the pathway. The electric field is scaled for the input RF power of 100 W, which produces a local background SAR near the wall at the longitudinal center of the phantom at (x,y,z) = (0.165, 0, 0.325). The plot is the background tangential electric field in the ASTM phantom using the B_1 field from the RF coil. The magnitude of B_{1rms} is 1.4244 μT.

5.5.2 Calculation of temperature rise values using the transfer function

Temperature rise for the different leads was calculated using equation 5.4. S_{21} is the measured S_{meaus} that was obtained in transfer function measurements. As an example of the process is presented here for the open and shorted 80-cm coaxial lead. Figure 5.25 plots the transfer functions and Figure 4.10 shows plots of the measured temperature rises vs. time.

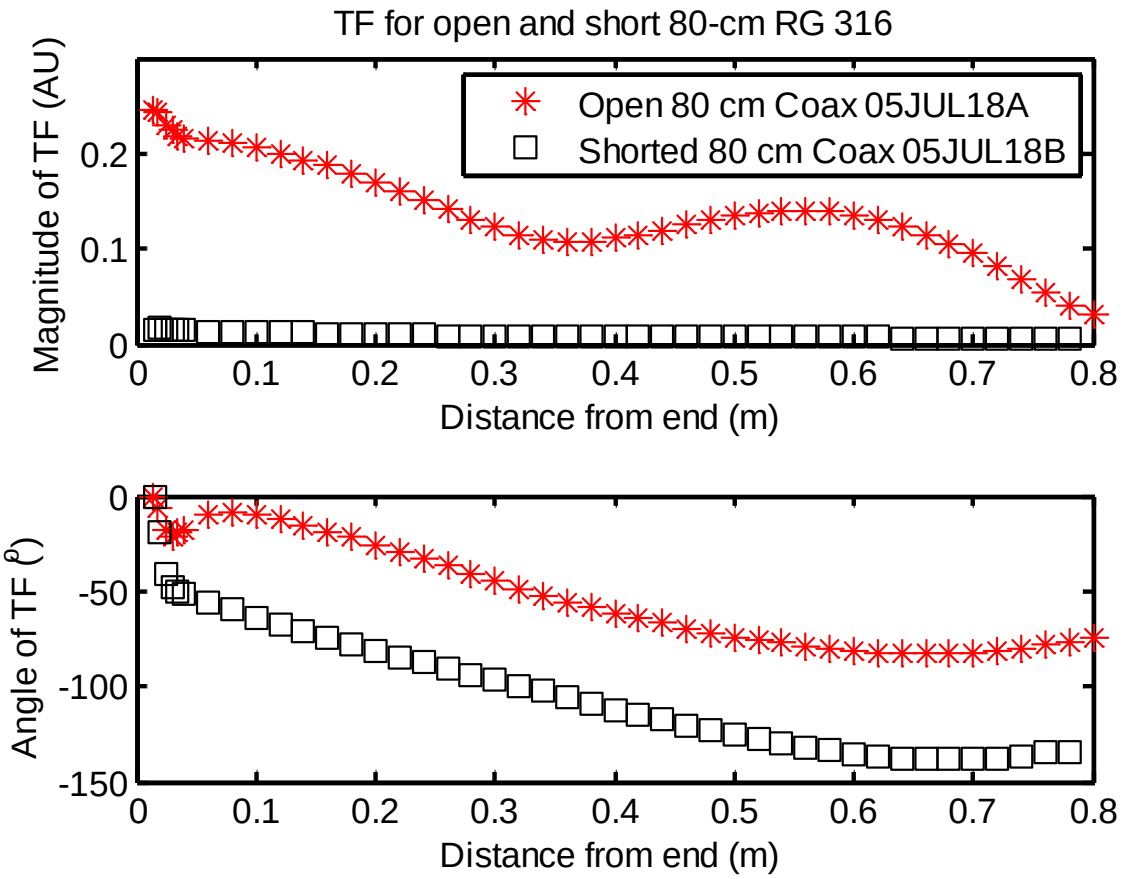

Figure 5.25 Comparison of the measured electric field transfer function for the 80 cm RG 316 shielded model lead in open and short configurations. Impedance for short configuration for 80 cm RG 316 coax at the proximal end is zero. As a result, current is non-zero. Hence, the transfer function is non-zero at the end. For the case of the open configuration, the impedance of 80 cm RG 316 open coax at the proximal end is infinite. As a result, the current is zero. Hence, the transfer function is zero at the end. Also, the magnitude of transfer function along the shield is less for the short configuration as compared to open configuration, as a consequence of this sample having a length equal to the quarter wave-length. These parameters will be different for actual leads in practice since the actual lead, in general, will have a length different from a quarter wavelength.

Table 5.2 shows the measured, and calculated temperature rises for open and shorted 80-cm RG 316 model implant. The temperature rises are calculated with the transfer functions of Figure 5.25. The transfer function is scaled so that the measured and calculated rises for the open lead are the same. The same scaling factor is used for both of the measured temperature functions.

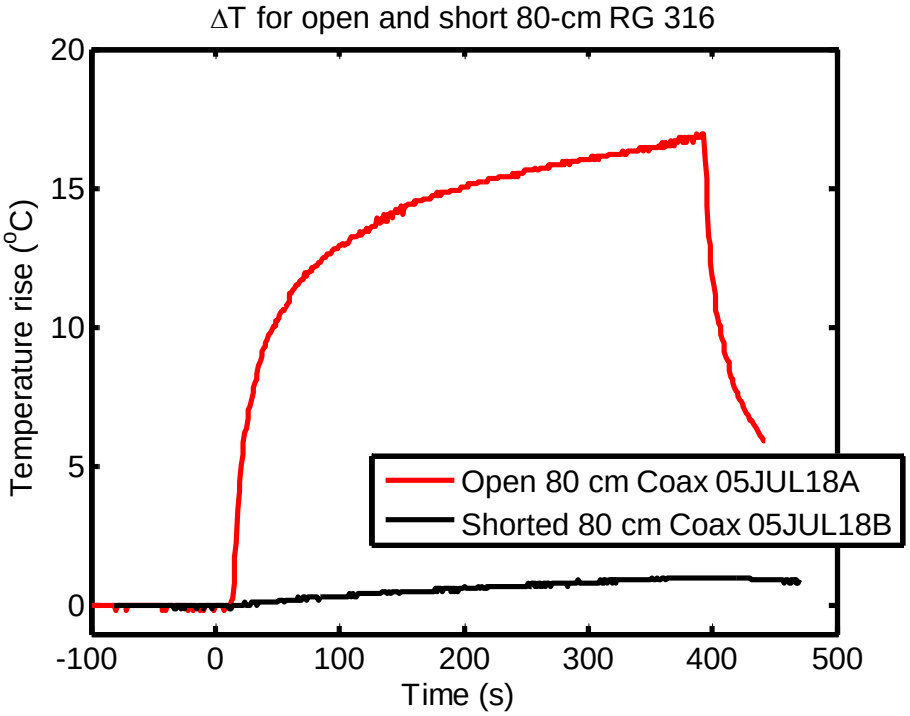

Figure 4.10 Measured scaled temperature rise vs. time for open and short conditions for 80 cm shielded lead electrode at 64MHz. Length of the shield is 77 cm. The maximum temperature rise for open, shielded lead is 16.35°C and for short shielded lead is 1.01°C. The significant temperature rises are due to the lead being quarter-wave in length. For the shorted able, the input impedance at the electrode end is essentially open-circuit, resulting in minimal temperature rise whereas the cable with open end has a short-circuit input resulting in large temperature rise.

Table 5.2. Comparison of measured and calculated temperature rises for open and shorted 80-cm RG 316 model implant.

Configuration of 80 cm Shielded RG 316	**Measured max ΔT (°C)**	**Calculated max ΔT(°C)**
Open	16.35	16.94
Short	1.01	1.11

5.6 Summary and Conclusion

In this chapter, a brief introduction of transfer function concepts to evaluate RF-induced heating is discussed in following section 5.1. A general background review is also presented. Next, we describe the experimental setup used to evaluate transfer function in detail section 5.2. We present measurement results of the transfer function and temperature rise for our proposed electrodes for all four structures.

Since heating is proportional to the transfer function, shields need to be placed on the electrode at the location where it can minimize the magnitude or phase of the transfer function. At 64 MHz, maximum heating takes place for 80 cm length of the electrode for open configuration. For the same length of electrode, heating can be minimized by placing a short at the end. It has been observed that at 64 MHz for the case of the open configuration, temperature rise decreases from 16.35°C to 1.01 °C as compared to a shielded electrode for the same configuration as shown in Table 5.2. Length of the electrode is 80 cm. This is an 80% decrease in temperature rise. If we compare the transfer function magnitude, we observe that magnitude of transfer function decreases at places where the shield is located At 128 MHz, maximum heating takes place for 45 cm length of the electrode for open configuration. For the same length of electrode, heating can be minimized by placing a metallic short at the end.

The design objective is for the addition of the shield to reduce heating at the electrode. It should be noted that the temperature rise at the electrode with a shield would differ from the temperature rise for the unshielded electrode for the following reasons.

1) The tangential electric field under the shield will be minimal whereas the tangential electric field is equal to the background value for the unshielded lead.

2) The tangential component of the scattered electric field at the edges of the shield will be different, and likely larger in magnitude, compared to background tangential electric field.

3) The electric field transfer function in the presence of shield will differ from the electric field transfer function for model lead without the shield. This is because

the effective wavelength and damping factors for current waves on the lead are different when the insulation of the lead is surrounded by metal compared to when it is surrounded by the metal shield.

To conclude, transfer function analysis is a good estimate of heating of electrode.

1. A proper understanding of transfer function concepts as applied to proposed electrode structures is presented in this chapter.
2. Measured maximum temperature rise for the open RG 316 is a factor 16.6 greater than for the shorted cable
3. Calculated maximum temperature rise for the RG 316 in the open configuration is 15.3 times greater than that for the short configuration.
4. The agreement between measured and calculated rises demonstrates the validity of the transfer function method for assessing heating of the lead of an active implant.

6. TRANSMISSION LINE MODEL FOR THE SHIELDED LEAD WITH GENERATOR

The purpose of this section is to develop a physical model for how the shield on a lead wire affects the heating at the electrode. The model is based on the propagation of current waves on the shield and the lead wire. The physical model is termed a "transmission line model" given that the model equations follow those used for describing voltage and current waves on a transmission line.

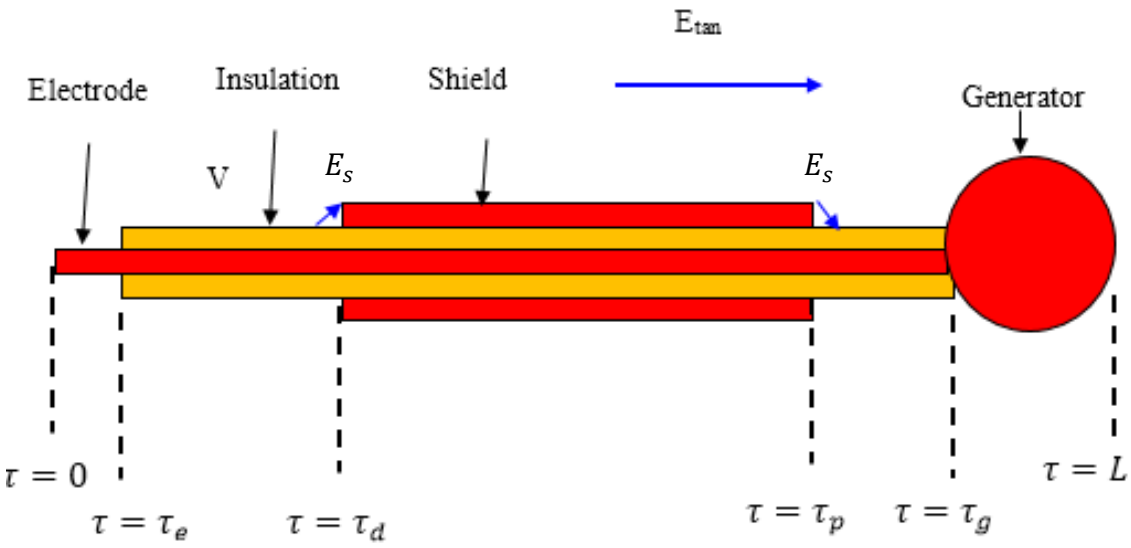

Figure 6.1 Physical Model of Shielded Lead with the generator. Blue arrows in the figure indicate the tangential electric field E_{tan}.

Figure 6.1 shows the physical model for a shielded lead. The tangential component E_{tan} of the background electric field will induce currents and electric charge on the shield. These will produce a scattered electric field E_s at the edges of the shield. The tangential component of the scattered field will induce currents on the central conductor. These currents will propagate on the center conductor. E_{tan} will also induce currents on sections of the lead that are not covered by the shield. The total induced current, which is due to scatter field E_s and tangential background electric field E_{tan} in unshielded regions of the lead, is transmitted from the electrode and will induce power in the surrounding tissue.

Let τ represent parametric distance along the lead and let $\tau = 0$ be at the distal end of the electrode. Other key values for τ are listed in Table 6.1.

The temperature rise ΔT at the electrode with the shield present may be expressed as

$$\Delta \mathrm{T} = \left| \Delta \mathrm{V}_{gen} S_E(\tau_g) + \int_0^{\mathrm{L}} \mathrm{S_E}(\tau) \mathrm{E_{tan}}(\tau) \mathrm{d}\tau \right|^2 \tag{6.1}$$

where S_E is the electric field transfer function, E_{tan} is the tangential electric field.

$\Delta \mathrm{V}_{gen}$ is the effective voltage injected by the generator at the end of the lead and is given by

$$\Delta \mathrm{V}_{gen} = (\mathrm{L} - \tau_g) \mathrm{E_{tan}} \frac{L + \tau_g}{2} \tag{6.2}$$

The transfer function S_E can be viewed as consisting of two sections.

(1) Transfer function due to the coupling of the background tangential electric field E_{tan} with the exposed sections of the lead. This is termed as S_E^{lead}, which applies for $\tau_e < \tau < \tau_d$ and $\tau_p < \tau < \tau_g$. Under the shield, it is zero since the shield is assumed to result in $E_{tan} = 0$.

(2) Transfer function due to the coupling of the background tangential electric field E_{tan} with the shield. This is termed S_E^{shield} and applies for $\tau_d < \tau < \tau_p$. S_E^{shield} is due to the induced RF current on the shield producing electric charge at the distal and proximal ends of the shield. As depicted in Figure 6.1, this electric charge will produce a scattered electric field E_s at the edges of the shield that is incident on the center conductor. The currents induced by E_s will propagate on the center conductor, and contribute to the scattered electric field at the electrode.

Let S_Q^{shield} be the transfer function for induction of electric charge at the edges of the shield. The transfer function. S_E^{shield} can then be expressed as

$$S_E^{shield}(\tau) = \Gamma_d S_E^{lead}(\tau_d) S_Q^{shield}(\tau - \tau_d) + \Gamma_p S_E^{lead}(\tau_p) S_Q^{shield}(\tau_p - \tau) \tag{6.3}$$

where Γ_d and Γ_p are complex coupling factors at the ends of the shield that depend on the geometry of the interface between the shield and the center conductor. Physically it quantifies the amount of current leaking from the edges of the shield. The current that is induced into the center conductor by scatter electric field E_s is proportional to S_E^{lead} (transfer function due to the coupling of background tangential electric field E_{tan} with the exposed sections of the lead) at the edges of the shield. Hence the terms $S_E^{shield}(\tau_d)$ and $S_E^{shield}(\tau_p)$ appear in equation 6.3.

The total transfer function in equation 6.1 for the shielded lead is expressed as

$$S_E(\tau) = S_E^{lead}(\tau) \text{ for } \tau_e < \tau < \tau_d \text{ or } \tau_p < \tau < \tau_g \tag{6.4}$$

$$S_E(\tau) = S_E^{shield}(\tau) \text{ for } \tau_d < \tau < \tau_p \tag{6.5}$$

In the absence of the shield, the temperature rise at the electrode is

$$\Delta T_{no\_shield} = \left| \int_0^{\mathrm{L}} S_E^b(\tau) \mathrm{E}_{\tan}(\tau) \mathrm{d}\tau + \Delta \mathrm{V}_{gen} S_E^b(\tau_g) \right|^2 \tag{6.6}$$

where S_E^b is the electric field transfer function for the bare (unshielded) lead. The scattered electric field E_s at the ends of the shield is due to charge build-up due to the currents that are induced on the shield.

6.1 Determination of transmission line parameters for coaxial wire RG 316

The test structure for the measurements is RG 316 coaxial cable. The dielectric is Teflon, which has a relative dielectric constant of 2.1. The insulating jacket is made from Teflon.

Table 6.1 Values of parametric distance τ at key locations in the model of Figure 6.1 for the shielded lead.

Location in model	**Value of parametric distance τ**
Electrode end	0
Electrode end	τ_e
Distal end of shield	τ_d
Proximal end of shield	τ_p
Edge of generator	τ_g
End of generator	L

The electric field transfer function is the relationship between the electric field at the electrode relative to the input tangential electric field at a point along the lead [91]. Measurements of the electric field transfer function on RG 316 structures are described in section 5.3.1. We used measurements of the transfer function to determine transmission line parameters for the modeling in the phantom material of inner conductor and insulation of the RG 316 cable.

As a starting point for values of the transmission line model, the wave characteristics are those calculated from equations provided by King [98]. The calculated values of Z_0 , α and λ are listed in the first three rows of Table 6.3

Table 6.2. Parameters for the RG 316 coaxial cable that served as a model implant in the measurements of the electric field transfer function and RF heating.

Parameter	Value
Diameter of inner conductor	0.51 mm
Diameter of inner insulation	1.50 mm
Diameter of shield	2.0 mm
Diameter of jacket	2.5 mm
Dielectric constant of Teflon insulation	2.1

Table 6.3. Calculated parameters for transmission line model of the inner conductor with insulation of RG 316. The wire is immersed in saline with conductivity $\sigma = 0.47$ S/m and relative dielectric constant 77. The parameters are calculated from equations by King [98]

Parameter	Value at 64 MHz	Value at 128 MHz
Characteristic impedance Z_0	102 - 9.7 j Ω	97.9 - 11.6 j Ω
Loss factor α	0.42	1.01
Propagation constant β (King)	4.45 m^{-1}	8.52 m^{-1}
Propagation constant β (Best fit)	4.188 m^{-1}	8.267 m^{-1}

Figure 6.2 and Figure 6.3 are plots of the measured and calculated transfer functions for 45-cm and 80-cm inner insulation with wire from RG 316 cable. The transfer functions are calculated as follows, which follows the approach presented by Nyenhuis [94]

Consider a transmission line with parameters of loss factor α, propagation constant β, the characteristic impedance Z_0, electrode impedance $Z_{elec,}$ and generator impedance Z_{gen}. Parametric distance along the lead is τ, with $\tau = 0$ at the electrode and $\tau = L$ at the generator.

For the calculation, we use the formula for input impedance Z_{in}. For a section of transmission line of length *l* terminated at the load, reflection coefficient ρ is given by

$$Z_{in} = Z_0 \frac{1 + \rho e^{-2\gamma(l)}}{1 - \rho e^{-2\gamma(l)}} \tag{6.7}$$

where $\gamma = \alpha + j\beta$ is the complex propagation constant and Z_0 is the characteristic impedance.

Equation 6.7 is the first of two underlying equations for the transmission line model of a lead. The second equation involves the relationship between input current at a location along the line and the current that appears across the load. Assume an incremental current input I_{in} at a distance *l* from the end of a transmission line with uniform characteristics over its lead and a load at the end. The current across the load is then

$$I_{load} = I_{in} \frac{1 - \rho}{e^{\gamma(\tau)} - \rho e^{-\gamma(\tau)}} \tag{6.8}$$

The electric field transfer function S_E at a location of distance τ from the electrode end is proportional to the product of the input current and the fraction of the input current that appears across the load. The input drive is the tangential electric field E_{tan} that produces a voltage ΔV over a distance $\Delta\tau$. The input current is

$$I_{in} = \frac{\Delta V}{Z_{in\_gen} + Z_{in\_elec}} \tag{6.9}$$

where Z_{in_elec} and Z_{in_gen} are impedances looking toward the electrode and the generator.

Consider the transmission line model Figure 6.1 of the electrode. If V is the excitation at a distance τ from the electrode end such that $\tau < \tau_d$, then Z_{in_elec} and Z_{in_gen} are calculated as follows

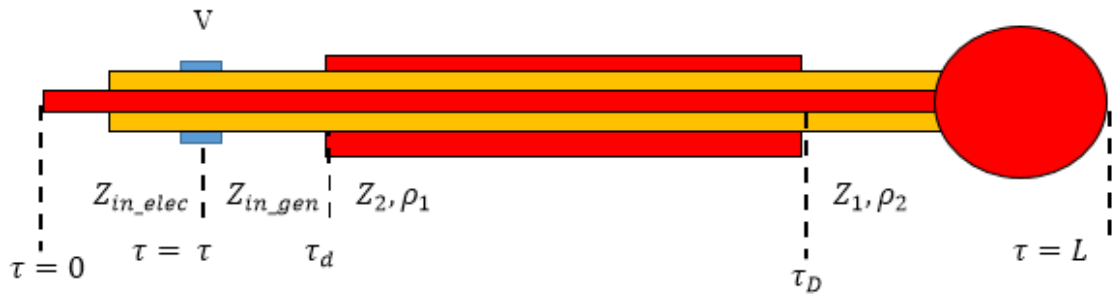

A) Impedance Z_1 at end of the shield $\tau = \tau_D$ looking towards the generator is given by

$$Z_1 = Z_{ns}\frac{e^{\gamma_{ns}(L-\tau_D)} + \rho_{gen}e^{-\gamma_{ns}(L-\tau_D)}}{e^{\gamma_{ns}(L-\tau_D)} - \rho_{gen}e^{-\gamma_{ns}(L-\tau_D)}} \tag{6.9.1}$$

where $\rho_{gen} = \frac{Z_g - Z_{ns}}{Z_g + Z_{ns}}$ Z_{ns} is the characteristic impedance and γ_{ns} is the complex propagation constant of an unshielded section of the lead. ρ_{gen} is the complex reflection coefficient at the generator end. Z_g is the impedance of the generator.

B) Impedance Z_2 at end of the shield $\tau = \tau_d$ looking towards the generator is given by

$$Z_2 = Z_s \frac{e^{\gamma_s(\tau_D - \tau_d)} + \rho_2 e^{-\gamma_s(\tau_D - \tau_d)}}{e^{\gamma_s(\tau_D - \tau_d)} - \rho_2 e^{-\gamma_s(\tau_D - \tau_d)}} \tag{6.9.2}$$

where $\rho_2 = \frac{Z_1 - Z_s}{Z_1 + Z_s}$ Z_s is the characteristic impedance and γ_s is the complex propagation constant of a shielded section of the lead. ρ_2 is the complex reflection coefficient at Z_1

C) Impedance Z_{in_gen} at voltage V excitation point $\tau = \tau$ looking towards the generator is given by

$$Z_{in\_gen} = Z_{ns} \frac{e^{\gamma_{ns}(\tau_d - \tau)} + \rho_1 e^{-\gamma_{ns}(\tau_d - \tau)}}{e^{\gamma_{ns}(\tau_d - \tau)} - \rho_1 e^{-\gamma_{ns}(\tau_d - \tau)}} \tag{6.9.3}$$

where $\rho_1 = \frac{Z_2 - Z_{ns}}{Z_2 + Z_{ns}}$ ρ_1 is the complex reflection coefficient at the Z_2 .

D) Impedance Z_{in_elec} at voltage V excitation point $\tau = \tau$ looking towards the electrode is given by

$$Z_{in\_elec} = Z_{ns} \frac{e^{\gamma_{ns}(-\tau)} + \rho_e e^{-\gamma_{ns}(-\tau)}}{e^{\gamma_{ns}(-\tau)} - \rho_e e^{-\gamma_{ns}(-\tau)}} \tag{6.9.4}$$

where $\rho_e = \frac{Z_e - Z_{ns}}{Z_e - Z_{ns}}$ Z_e is the impedance at the electrode end. ρ_e is the complex reflection coefficient at the electrode end.

Current due to V excitation point is given by

$$I_{in} = \frac{V}{Z_{in\_elec}(\tau) + Z_{in\_gen}(\tau)} \tag{6.9.5}$$

For excitation at $\tau_d < \tau < \tau_p$ and $\tau_d < \tau < \tau_p$, calculations of $Z_{in_elec}$and Z_{in_gen} equations 6.9.1-6.9.4 will be different.

The transfer function is proportional to the current across the electrode for unit ΔV Utilizing Equations 6.8 and 6.9 yields

$$S_E = KI_{electrode} = K\frac{1 - \rho_{elec}}{e^{\gamma(\tau)} - \rho_{elec}e^{-\gamma(\tau)}}\frac{1}{Z_{in\_gen} + Z_{in\_elec}} \tag{6.10}$$

where K is a scaling constant and $\rho_{elec}$is the reflection coefficient at the electrode.

Figure 6.2 and Figure 6.3 demonstrate that the transmission line model yields a good match to the measured electric field transfer function for the inner conductor of the RG 316. The fitting parameters of Z_0 and α are from the King calculation [98]. The fitted propagation constant β is less than calculation by 6% at 64 MHz and 3% at 128 MHz. Differences between best fit and calculated β may be due to

- Difference between the assumed value of 2.1 for permittivity ε_r and the true value for the Teflon insulation
- Difference between the calculated S_E in infinite space and the measured S_E in the finite phantom - scattering form the phantom walls has a small influence on the transfer function.

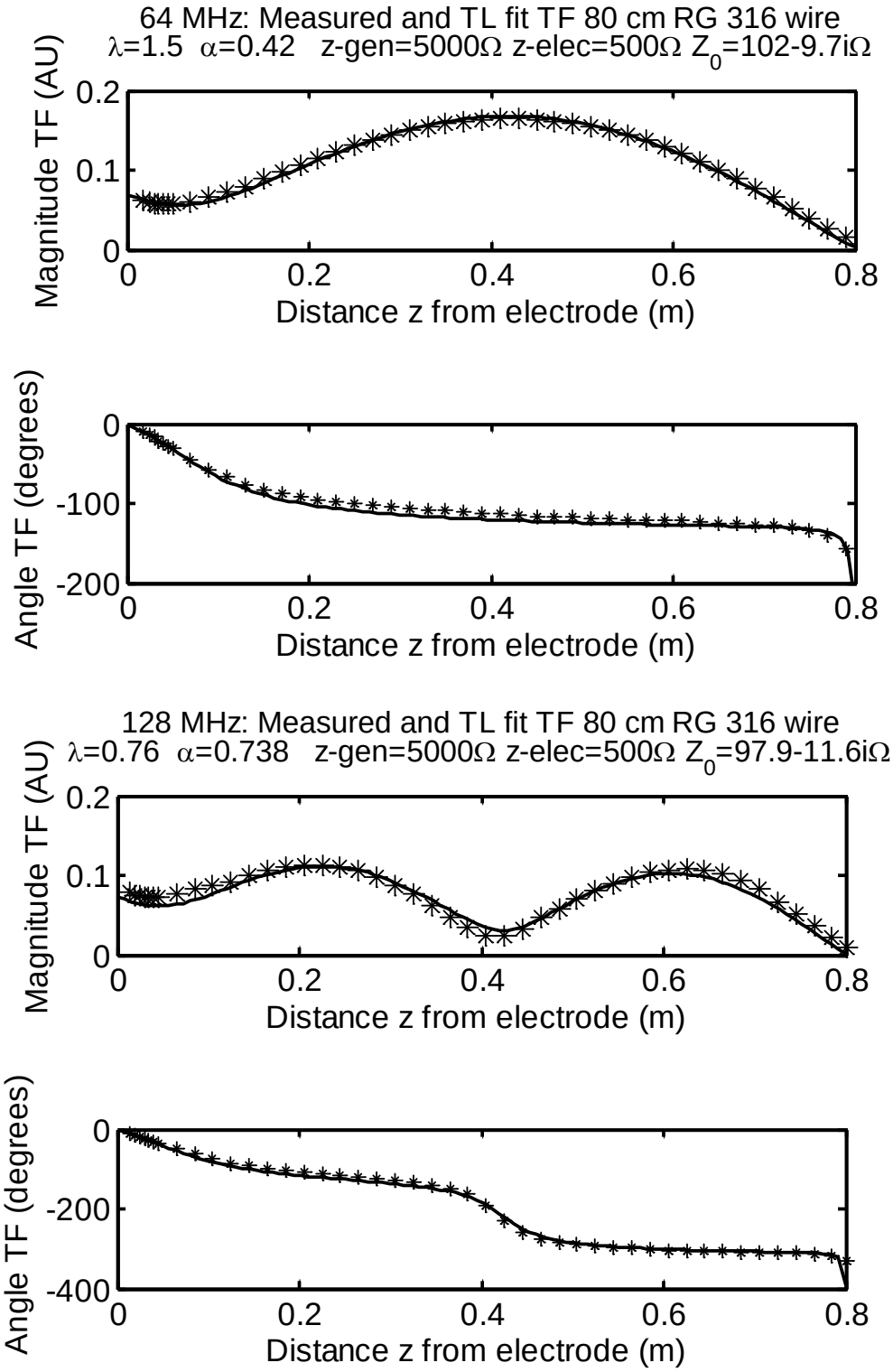

Figure 6.2 Calculated and measured transfer function for unshielded 80cm model lead at 64 MHz (top) and 128 MHz (bottom). The wire is open at the end and there is a 6-mm of insulation removed at the distal end to model an electrode. Wire is the inner insulation with conductor for RG 316 coaxial cable.

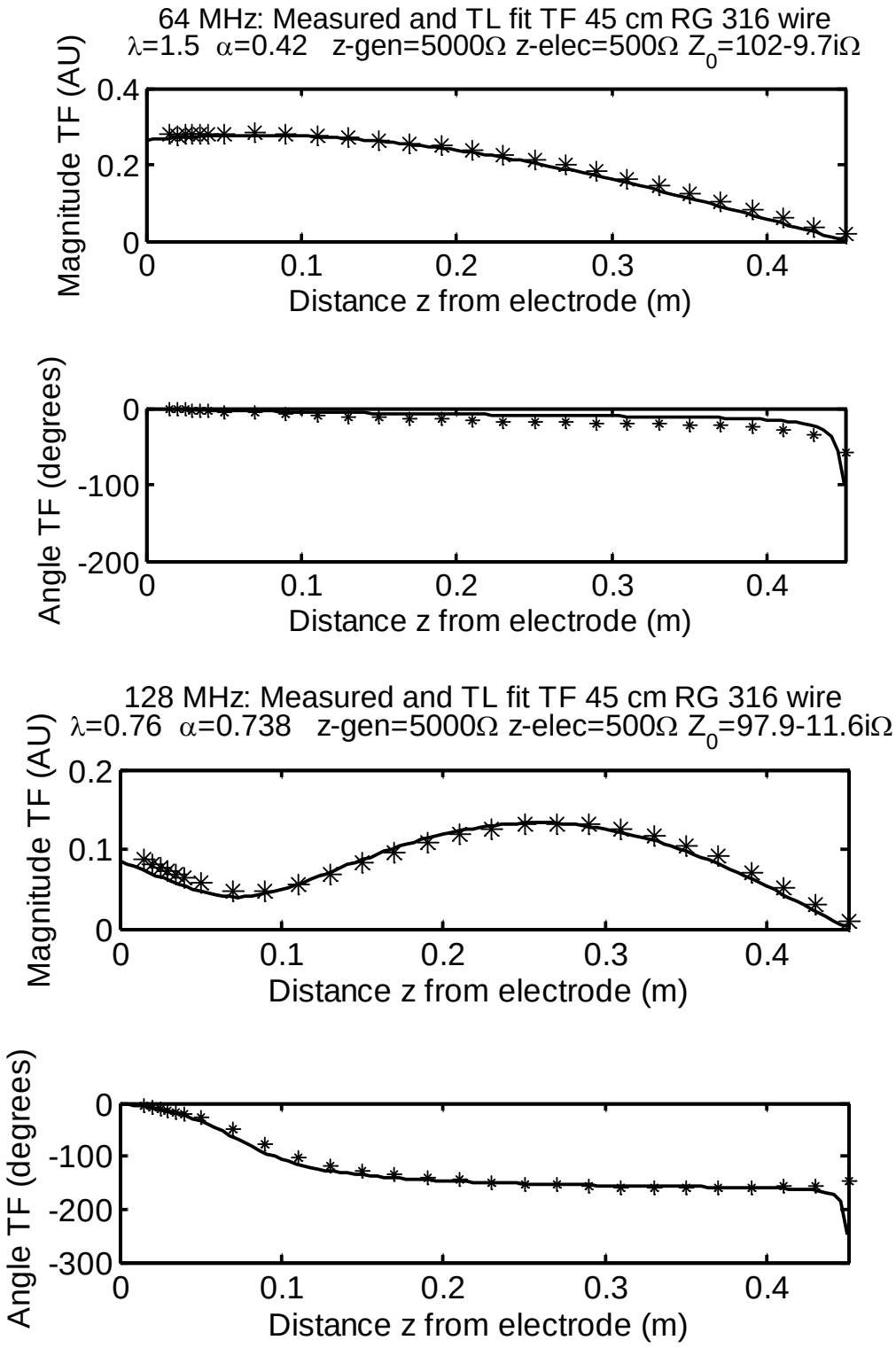

Figure 6.3 Calculated and measured transfer function for unshielded 45cm model lead at 64 MHz (top) and 128 MHz(bottom). The wire is open at the end and the, re is a 6-mm of insulation removed at the distal end to model an electrode. Wire isThe wire inner insulation with conductthe or for RG 316 coaxial cable.

6.2 Transfer function for current propagation on the shield of the RG 316 cable

As is depicted in Figure 6.1, RF current that is induced on the shield will produce a scattered electric field at the edges. The scattered field is proportional to the induced charge Q at the edge of the shield. The charge Q is proportional to the electric field transfer function for the shield.

Calculation of the transmission line parameters follows the method for the inner conductor. Table 6.4 lists the parameters for the calculation. As for the inner conductor, Z_0 and α are those calculated with the King formula [98]. Figure 6.4 shows the plot of the transfer functions calculated with the Bemcalc Method of Moments (MOM) program and the transmission line fit. The MOM program is written in MATLAB and utilizes equations from [99] The best propagation constants are less than the King calculation by 11.7% at 64 MHz and 13.0% at 128 MHz. The difference is likely due to that King formula [98] is an approximation whereas the MOM program provides essentially the exact transfer function in a continuous medium.

Table 6.4. Calculated parameters for transmission line model shield and jacket of the RG 316 coaxial cable. The shield has a metal diameter of 2.0 mm and the jacket has a diameter of 2.5 m. Insulation is Teflon. The wire is immersed in saline with conductivity σ = 0.47 S/m and relative dielectric constant 77. The parameters are calculated based on equations provided by King [98].

Parameter	Value at 64 MHz	Value at 128 MHz
Characteristic impedance Z0	40.5 -5.0j Ω	38.2 - 6.1j Ω
Loss factor α	1.05	2.55
Propagation constant β (King)	8.53 m^{-1}	16.1 m^{-1}
Propagation constant β (Best fit)	7.85 m^{-1}	14.0 m^{-1}

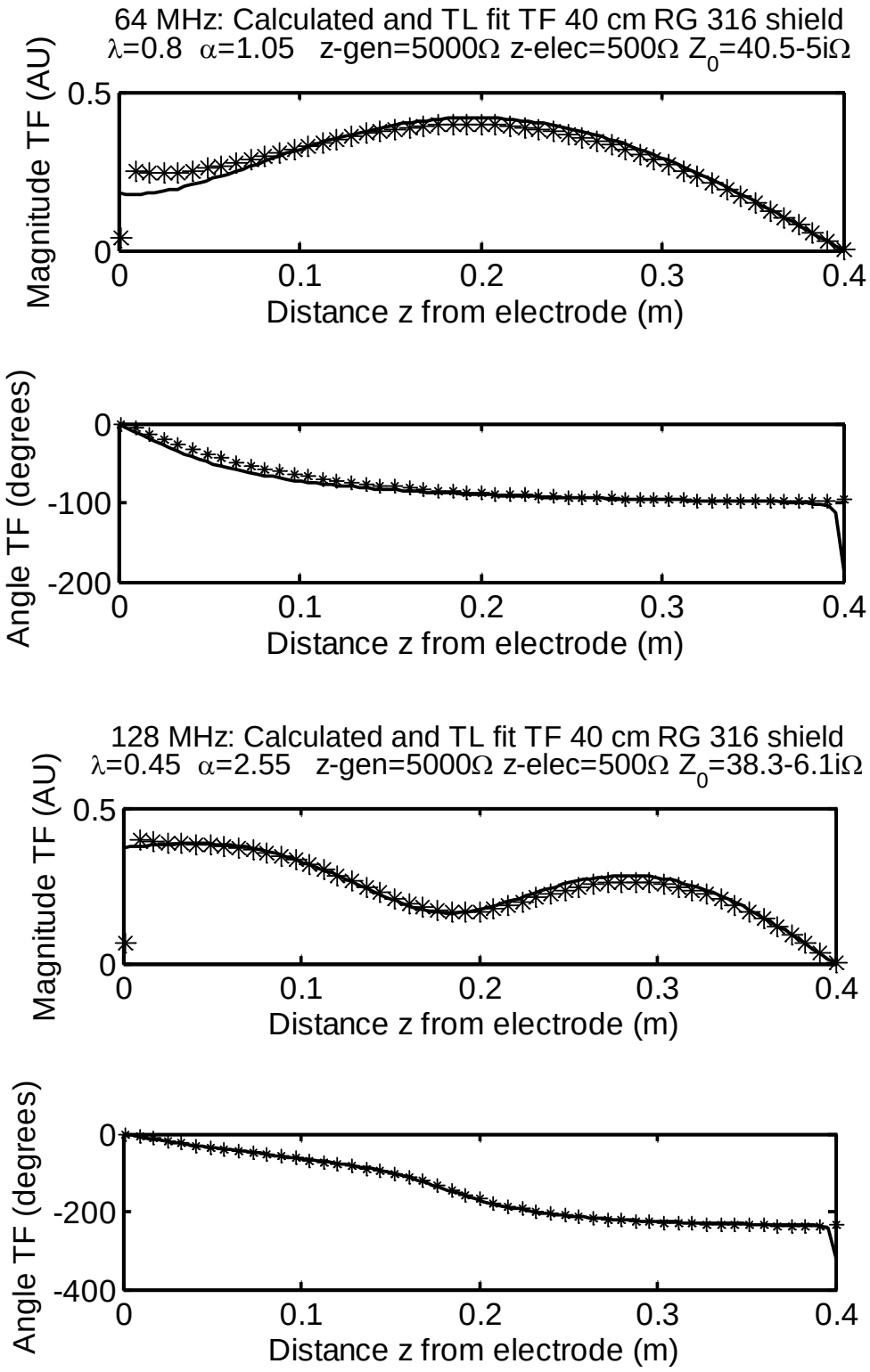

Figure 6.4. Calculated and measured transfer function for shielded 40cm model lead at 64 MHz (top) and 128 MHz (bottom). The wire has parameters of the shield and jacket of an RG 316 coaxial cable.

6.3 Electric field transfer function for shielded lead models based on RG316 cable

In this section, we calculate the electric field transfer function for shielded lead models and compare it to the measured transfer functions. The general model is based on Figure 6.1 The transmission line model is used to calculate the transfer function. Based on the discussion above, Table 6.5 lists the constants for the model.

In the physical tests, the model electrode was a 6-mm long section of the central conductor. The model generator was in the form of a US half dollar coin. This model has a surface area similar to that of a small pacemaker. Impedances for model electrode and generator are calculated based on formulas from Smythe [100]

For the generator, with radius a, large compared to height 2b, the capacitance is given by

$$C_{gen} = 4\pi\left(\frac{2a}{\pi}\right)\left(1+\frac{2b}{\pi a}\right)\varepsilon_m \tag{6.11}$$

where ε_m is the dielectric constant of the medium given by $\varepsilon_m = \left(\varepsilon - j\frac{\sigma}{\omega}\right)$

For generator, 2a=30.61 mm and 2b=2.15 mm. σ is 0.47s/m and ε=78ε_0 (water)

For the electrode, with radius a small compared to height 2b, the capacitance is given by

$$C_{elec} = 4\pi\left(\frac{2a}{\pi}\right)\left(1+0.87(b/a)^{0.76}\right)\varepsilon_m \tag{6.12}$$

For electrode, 2a=0.51 mm and 2b=6 mm
The impedance relative to infinity in the phantom is

$$Z = \left(j\frac{1}{\omega C}\right) \tag{6.13}$$

where $\omega = 2\pi f$ is the angular frequency.

Table 6.5. Values of constants for the transmission line model of the lead.

Frequency (MHz)	Section	Z_0 (Ω)	α	β (1/m)
64	Exposed lead	102 -9.7 j	0.42	4.19
64	Inside shield	50	0	2.01
64	Surface of shield	40.5 -5.0j	1.05	7.85
128	Exposed lead	97.9 - 11.6 j	1.01	8.52
128	Inside shield	50	0	4.02
128	Surface of shield	38.2 - 6.1j	2.55	14

Table 6.6. Impedance values for the model lead and generator.

Structure	Freq.(MHz)	a (mm)	2b(mm)	C per Smythe (pF)	Z
Electrode	64	0.255	6	9.39-15.9j	116 - 68.5j
Electrode	128	0.255	6	9.38 - 7.95j	65.3 - 77.2j
Generator	64	15.3	2.15	88.3-150j	12.3-7.3j
Generator	128	15.3	2.15	88.3 - 75j	6.94 - 8.2 j

6.4 Calculation of transfer functions with the transmission line model

The transfer function for the transmission line of Figure 6.1 was calculated based on equations 6.8 and 6.9 with a MATLAB program (calc_shielded_TF.m). The key function inside the program is Zin_rho_TL4. This function has as its input the values of τ, γ, Z_0 and parallel impedance along the length of the line, as well as the generator and electrode impedances at the end of the line. The function provides matrices with impedance to the electrode (I_ratio_mat_elec), and generator (I_ratio_mat_gen) ends along the length of the line, the reflection coefficients looking toward the electrode and generator ends of the line, and ratio between injected current and the current that appears at the end of the line (I_ratio_mat_elec and I_ratio_mat_gen). With this function, the electric field transfer function is calculated as

$$S = \frac{1.}{Z\_in\_mat\_gen + Z\_in\_mat} \frac{I\_ratio\_mat\_elec(1).}{I\_ratio\_mat\_elec}$$

The function Zin_rho_TL4 was used to calculate the transfer function on the center conductor and the outside of the shield using parameters in Table 6.5 and Table 6.6. The values of Γ_d and $\Gamma_{p.}$ are adjusted to provide the best fit to the measured transfer function.

Results of the calculated transfer functions were plotted along with the measured data. In the plots, the magnitude measured S is the actual S_{21} from the network analyzer. The calculated TF was scaled to provide the best overlap with the measurement. In the measurements, the same electrode was directly connected to a cable leading to port 2 of the VNA. Thus at each of the measurement frequencies, 64 MHz, and 128 MHz, the magnitude of S is proportional to the actual magnitude.

Figure 6.2 shows that the transmission line model provides a good agreement to the measured TF. Agreement between the calculated and measured TF was also good for the un-shielded wire terminated by the half-dollar model generator, as shown in Figure 6.6.

Figure 6.5 confirms the physical model of Figure 6.1. The red arrow indicates the step in the transfer function for the 45 cm shielded lead, which has the edge of the shield at a distance of 9 cm from the end.

Figure 6.7 shows the transfer functions for 45-cm cable. The TF shows there is current injection into the central conductor for the shorted lead. For the lead with an open at the proximal end, there is no current injection into the central conductor, which is evidenced by the magnitude of the TF being effectively zero at the end. The worst agreement between calculated and measured transfer functions occurred for shielded leads with the model generator. Figure 6.8 shows calculated and measured transfer functions for 80-cm shielded cable with half-dollar termination. There is a phase difference between measurement and calculation. The difference may be due to injection of current at the proximal end of the lead and the large phase shift associated with this injection.

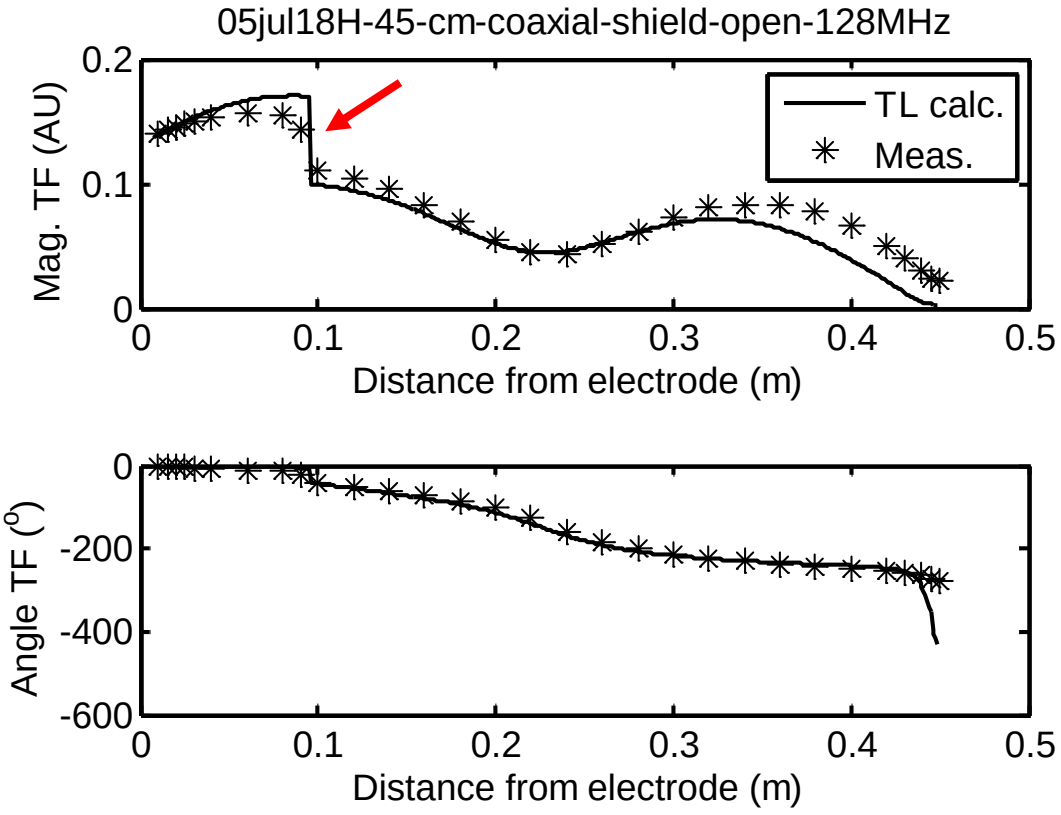

Figure 6.5. Confirmation of transmission line model of physical electrode. The red arrow indicates the step in the transfer function for the 45 cm shielded lead, which has the edge of the shield at a distance of 9 cm from the end.

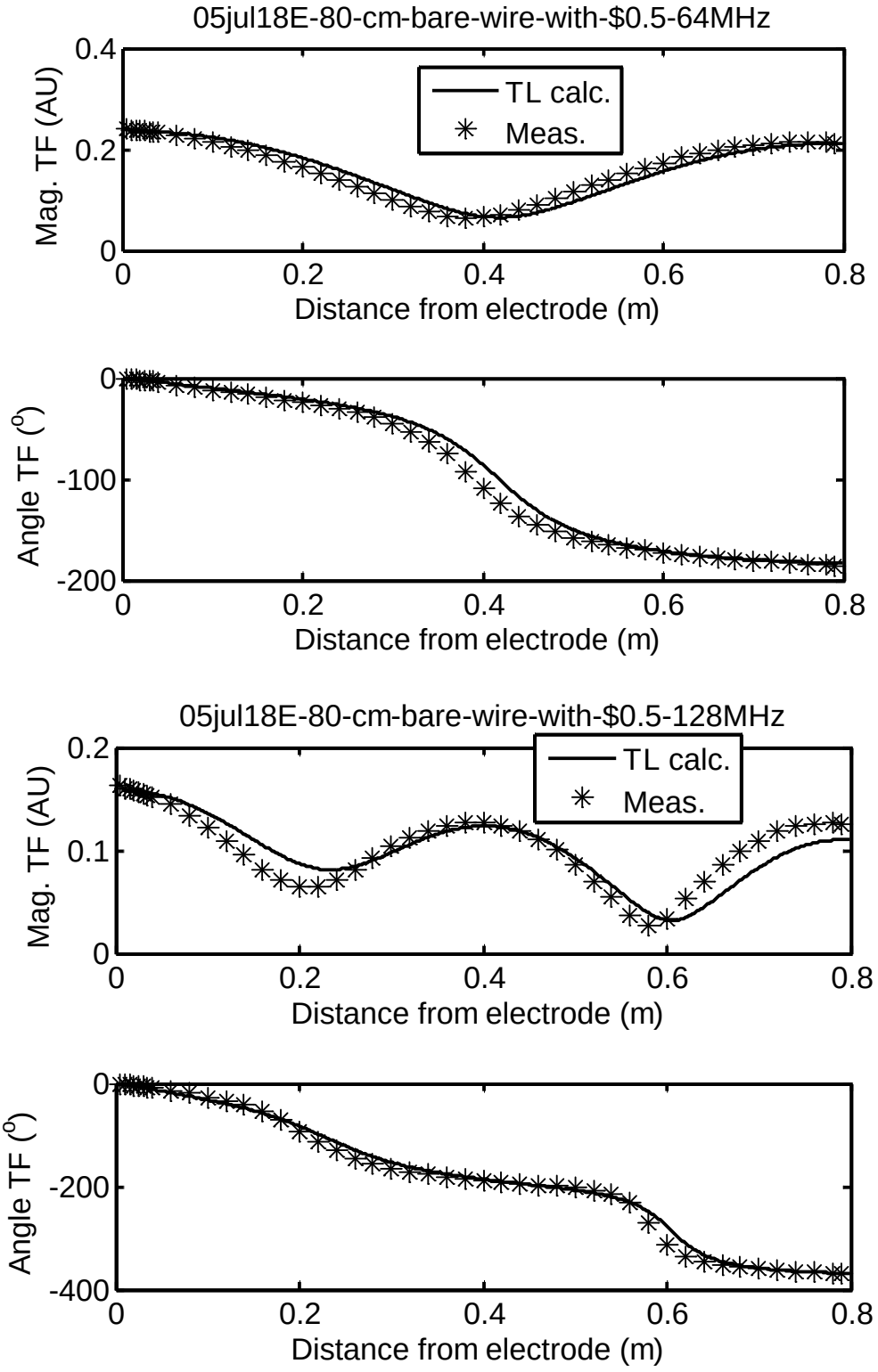

Figure 6.6. Calculated and measured transfer functions for unshielded lead with gen. Generator is in the form of a half-dollar coil. The top is for 64 MHz, and the bottom is for 128 MHz.

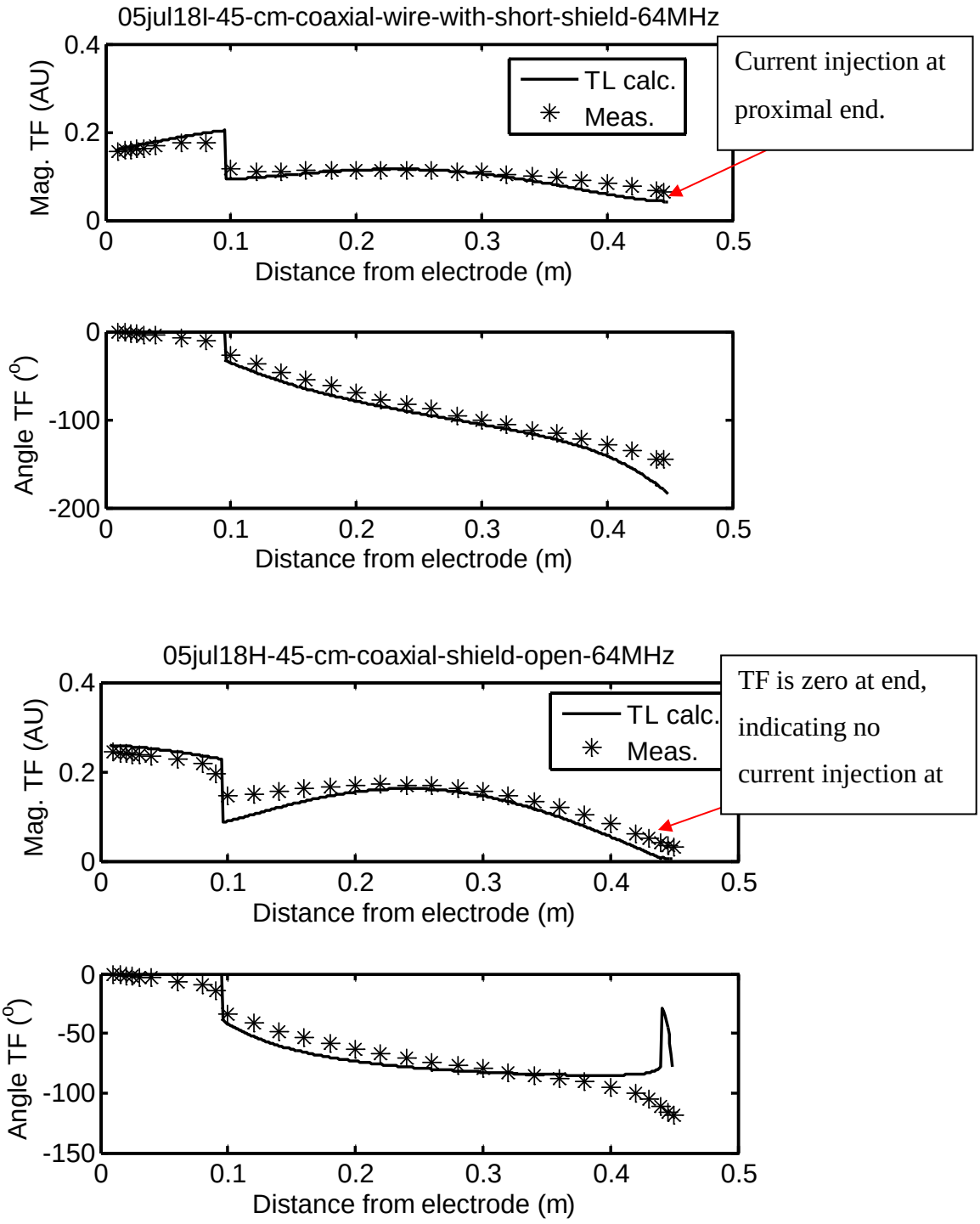

Figure 6.7. Calculated and measured transfer functions for 45cm RG 316 model lead Top is for shorted proximal end and bottom is for open proximal end. For the lead with a short at the proximal end, magnitude of the TF is greater than zero at the proximal end, indicating that there is injection of current from the shield to the center conductor. For the lead with an open at the proximal end (z=0.45 m), the magnitude of the TF is near zero at the end.

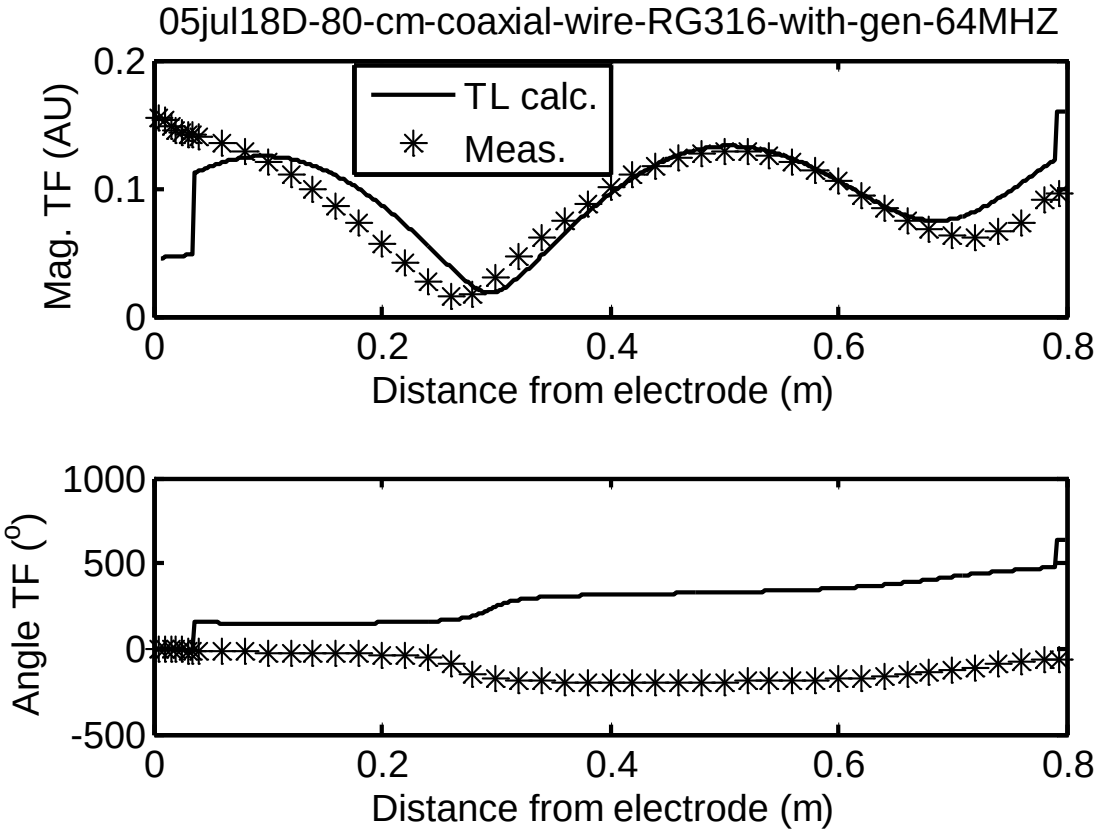

Figure 6.8. Calculated and measured transfer functions for 80cm model lead w/ gen. The generator is half-dollar termination. There is a phase difference between measurement and calculation. The difference may be due to injection of current at the proximal end of the lead and the large phase shift associated with this injection.

6.5 Summary

A physical model for how the shield on a lead wire affects the heating at the electrode is presented in this chapter. The model is based on the propagation of current waves on the shield and the lead wire. Comparison of the measured and calculated transfer function for RG 316 for different configurations is provided.

The measured and calculated transfer function is in good agreement with each other. The worst agreement between calculated and measured transfer functions occurred for shielded leads with the model generator. Figure 6.8 shows calculated and measured transfer functions for 80-cm shielded cable with half-dollar termination. There is a phase difference

between measurement and calculation. The difference may be due to injection of current at the proximal end of the lead and the large phase shift associated with this injection.

Voltage is induced along the length of the lead due to background electric field. However, if the shield is sufficiently long, the magnitude of induced voltage should be less for the shielded lead than for the bare lead, even though the tangential electric field at the edge of the shield may be larger than the background electric field.

Assume that we start with a given lead for which we wish to reduce the RF heating by addition of the shield. The design variables are straightforward:

(a) Value of distal location of the shield τ_d .

(b) Value of the proximal location of the shield τ_p .

An important factor in the temperature rise of the shielded lead is the magnitude of the transfer function, calculated for shielded lead models assuming there is no coupling between E_{tan} and shield. It may be feasible to place the edges of the shield at locations where this magnitude of the transfer function is the smallest to minimize temperature rise and RF heating due to MRI.

7. EXPERIMENTAL VALIDATION AND CASE STUDY FOR A LEAD USED WITH A NEUROSTIMULATION SYSTEM

To further illustrate the concept of shielding in open and short configurations, this section describes the in-vitro temperature rise and transfer function measurements for a commercially available neurostimulation system, the Vagus Nerve Stimulation, VNS Therapy, NeuroCybernetic Prosthesis (NCP) System (Livanova Inc (formerly Cyberonics), Houston, TX). The tests and analysis were made on a system used for VNS Therapy- the model 303 lead and either Model 102 (Big) or Model 103 (small) pulse generator. Results of tests of MRI-related heating for physiological paths in a rectangular phantom have been published for this system [94].

7.1 Physical description of Cyberonics lead

Model 303 lead is a bipolar electrical lead and consists of two filars and is 43 cm in length. There are two electrodes made up of platinum foil that is located at the end of the lead [94]. The VNS therapy lead trasnmits stimulation from the VNS therapy generator to the left vagus nerve in the neck. The measurements were made for an unshielded-shielded lead with a pulse generator and unshielded-shielded lead with an insulating cap at the end. The lead is made up of the pin that is connected to a model generator on one end. The other end of the lead contains the stimulation electrodes and anchor tether.

7.2 Method to evaluate Electric Field Transfer function

For measurement of electric field transfer function, the model 303 lead with and without a capped insulator, with and without the model 102 and with and without model 103 pulse generator was placed in the test apparatus as shown in Figure 7.2. The reader is referred to a section of Chapter 5 for a detailed description of transfer function measurement. The toroidal coil as shown in Figure 7.2 was moved along the length of the lead to measure magnitude and phase of S_{21} as a function of the location of the coil.

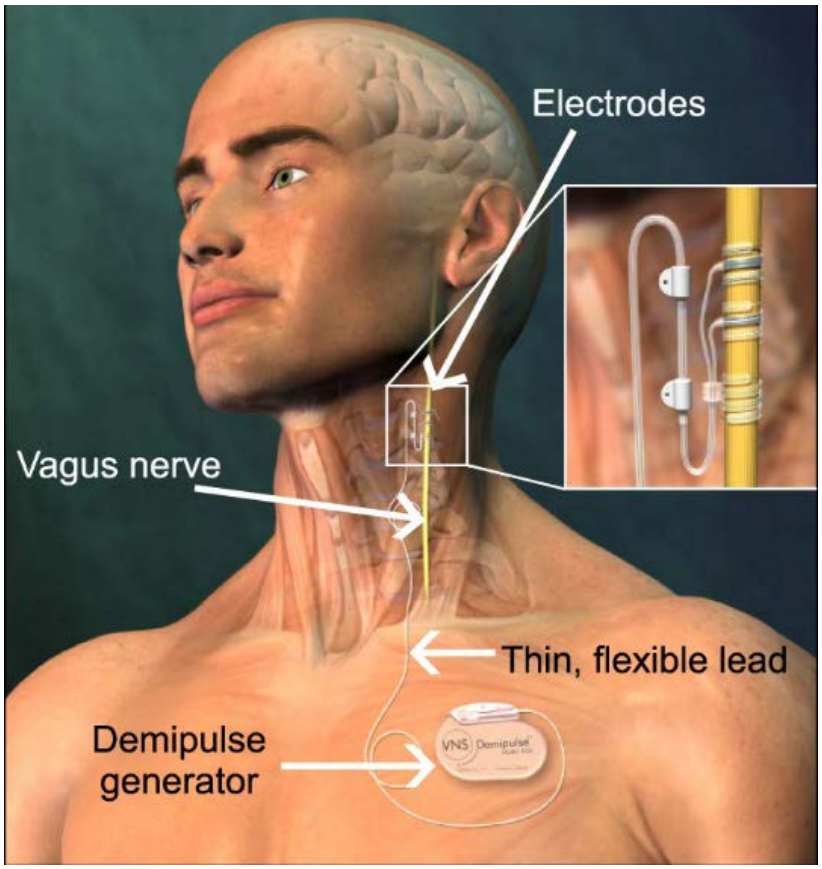

Figure 7.1 Model 303 Cyberonics Lead [101]

Figure 7.2 Setup to measure electric field transfer function for Cyberonics lead

7.2.1 Results for measurement of the transfer function for Cyberonics lead

7.2.1.1 Measurement of the electric field transfer function for Cyberonics Lead capped at the end

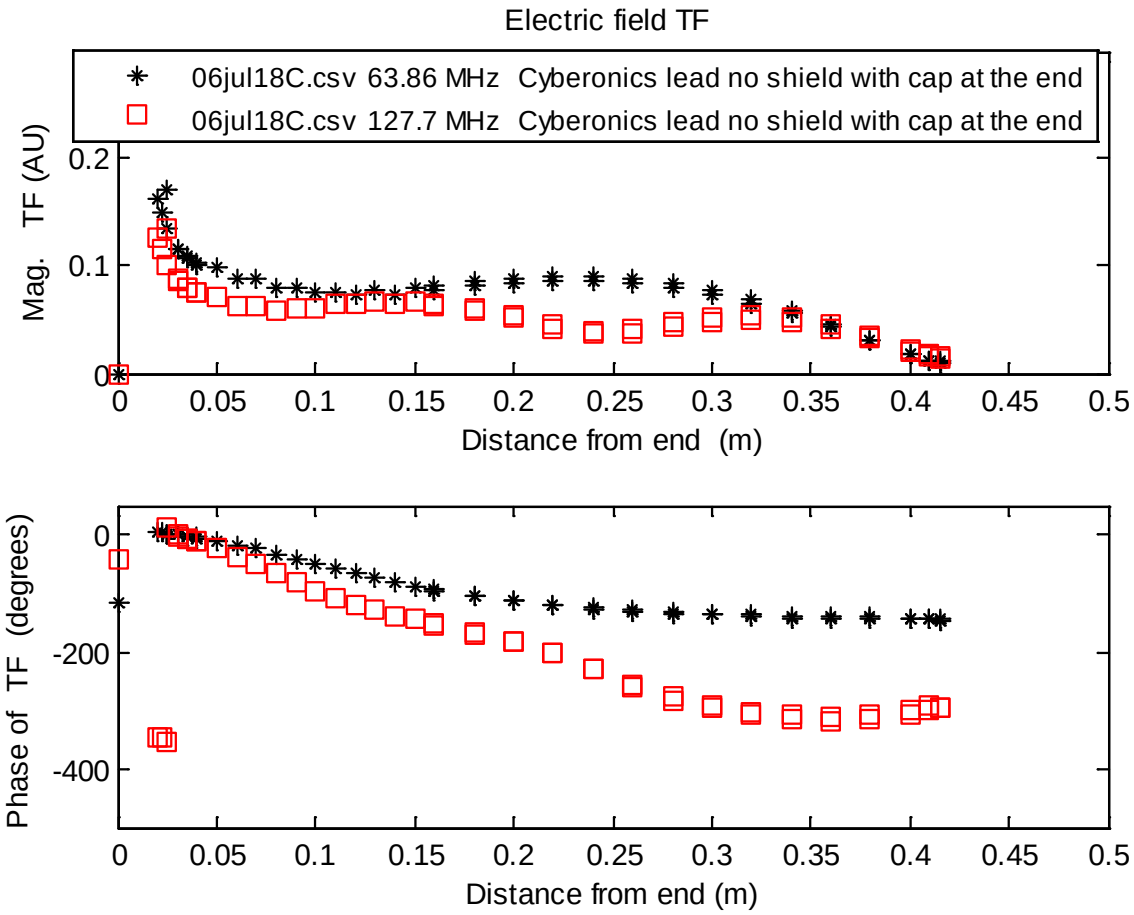

Figure 7.3 Measured transfer function for capped Cyberonics lead Top plot is the magnitude, and the bottom plot is the phase of the transfer function.

7.2.1.2 Measurement of the electric field transfer function for Shielded Cyberonics Lead capped at the end

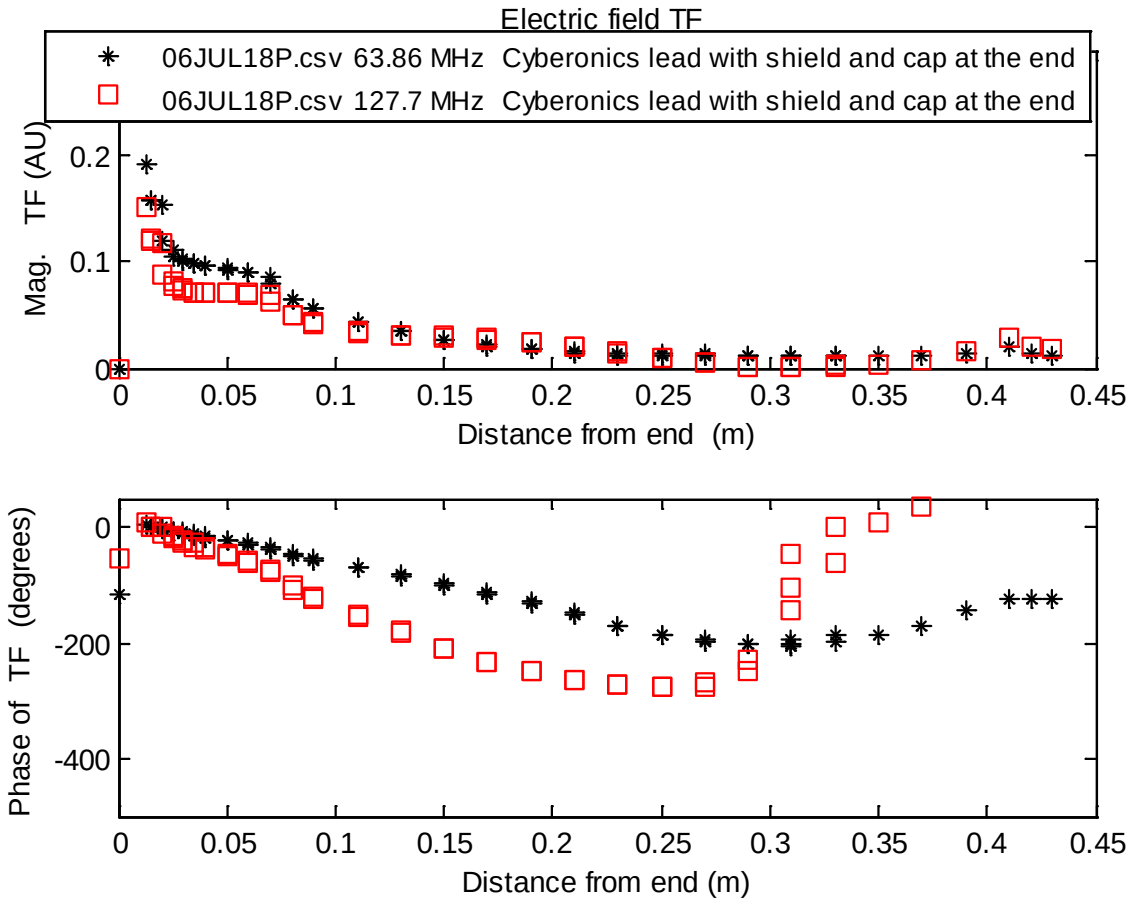

Figure 7.4 Measured transfer function for capped Cyberonics lead with shield Top plot is the magnitude, and the bottom plot is the phase of the transfer function. The shield is present along the length of the lead. The presence of shield decreases the magnitude of transfer function when compared to the magnitude of the transfer function for unshielded Cyberonics lead.

7.2.1.3 Measurement of the electric field transfer function for unshielded Cyberonics Lead with a Model 102 generator at the end

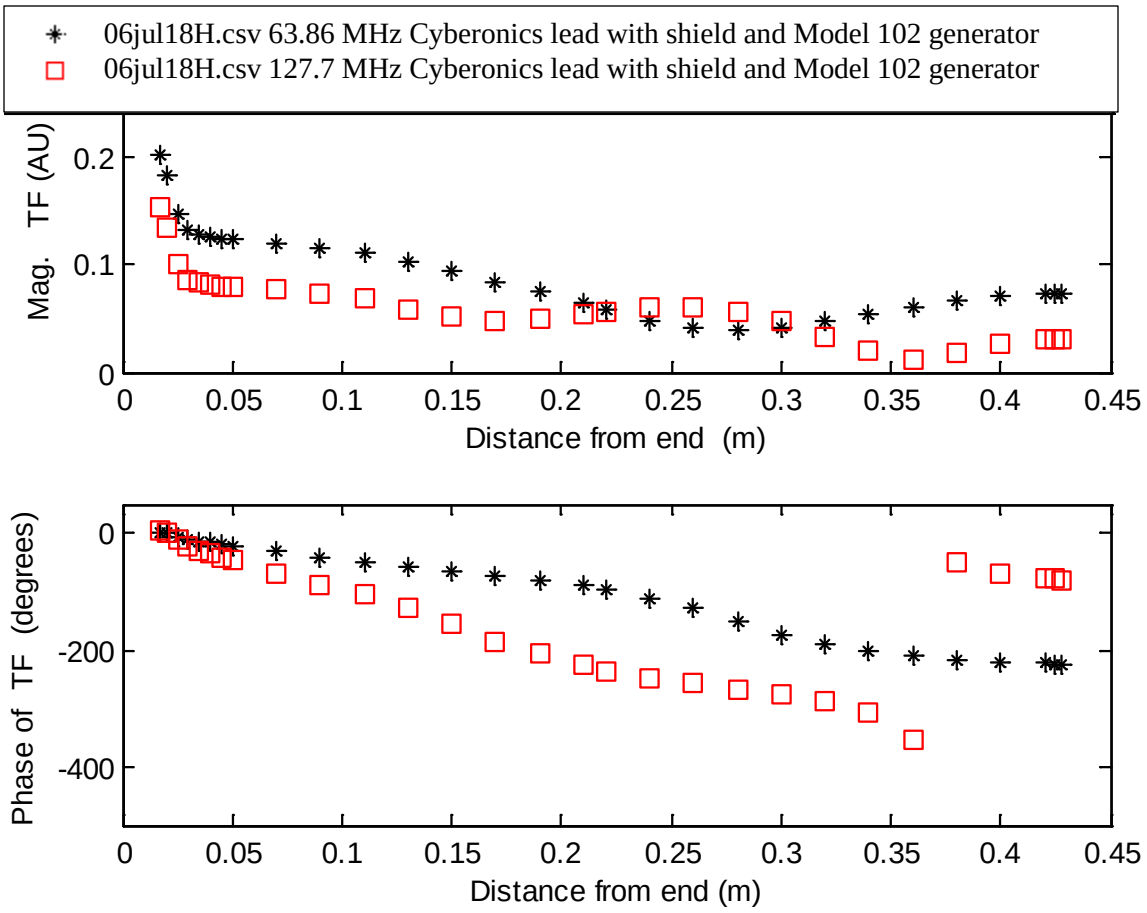

Figure 7.5 Measured transfer function for Cyberonics lead with generator Model 102 generator is attached at the end. The top plot is the magnitude, and the bottom plot is the phase of the transfer function.

7.2.1.4 Measurement of Transfer function shielded Cyberonics Lead with a Model 102 generator at the end

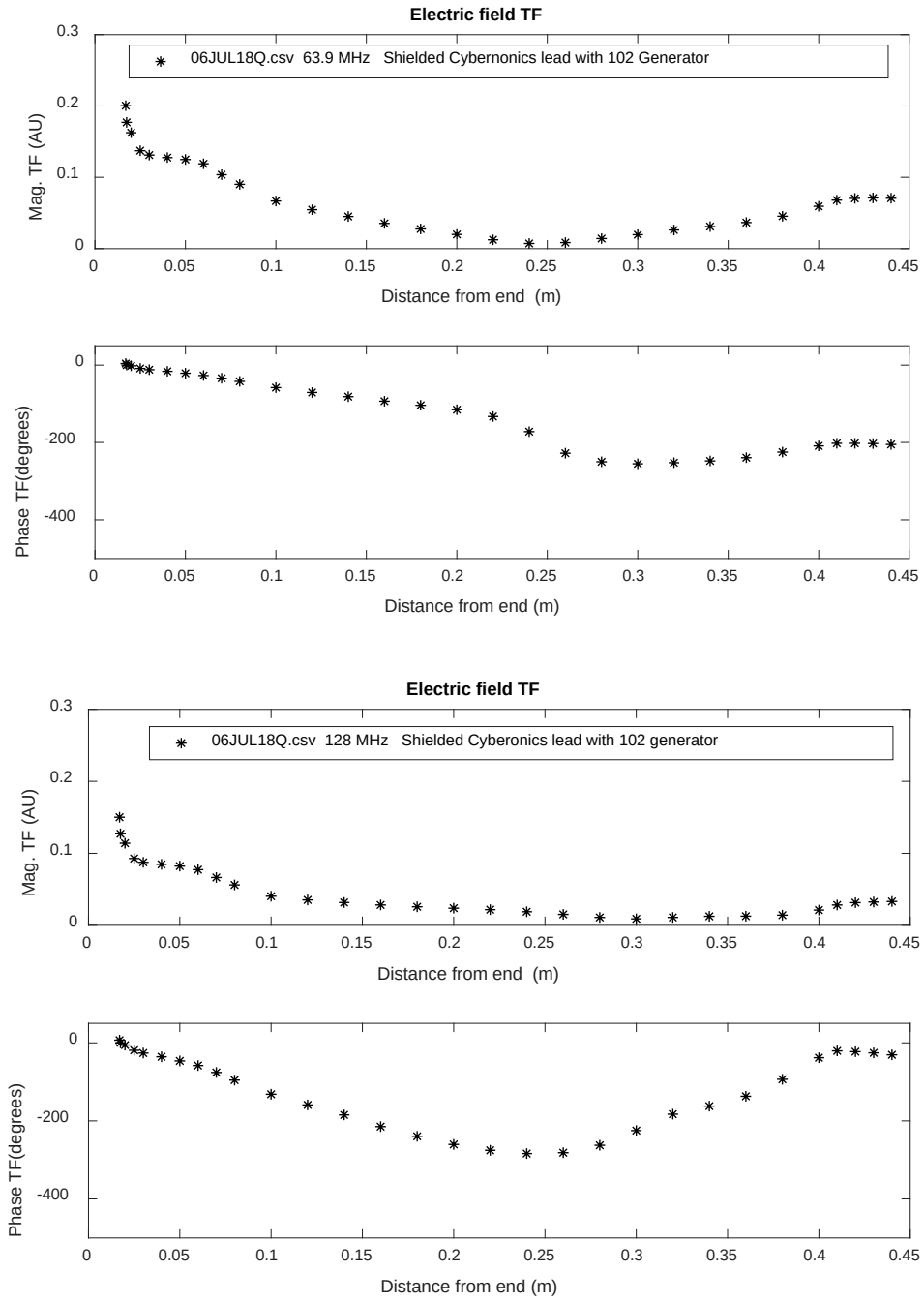

Figure 7.6 Measured transfer function for Cyberonics lead with shield and generator Model 102 generator is attached at the end. The top plot shows measurements at 64 MHz, and the bottom shows measurements at 128 MHz. The shield is present along the length of the lead. The presence of shield decreases the magnitude of transfer function when compared to the magnitude of the transfer function for unshielded Cyberonics lead with model 102 generator.

7.2.1.5 Measurement of Transfer function unshielded Cyberonics Lead with a Model 103 generator at the end

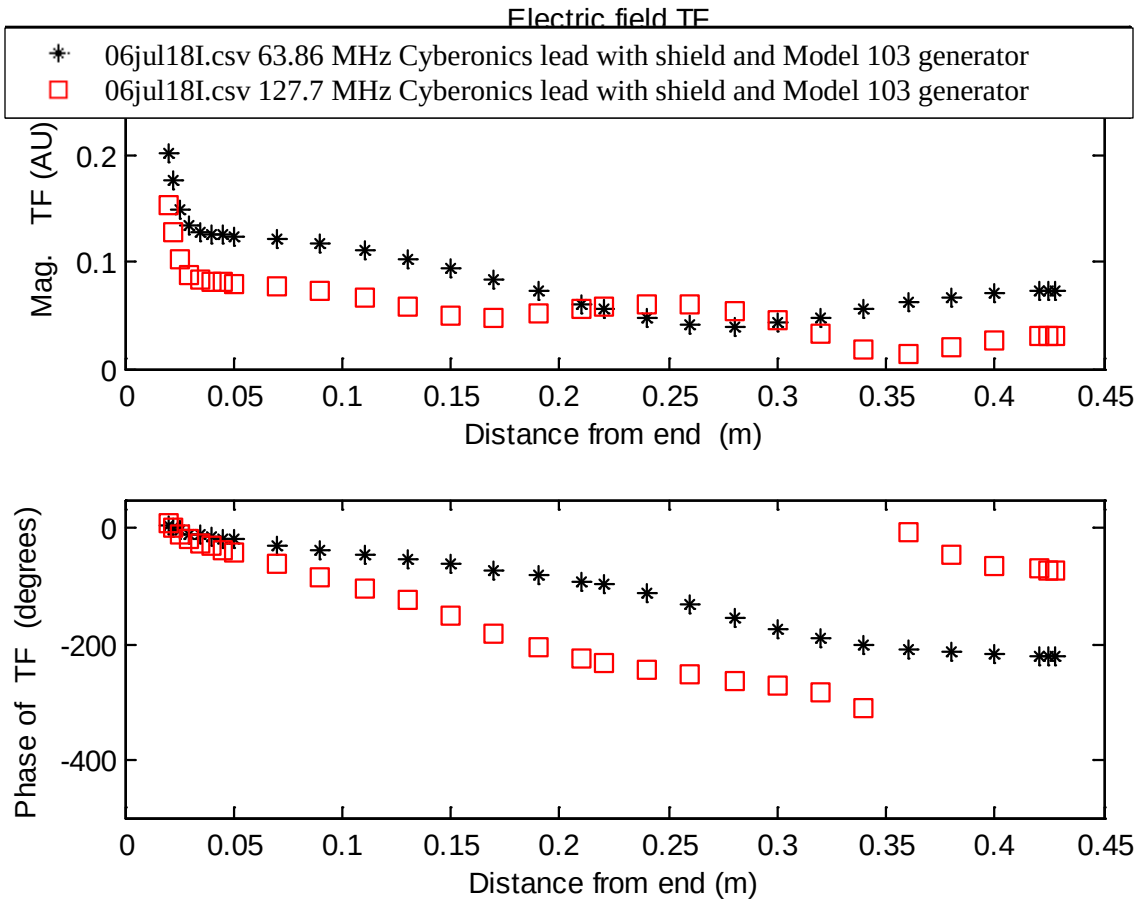

Figure 7.7 Measured transfer function for Cyberonics lead with generator Model 103 generator is attached at the end. The top plot is the magnitude, and the bottom plot is the phase of the transfer function.

7.2.1.6 Measurement of Transfer function shielded Cyberonics Lead with a 103 generator at the end

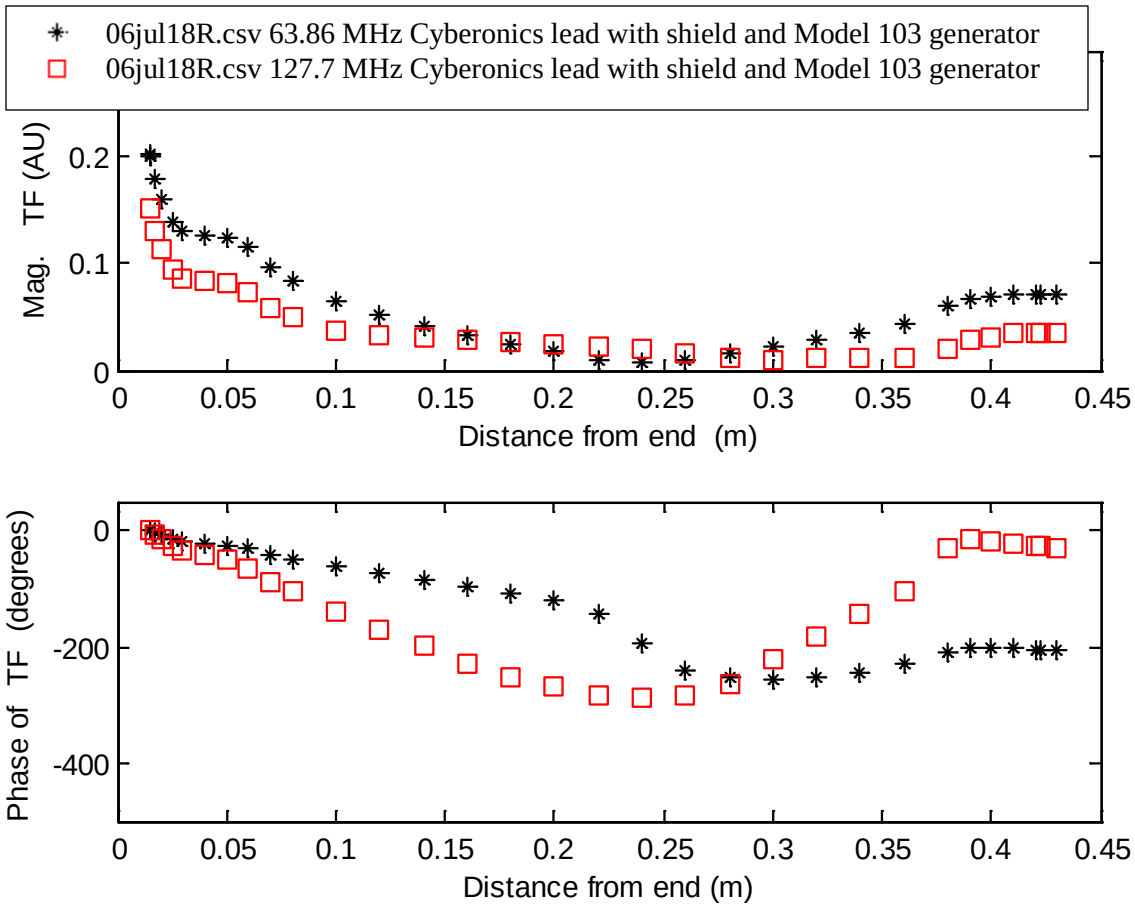

Figure 7.8 Measured transfer function for Cyberonics lead with shield and generator Model 103 generator is attached at the end. The top plot is the magnitude, and the bottom plot is the phase of the transfer function. The shield is present along the length of the lead. The presence of shield decreases the magnitude of transfer function when compared to the magnitude of the transfer function for unshielded Cyberonics lead with model 103 generator.

7.3 Method to evaluate Temperature Rise for Cyberonics lead

For measurement of temperature rise, the model 303 lead with and without a capped insulator, with and without the model 102 and with and without the model 103 pulse generator was placed in the test apparatus section 7.3.1. The reader is referred to section 3.4 for a detailed explanation of temperature rise measurement. Neoptix fiber optic cables were attached to two electrodes as shown in Figure 7.9. The VNS lead having the temperature sensor was fixed on a plastic mat using plastic mounting screws. The entire assembly was placed in an ASTM phantom. The phantom was kept in an RF coil for temperature measurement. RF power was applied for 6 minutes.

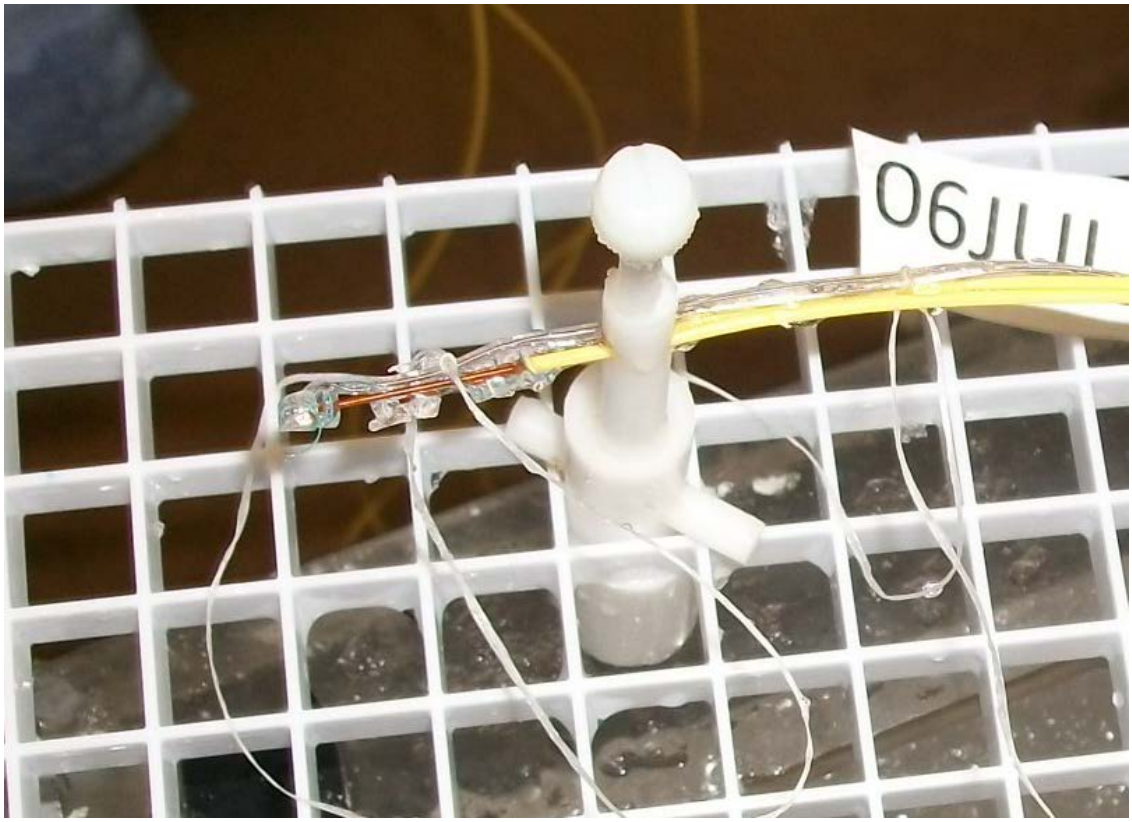

Figure 7.9 Neoptix temperature probe contact with electrodes of Cyberonics lead for temperature rise measurement

7.3.1 Results for measurement of temperature rise for Cyberonics lead.

7.3.1.1 Measurement of Temperature Rise for Cyberonics Lead with Model 102 generator at the end.

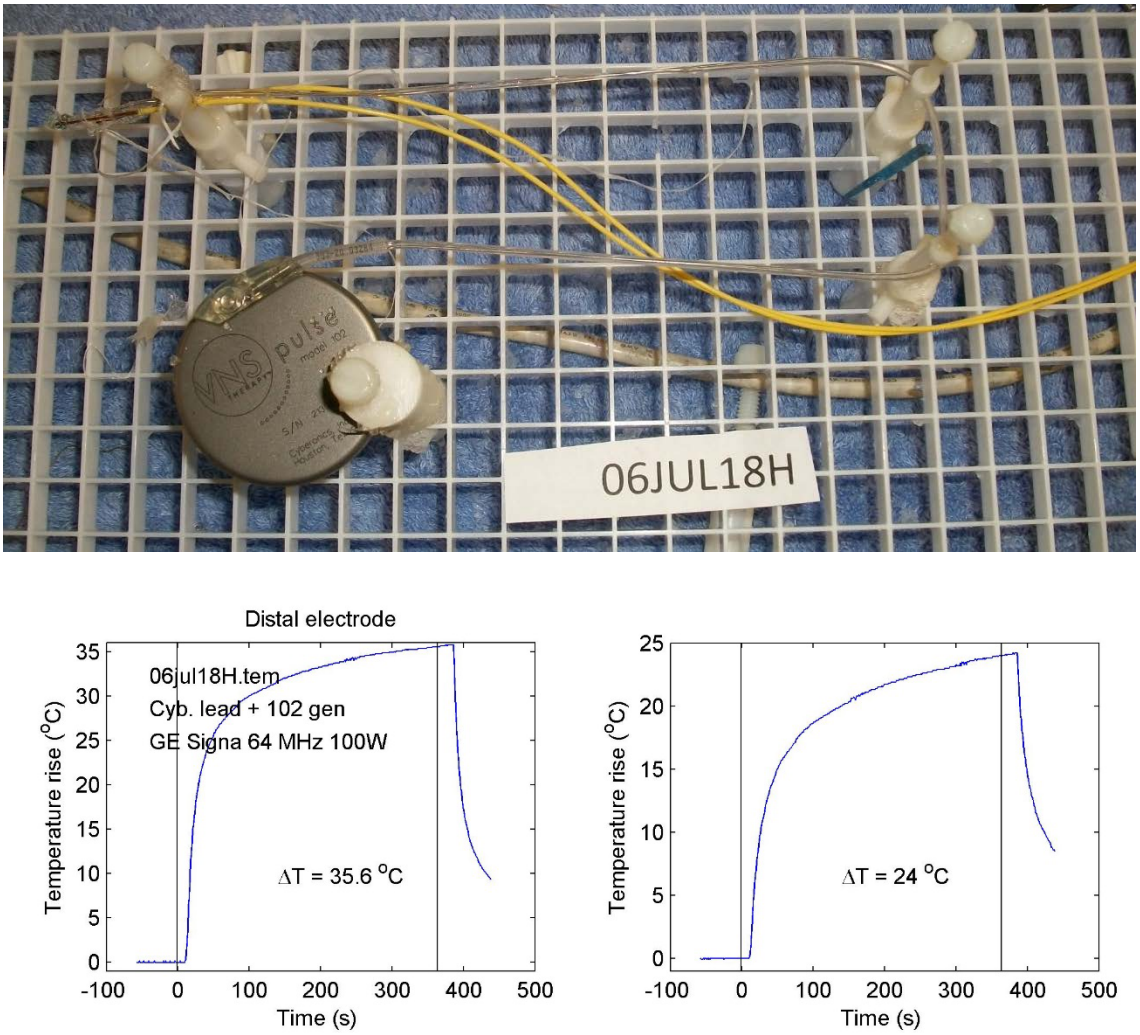

Figure 7.10 Measured Temperature rise for Cyberonics lead with a generator. Model 102 generator is attached at the end. The top plot shows measurement setup and bottom plot is temperature rise value after six minutes of 100 W of RF power. Two neoptix temperature probes are used for temperature rise measurement for redundancy. The measured temperature rise at the tip of the lead is 35.6°C. Local background SAR at 100 W of RF power is 5.56 W/kg.

7.3.1.2 Measurement of Temperature Rise for Cyberonics Lead capped at the end

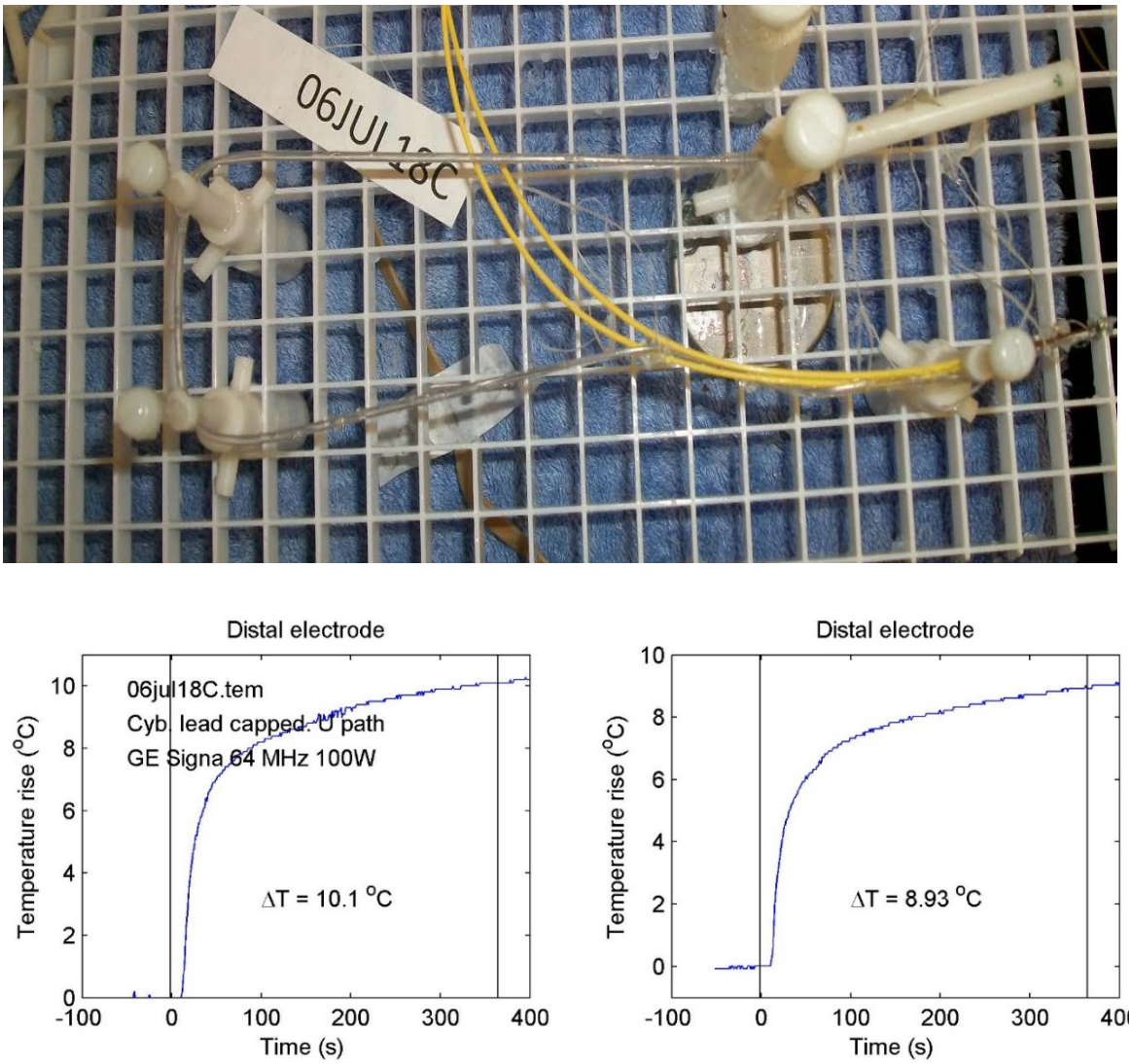

Figure 7.11 Measured Temperature rise for Cyberonics lead capped at the end. The top plot shows measurement setup and bottom plot is temperature rise value after six minutes of 100 W of RF power. Two neoptix temperature probes are used for temperature rise measurement for redundancy. The measured temperature rise at the tip of the lead is 10.1°C. Local background SAR at 100 W of RF power is 5.56 W/kg.

7.3.1.3 Measurement of Temperature Rise for Shielded Cyberonics Lead capped at the end

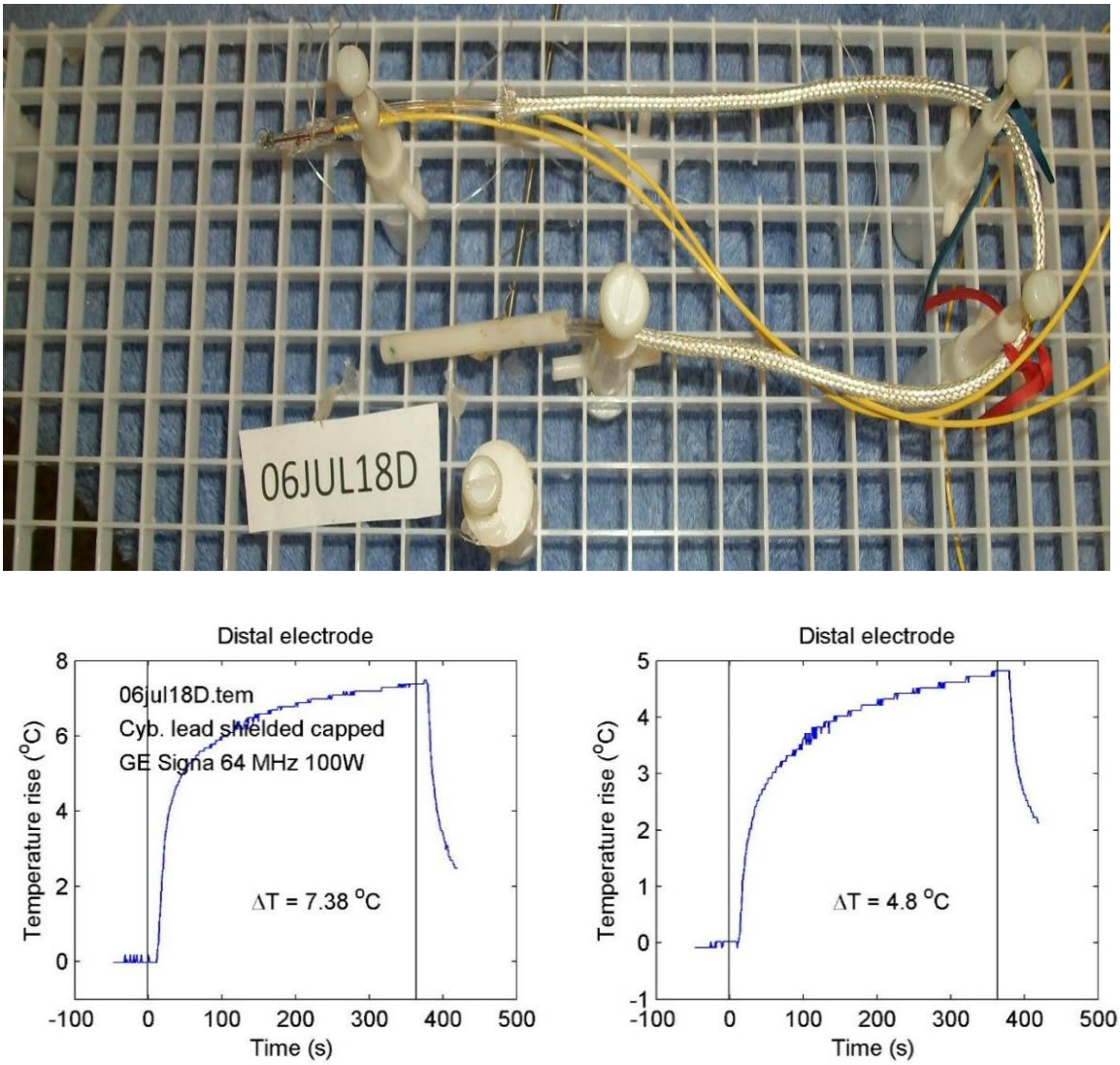

Figure 7.12 Measured Temperature rise for shielded Cyberonics lead cap at the end. The top plot shows measurement setup and bottom plot is temperature rise value after six minutes of 100 W of RF power. Two neoptix temperature probes are used for temperature rise measurement for redundancy. The measured temperature rise at the tip of the lead is 7.38ºC. Local background SAR at 100 W of RF power is 5.56 W/kg.

7.3.1.4 Measurement of Temperature Rise for Shielded Cyberonics Lead with model 103 generator at the end

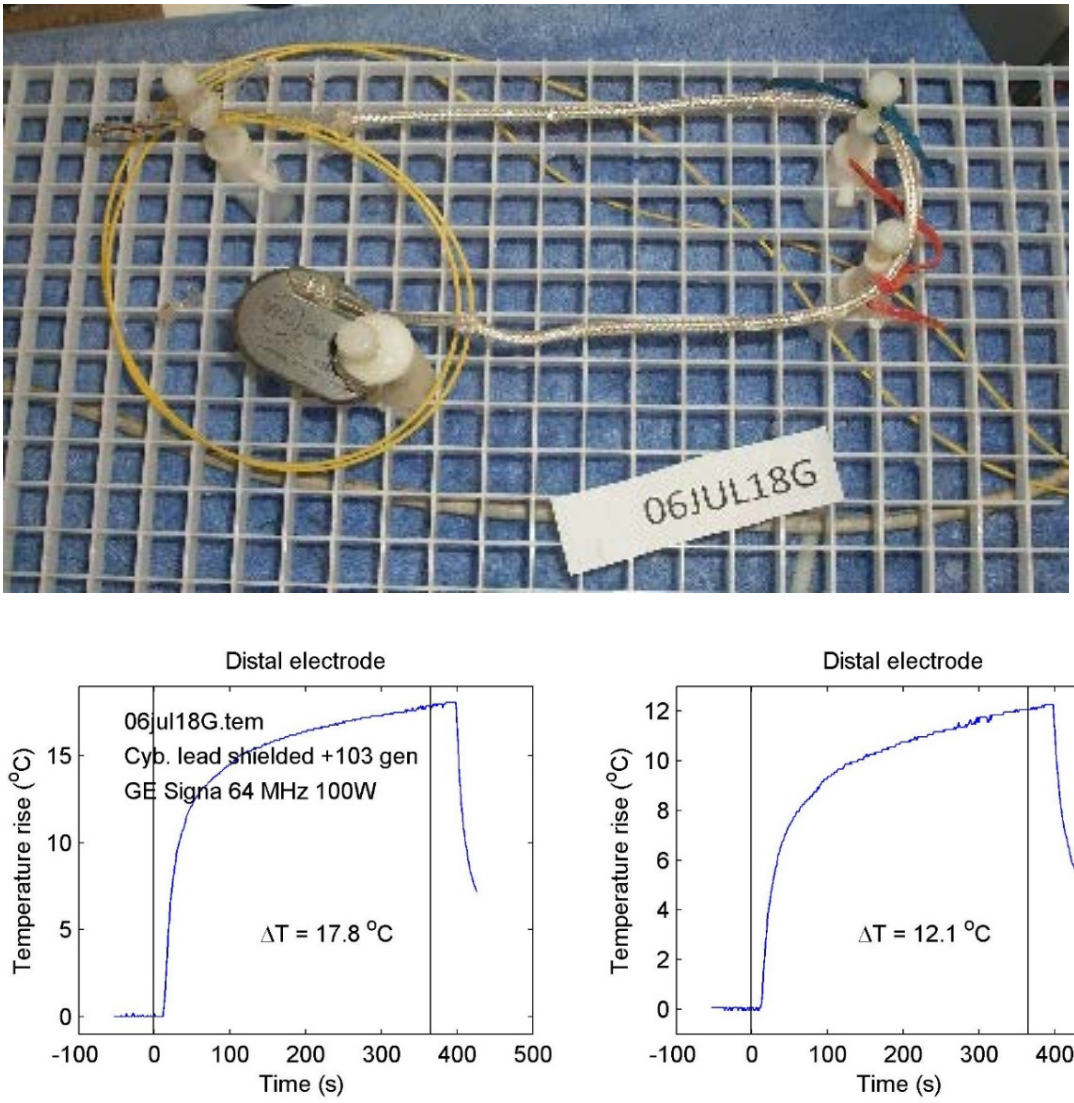

Figure 7.13 Measured Temperature rise for shielded Cyberonics lead with generator. Model 103 generator is attached at the end. The top plot shows measurement setup and bottom plot is temperature rise value after six minutes of 100 W of RF power. Two neoptix temperature probes are used for temperature rise measurement for redundancy. The measured temperature rise at the tip of the lead is 17.8°C. Local background SAR at 100 W of RF power is 5.56 W/kg.

7.3.1.5 Measurement of Temperature Rise for Shielded Cyberonics Lead with Model 102 generator at the end

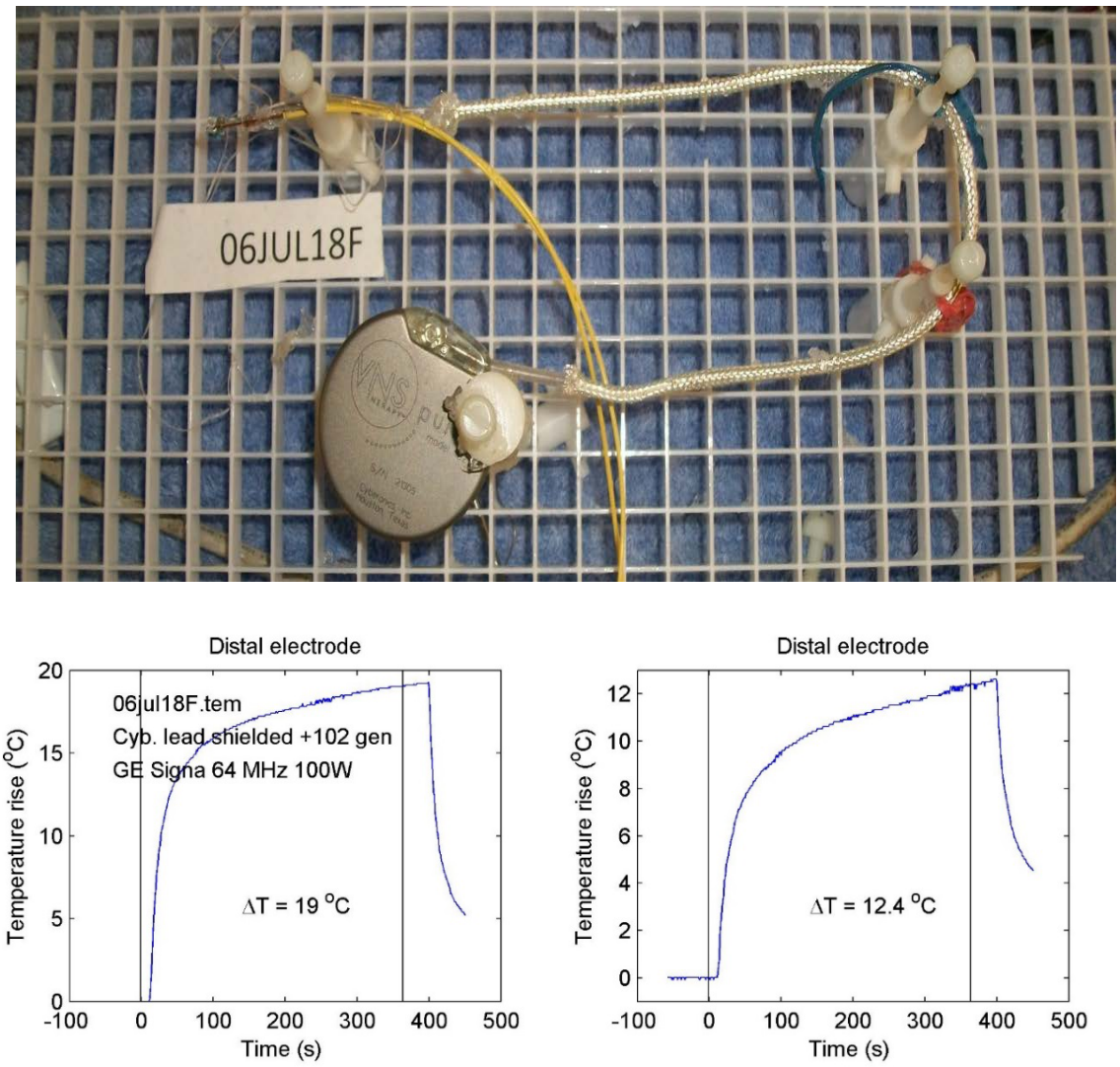

Figure 7.14 Measured Temperature rise for shielded Cyberonics lead with generator. Model 102 generator is attached at the end. The top plot shows measurement setup and bottom plot is temperature rise value after six minutes of 100 W of RF power. Two neoptix temperature probes are used for temperature rise measurement for redundancy. The measured temperature rise at the tip of the lead is 19°C. Local background SAR at 100 W of RF power is 5.56 W/kg.

7.3.1.6 Measurement of Temperature Rise for Cyberonics Lead with Model 103 generator at the end

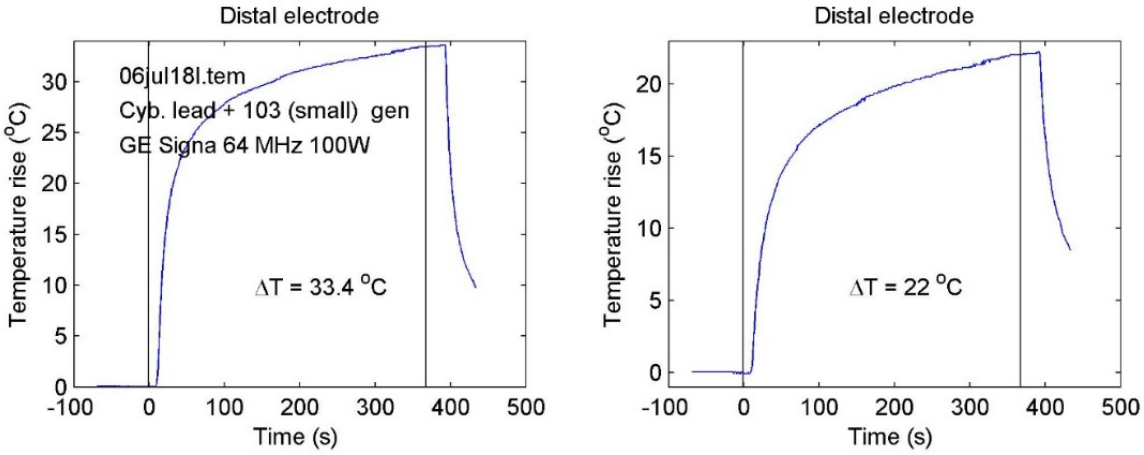

Figure 7.15 Measured Temperature rise for Cyberonics lead with generator. Model 103 generator is attached at the end. The top plot shows measurement setup and bottom plot is temperature rise value after six minutes of 100 W of RF power. Two neoptix temperature probes are used for temperature rise measurement for redundancy. The measured temperature rise at the tip of the lead is 33.4°C. Local background SAR at 100 W of RF power is 5.56 W/kg.

.

7.3.2 Pathways for the model leads and background E_{tan} in the physical tests

As explained in section 5.5, to calculate measured temperature rises, background tangential electric field is calculated along the same pathway where the lead is located in the same. Cyberonics lead with a generator on the test grid is as shown below. The grid was flipped over, and the lead was that serves as a model lead. The same pathway was used for all the tests on the Cyberonics lead Figure 7.16.

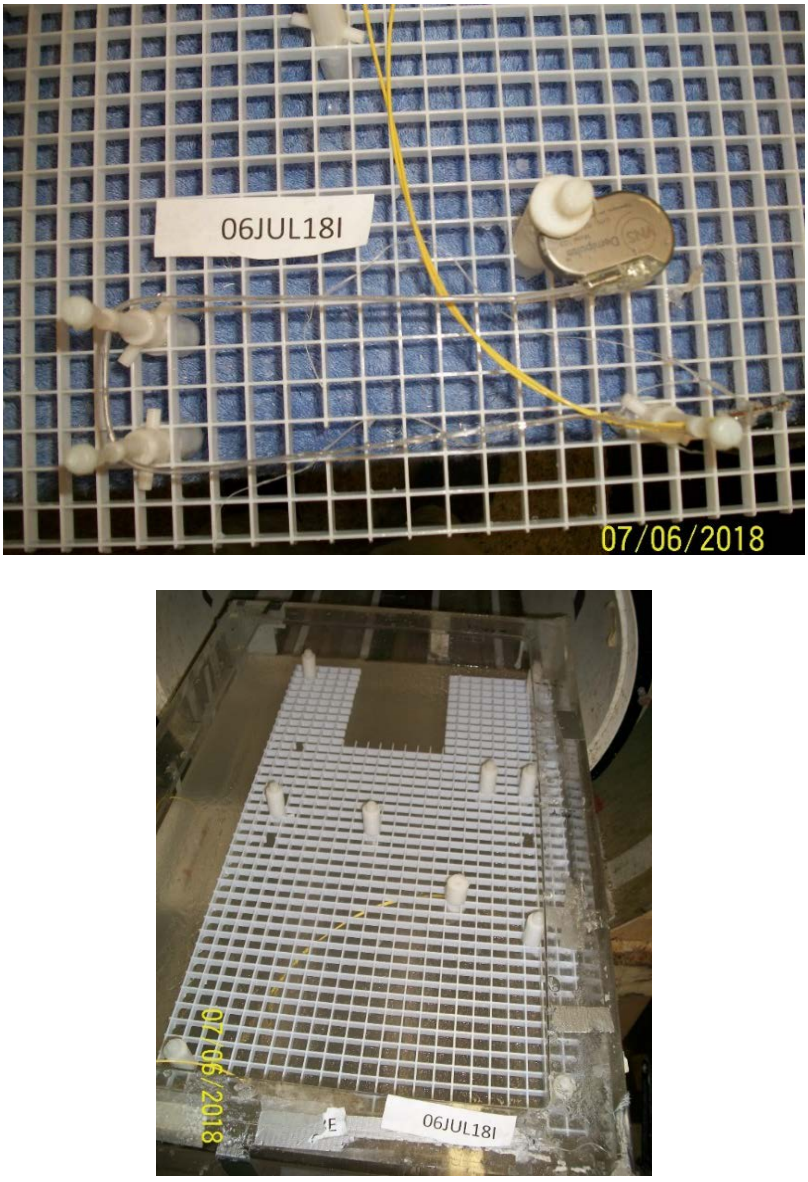

Figure 7.16 Pathway for Model 303 Cyberonics lead for temperature measurement. The same pathway was used for all of the tests on the various configurations for Cyberonics lead. Also shown, is the Cyberonics lead with Neoptix cables placed on the plastic mat. The plastic mat is kept in phantom that goes inside MRI coil.

Figure 7.17 shows the pathway for the Model 303 Cyberonics lead superimposed on the calculated electric field distribution in the phantom. Also shown is the background tangential electric field along the pathway Figure 7.18. The electric field is scaled for the input RF power of 100 W, which produces a local background SAR near the wall at the longitudinal center of the phantom at (x,y,z) = (0.165, 0, 0.325).

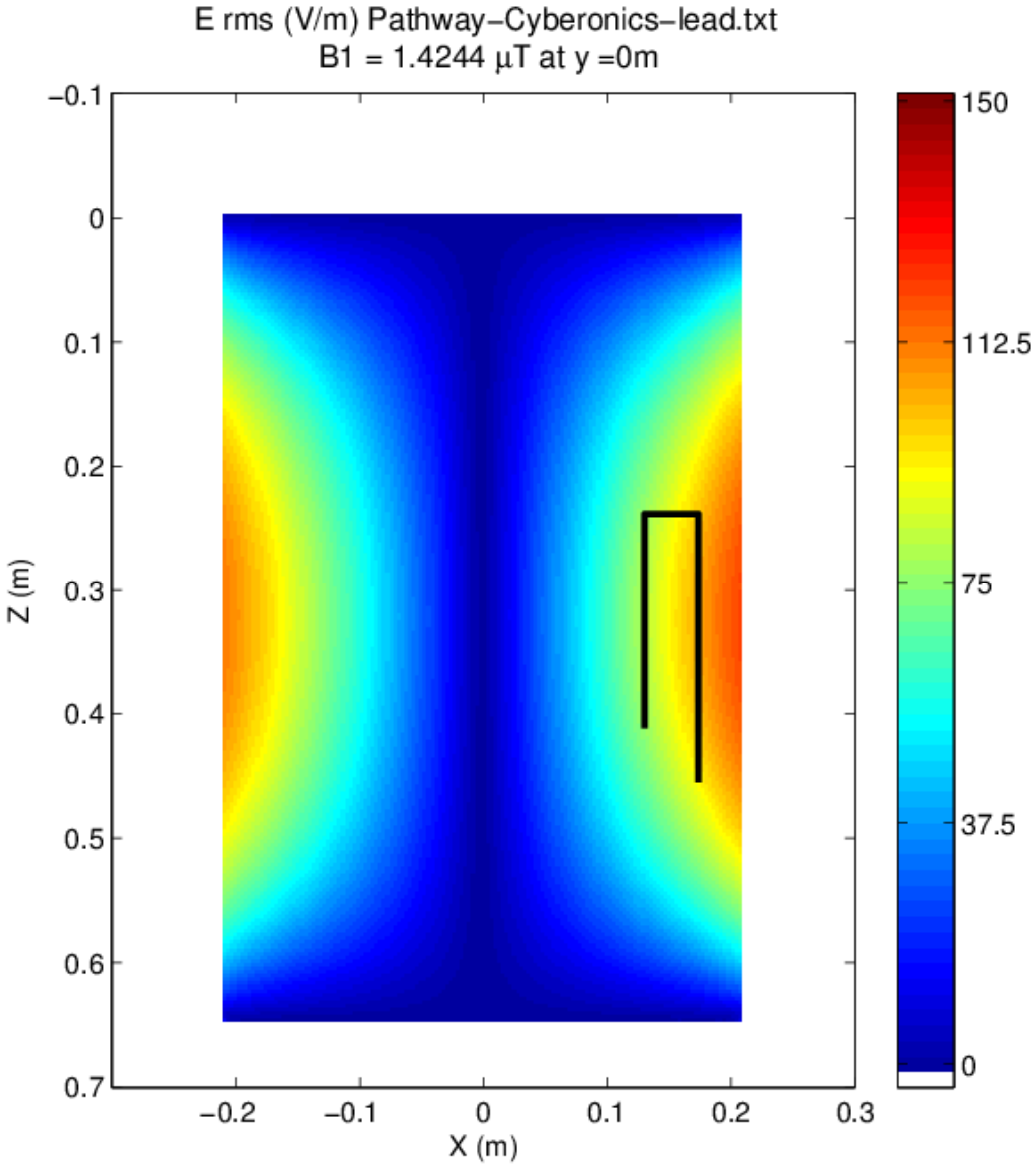

Figure 7.17 Path for the Cyberonics lead superimposed on the E_{rms} in the physical tests in the ASTM phantom The electric field is scaled for the input RF power of 100 W, which produces a local background SAR near the wall at the longitudinal center of the phantom at (x,y,z) = (0.165, 0, 0.325). The plot is the background tangential electric field in the ASTM phantom using the B_1 field from the RF coil. The magnitude of B_{1rms} is 1.4244 µT.

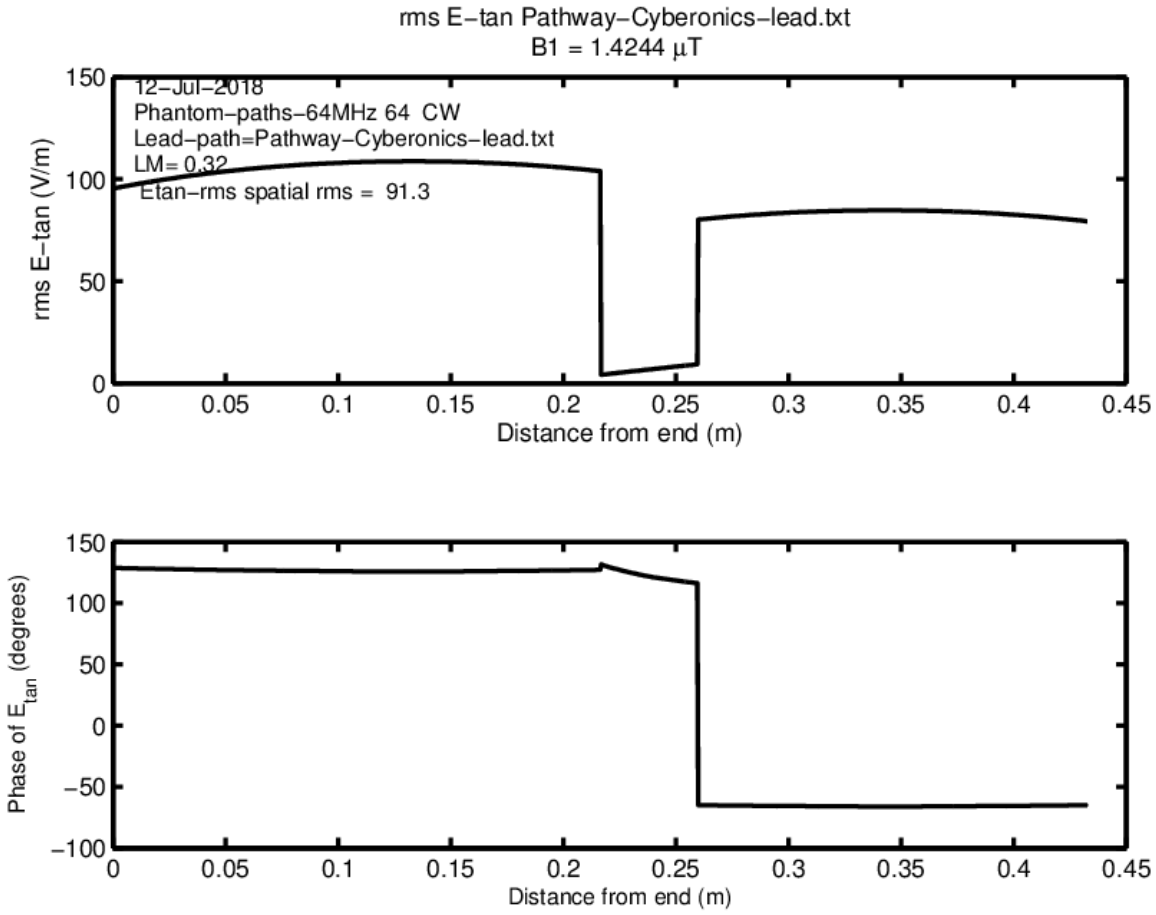

Figure 7.18 Magnitude and phase of trajectory for background tangential electric field E_{tan} over the length of the lead. The phase of background tangential electric field E_{tan} differs by about 180° between the different branches of the lead. The background tangential electric field is plot in the ASTM phantom using the B_1 field from the RF coil. The magnitude of B_{1rms} is 1.4244 μT.

Table 7.1 lists temperature rises for the Cyberonics lead with and without shielding for different termination conditions at 64 MHz. Calculated rises are based on measured transfer function as presented in section 7.2.1 and equation 5.1 The same scaling factor is used for all of the transfer function measurements. For the lead with a small generator, the presence of the shield reduces the measured temperature rise by 35.3% and the calculated temperature rise by 43.1%.

Table 7.1. Measured and calculated temperature rises for Cyberonics lead with and without the shield. Dimensions of the generator are shown in Table 7.2

Test Run	Configuration	Meas. ΔT (°C)	Calc. ΔT (°C)	Diff. ΔT Meas. vs. calc (°C)
06jul18C	No shield with a cap at the end	10.1	16.3	-6.2
06jul18D	Shield with a cap at the end	7.38	11.2	-3.8
06jul18H	No shield with model 103 Gen	35.6	30.5	5.1
06jul18I	No shield with model 103 Gen	33.4	30.3	3.1
06jul18P (repeated)	Shield with a cap at the end	7.38	11.5	-4.1
06jul18F	Shield with model 102 Gen	19	19.1	-0.1
06jul18G	Shield with model 103 Gen	17.8	19.6	-1.8

7.4 Discussion and Summary

Figure 7.3 shows the measured transfer function magnitude and phase for the Cyberonics lead at 64 MHz and 128 MHz. Figure 7.4 shows the measured transfer function magnitude and phase for the shielded Cyberonics lead at 64 MHz and 128 MHz. Transfer function magnitude decrease in the presence of shield. As a result, temperature rises for the case of shielded Cyberonics lead is less as shown in Table 7.1.

Figure 7.10-Figure 7.15 shows cyberonics lead with a generator attached at the end. Two model generators of different size Model 102 and model 103 is used in this experiment [102]. It is shown that there is the insignificant difference in the magnitude and phase of transfer function when the size of the generator is changed. Thus, the size of the generator has no impact on the temperature rise of the electrode.

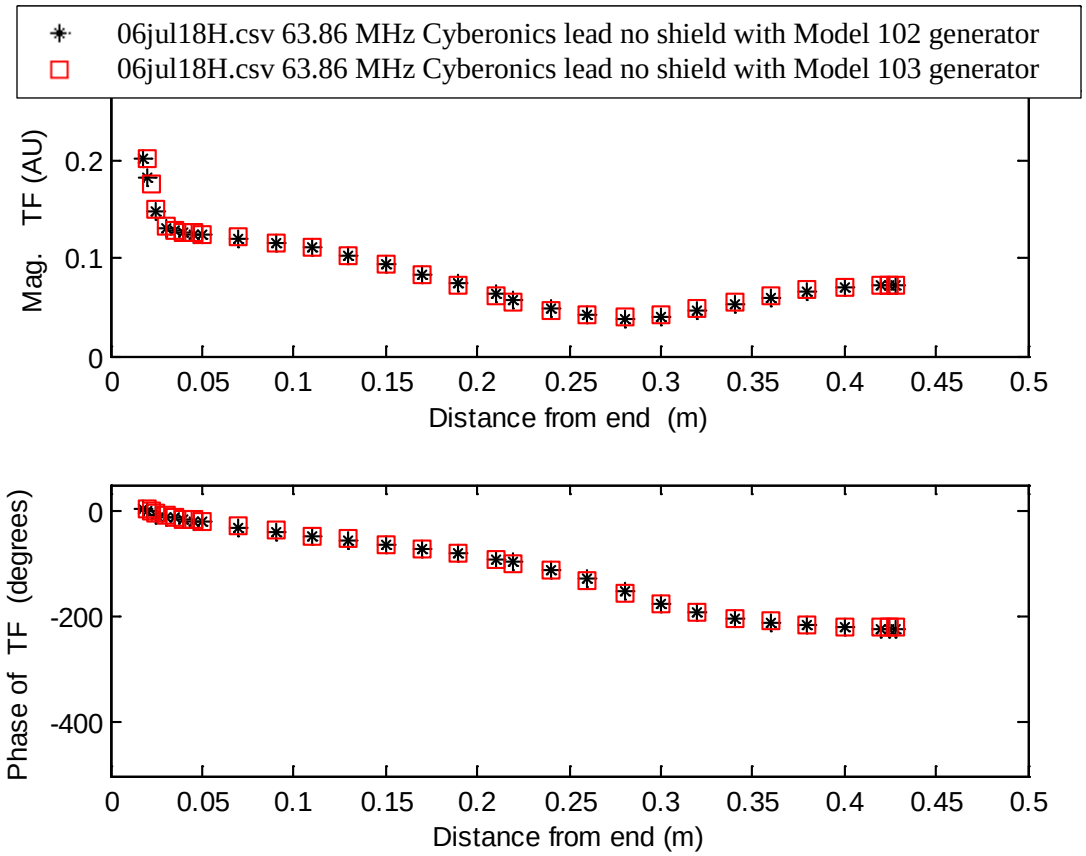

Figure 7.19 Comparison of the measured electric field transfer function for unshielded Cyberonics lead with a generator. Model 103 generator (small) and model 102 generator (big) is attached at the end. The magnitude of transfer function along the lead is same and is independent of the generator size attached at the end. The generator provides a path of low impedance to the flow of current. The impedance at the proximal end of the lead is zero (due to the attached generator), hence the current is non-zero. As a result, the magnitude of the transfer function is non-zero at the end. Dimensions of model 102 and model 103 generator is shown in Table 7.2

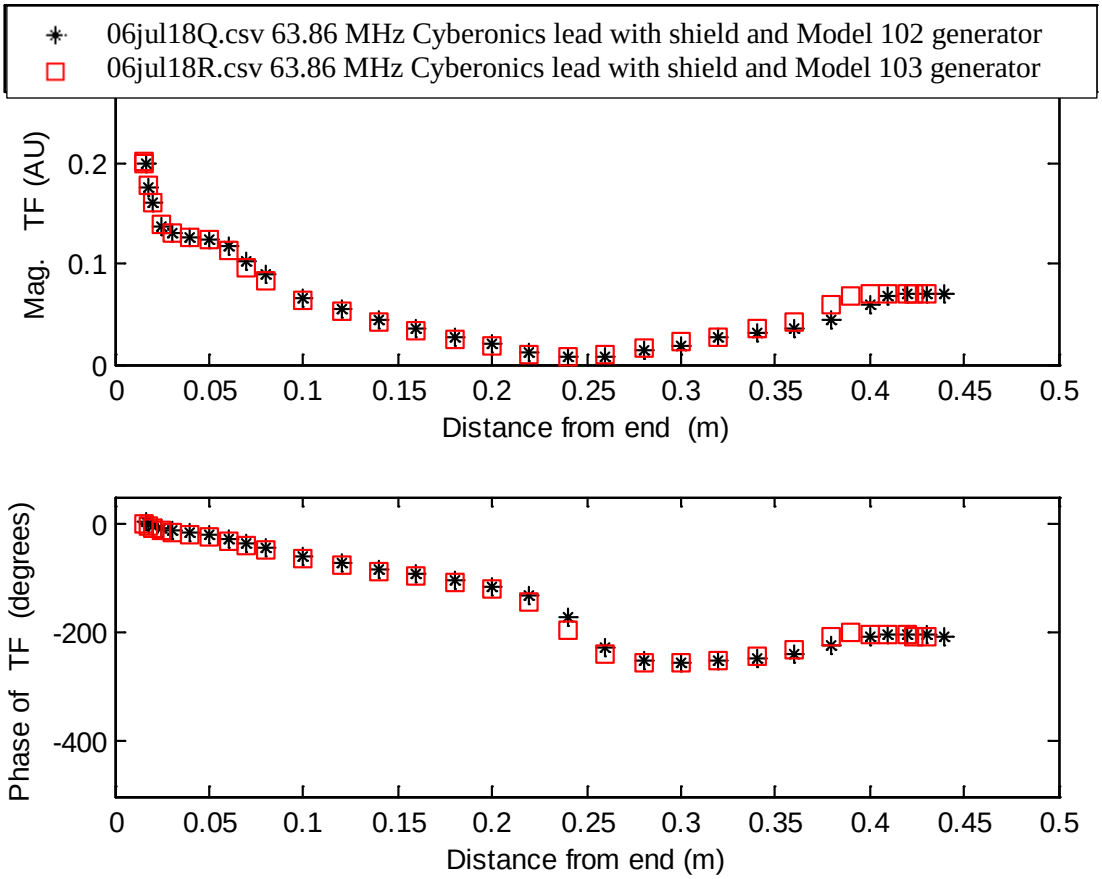

Figure 7.20 Comparison of the measured electric field transfer function for shielded Cyberonics lead with different generator size. Model 103 generator (small) and model 102 generator (big) is attached at the end. The magnitude of transfer function along the lead is same and is independent of the generator size attached at the end. The generator provides a path of low impedance to the flow of current. The impedance at the proximal end of the lead is zero (due to the attached generator), hence the current is non-zero. As a result, the magnitude of the transfer function is non-zero at the end. Dimensions of model 102 and model 103 generator is shown in Table 7.2

Table 7.2 Comparison of VNS Therapy Generators

Generator Model	**102**	**103**
Lead Compatibility	Single Pin	Single Pin
Thickness	7 mm	7 mm
Volume	14 cc	8 cc
Weight	25 g	16 g

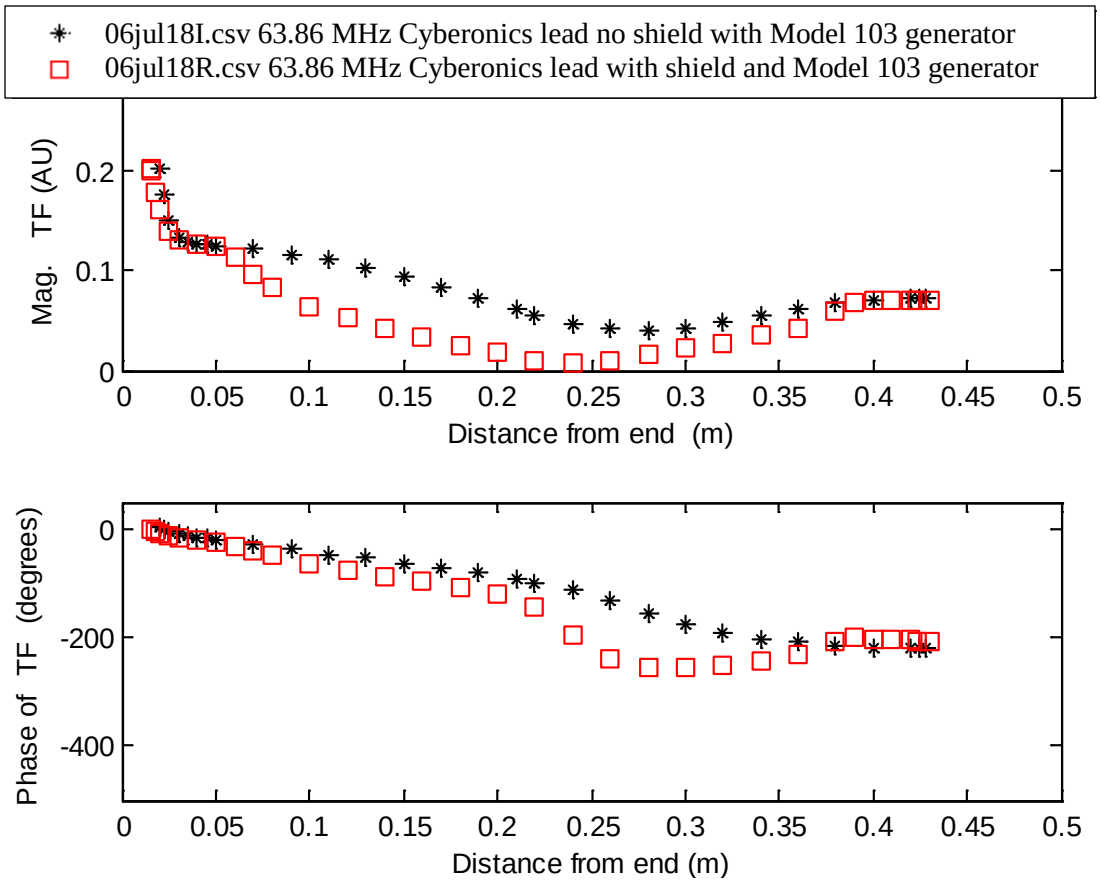

Figure 7.21 Comparison of the measured electric field transfer function for shielded-unshielded Cyberonics lead with model 103 generator at the end. The magnitude of transfer function along the Cyberonics lead is less for the shielded configuration as compared to the unshielded configuration. Also, the generator provides a path of low impedance to the flow of current. The impedance at the proximal end of the lead is zero (due to the attached generator), hence the current is non-zero. As a result, the magnitude of the transfer function is non-zero at the end.

At 64 MHz, minimum heating takes place for the case of the shielded lead with the capped end. This is evident from Figure 7.4 where transfer function is minimum. The temperature rise, in this case, is 7.38^{o}C . Table 7.1 compares measured and calculated temperature values. Temperature values are calculated from measured transfer function values. It can be concluded that at 128 MHz, minimum heating will take place in the case of the shielded lead with the generator.

8. SUMMARY OF KEY ACCOMPLISHMENTS AND RECOMMENDATIONS FOR FUTURE WORK

8.1 Conclusions and Key accomplishments from this work

A) The temperature profile for model leads with different lengths, different shield coverage and different terminations conditions at the proximal end of the model lead.

In chapter 4, we present a comprehensive simulation temperature profile of model leads at 64 MHz and 128 MHz. Figure 4.11 and Figure 4.12 summarizes key computational results at 64 MHz and 128 MHz. Temperature rise vs. length of the model lead is calculated for leads with and without shielding and with open and short terminations. The temperature rise tends to increase with increasing length. Greatest temperature rise occurs for the unshielded leads.

B) A physical model for how a conducted shield can reduce heating at the electrode of the lead wire of an implant.

In chapter 6, we present a physical model of the shielded lead with the generator.

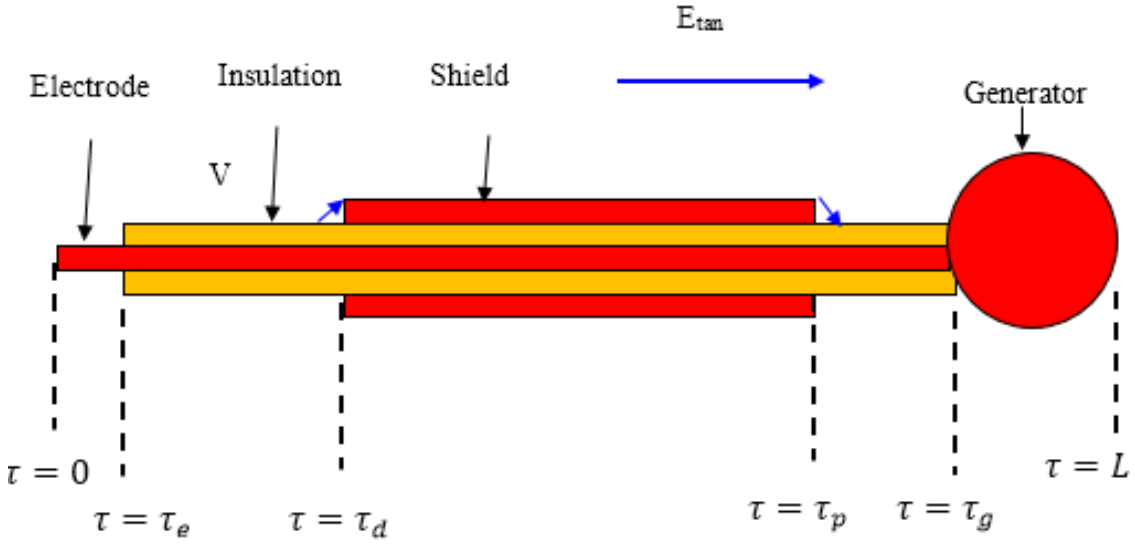

Figure 6.1 Physical Model of Shielded Lead with the generator.

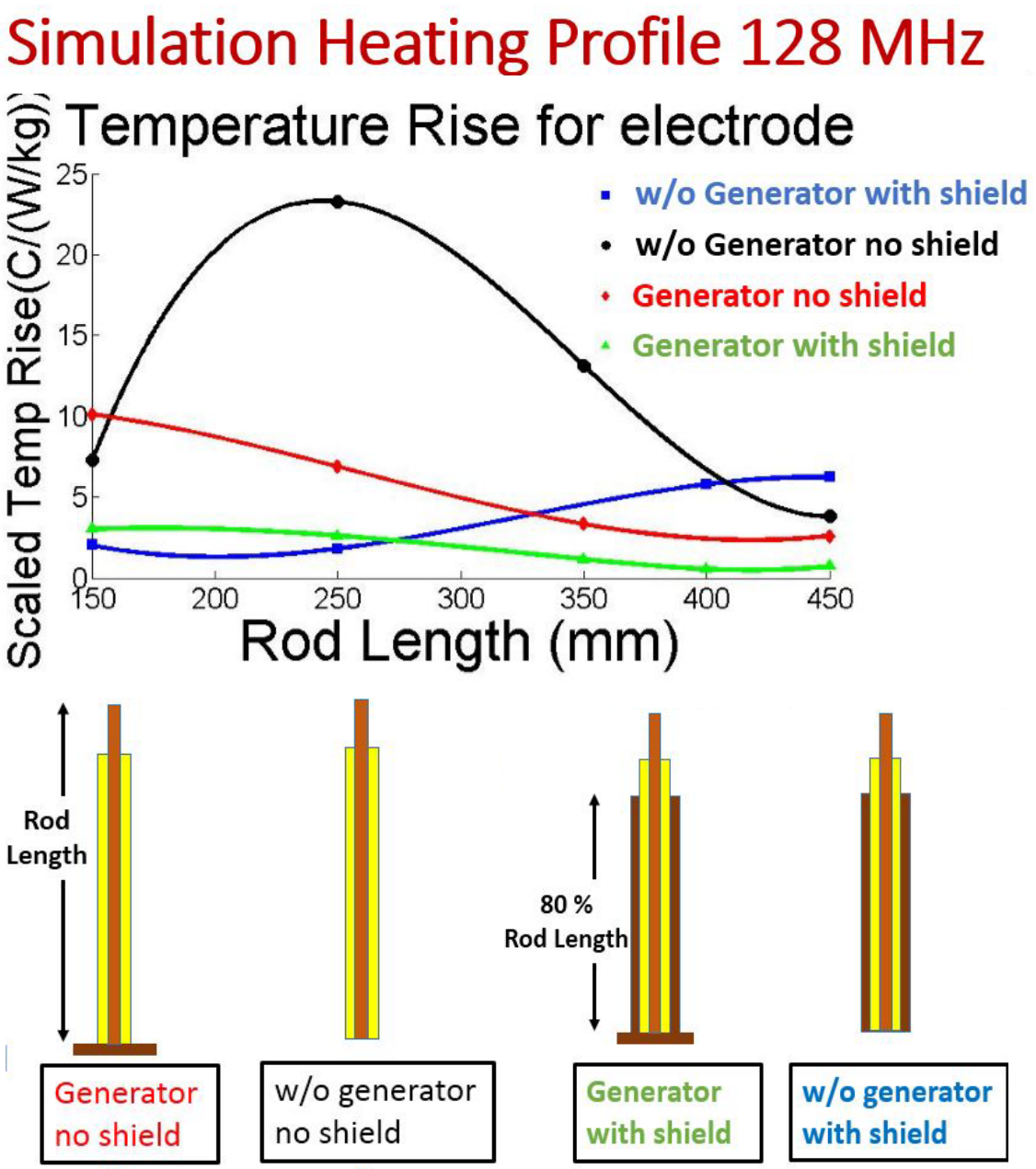

Figure 4.11 Simulation heating profile for all model implants at 128 MHz. Length of the shield is 80% of rod length. For a case of the electrode of length 40 cm (quarter wavelength at 128 MHz), the temperature rise is minimum in the presence of shield and generator (short) and is 0.2°C. Local background SAR along the length of the lead is 1 W/kg. Maximum temperature rises occur for unshielded model lead without a generator. The maximum temperature rise for open, shielded lead is 6°C and for short shielded lead is less than 4°C. The significant temperature rises are due to the lead being quarter-wave in length. For the shorted able, the input impedance at the electrode end is essentially open-circuit, resulting in minimal temperature rise whereas the cable with open end has a short-circuit input resulting in large temperature rise. The temperature rise is consistently less than 4°C throughout the length.

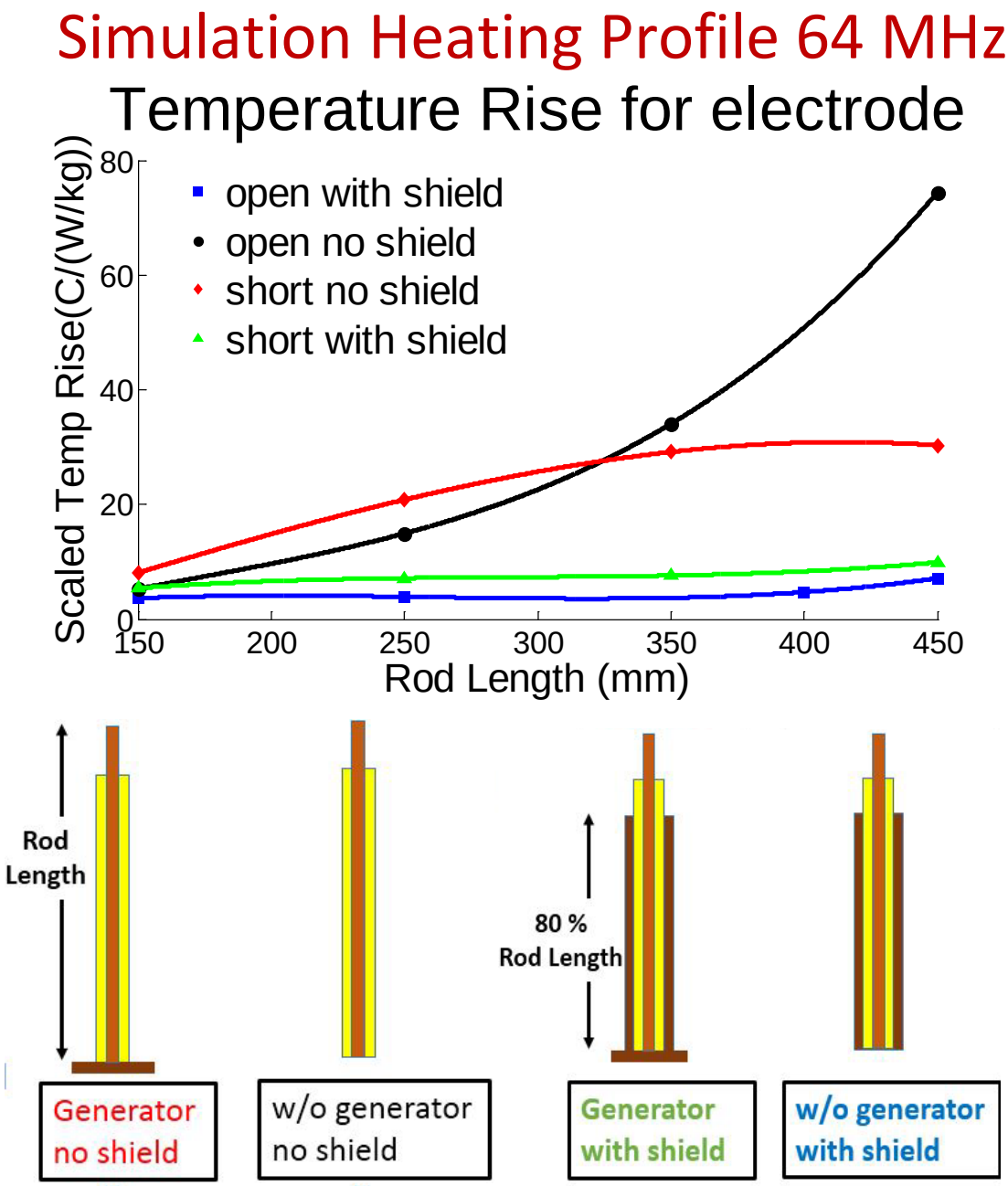

Figure 4.12 Simulation heating profile for all model implants at 64 MHz. Lowest rises occur for the shielded leads with a generator. Length of the shield is 80% of rod length. The temperature rise is minimum in the presence of shield for open configuration and is around 10^{o}C. Local background SAR along the length of the lead is 1 W/kg. The maximum temperature rise for open unshielded lead is 65^{o}C and for short unshielded lead is 35.8^{o}C. The temperature rise is consistently less than 10 ^{o}C for open lead without the shield.

Blue arrows in Figure 6.1 indicate the background tangential electric field E_{tan}. The background electric field will induce currents and electric charge on the shield. These will produce a scattered electric field E_s at the edges of the shield. The tangential component of the scattered field will induce currents on the central conductor. These currents will propagate on the center conductor. The current that is transmitted from the electrode will induce power in the surrounding tissue.

The shield thus results in the minimal tangential electric field on the conductor underneath it. However, the shield also redirects the incident tangential electric field resulting in a scattered electric field E_{tan} that produces a tangential electric field at the edges of that shield that is incident on the center. Equations 6.1-6.13 present a model for the calculation of the transfer function for the shielded lead.

Assume that we start with a given lead for which we wish to reduce the RF heating by addition of the shield. The design variables are straightforward:

(a) Value of distal location of the shield τ_d .

(b) Value of the proximal location of the shield τ_p .

A dramatic example for validation of the shield model is the case of an 80-cm long model lead in the form of an 80-cm long section of RG 316 coaxial cable. This length of the model implant has an electrical length of a quarter wavelength at 64 MHz. Figure 5.25 shows the measured electric field transfer function for the model lead with the end in open or short configuration.

For the cable shorted at the end, the input impedance looking into the section of the transmission line at the distal edge of the shield approaches infinity. The transfer function at the distal end of the shield is minimal. The scattered electric field from the edge of the shield induces minimum current into the center conductor, and the magnitude of the overall transfer function is small.

For the cable open at the end, the input impedance looking into the transmission line at the distal edge of the shield approaches zero. The transfer function at the distal end

of the shield is then large. The scattered electric field from the edge of the shield induces significant current into the center conductor, and the magnitude of the overall transfer function is substantial.

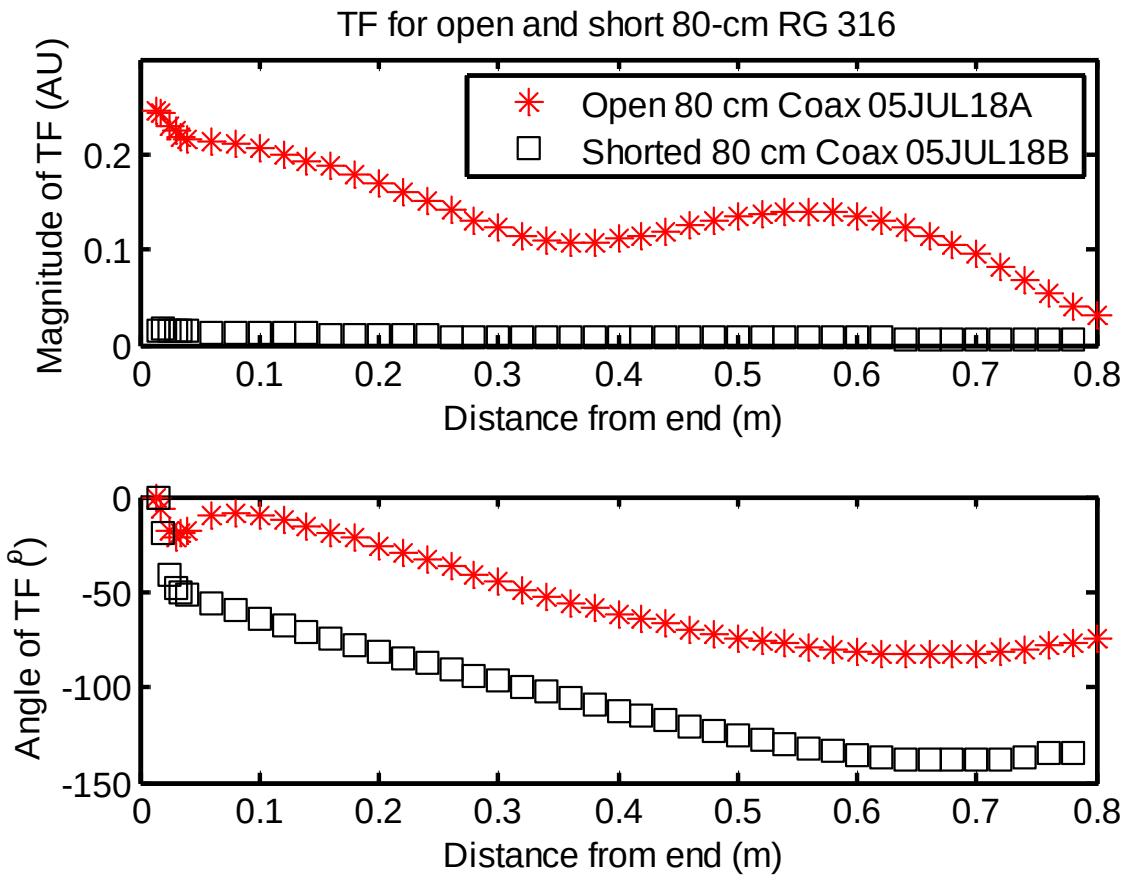

Figure 5.25 Comparison of the measured electric field transfer function for the 80 cm RG 316 shielded model lead in open and short configurations. Impedance for short configuration at the proximal end is zero. As a result, current is non-zero. Hence, the transfer function is non-zero at the end. Impedance for open configuration at the proximal end is infinite. As a result, the current is zero. Hence, the transfer function is zero at the end. Also, the magnitude of transfer function along the shield is less for the shorted lead as compared to open lead, as a consequence of this sample lead having a length equal to the quarter wave-length. These parameters will be different for actual leads in practice since the actual lead, in general, will have a length different from a quarter wavelength.

The relative magnitudes of the transfer functions for open and shorted TG 316 model lead are manifested in the temperature rises in a heating test performed according to ASTM F2182-11a. Figure 4.10 shows the measured temperature rises vs. time. As

predicted by the relative magnitudes of the electric field transfer functions, the temperature rise is much greater for the open model lead. Measured temperature rise and transfer function depended on terminations conditions, with the open lead exhibiting a temperature rise 16 times greater than the shorted lead as evident from the measurements and validated by calculations from the physical model.

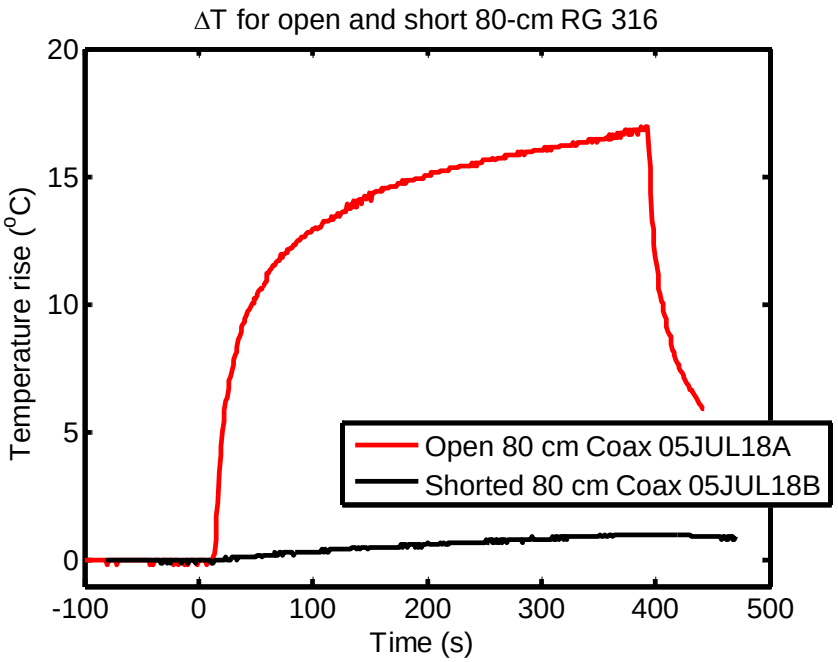

Figure 4.10 Measured scaled temperature rise vs. time for open and short conditions for 80 cm shielded lead electrode at 64MHz. Length of the shield is 77 cm. The maximum temperature rise for open, shielded lead is 16.35°C and for short shielded lead is 1.01°C. The significant temperature rises are due to the lead being quarter-wave in length. For the shorted able, the input impedance at the electrode end is essentially open-circuit, resulting in minimal temperature rise whereas the cable with open end has a short-circuit input resulting in large temperature rise.

Table 5.2 Comparison of measured and calculated temperature rises for open and shorted 80-cm RG 316 model implant. The calculated temperature rises are with the transfer functions of Figure 5.25. The transfer function is scaled so that the measured and calculated rises for the open lead are the same. The same scaling factor is used for both measured temperature functions.

Configuration of 80 cm Shielded RG 316	**Measured max ΔT (°C)**	**Calculated max ΔT (°C)**
Open	16.35	16.94
Short	1.018	1.11

C) Transmission line model for prediction of the transfer function and lead heating for different geometries.

The transmission line parameters for model leads were derived from the calculation and transfer function measurement. The transfer function model is derived from Figure 6.1 Figure 6.7 shows a measured and calculated transfer function for a shielded lead. For a practical lead, transmission line characteristics can be derived from measurement.

To quantitatively test the model, temperature rise for shielded and unshielded model leads have been calculated with the FDTD method, and measurements corresponding to the calculations were made in an ASTM rectangular phantom. Measured magnitude and phase of the transfer function at 64 MHz and 128 MHz for shielded leads in different configurations have been presented. Temperature rises were calculated for different lengths of shielded and unshielded leads. Confirming measurements were made for a quarter-wavelength coaxial cable model of the lead. The physical model of the lead was validated by comparing the calculated transfer functions values to measured values. There is a good agreement between measured values and calculated values. Thereby validating our physical model.The transmission line model can then be used to explore the impact of shield position and length on an active lead wire. Evaluating shield performance for reduction of RF heating will be determined much quickly with the transmission line model rather than with physical measurements. However, physical tests are recommended on selected leads to confirm the accuracy of the transmission line calculations.

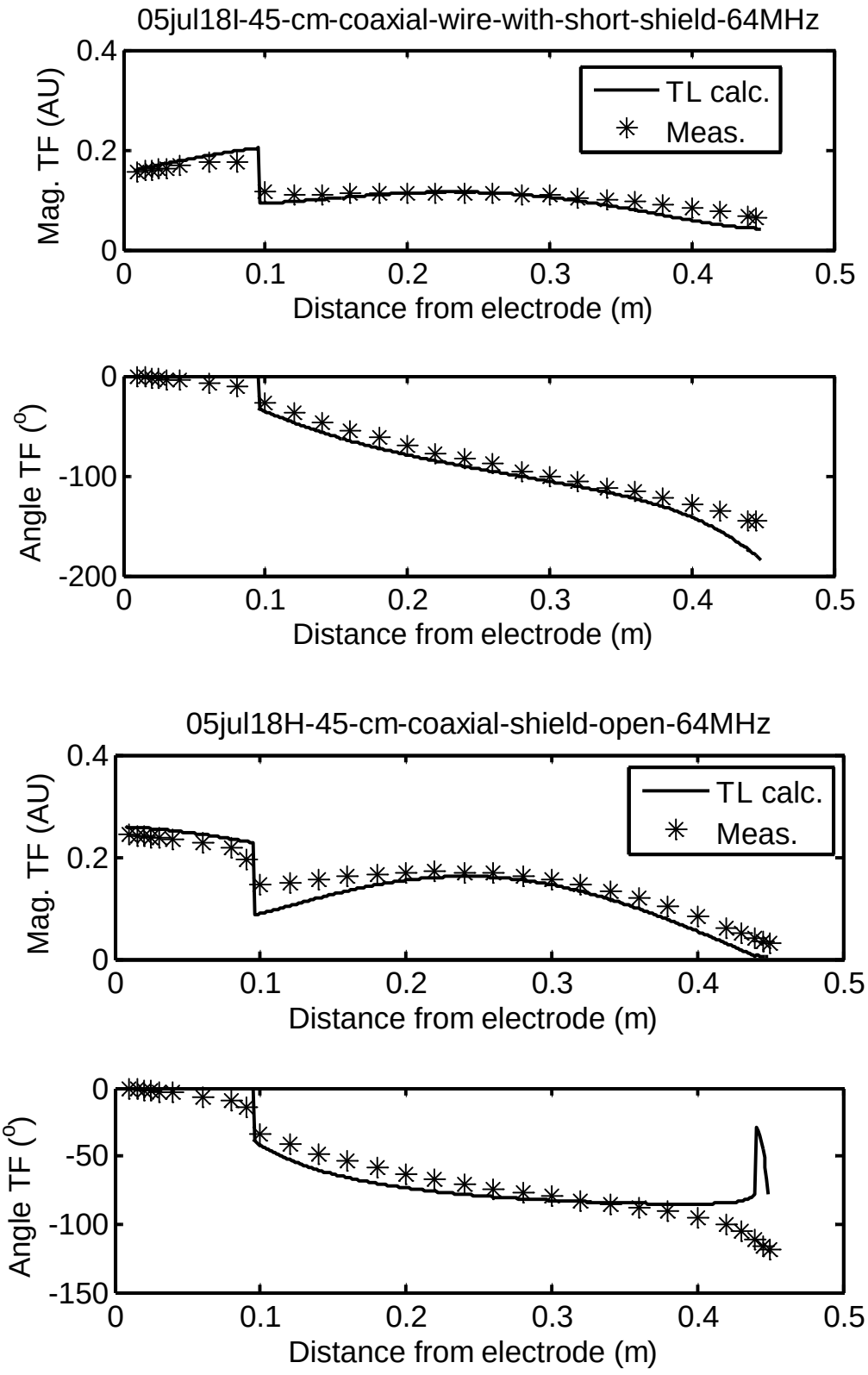

Figure 6.7. Transfer functions for 45-cm cable. The top is for the shorted proximal end, and the bottom is for the open proximal end.

D) Case study on the impact of the shield on RF heating at the electrode of a commercial neuro stimulator.

In-vivo temperature rises are presented for the Vagus Nerve Stimulation, VNS Therapy, NeuroCybernetic Prosthesis (NCP) System (Livanova Inc (formerly Cyberonics), Houston, TX). The author makes no recommendation on the MRI safe compatibility of the implant. The first and second test structure was the Cyberonics 302 lead with two different generators in size Model 102 and Model 103. The third test structure was the same lead with the generator replaced by an insulating cap. The electric field transfer function and RF-induced temperature rise were measured at 64 MHz. The temperature rise was also calculated based on the measured electric field transfer function. Figure 8.1 shows the plot of calculated vs. measured rise. The agreement between calculation and measurement is relatively good, validating that the transfer function is an effective predictor of RF-induced temperature rise. The addition of a conducting shield to the Cyberonics lead results in about a one-third reduction in the maximum temperature rise.

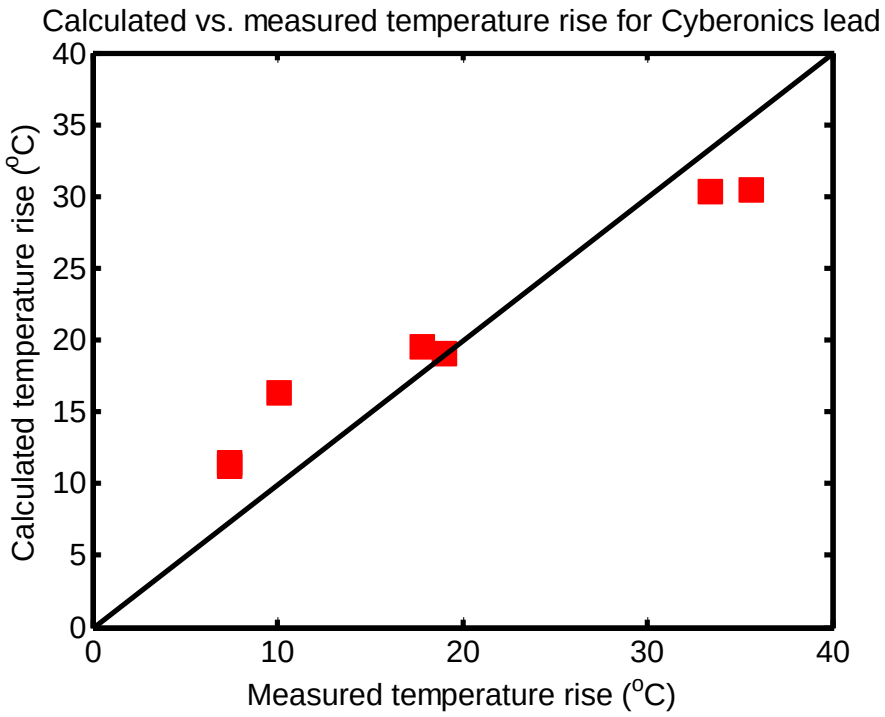

Figure 8.1 Measured vs. calculated temperature rises for Cyberonics shielded and unshielded lead with two generators and a cap at the proximal end. Data points are from Table 7.1. Calculated temperature rises are based on the transfer function and E_{tan} from Figure 7.17 along the path of the lead.

A more comprehensive assessment of in-vivo temperature rise in the case of Model 303 lead will include. Nevertheless, the measurements and calculations demonstrate that the temperature rise at the electrode of VNS System depends greatly on the terminations conditions of the generator and shielding presence.

8.2 Future Work

The primary thrust of this work has been in the analysis of metallic shielding for reduction of RF-induced heating of electrodes during MRI for active implants. However, based on the limitations observed in the current efforts, as well as some interesting questions and findings that arose through the course of this work, some potential next steps have been identified.

A practical implementation of a shielded lead requires optimizing multiple requirements of biocompatibility, shield reliability, and producing a lead that is not too mechanically stiff. This is a task for manufacturers of the lead wires. Medtronic, as an example, has dealt with the various design factors and is now marketing SureScan leads.

Another practical issue is that the wavelength for 3T MRI (128 MHz) will be about half of the wavelength for 1.5T MRI (64 MHz). Thus, it is possible that a shielded lead with minimal RF heating at 1.5 will have significant RF heating at 3T. The converse could also apply.

The FDTD computations performed for this work is three-dimensional. Given the long length to diameter ratio for the model leads, significant memory and computer time were required to perform the calculations. Given that the cylindrical symmetry of the structures, the computations could have been performed more efficiently with a 2-D FDTD program with cylindrical symmetry. With a 2-D FDTD program, a wider variety of idealized leads, including longer length, could be modeled. Secondly, with a 2-D FDTD program, it would be possible to mesh fine dimensions of model lead for, e.g., we can mesh electrodes of Cyberonics lead more accurately using a 2-D FDTD program.

The relevant parameter for heating is the actual temperature rise in the patient during MRI. This approach is defined in Nyenhuis [94]. For the shielded model leads, the next plan of work could be

(a) Define a trajectory of the lead in the human model.
(b) Calculate the electric field distribution in the patient during MRI in a human model such as Hugo [94] along that trajectory.
(c) Use equation 6.1 to determine the in-vivo temperature rise during MRI.

An important factor in the temperature rise of the shielded lead is the magnitude of the transfer function, calculated for shielded lead models assuming there is no coupling between background tangential electric field and the shield. To minimize temperature rise and RF heating due to MRI, the edges of the shield are placed at locations where the magnitude of this transfer function of the inner conductor is minimal. This is demonstrated by the equations 6.1-6.13 in chapter 6. The transfer function at the edges of the shield will then depend on the length of the shield present and termination conditions. In other words, a general guideline to design shielded leads to reduce RF-induced heating involves placing the edges of the shield at locations where the magnitude of the transfer function of the inner conductor is minimal. The physical model of the shielded lead (as described in chapter 6) provides the design methodology for the same.

The temperature rise at the electrodes of an implanted neurostimulator during MRI scans must be less than the threshold of approximately $6^{o}C$ to prevent tissue damage [103]. Shielded leads are presented as a method to reduce RF-heating responsible for temperature rise at the electrodes. This work provided a qualitative and quantitative understanding of how a conducting metallic shield over a lead will reduce RF heating at the electrode during MRI scans. A physical model and equations for reduction of RF heating by a shielded lead have been presented. The information provided by this work is expected to facilitate the development of lead wires with reduced RF-induced heating. The availability of lead wires with reduced heating will allow expanded access to MRI by patients.

REFERENCES

[1] IMV. MR Market Outlook Report. [Accessed]

[2] WiseGuy. Global MRI Market Research Report. [Accessed]

[3] M. Desai, L. Hargens, M. Breitenfeldt, A. Doth, M. Ryan, C. Gunnarsson, and S. Yair, "The Rate of Magnetic Resonance Imaging in Patients With Spinal Cord Stimulation," Spine, vol. 40, no. 9, pp. E531-E537, 01/20/2015 2015.

[4] Scanning patients with MR Conditional implants. Available: https://www.usa.philips.com/healthcare/education-resources/publications/fieldstrength/mri-and-mr-conditional-implants. [Accessed: July 16, 2018]

[5] R. M. Levy, "MRI-compatible neuromodulation devices: critical necessity or desirable adjunct?," Neuromodulation, vol. 17, no. 7, pp. 619-26, Oct 2014.

[6] MRI-friendly defibrillator implant opens doors for thousands of cardiac patients currently denied MRIs. Available: https://medicalxpress.com/news/2013-01-mri-friendly-defibrillator-implant-doors-thousands.html. [Accessed: July 16, 2018]

[7] R. C. Semelka, D. M. Armao, J. Elias, Jr., and W. Huda, "Imaging strategies to reduce the risk of radiation in CT studies, including selective substitution with MRI," (in eng), J Magn Reson Imaging, vol. 25, no. 5, pp. 900-9, May 2007.

[8] A. B. d. Gonzalez, M. Mahesh, K. Kim, M. Bhargavan, R. Lewis, F. Mettler, and C. Land, "Projected cancer risks from computed tomographic scans performed in the United States in 2007," Arch Intern Med, vol. 169, no. 22, pp. 2071-7, 2009.

[9] J. A. Nyenhuis, P. Sung-Min, R. Kamondetdacha, A. Amjad, F. G. Shellock, and A. R. Rezai, "MRI and implanted medical devices: basic interactions with an emphasis on heating," IEEE Transactions on Device and Materials Reliability, vol. 5, no. 3, pp. 467-480, 2005.

[10] S. A. Mohsin, J. A. Nyenhuis, and R. Masood, "Interaction of medical implants with the MRI electromagnetic fields," Progress In Electromag Research C, pp. 195-202, 2010.

[11] D. Formica and S. Silvestri, "Biological effects of exposure to magnetic resonance imaging: an overview," Biomed Eng Online, vol. 3, p. 11, Apr 22 2004.

[12] E. T. Martin, J. A. Coman, F. G. Shellock, C. C. Pulling, R. Fair, and K. Jenkins, "Magnetic resonance imaging and cardiac pacemaker safety at 1.5-Tesla," J Am Coll Cardiol, vol. 43, no. 7, pp. 1315-24, Apr 7 2004.

[13] A. K. Silva, E. L. Silva, E. S. Egito, and A. S. Carrico, "Safety concerns related to magnetic field exposure," Radiat Environ Biophys, vol. 45, no. 4, pp. 245-52, Nov 2006.

[14] F. G. Shellock and J. V. Crues, "MR procedures: biologic effects, safety, and patient care," Radiology, vol. 232, no. 3, pp. 635-52, Sep 2004.

[15] Y. Liu, J. Chen, F. G. Shellock, and W. Kainz, "Computational and experimental studies of an orthopedic implant: MRI-related heating at 1.5-T/64-MHz and 3-T/128-MHz," J Magn Reson Imaging, vol. 37, no. 2, pp. 491-7, Feb 2013.

[16] Y. Liu, W. Kainz, S. Qian, W. Wu, and J. Chen, "Effect of insulating layer material on RF-induced heating for external fixation system in 1.5 T MRI system," Electromagn Biol Med, vol. 33, no. 3, pp. 223-7, Sep 2014.

[17] Y. Liu, J. Shen, W. Kainz, S. Qian, W. Wu, and J. Chen, "Numerical investigations of MRI RF field induced heating for external fixation devices," Biomed Eng Online, vol. 12, p. 12, Feb 9 2013.

[18] Y. Liu, J. Shen, W. Kainz, S. Qian, W. Wu, and J. Chen, "Computational study of external fixation devices surface heating in MRI RF environment," presented at the IEEE Symposium on Electromagnetic Compatibility, Pittsburg, 2012.

[19] X. Huang, J. Zheng, X. Wu, M. Kono, H. Hozono, W. Kainz, F. Yang, and J. Chen, "MRI Heating Reduction for External Fixation Devices Using Absorption Material," IEEE Transactions on Electromagnetic Compatibility, vol. 57, no. 4, pp. 635-642, 2015.

[20] X. Huang, "Reduction of MRI RF Coil Induced Heating for External Fixation Devices," Ph.D. dissertation, ECE, University of Houston, 2016.

[21] J. Chen, "Use of absorption material to reduce radio frequency-induced heating in external fixation devices," United States Patent 20160228151, 2016.

[22] S. McCabe and J. Scott, "Technique to assess the compatibility of medical implants to the RF field in MRI," in 2015 Asia-Pacific Microwave Conference (APMC), 2015, vol. 2, pp. 1-3.

[23] S. McCabe and J. Scott, "A Novel Implant Electrode Design Safe in the RF Field of MRI Scanners," IEEE Transactions on Microwave Theory and Techniques, vol. 65, no. 9, pp. 3541-3547, 2017.

[24] S. McCabe, J. Scott, and S. Butler, "Electromagnetic techniques to minimize the risk of hazardous local heating around medical implant electrodes during MRI scanning," in 2015 European Microwave Conference (EuMC), 2015, pp. 702-705.

[25] S. O. McCabe and J. B. Scott, "New MRI-safe implant electrode design," in 2016 IEEE MTT-S International Microwave Symposium (IMS), 2016, pp. 1-3.

[26] S. O. McCabe and J. B. Scott, "Cause and Amelioration of MRI-Induced Heating Through Medical Implant Lead Wires," presented at the 21st Electronics New Zealand Conference (ENZCon), Hamilton, New Zealand, 2014.

[27] S. O. McCabe and J. B. Scott, "Implant Conductor assembly with improved Radio Frequency properties," World Patent 2017086805, 2017.

[28] S. O. McCabe and J. B. Scott, "A surgical implant conductor with increased radio frequency alternating current resistance," United States Patent 20180147405, 2018.

[29] S. McCabe, "MRI-safe Implantable Electrode Leads," PhD PhD Thesis, ECE, The University of Waikato, 2016.

[30] J. L. Helfer, R. W. Gray, S. G. MacDonald, and T. W. Bibens, "Can pacemakers, neurostimulators, leads, or guide wires be MRI safe? Technological concerns and possible resolutions," Minim Invasive Ther Allied Technol, vol. 15, no. 2, pp. 114-20, 2006.

[31] J. L. Helfer and X. Wang, "Magnetically shielded conductor," United States Patent 6930242, 2005.

[32] X. Wang, H. J. Greenwald, J. L. Helfer, R. W. Gray, and M. L. Weiner, "Magnetic resonance imaging coated assembly," United States Patent 6765144, 2004.

[33] X. Wang, H. J. Greenwald, J. L. Helfer, R. W. Gray, and M. L. Weiner, "Magnetic resonance imaging coated assembly," United States Patent 7473843, 2009.

[34] X. Wang, H. J. Greenwald, J. L. Helfer, R. W. Gray, and M. L. Weiner, "Magnetic resonance imaging coated assembly," United States Patent 20060118319, 2006.

[35] X. Wang, H. J. Greenwald, R. E. Miller, J. L. Helfer, and R. Gray, "Magnetically shielded assembly," United States Patent 7162302, 2007.

[36] X. Wang, "Nanomagnetic shielding assembly," United States Patent 6906256, 2005.

[37] X. Wang and H. J. Greenwald, "Nanomagnetically shielded substrate," United States Patent 6864418, 2005.

[38] X. Wang and H. J. Greenwald, "Nanomagnetically shielded substrate," United States Patent 20040256131, 2004.

[39] M. E. Ladd and H. H. Quick, "Reduction of resonant RF heating in intravascular catheters using coaxial chokes," (in eng), Magn Reson Med, vol. 43, no. 4, pp. 615-9, Apr 2000.

[40] P. A. Bottomley, P. V. Karmarkar, J. M. Allen, and W. A. Edelstein, "Methods and apparatus for fabricating leads with conductors and related flexible lead configurations," United States Patent 20080262584, 2008.

[41] P. A. Bottomley, P. V. Karmarkar, J. M. Allen, W. A. Edelstein, P. Piferi, and B. Gore, "Methods and apparatus for fabricating leads with conductors and related flexible lead configurations," United States Patent 20160220812, 2016.

[42] E. Atalar, J. Allen, P. Bottomley, W. Edelstein, and P. V. Kamarkar, "MRI-safe high impedance lead systems," United States Patent 20130245741, 2013.

[43] E. Atalar, J. Allen, P. Bottomley, W. Edelstein, and P. V. Kamarkar, "MRI-safe high impedance lead systems," United States Patent 8688226, 2014.

[44] P. A. Bottomley, P. V. Karmarkar, J. M. Allen, and W. A. Edelstein, "MRI and RF compatible leads and related methods of operating and fabricating leads," United States Patent 20080243218, 2008.

[45] P. A. Bottomley, A. Kumar, W. A. Edelstein, J. M. Allen, and P. V. Karmarkar, "Designing passive MRI-safe implantable conducting leads with electrodes," Med Phys, vol. 37, no. 7, pp. 3828-43, Jul 2010.

[46] P. A. Bottomley, W. A. Edelstein, A. Kumar, J. M. Allen, and P. V. Karmarkar, "Towards MRI-safe implanted leads: a comparative evaluation of four designs," in ISMRM, Stockholm, 2010.

[47] P. A. Bottomley, W. A. Edelstein, A. Kumar, J. M. Allen, and P. V. Karmarkar, "Resistance and Inductance Based MRI-Safe Implantable Lead Strategies," in ISMRM, Hawaii, 2009.

[48] C. D. Wahlstrand, T. B. Hoegh, G. A. Hrdlicka, T. E. Cross Jr., and J. M. Olsen, "Lead electrode for use in an MRI-safe implantable medical device," United States Patent 7174219, 2007.

[49] C. D. Wahlstrand, R. M. Skime, G. A. Hrdlicka, J. M. Olsen, and S. L. Bolea, "MRI-Safe Implantable Medical Device," United States Patent 20110071605, 2011.

[50] C. D. Wahlstrand, T. B. Hoegh, J. M. Olsen, S. L. Bolea, and G. A. Hrdlicka, "Lead electrode for use in an mri-safe implantable medical device," United States Patent 20120010689, 2012.

[51] C. D. Wahlstrand, G. A. Hrdlicka, R. M. Skime, P. Przybyszewski, and T. E. Cross Jr., "Energy shunt for producing an MRI-safe implantable medical device," United States Patent 20050070972, 2005.

[52] C. D. Wahlstrand, G. A. Hrdlicka, T. E. Cross Jr., T. B. Hoegh, J. M. Olsen, and S. L. Bolea, "MRI-safe implantable lead," United States Patent 8676340, 2014.

[53] P. Serano, L. M. Angelone, H. A. Katnani, E. N. Eskandar, and G. Bonmassar, "A Novel Brain Stimulation Technology Provides Compatibility with MRI," in Scientific reports, 2015.

[54] C. K. Chou and A. W. Guy, "Carbon-loaded Teflon electrodes for chronic EEG recordings in microwave research," J Microw Power, vol. 14, no. 4, pp. 399-404, Dec 1979.

[55] G. Bonmassar, "Resistive tapered stripline (RTS) in electroencephalogram recordings during MRI," IEEE Transactions on Microwave Theory and Techniques, vol. 52, no. 8, pp. 1992-1998, 2004.

[56] G. Bonmassar, N. Hadjikhani, J. R. Ives, D. Hinton, and J. W. Belliveau, "Influence of EEG electrodes on the BOLD fMRI signal," Hum Brain Mapp, vol. 14, no. 2, pp. 108-15, Oct 2001.

[57] L. Lemieux, A. Salek-Haddadi, O. Josephs, P. Allen, N. Toms, C. Scott, K. Krakow, R. Turner, and D. R. Fish, "Event-related fMRI with simultaneous and continuous EEG: description of the method and initial case report," Neuroimage, vol. 14, no. 3, pp. 780-7, Sep 2001.

[58] R. I. Goldman, J. M. Stern, J. Engel, Jr., and M. S. Cohen, "Acquiring simultaneous EEG and functional MRI," Clin Neurophysiol, vol. 111, no. 11, pp. 1974-80, Nov 2000.

[59] M. M. Elwassif, A. Datta, A. Rahman, and M. Bikson, "Temperature control at DBS electrodes using a heat sink: experimentally validated FEM model of DBS lead architecture," J Neural Eng, vol. 9, no. 4, p. 046009, Aug 2012.

[60] R. W. Gray, W. T. Bibens, and F. G. Shellock, "Simple design changes to wires to substantially reduce MRI-induced heating at 1.5 T: implications for implanted leads," Magn Reson Imaging, vol. 23, no. 8, pp. 887-91, Oct 2005.

[61] C. Jiang, X. Mo, J. Ding, Y. Dong, F. Zhang, H. Hao, and L. Li, "Deep brain stimulation lead design to reduce radio-frequency heating in MRI," Electronics Letters, vol. 50, no. 25, pp. 1898-1900, 2014.

[62] B. A. Tranchina, "Method for fabricating a stimulation lead to reduce MRI heating," United States Patent US8601672B2, 2009.

[63] J. A. Nyenhuis, "RF Heating: RF and Implants," presented at the ISMRM, Toronto, 2008.

[64] J. Wang, W. Mao, M. Qiu, M. B. Smith, and R. T. Constable, "Factors influencing flip angle mapping in MRI: RF pulse shape, slice-select gradients, off-resonance excitation, and B0 inhomogeneities," Magn Reson Med, vol. 56, no. 2, pp. 463-8, Aug 2006.

[65] ASMTM 2182-11a: Standard Test Method for Measurement of Radio Frequency Induced Heating On or Near Passive Implants During Magnetic Resonance Imaging, 2011.

[66] Don’t fear pacemakers. Available: https://www.health.harvard.edu/heart-health/dont-fear-pacemakers. [Accessed: July 16, 2018]

[67] F. G. Shellock, T. O. Woods, and J. V. Crues, 3rd, "MR labeling information for implants and devices: explanation of terminology," Radiology, vol. 253, no. 1, pp. 26-30, Oct 2009.

[68] J. G. Delfino and T. O. Woods, "New Developments in Standards for MRI Safety Testing of Medical Devices," Current Radiology Reports, vol. 4, no. 6, p. 28, 2016/03/29 2016.

[69] T. Woods, "Establishing Safety and Compatibility of Passive Implants in the Magnetic Resonance (MR) Environment " U.S Department of Health and Human Services, FDA-CDRH-OSEL2014.

[70] ISO/TS 10974:2018:Assessment of the safety of magnetic resonance imaging for patients with an active implantable medical device, 2018.

[71] E. Cabot, T. Lloyd, A. Christ, W. Kainz, M. Douglas, G. Stenzel, S. Wedan, and N. Kuster, "Evaluation of the RF heating of a generic deep brain stimulator exposed in 1.5 T magnetic resonance scanners," Bioelectromagnetics, vol. 34, no. 2, pp. 104-13, Feb 2013.

[72] E. Cabot, E. Zastrow, and N. Kuster, "Safety assessment of AIMDs under MRI exposure: Tier3 vs. Tier4 evaluation of local RF-induced heating," 2014 International Symposium on Electromagnetic Compatibility, Tokyo, pp. 237-240, 2014.

[73] IEC 60601-2-33:2010+A1:2013+A2 Medical electrical equipment - Part 2-33: Particular requirements for the basic safety and essential performance of magnetic resonanceequipment for medical diagnosis, 2015.

[74] IEEE Standard for Safety Levels with Respect to Human Exposure to Radio Frequency Electromagnetic Fields, 3 kHz to 300 GHz, 2006.

[75] D. C. Gross and O. P. Simonetti, "In vivo and post-mortem measurements of radio frequency induced heating during MRI of pigs implanted with vascular stents," Journal of Cardiovascular Magnetic Resonance, vol. 18, no. 1, p. P53, 2016/01/27 2016.

[76] B. Stem, "Computer modeling and simulation of implantable medical device heating due to mri gradient coil fields," MS thesis, ECE, Purdue University, 2014.

[77] G. Calcagnini, M. Triventi, F. Censi, E. Mattei, P. Bartolini, W. Kainz, and H. I. Bassen, "In vitro investigation of pacemaker lead heating induced by magnetic resonance imaging: role of implant geometry," J Magn Reson Imaging, vol. 28, no. 4, pp. 879-86, Oct 2008.

[78] E. Mattei, G. Calcagnini, F. Censi, M. Triventi, and P. Bartolini, "Role of the lead structure in MRI-induced heating: In vitro measurements on 30 commercial pacemaker/defibrillator leads," Magn Reson Med, vol. 67, no. 4, pp. 925-35, Apr 2012.

[79] E. Mattei, G. Calcagnini, F. Censi, M. Triventi, and P. Bartolini, "Numerical model for estimating RF-induced heating on a pacemaker implant during MRI: experimental validation," IEEE Trans Biomed Eng, vol. 57, no. 8, pp. 2045-52, Aug 2010.

[80] E. Mattei, G. Calcagnini, M. Triventi, F. Censi, P. Bartolini, W. Kainz, and H. Bassen, "MRI induced heating of pacemaker leads: effect of temperature probe positioning and pacemaker placement on lead tip heating and local SAR," Conf Proc IEEE Eng Med Biol Soc, vol. 1, pp. 1889-92, 2006.

[81] E. Mattei, G. Gentili, F. Censi, M. Triventi, and G. Calcagnini, "Impact of capped and uncapped abandoned leads on the heating of an MR-conditional pacemaker implant," Magn Reson Med, vol. 73, no. 1, pp. 390-400, Jan 2015.

[82] E. Mattei, M. Triventi, G. Calcagnini, F. Censi, W. Kainz, H. I. Bassen, and P. Bartolini, "Temperature and SAR measurement errors in the evaluation of metallic linear structures heating during MRI using fluoroptic probes," Phys Med Biol, vol. 52, no. 6, pp. 1633-46, Mar 21 2007.

[83] E. Mattei, M. Triventi, G. Calcagnini, F. Censi, W. Kainz, G. Mendoza, H. I. Bassen, and P. Bartolini, "Complexity of MRI induced heating on metallic leads: experimental measurements of 374 configurations," Biomed Eng Online, vol. 7, p. 11, Mar 3 2008.

[84] M. Triventi, E. Mattei, G. Calcagnini, F. Censi, P. Bartolini, W. Kainz, and H. Bassen, "Magnetic-resonance-induced heating of implantable leads," Ann Ist Super Sanita, vol. 43, no. 3, pp. 229-40, 2007.

[85] P. Nordbeck, F. Fidler, M. T. Friedrich, I. Weiss, M. Warmuth, D. Gensler, V. Herold, W. Geistert, P. M. Jakob, G. Ertl, O. Ritter, M. E. Ladd, W. R. Bauer, and H. H. Quick, "Reducing RF-related heating of cardiac pacemaker leads in MRI: implementation and experimental verification of practical design changes," (in eng), Magn Reson Med, vol. 68, no. 6, pp. 1963-72, Dec 2012.

[86] P. Nordbeck, O. Ritter, I. Weiss, M. Warmuth, D. Gensler, N. Burkard, V. Herold, P. M. Jakob, G. Ertl, M. E. Ladd, H. H. Quick, and W. R. Bauer, "Impact of imaging landmark on the risk of MRI-related heating near implanted medical devices like cardiac pacemaker leads," Magn Reson Med, vol. 65, no. 1, pp. 44-50, Jan 2011.

[87] P. Nordbeck, I. Weiss, P. Ehses, O. Ritter, M. Warmuth, F. Fidler, V. Herold, P. M. Jakob, M. E. Ladd, H. H. Quick, and W. R. Bauer, "Measuring RF-induced currents inside implants: Impact of device configuration on MRI safety of cardiac pacemaker leads," Magn Reson Med, vol. 61, no. 3, pp. 570-8, Mar 2009.

[88] R. Guo, J. Zheng, J. Chen, and W. Kainz, "RF-induced heating comparison between in-vivo and in-phantom for 1.5T MRI," in 2016 IEEE International Symposium on Electromagnetic Compatibility (EMC), 2016, pp. 121-125.

[89] J. A. Nyenhuis and C. R. Miller, "Calculation of heating of passive implants by the RF electromagnetic field in MRI," in 2011 XXXth URSI General Assembly and Scientific Symposium, 2011, pp. 1-4.

[90] M. Kozlov and G. Schaefers, "Analysis of power deposition and temperature rise due to presence of an implant inside a 1.5 t MRI RF coil," in 2015 37th Annual International Conference of the IEEE Engineering in Medicine and Biology Society (EMBC), 2015, pp. 5797-5800.

[91] S. M. Park, R. Kamondetdacha, and J. A. Nyenhuis, "Calculation of MRI-induced heating of an implanted medical lead wire with an electric field transfer function," J Magn Reson Imaging, vol. 26, no. 5, pp. 1278-85, Nov 2007.

[92] J. Jallal, "A standard implant for the determination of RF-induced local SAR in MRI heating Tests," MS MS thesis, ECE, Purdue University, 2009.

[93] S. Feng, R. Qiang, W. Kainz, and J. Chen, "A Technique to Evaluate MRI-Induced Electric Fields at the Ends of Practical Implanted Lead," IEEE Transactions on Microwave Theory and Techniques, vol. 63, no. 1, pp. 305-313, 2015.

[94] J. A. Nyenhuis, " Using MRI Simulations and Measurements to evaluate RF heating of Active Implants," in MRI Bioeffects, Safety, and Patient Management, F. Shellock and J. Crues, Eds., 2014.

[95] D. Li, X. Ji, J. Zheng, C. Pan, J. Chen, and W. Kainz, "A Novel Design of Implantable Esophageal Stent to Reduce the MRI RF-Induced Heating," IEEE Transactions on Electromagnetic Compatibility, vol. 59, no. 3, pp. 805-812, 2017.

[96] D. Li, J. Zheng, Y. Liu, C. Pan, W. Kainz, F. Yang, W. Wu, and J. Chen, "An Efficient Approach to Estimate MRI RF Field Induced In Vivo Heating for Small Medical Implants," IEEE Transactions on Electromagnetic Compatibility, vol. 57, no. 4, pp. 643-650, 2015.

[97] S. Atash-bahar, H. H. Sigmarsson, and D. Thompson, "Implantable neurostimulator lead transfer function based on the transmission line model," in 2017 IEEE International Symposium on Antennas and Propagation & USNC/URSI National Radio Science Meeting, 2017, pp. 401-402.

[98] R. King, "Antennas in material media near boundaries with application to communication and geophysical exploration, Part II: The terminated insulated antenna," IEEE Transactions on Antennas and Propagation, vol. 34, no. 4, pp. 490-496, 1986.

[99] P. E. Atlamazoglou and N. K. Uzunoglu, "A Galerkin moment method for the analysis of an insulated antenna in a dissipative dielectric medium," IEEE Transactions on Microwave Theory and Techniques, vol. 46, no. 7, pp. 988-996, 1998.

[100] W. Smythe, Static and Dynamic Electricity. 1950.

[101] A. Shah, F. Carreno, and A. Frazer, Therapeutic Modalities for Treatment Resistant Depression: Focus on Vagal Nerve Stimulation and Ketamine. 2014, pp. 83-93.

[102] VNS Therapy Products. Available: http://eu.cyberonics.com/en/vns-therapy-for-epilepsy/healthcare-professionals/vns-therapy/about-products. [Accessed: July 16, 2018]

[103] R. J. Coffey, R. Kalin, and J. M. Olsen, "Magnetic resonance imaging conditionally safe neurostimulation leads: investigation of the maximum safe lead tip temperature," (in en), Neurosurgery, vol. 74, no. 2, pp. 215-24; discussion 224-5, 2014.

VITA

Krishna Mukesh Singhal was born in Surat, India. Krishna received his Bachelor of Technology in Electronics and Communication Engineering from Nirma University, Ahmedabad in 2011. After graduation, Krishna enrolled at Purdue University in the PhD program in Electrical and Computer Engineering. At Purdue, he joined the MR Safety group in spring 2014 and pursued his research in the area of RF safety of Medical Implants under Prof John A. Nyenhuis. While at Purdue, he did his internship at Intel Corporation in SOC and Chipset Group, Folsom USA and was recipient of Departmental Impact Awards for consecutive quarters in 2013.